THE UNIVERSITY OF HULL

Intermetallic Compounds by Reductive Annealing

being a Thesis submitted for the Degree of Doctor of Philosophy

in the University of Hull

by

Rebecca Louise Kift
MChem (Hons)

November 2010

Acknowledgements

First and foremost, I would like to express my deepest gratitude to my supervisor, Dr Tim Prior, who has given me a considerable amount of support and guidance throughout my PhD. I would also like to thank Dr M. Grazia Francesconi for giving me the initial inspiration to work in solid state chemistry.

I am incredibly grateful to the friends I have made over the course of my PhD, who have made the department a great place to work, and supported me in many ways - many thanks go to Dr David Headspith, Mark Harrison, Dr Vincent Rocher and Rachel Smith. I would also like to thank past and present members of the Inorganic group, especially Dr Phil King for his advice and for those much-needed coffee breaks! Many thanks go to past project students including Robert Mitchell, Matt Simmons, Nick Drewett, Chris Kavanagh, Osman Goch and Andy Sharpe, for contributing to the positive atmosphere in the lab. Special thanks go to Stewart Bradley for opening up a whole new area of research into transition metal tellurides.

In addition, I would like to thank the technical staff in the department, especially Carol Kennedy for carrying out CHN analysis and providing me with lab equipment, no questions asked! I would also like to thank Bob Knight for carrying out ICP-MS, and Nigel Parkin and Mike Dunn for designing and constructing lab equipment.

I would like to thank Dr I. D. Watts at UCL for carrying out magnetic susceptibility measurements, and the EPSRC National Crystallography Service in Southampton for collecting single crystal x-ray diffraction data.

Thanks go to the University of Hull and EPSRC for providing me with a studentship enabling me to carry out this work.

Finally, I would like to express my gratitude to my family: I am eternally grateful, especially to Mum, Dad and Auntie Lynne for their longstanding support and the encouragement they have given me to achieve the best I possibly can. I would not have got to where I am today without them. Last but not least, I would like to thank Helen for supporting me in every possible way.

Publications and Presentations

Publications and presentations containing work described within this thesis:

1. R. L. Kift and T. J. Prior, *J. Alloys Compd*., 2010, **505**, 428-433.

2. T. J. Prior and R. L. Kift, *Acta Crystallogr., Sect. B: Struct. Sci*., 2010, *in press.*

3. T. J. Prior and R. L. Kift, *J. Chem. Crystallogr*., 2009, **39**, 558-563.

4. R. L. Kift, 'Low Temperature Synthesis of Transition Metal Antimonides' (oral presentation), RSC Dalton Division Northern Regional Meeting, University of Hull, 7th July 2010.

5. R. L. Kift, 'Low Temperature Synthesis of Transition Metal Antimonides' (oral presentation), PhD Colloquia, University of Hull, 5th July 2010.

6. R. L. Kift, 'Low Temperature Synthesis of New Ternary Intermetallics' (poster presentation), RSC Solid State Group Christmas Meeting, Open University, Milton Keynes, 17th-18th December 2009.

7. R. L. Kift, 'Low Temperature Synthesis of Intermetallics' (poster presentation), RSC Dalton Division Northern Regional Meeting, University of Manchester, 7th July 2009.

8. R. L. Kift, 'Low Temperature Synthesis of Intermetallics' (poster presentation), RSC Solid State Group Christmas Meeting, Southampton, 18th-19th December 2008.

Abstract

The majority of the work described in this thesis focuses on the development of a new synthetic route to binary and ternary intermetallic compounds, which avoids the need for reaction at very high temperatures, multi-step reactions, reaction under vacuum and/or the synthesis of precursors. The route was adapted from a synthetic route reported for the synthesis of ternary and quaternary nitrides adopting the η-carbide and filled β-manganese structures, where mixed metal oxides were reduced under an atmosphere of 10% hydrogen in nitrogen. In this work, binary intermetallic compounds including metal antimonides, germanides and bismuthides were prepared by reducing mixed metal oxides under 10% hydrogen in argon. A variety of high purity antimonides were synthesised, including NiSb, CoSb, $CoSb_3$, Cu_2Sb and SnSb. Tailoring of some of the properties of these antimonides was attempted by introducing other atoms into the crystal structures, thereby forming ternary compounds. The most notable ternary antimonides prepared include the solid solution of NiSb in CoSb, and the solid solution of $RhSb_3$ in $CoSb_3$. The Sb-Sb bond lengths in the solid solution of NiSb in CoSb display an unexpected trend, passing through a minimum. Reasons for this based on electronic grounds are suggested. Notably the Te-Te bond length within the solid solution of NiTe in CoTe does not display this variation. The solid solution of $RhSb_3$ in $CoSb_3$ is potentially very useful as the introduction of rhodium into the structure may alter the thermoelectric behaviour of the material. However, thermoelectric measurements on the compounds are yet to be carried out.

Other work described in this thesis focuses on attempts to synthesise transition metal nitrides, firstly by extending a synthetic route reported for the synthesis of η-carbide and filled β-manganese nitrides by introducing germanium into Fe_3Mo_3N, Co_3Mo_3N and the hypothetical compound 'Ni_3Mo_3N', and secondly by the thermal treatment of potential precursors to binary transition metal nitrides. The synthesis and magnetic properties of Fe_2GeMo_3N, Co_2GeMo_3N and Ni_2GeMo_3N are discussed, and the synthesis of solid solutions of Fe_2GeMo_3N and Ni_2GeMo_3N in Co_2GeMo_3N are described. In addition, experiments to determine whether a small interstitial (in this case nitrogen) is needed to stabilise certain compounds adopting the η-carbide and filled β-manganese structures are described. The preparation, crystal structures and thermal treatment of metal urea

complexes as potential precursors to binary nitrides are also discussed. Two of the metal urea complexes synthesised, ($[Cr(urea)_4(H_2O)_2][NO_3]_3$ and $[Fe(urea)_6][NO_3]$), are particularly interesting: $[Cr(urea)_4(H_2O)_2][NO_3]_3$ crystallises in a primitive, but close to C-centred unit cell, and $[Fe(urea)_6][NO_3]_3$ crystallises in a C-centred cell which is related by a five-fold expansion to a smaller pseudo C-centred cell previously reported for the same structure.

1.0 Introduction 1
1.1 Alloys, Intermetallics and Solid Solutions 1
1.2 Synthesis of Intermetallics 3
1.3 Structures of Binary Transition Metal Antimonides 5
1.3.1 MSb Stoichiometry 5
1.3.1.1 NiAs Structure 6
1.3.1.2 MnP Structure 8
1.3.1.3 NaCl Structure 9
1.3.1.4 ZnAs Structure 10
1.3.1.5 ZrSb Structure 12
1.3.2 MSb_2 Stoichiometry 13
1.3.2.1 FeS_2 Structure (*Pyrite*) 13
1.3.2.2 FeS_2 Structure (*Marcasite*) 15
1.3.2.3 $FeAs_2$ Structure 16
1.3.2.4 $CoSb_2$ Structure 17
1.3.2.5 $CuAl_2$ Structure 19
1.3.3 MSb_3 Stoichiometry 20
1.3.3.1 $CoAs_3$ Structure (*Skutterudite*) 20
1.3.4 M_2Sb Stoichiometry 22
1.3.4.1 Cu_2Sb Structure 22
1.3.4.2 La_2Sb Structure 24
1.3.5 M_3Sb Stoichiometry 26
1.3.5.1 Cr_3Si Structure 27
1.3.5.2 Cu_3Ti Structure 28
1.3.6 Other Relevant Structures 29
1.3.6.1 Mo_3Sb_7 29
2.0 Experimental 32
2.1 Synthetic Methods 32
2.1.1 Reductive Synthesis 32
2.1.2 Single Crystal Preparation 32
2.2 Structural Determination 33

2.2.1 Crystallography 33
2.2.1.1 Unit Cells and Crystal Systems 33
2.2.1.2 Lattice Types 34
2.2.1.3 Symmetry 35
2.2.1.4 Miller Indices 36
2.2.2 X-ray Diffraction 37
2.2.2.1 Generation of X-ray Radiation 37
2.2.2.2 Bragg's Law 38
2.2.2.3 Intensities of Diffracted X-rays 40
2.2.3 X-ray Powder Diffraction 42
2.2.3.1 Data Collection 42
2.2.3.2 Rietveld Method 43
2.2.4 Single Crystal X-ray Diffraction 48
2.2.4.1 Data Collection 48
2.2.4.2 Fourier Summation 49
2.2.4.3 Structure Solution 50
2.2.4.3.1 Direct Methods 50
2.2.4.3.2 Patterson Method 50
2.3 Physical Measurements 51
2.3.1 SQUID Magnetometry 51
2.3.1.1 Magnetism 51
2.3.1.1.1 Curie and Curie-Weiss Laws 52
2.3.1.1.2 Pauli Paramagnetism 54
3.0 First Steps: Binary Intermetallics 55
3.1 Transition Metal Nitrides: Background to the Method 55
3.2 Antimonides 56
3.2.1 Iron Antimonides 56
3.2.1.1 ε-FeSb 57
3.2.1.2 $FeSb_2$ 57
3.2.2 Cobalt Antimonides 60
3.2.2.1 CoSb 64

3.2.2.2 $CoSb_2$ 65
3.2.2.3 $CoSb_3$ 67
3.2.3 Nickel Antimonides 69
3.2.3.1 NiSb 70
3.2.3.2 $NiSb_2$ 71
3.2.4 Copper Antimonides 73
3.2.4.1 “CuSb” 73
3.2.4.2 Cu_2Sb 74
3.2.4.3 Cu_3Sb 75
3.2.4.4 $Cu_{10}Sb_3$ and $Cu_{11}Sb_3$ 77
3.2.4.5 Cu_4Sb 78
3.2.5 Zinc Antimonides 79
3.2.5.1 ZnSb 79
3.2.6 Molybdenum Antimonides 80
3.2.6.1 Mo_3Sb_7 80
3.2.7 Tungsten Antimonides 82
3.2.7.1 W_3Sb_7 82
3.2.8 Tin Antimonides 83
3.2.8.1 SnSb 83
3.3 Germanides 86
3.3.1 Iron Germanides 86
3.3.1.1 FeGe 86
3.3.1.2 Fe_3Ge and Fe_5Ge_3 88
3.3.2 Cobalt Germanides 89
3.3.2.1 CoGe and Co_2Ge 89
3.3.3 Nickel Germanides 89
3.3.3.1 NiGe and Ni_3Ge 89
3.3.4 Copper Germanides 89
3.3.4.1 Cu_3Ge 90
3.4 Bismuthides 90
3.4.1 Iron, Cobalt and Zinc Bismuthides 90

3.4.2 Nickel Bismuthides 90
3.4.2.1 NiBi 91
3.4.2.2 $NiBi_3$ 92
3.4.3 Copper Bismuthides 94
3.5 Reaction Mechanism 95
3.6 Scope of the Method 95
4.0 Substitutions in Compounds Crystallising with the Nickel Arsenide Structure 100
4.1 Antimonides 100
4.1.1 Introduction of Ni into CoSb ($Co_{1-x}Ni_xSb$) 100
4.1.2 Introduction of Cu into CoSb ($Co_{1-x}Cu_xSb$) 110
4.1.3 Introduction of Cu into NiSb ($Ni_{1-x}Cu_xSb$) 114
4.1.4 Introduction of Fe into CoSb ($Co_{1-x}Fe_xSb$) 124
4.2 Tellurides 130
4.2.1 Metalloid Site Substitutions 130
4.2.1.1 Introduction of Te into CoSb ($CoSb_{1-x}Te_x$) 130
4.2.1.2 Introduction of Te into NiSb ($NiSb_{1-x}Te_x$) 132
4.2.2 Transition Metal Site Substitutions 133
4.2.2.1 Introduction of Ni into CoTe ($Co_{1-x}Ni_xTe$) 133
4.2.2.2 Introduction of Cu into CoTe ($Co_{1-x}Cu_xTe$) 139
4.2.2.3 Introduction of Cu into NiTe ($Ni_{1-x}Cu_xTe$) 139
4.3 Summary 139
5.0 Substitutions in Compounds Crystallising with the Skutterudite ($CoAs_3$) Structure 141
5.1 Transition Metal Site Substitutions 141
5.1.1 Introduction of Rh into $CoSb_3$ ($Co_{1-x}Rh_xSb_3$) 141
5.1.2 Introduction of Ir into $CoSb_3$ ($Co_{1-x}Ir_xSb_3$) 150
5.1.3 Introduction of Cu into $CoSb_3$ ($Co_{1-x}Cu_xSb_3$) 154
5.1.4 Introduction of Zn into $CoSb_3$ ($Co_{1-x}Zn_xSb_3$) 155
5.2 Attempted Synthesis of the Isoelectronic Phase, $Fe_{0.5}Ni_{0.5}Sb_3$ 155
5.3 Metalloid Site Substitutions 156
5.3.1 Introduction of Sn into $CoSb_3$ ($CoSb_{3-x}Sn_x$) 156
5.3.2 Introduction of Bi into $CoSb_3$ ($CoSb_{3-x}Bi_x$) 158

5.4 Summary 158
6.0 Substitutions in Cu_2Sb 160
6.1 Transition Metal Site Substitutions 160
6.1.1 Introduction of Mn into Cu_2Sb ($Cu_{2-x}Mn_xSb$) 160
6.1.2 Introduction of Fe into Cu_2Sb ($Cu_{2-x}Fe_xSb$) 161
6.1.3 Introduction of Co into Cu_2Sb ($Cu_{2-x}Co_xSb$) 161
6.1.4 Introduction of Ni into Cu_2Sb ($Cu_{2-x}Ni_xSb$) 162
6.1.5 Introduction of Ag into Cu_2Sb ($Cu_{2-x}Ag_xSb$) 165
6.2 Metalloid Site Substitutions 165
6.2.1 Introduction of Te into Cu_2Sb ($Cu_2Sb_{1-x}Te_x$) 165
6.3 Summary 166
7.0 Transition Metal Nitrides: η-Carbide and Filled β-Manganese Nitrides, and Precursor Routes to Binary Nitrides 167
7.1 η-Carbide Nitrides 167
7.1.1 η-Carbide Structure 167
7.1.1 Synthetic Routes 169
7.2 Filled β-Manganese Nitrides 170
7.2.1 Filled β-Manganese Structure 170
7.2.1 Synthetic Routes 171
7.3 Synthesis of η-Carbide Nitrides *via* Reduction-Nitridation 172
7.3.1 M_2GeMo_3N (M = Fe, Co, Ni) 173
7.3.2 M_2GeMo_3 (M = Fe, Co, Ni) 183
7.3.3 η-Carbide Solid Solutions 184
7.3.3.1 Introduction of Fe into Co_2GeMo_3N ($Co_{2-x}Fe_xGeMo_3N$) 184
7.3.3.2 Introduction of Ni into Co_2GeMo_3N ($Co_{2-x}Ni_xGeMo_3N$) 186
7.4 Synthesis of Filled β-Manganese Nitrides *via* Reduction-Nitridation 189
7.4.1 Ni_2Mo_3N 189
7.4.2 Ni_2Mo_3 190
7.5 Precursor Routes to Binary Transition Metal Nitrides 191
7.5.1 Preparation and Thermal Treatment of Transition Metal Urea Nitrate Complexes 192

7.5.1.1 $[Cr(urea)_4(H_2O)_2][NO_3]_3$ 192
7.5.1.2 $[Fe(urea)_6][NO_3]_3$ 196
7.5.1.3 $Cu(urea)_2(H_2O)_3(NO_3).(urea).(NO_3)$ 199
7.5.1.4 $[Zn(urea)_4(H_2O)_2][NO_3]_2$ 202
7.5.1.5 $[Co(urea)_4(H_2O)_2][NO_3]_2$ 204
7.5.1.6 $[Ni(urea)_4(H_2O)_2][NO_3]_2$ 205
7.5.2 Reaction of Transition Metal Nitrates with Urea 205
7.6 Summary 206
8.0 Conclusions 208
9.0 Appendix 211
10.0 References 238

1.0 Introduction

This work concerns, amongst other things, the synthesis of compounds which are referred to here as 'intermetallics'. The current chapter aims to define this term and discuss the synthesis and structures of relevant intermetallic compounds, in particular binary transition metal antimonides.

1.1 Alloys, Intermetallics and Solid Solutions

Solid solutions are homogeneous solids which exist over a range of composition and retain the crystal structure of the parent compound.[1] There are several types of solid solution. The most well known solid solutions are based on a metallic array and are therefore classed as alloys. Solid solutions forming alloys are split into two types: substitutional and interstitial.[1] Interstitial solid solutions are formed when the solute atoms fit into the interstices between solvent atoms. Solute atoms are defined as those with the lower concentration in the solution, when compared with the solvent atoms. This system is only viable when the solute atoms are much smaller than the solvent atoms. A good example of an interstitial solid solution is that of carbon in γ-Fe, which forms the basis of steels. Substitutional solid solutions are formed when some of the solute atoms in the solution replace an equal number of solvent atoms.[1] The two types of atom are then situated on the same crystallographic site. The relative sizes of the atoms are important when forming a substitutional solid solution: the crystal structure may have to distort in order to accommodate a larger atom, and this is only possible to a limited degree. Hume-Rothery *et al*. discovered that the solubility of one element in another is very limited if the atoms differ in size by more than 15%.[2]

A huge variety of solid solutions are based on a range of crystal structures, not just on a metallic array. The chemistry of these solid solutions is generally very important, as the properties of a material can often be tailored by introducing different atoms into the structure. The solid solution $BaHf_{1-x}Zr_xN_2$ is an example of this type of solid solution, where both $BaHfN_2$ and $BaZrN_2$ crystallise with the same structure.[3] In addition, the double-substituted perovskite $La_{1-y}Sr_yCo_{1-x}Fe_xO_{3-\delta}$ is another example of this type of solid

solution.[4] The solid solutions dealt with in this work are of this type *i.e.* they are not based on the crystal structure of a metal.

Solid solutions can be ordered or disordered, and can undergo transitions between the two states.[1] High temperature solid solutions are usually disordered. However, upon slow cooling or annealing at a low temperature a transition to an ordered structure can occur. Ordering of a solid solution usually results in the construction of a superstructure (long-range order). The formation of a superstructure is more likely if the solute atoms have a tendency to remain as far apart as possible. This can be thought of as a method of reducing the lattice strain caused by the introduction of the solute atoms. It follows that the greater the difference in size between the solute and solvent atoms, the higher the chance of superstructure formation.

If the atoms have significantly different electronegativities, there is a tendency for a stable *intermetallic* compound to be formed rather than an *alloy*.[1] An intermetallic compound is loosely defined as a compound consisting of two or more metals: the metal is defined as a material which has a negative relationship between temperature and electronic conductivity,[5] thereby including metalloids in the definition. Intermetallic compounds display several features, including the following:

- A lack of simple bonding or valence rules and closed-shell states[5]
- Delocalised bonding of the valence electrons[5]
- Complex bonding, dependent on the elements involved, the structure and the stoichiometry[5]

The third point displays the principal difference between alloys and intermetallics: alloys tend to exhibit metallic bonding, whereas the bonding in intermetallics usually consists of a mixture of metallic, covalent and ionic bonding. This mixed bonding means that oxidation states are difficult to assign and are often meaningless in compounds of this nature. It also explains why many intermetallic compounds are non-stoichiometric. The other main difference between alloys and intermetallics is that alloys are based on the crystal structure of the parent metal, whereas intermetallics are not. Most of the work discussed here deals with intermetallic compounds, in particular transition metal antimonides.

1.2 Synthesis of Intermetallics

Intermetallic compounds are conventionally synthesised by the direct melting of elemental starting reagents in the absence of oxygen. Reactions must therefore be carried out in either a vacuum or in an argon atmosphere. By carrying out these reactions in the melt the rate of diffusion of atoms is increased. However, this synthetic method has several limitations. Firstly, control over the product stoichiometry is limited if the product formed melts incongruently *i.e.* it does not melt uniformly, and therefore crystallises in undesired phases. Secondly, the final products obtained *via* this technique are generally thermodynamically stable. It is therefore difficult to obtain metastable products, or those which are only stable at low temperatures. Arc melting is an adaptation of this conventional route; the temperature reached in an arc furnace is much higher than that reached in a conventional electric furnace, allowing very high temperature reactions to be carried out.

Intermetallic compounds can also be synthesised by powder metallurgy routes. The most common of these is the 'shake and bake' method, routinely used in many areas of solid state chemistry. In this type of reaction, powdered starting reagents are intimately mixed, often compressed, and heated at high temperatures (often of the order of 1000 °C). Performing this type of reaction using finely ground powders rather than particles of larger size maximises the inter-phase contact and increases the rate at which a homogeneous product is obtained. Compression of the mixed reagents, *e.g.* by pelletising, usually leads to a faster reaction, as the diffusion of atoms through grain boundaries is increased. A high temperature is required in order to enable the breaking of bonds and the diffusion of atoms through the solid. The relationship between the diffusion coefficient and the temperature is described by a modified version of the Arrhenius equation, so that the higher the temperature, the faster the rate of diffusion of atoms through the solid. Other less conventional routes to intermetallic compounds, and specifically binary transition metal antimonides, include:

Co-precipitation: Co-precipitation is a solution-based technique which allows a high degree of homogenisation to be achieved between reagents, as well as a small particle size, thereby speeding up the rate of reaction. The procedure is usually carried out by dissolving metal oxalates in water, mixing, and heating to promote evaporation of the water.[6] The

oxalates are gradually precipitated together, resulting in a fine powder containing the metal cations mixed together on an atomic scale. The powder is then heated as normal, although as a result of the high degree of homogenisation, much lower temperatures are required for the reaction to occur. There are, however, several drawbacks to the method: different solubilities of the two reagents in water, different precipitation rates and the supersaturation of solutions all give rise to problems. Co-precipitation techniques have been used in the past to prepare transition metal antimonides. $CoSb_3$, in particular, was synthesised by the co-precipitation of cobalt oxalate and antimony trioxide.[7] Co-precipitation was followed by a period of calcining (350 °C) and a period of reduction under hydrogen (450 – 600 °C).

Metathesis: The synthesis of transition metal antimonides *via* the metathetical reaction of Na_3Sb with transition metal halides has been reported by Hector and Parkin[8] and also Carmalt *et al.*[9] Hector and Parkin reported the synthesis of various transition metal antimonides *via* an exothermic self-propagating reaction initiated at temperatures of between 25 and 500 °C, under a nitrogen atmosphere.[8] NaCl is formed as a by-product in this reaction (when the transition metal halide used is a chloride), and due to its high lattice enthalpy its formation is the driving force for the reaction. In addition, Na_3Sb has a low stability, and therefore a high reactivity. Carmalt *et al.* adapted a metathetical route in order to form nickel and cobalt antimonides *via* refluxing a mixture of Na_3Sb and a transition metal bromide (*e.g.* $NiBr_2$) in toluene for 48 hours (under a nitrogen atmosphere), washing with ethanol and distilled water, and drying the resulting powder under vacuum.[9] This was followed by a period of annealing under vacuum, at 500 °C for 48 hours.

Polyol process: The polyol process exploits high-boiling polyalcohol solvents, which also act as mild reducing agents when heated.[10] It was originally developed for the synthesis of nanocrystalline powders of palladium and other late transition metals. It has since been modified to produce nanocrystals of a variety of elements, alloys and intermetallics,[10] including binary transition metal antimonides. Cable *et al.* synthesised PtSb, CoSb and $CoSb_3$ *via* a modification of the polyol process.[10] Starting reagents were dissolved in tetraethylene glycol, reduced at room temperature with sodium borohydride, and subsequently heated to a temperature of between 175 and 240 °C. Reactions and manipulations were carried out under an argon atmosphere. The starting reagents used were

K_2PtCl_6 and $SbCl_3$ to produce PtSb, and $Co(OOCCH_3)_2.4H_2O$ and $SbCl_3$ in the appropriate stoichiometric ratio to produce CoSb and $CoSb_3$.

Mechanical alloying: Mechanical alloying is a dry milling process in which blended crystalline powders are violently deformed by grinding under a controlled atmosphere.[11] It is particularly useful for the synthesis of alloys whose components have a high melting point. Amornpitoksuk and Suwanboon prepared $CoSb_2$ by mechanical alloying.[12] Elemental cobalt and antimony powders were milled in a ball mill under an argon atmosphere. The synthesis of nanocrystalline $CoSb_2$ was complete after 30 hours. Peaks in the x-ray powder diffraction profile of $CoSb_2$ were broad and weak, suggesting poor crystallinity. However, the peak size and shape was attributed to the small crystallite size achieved by ball milling.

Due to the high temperatures required for the direct synthesis of intermetallics from the elements, and the need of a vacuum and/or multi-step reactions encountered in other less traditional routes, the development of a new low temperature simple synthetic route is desirable. A route of this nature is presented in this work.

1.3 Structures of Binary Transition Metal Antimonides

Binary transition metal antimonides have been shown to exhibit properties that can be utilised in a range of applications. Some of these properties include thermoelectric behaviour,[13] superconductivity[14] and semiconductivity.[15] They also have a potential use as lithium-ion battery anode materials.[16,17,18] As mentioned in section 1.1, the bonding in intermetallics is often very complicated, with no single type of bonding predominating over another. The relationships between bonding and structure within and between different intermetallic compounds are therefore of great academic interest. This section aims to describe the synthesis and structures of binary transition metal antimonides, and discuss the structural relationships between them.

1.3.1 MSb Stoichiometry

Binary transition metal antimonides with a 1:1 transition metal:antimony ratio adopt five different structure types. The most common of these is the nickel arsenide (NiAs) structure.

Other structure types that are commonly adopted by 1:1 transition metal antimonides include the sodium chloride (halite), zinc arsenide (ZnAs), zirconium antimonide (ZrSb) and manganese phosphide (MnP) structures. Table 1-1 gives a comprehensive overview of the structure types adopted by 1:1 transition metal antimonides.

Sc NaCl	**Ti** NiAs	**V** NiAs	**Cr** NiAs	**Mn** NiAs	**Fe** NiAs	**Co** NiAs	**Ni** NiAs	**Cu** N/A	**Zn** ZnAs
Y NaCl	**Zr** ZrSb	**Nb** N/A	**Mo** N/A	**Tc** N/A	**Ru** MnP	**Rh** MnP	**Pd** NiAs	**Ag** N/A	**Cd** ZnAs
	Hf ZrSb	**Ta** N/A	**W** N/A	**Re** N/A	**Os** N/A	**Ir** NiAs	**Pt** NiAs	**Au** N/A	**Hg** N/A

Table 1-1: Structures adopted by 1:1 binary transition metal antimonides. N/A indicates that no 1:1 phase exists

1.3.1.1 NiAs Structure

Nickel arsenide crystallises in the space group $P6_3/mmc$ and contains two NiAs units in the hexagonal unit cell (Figure 1-1). The nickel atom is located at the cell origin (0, 0, 0), and the arsenic atom is located on (⅓, ⅔, ¼).

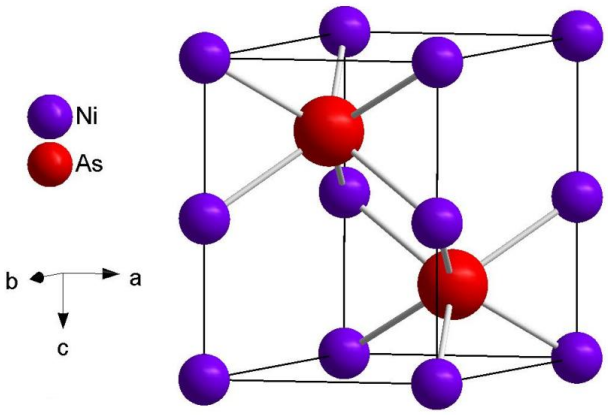

Figure 1-1: Unit cell of nickel arsenide

The structure can be described in terms of the filling of octahedral holes or in terms of the arrangement of polyhedra. In the hole filling description, there is an *hcp* (hexagonal close packed) array of arsenic atoms with nickel atoms occupying all of the octahedral holes.

This results in the formation of $NiAs_6$ octahedra, which share pairs of opposite faces to form chains running parallel to the *c* axis, and which share edges in the *ab* plane (Figure 1-2). Alternatively, the structure can be described in terms of edge-sharing $AsNi_6$ trigonal prisms, highlighted in yellow in Figure 1-2.

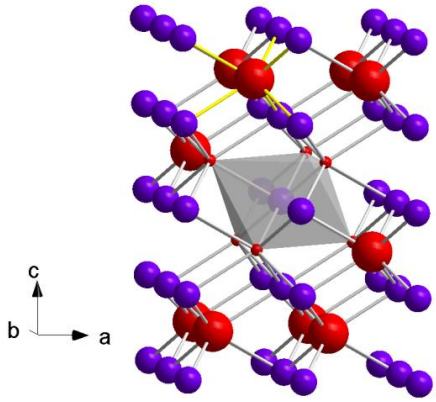

Figure 1-2: The nickel arsenide structure. The grey polyhedron represents the octahedral coordination of nickel. The yellow bonds represent the trigonal prismatic coordination of arsenic

The bonding in nickel arsenide is considered to be predominantly covalent. The presence of a highly polarising, small and relatively highly charged 'cation' and a large, polarisable 'anion' suggests that electrons will be shared rather than donated. In addition, the presence of face-sharing octahedra suggests the presence of short metal-metal distances (2.51 Å), consistent with a covalent structure.

The nickel arsenide structure is widely adopted by first row transition metal antimonides (those from Ti to Ni in the Periodic Table).[19,20,21,22,23,24] All Group 10 1:1 binary antimonides also adopt this structure,[23] as well as IrSb.[25]

Phases adopting the NiAs structure often exhibit broad ranges of homogeneity, but compositions rarely include the equiatomic ratio.[23] NiSb and CoSb are the only compounds of this type to exist with compositions either side of this ratio. Other compounds only form metal rich compositions ($M_{1+x}Sb$). In these metal rich compositions, the additional metal atoms are positioned on (⅓, ⅔, ¾).[23] This is discussed in more detail in section 3.2.2.

1.3.1.2 MnP Structure

Manganese phosphide crystallises in the space group *Pnma*, and contains four MnP units in the orthorhombic unit cell (Figure 1-3).

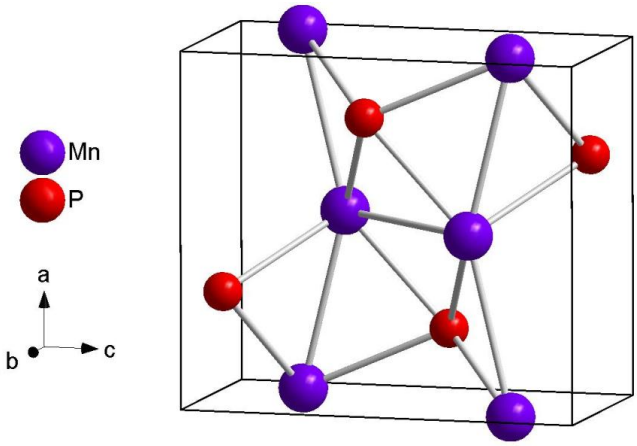

Figure 1-3: Unit cell of manganese phosphide

Each manganese atom is coordinated by six phosphorus atoms to form a distorted MnP_6 octahedron. The octahedra share edges in the *bc* plane, and faces in the *a* direction (Figure 1-4). The structure is related to the nickel arsenide structure, where $NiAs_6$ octahedra share edges in the *ab* plane, and faces in the *c* direction. It is likely that the distortion of the octahedra arises from the difference in size of the transition metal and pnictogen: in the nickel arsenide structure, the pnictogen is larger than the transition metal, whereas in the manganese phosphide structure, the transition metal is larger than the pnictogen.

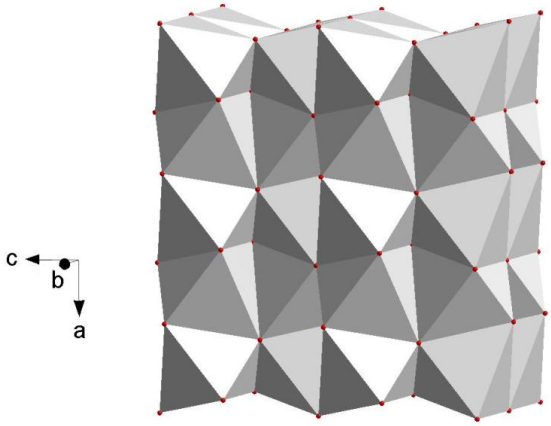

Figure 1-4: Structure of manganese phosphide, highlighting the connectivity of the distorted MnP_6 octahedra

The manganese phosphide structure is adopted by binary antimonides containing large transition metals, such as RuSb and RhSb.[26]

1.3.1.3 NaCl Structure

Sodium chloride crystallises in the space group $Fm\bar{3}m$, and contains four NaCl units in the cubic unit cell (Figure 1-5).

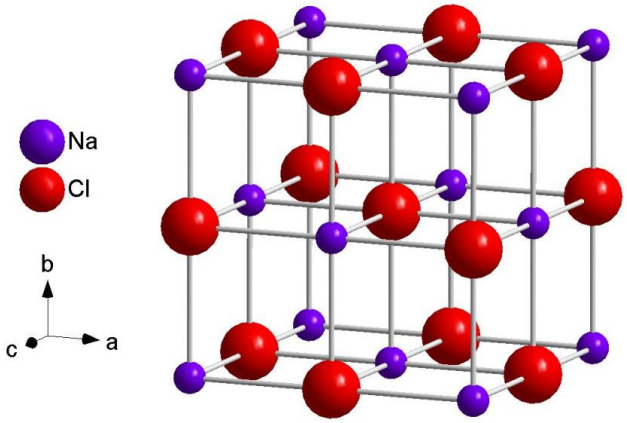

Figure 1-5: Unit cell of sodium chloride

The sodium chloride structure can be described in several ways. One description depicts the structure as consisting of two interpenetrating *fcc* (face centred cubic) arrays of sodium cations and chloride anions. It can also be described in terms of the packing arrangement. In this case, the chloride ions form a *ccp* (cubic close packed) array and the sodium ions occupy all of the octahedral holes. The cations and anions are coordinated in a 6:6 octahedral fashion, and therefore both the cation and anion sites are topologically identical. In addition, the structure can be described as a 3D array of edge- and corner-sharing octahedra (Figure 1-6).

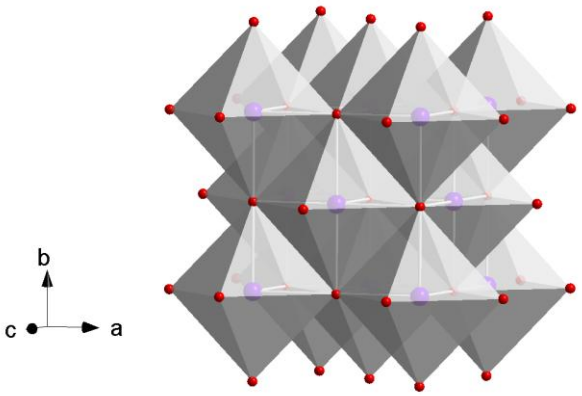

Figure 1-6: Polyhedral representation of the sodium chloride structure, highlighting the edge- and corner-sharing octahedra

The sodium chloride structure is adopted by ScSb and YSb.[27,28] This is most probably a result of the large size of both scandium and yttrium. Covalent structures tend to favour polarising atoms, which in the ionic state would be small, highly charged cations, whereas ionic structures tend to favour larger cations with lower charges. Sodium chloride is relatively ionic, with little metal-metal interaction due to long metal-metal distances (3.99 Å). Compared to the number of phases adopting the nickel arsenide structure, it is a far less common structure type for 1:1 binary transition metal antimonides to adopt.

1.3.1.4 ZnAs Structure

Zinc arsenide crystallises in the orthorhombic space group *Pbca*. The structure can be described in terms of Zn_2As_2 planar rings (diamonds), which are highlighted in Figure 1-7.[29]

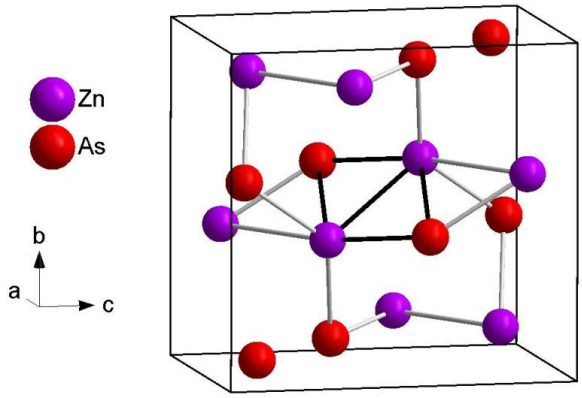

Figure 1-7: Unit cell of ZnAs, highlighting the Zn_2As_2 planar rings (black)

Each Zn_2As_2 diamond is linked to ten others, as shown in Figure 1-8.

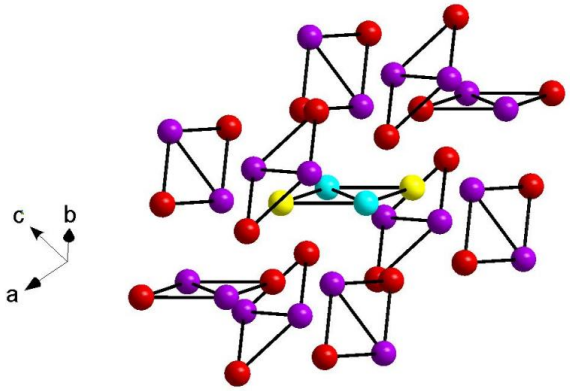

Figure 1-8: Structure of ZnAs, showing the array of Zn_2As_2 diamonds

The structure can also be described as an array of corner-sharing distorted $ZnAs_4$ tetrahedra, which is depicted in Figure 1-9.[29]

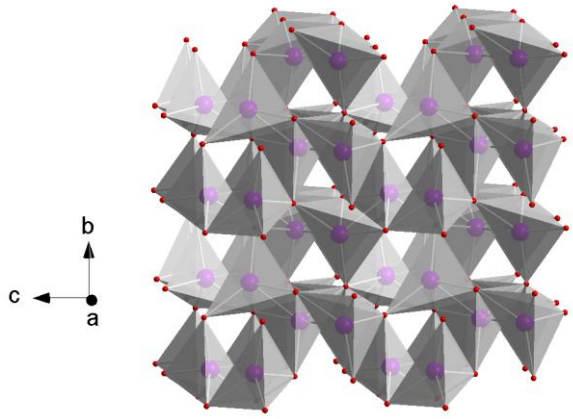

Figure 1-9: Structure of ZnAs, showing corner-sharing distorted $ZnAs_4$ tetrahedra

The ZnAs structure is adopted by ZnSb and CdSb.[30,31]

1.3.1.5 ZrSb Structure

ZrSb and HfSb crystallise in the orthorhombic space group *Cmcm*.[32] The unit cell is shown in Figure 1-10.

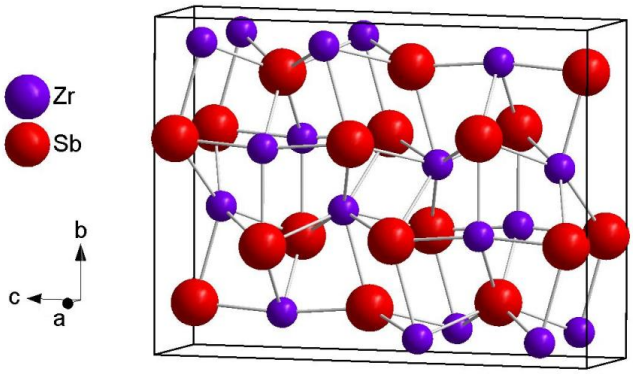

Figure 1-10: Unit cell of zirconium antimonide

The structure can be described in terms of sheets of interlinked co-facial chains of $SbZr_6$ trigonal prisms running parallel to the *a* axis. The antimony atoms at the centre of the trigonal prisms are coordinated by a seventh bond in a monocapped trigonal prismatic coordination to a zirconium atom of the neighbouring chain of trigonal prisms. This monocapping forces the chains to be staggered with respect to one another. The sheets are separated by layers of weakly bonded antimony atoms in the *ab* plane (Figure 1-11).[33]

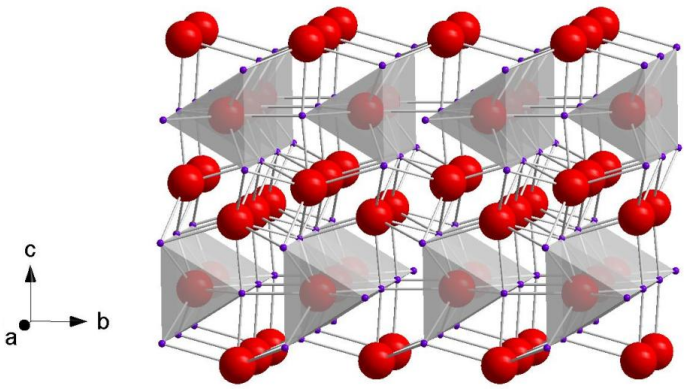

Figure 1-11: Polyhedral representation of ZrSb, showing chains of $SbZr_6$ trigonal prisms running parallel to the *a* axis

1.3.2 MSb_2 Stoichiometry

Binary transition metal antimonides with a 1:2 transition metal:antimony ratio adopt five main structure types: the $FeAs_2$, FeS_2 (marcasite or pyrite), $CoSb_2$ and $CuAl_2$ structure types. Other structure types adopted by 1:2 transition metal antimonides include the Co_2Si, $OsGe_2$, $TiAs_2$ and $MoAs_2$ structures. These less common structure types will not be discussed here. Table 1-2 gives a comprehensive overview of the structure types adopted by 1:2 transition metal antimonides.

Sc N/A	**Ti** $CuAl_2$	**V** $CuAl_2$	**Cr** $FeAs_2$	Mn N/A	**Fe** $FeAs_2$	**Co** $CoSb_2$	**Ni** $FeS_2^{(m)}$	Cu N/A	Zn N/A
Y N/A	**Zr** Co_2Si	**Nb** $OsGe_2$	Mo N/A	Tc N/A	**Ru** $FeAs_2$	**Rh** $CoSb_2$	**Pd** $FeS_2^{(p)}$	Ag N/A	Cd N/A
	Hf $TiAs_2$	**Ta** $MoAs_2$	W N/A	Re N/A	**Os** $FeAs_2$	**Ir** $CoSb_2$	**Pt** $FeS_2^{(p)}$	**Au** $FeS_2^{(p)}$	Hg N/A

Table 1-2: Structures adopted by 1:2 binary transition metal antimonides. N/A indicates that no 1:2 phase exists. $^{(m)}$ and $^{(p)}$ denote marcasite and pyrite structures, respectively

1.3.2.1 FeS_2 Structure (*Pyrite*)

FeS_2 (*Pyrite*) crystallises in the space group $Pa\bar{3}$, with four FeS_2 units in the cubic unit cell (Figure 1-12).

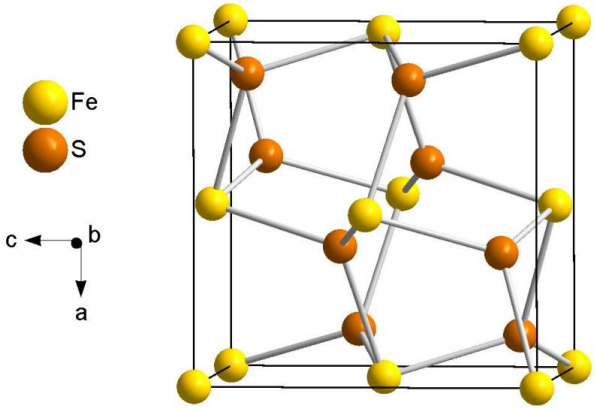

Figure 1-12: Unit cell of FeS_2 (*Pyrite*)

The pyrite structure is closely related to the NaCl structure;[34] the centres of the Fe atoms and the S_2 groups occupy the positions of Na^+ and Cl^-. This can be seen in Figure 1-13, which highlights the interactions between the sulfur atoms in the S_2 groups. If the unit cell was considered to be split into eight cubes, the S_2 groups would be located on alternate cube corners, parallel to the body diagonals of the octants. In this orientation, the S_2 groups point directly towards the iron atoms.

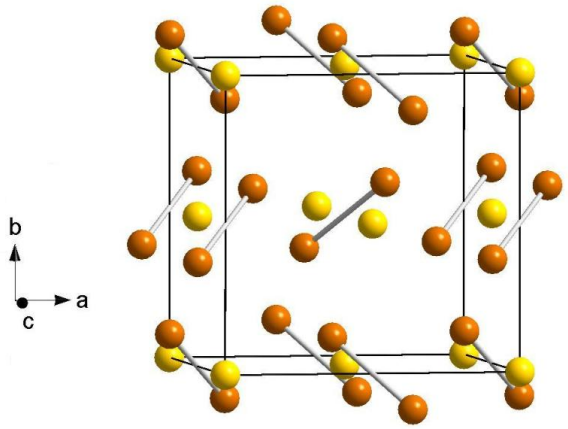

Figure 1-13: Structure of *Pyrite*, highlighting its relation to the NaCl structure

The structure can also be described in terms of corner-sharing FeS_6 octahedra or corner-sharing distorted SFe_3S tetrahedra.[35] These are shown in Figure 1-14.

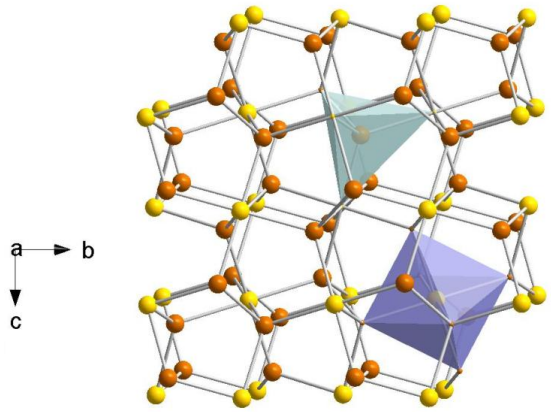

Figure 1-14: Diagram of the pyrite structure showing FeS_6 octahedra and distorted SFe_3S tetrahedra

The pyrite structure is adopted by $PdSb_2$, $PtSb_2$ and $AuSb_2$.[36]

1.3.2.2 FeS_2 Structure (*Marcasite*)

FeS_2 (*Marcasite*) crystallises in the space group *Pnnm*, and contains two FeS_2 units in the orthorhombic unit cell (Figure 1-15).

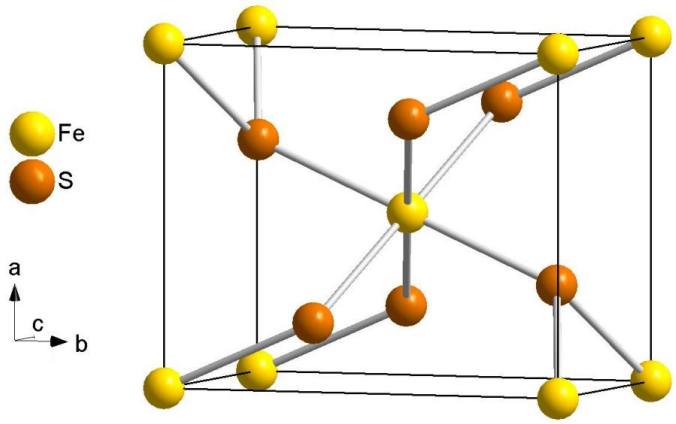

Figure 1-15: Unit cell of FeS_2 (*Marcasite*)

The structure consists of chains of edge-sharing FeS_6 octahedra, which run parallel to the *c* axis (Figure 1-16). The chains are connected to each other *via* corners. The structure is derived from the rutile structure, by rotating the chains of octahedra so that there are short S-S distances (2.21 Å) between the sulfur atoms of different chains.[34] This leads to an orthorhombic unit cell, compared to the tetragonal unit cell possessed by the rutile structure, where the distance between anions in different chains is much larger (3.33 Å).

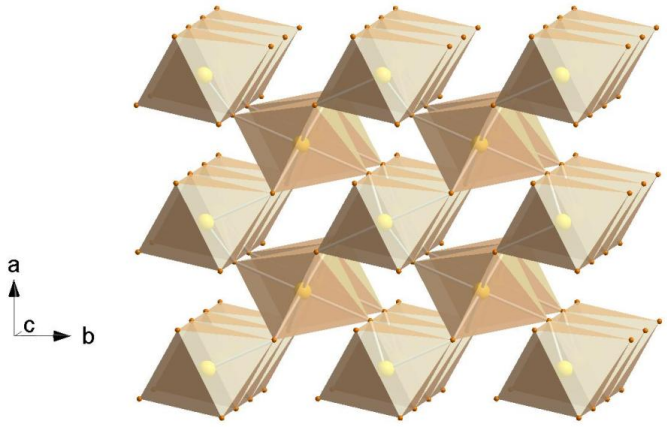

Figure 1-16: Structure of FeS_2 (marcasite), showing corner-linked chains of edge-sharing FeS_6 octahedra

Both the pyrite and the marcasite structures can be described in terms of FeS_6 octahedra. However, it is the connectivity of the octahedra that defines the two separate structural types. $NiSb_2$ is the only 1:2 binary transition metal antimonide that adopts the marcasite structure.[37]

1.3.2.3 $FeAs_2$ Structure

$FeAs_2$ (*Löllingite*) adopts a compressed marcasite structure, crystallising in the orthorhombic space group *Pnnm*. Occupied Wyckoff positions in the $FeAs_2$ and marcasite structures are the same; the structures are therefore isopuntal. The unit cell of $FeAs_2$ is shown in Figure 1-17.[34]

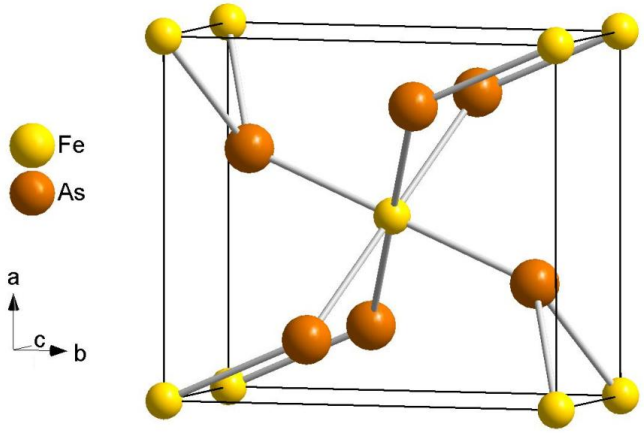

Figure 1-17: Unit cell of $FeAs_2$

The lattice parameters of $FeAs_2$ are a = 5.3001(5), b = 5.9838(5) and c = 2.8821(4) Å.[38] These differ from those of the marcasite structure (a = 4.4446(2), b = 5.4246(2), c = 3.3864(1) Å),[39] most notably by the compression of the c axis. Ratios of the unit cell parameters determine whether a compound will crystallise in the normal marcasite structure or the compressed marcasite structure: compounds with a c/a ratio of 0.74 and a c/b ratio of 0.62 crystallise in the normal marcasite structure, whereas compounds with a c/a ratio of 0.55 and a c/b ratio of 0.48 crystallise in the compressed marcasite structure.[34] The stated ratios are strict values; there are no intermediate cases. The structure of $FeAs_2$ is shown in Figure 1-18.

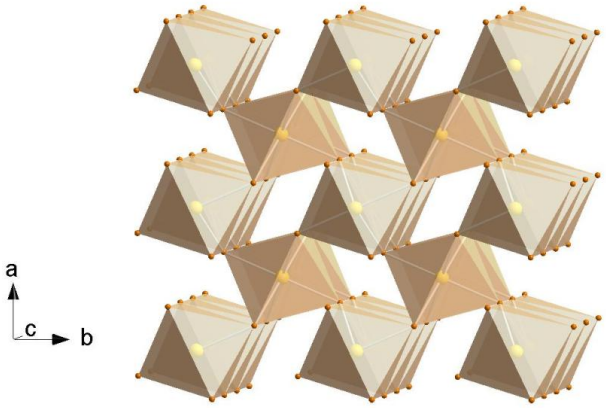

Figure 1-18: Structure of $FeAs_2$

The $FeAs_2$ structure is adopted by 1:2 antimonides of the Group 8 transition metals (Fe, Ru, Os),[40,41] as well as $CrSb_2$.[42]

1.3.2.4 $CoSb_2$ Structure

$CoSb_2$ is the binary prototype for the arsenopyrite structure, a superstructure of the marcasite structure,[43] which was first established for FeAsS.[44] $CoSb_2$ crystallises in the monoclinic space group $P2_1/c$. The unit cell is shown in Figure 1-19.

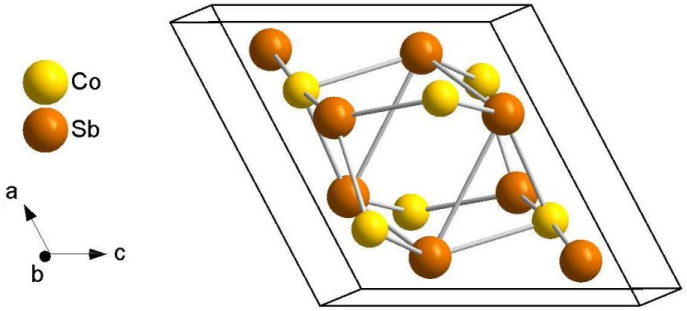

Figure 1-19: Unit cell of $CoSb_2$

The structure consists of distorted $CoSb_6$ octahedra joined *via* edges and corners (Figure 1-20). The distortion of the octahedra arises from a shifting of the Co atoms from the centres of the octahedra, resulting in alternately shorter and longer Co-Co distances, aligned almost parallel to [101].[45] Each Sb atom is coordinated to one other Sb atom, plus three Co atoms, in a tetrahedral arrangement.

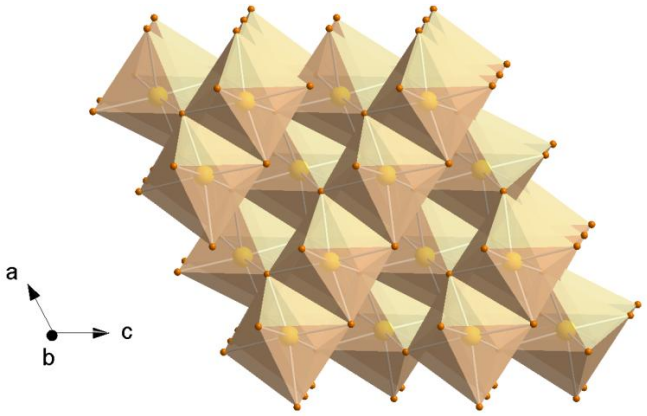

Figure 1-20: Structure of $CoSb_2$, showing edge and corner connectivity of distorted $CoSb_6$ octahedra

In the past (pre-1955), $CoSb_2$ has been wrongly classified as adopting the marcasite structure.[45] The reason for this lies in the fact that the true unit cell symmetry is monoclinic, but with a suitable choice of axes a pseudo-orthorhombic unit cell can result, with dimensions comparable to those of compounds adopting the marcasite structure.

$CoSb_2$ undergoes a transformation from the arsenopyrite structure to the marcasite structure at ~377 °C.[12] The low temperature arsenopyrite phase of $CoSb_2$ is a non-magnetic

semiconductor, and also exhibits thermoelectric properties. It also has applications as an anode material in lithium-ion batteries.

All of the Group 9 1:2 transition metal antimonides adopt the $CoSb_2$ structure.[45]

1.3.2.5 $CuAl_2$ Structure

$CuAl_2$ crystallises in the tetragonal space group *I*4/*mcm*. The unit cell is shown in Figure 1-21.

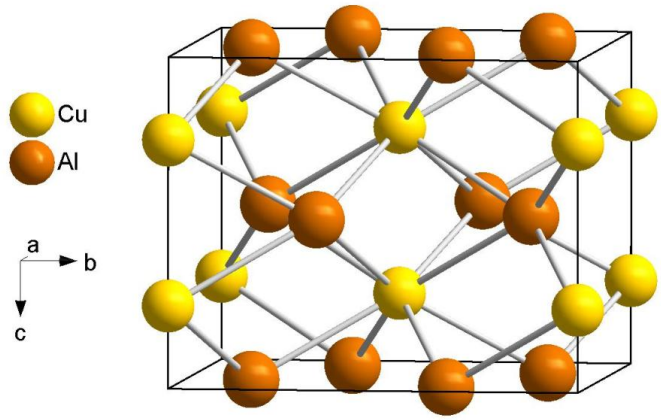

Figure 1-21: Unit cell of $CuAl_2$

The crystal structure of $CuAl_2$ has previously been described in various ways. Kripiakevich[46] and Schubert[47] have both described the structure as being built of piles of condensed [$CuAl_8$] square antiprisms along [001]. The antiprisms share faces in the *c* direction. This representation is shown in Figure 1-22.

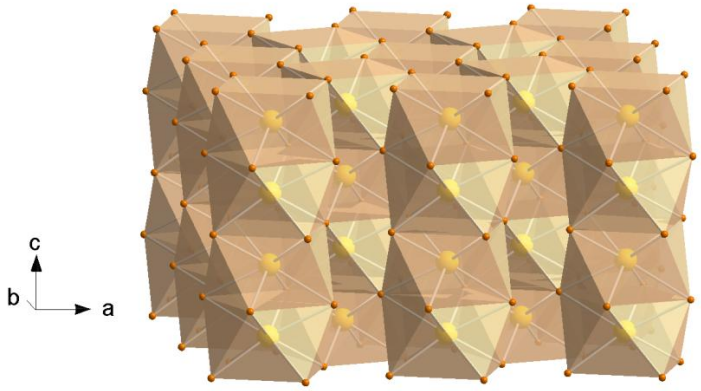

Figure 1-22: Structure of $CuAl_2$, highlighting face-sharing [$CuAl_8$] square antiprisms

The structure has also been described in terms of a system of interpenetrating (6,3) graphite-like aluminium nets, with copper atoms located in channels between the nets, parallel to the *c* axis.[48] This representation can be seen when considering only the two shortest Al-Al distances (Figure 1-23).

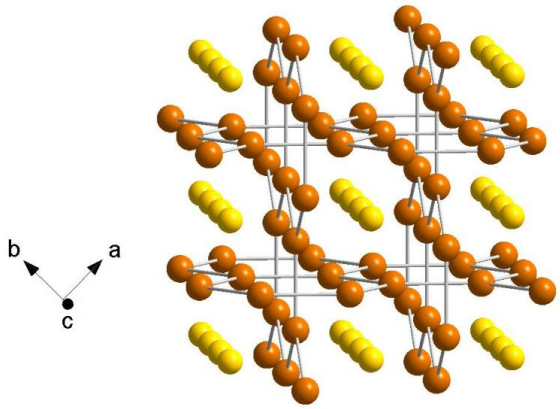

Figure 1-23: Structure of $CuAl_2$ in terms of interpenetrating (6,3) aluminium nets, with copper atoms located in channels along the *c* axis

The $CuAl_2$ structure is adopted by $TiSb_2$ and VSb_2.[19]

1.3.3 MSb_3 Stoichiometry

The $CoAs_3$ (*Skutterudite*) structure is the only structure type adopted by 1:3 transition metal antimonides. It is adopted by all of the Group 9 transition metal antimonides.[49]

1.3.3.1 $CoAs_3$ Structure (*Skutterudite*)

$CoAs_3$ crystallises in the cubic space group $Im\bar{3}$. The unit cell is shown in Figure 1-24.

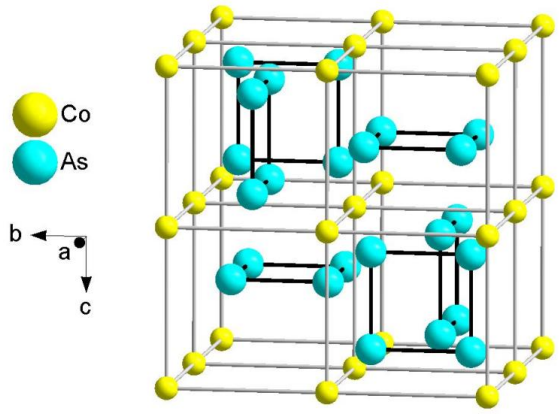

Figure 1-24: Unit cell of $CoAs_3$

The unit cell can be considered to be split into octants, with cobalt atoms positioned at the octant corners.[50] Planar As_4 units, which are not quite square, occupy six out of eight of the octants, with the other two octants remaining empty. From this structural representation, a relation to the ReO_3 structure is apparent; distortions from the ReO_3 structure (where each As atom would have eight equidistant neighbours) occur and enable closer approach of the As atoms to form these almost square As_4 units.

The skutterudite structure can also be described in terms of distorted corner-sharing $CoAs_6$ octahedra,[50] depicted in Figure 1-25.

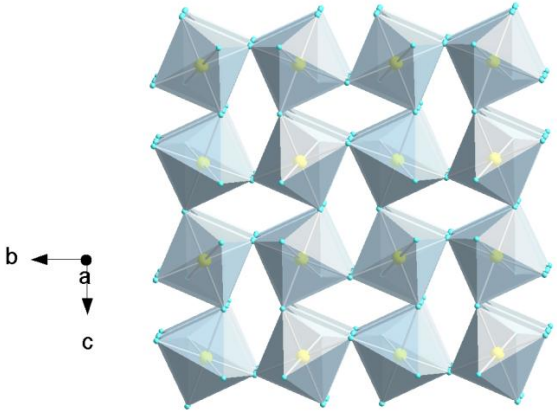

Figure 1-25: Polyhedral representation of $CoSb_3$

1.3.4 M_2Sb Stoichiometry

Binary transition metal antimonides with a 2:1 transition metal:antimony ratio adopt two main structure types: the Cu_2Sb structure and the La_2Sb structure. Other structure types adopted by 2:1 transition metal antimonides include the Co_2Si and Pd_2As structures. These less common structure types will not be discussed here. Table 1-3 gives a comprehensive overview of the structure types adopted by 2:1 transition metal antimonides.

Sc Cu_2Sb	**Ti** La_2Sb	**V** N/A	**Cr** N/A	**Mn** Cu_2Sb	**Fe** N/A	**Co** N/A	**Ni** N/A	**Cu** Cu_2Sb	**Zn** N/A
Y N/A	**Zr** La_2Sb	**Nb** N/A	**Mo** N/A	**Tc** N/A	**Ru** N/A	**Rh** Co_2Si	**Pd** Pd_2As	**Ag** N/A	**Cd** N/A
	Hf N/A	**Ta** N/A	**W** N/A	**Re** N/A	**Os** N/A	**Ir** N/A	**Pt** N/A	**Au** N/A	**Hg** N/A

Table 1-3: Structures adopted by 2:1 transition metal antimonides. N/A indicates that no 2:1 phase exists

1.3.4.1 Cu_2Sb Structure

Cu_2Sb crystallises in the tetragonal space group *P*4/*nmm*. The unit cell is shown in Figure 1-26. It is also referred to as the *anti*-PbFCl structure, and is also adopted by Sc_2Sb and Mn_2Sb.[51]

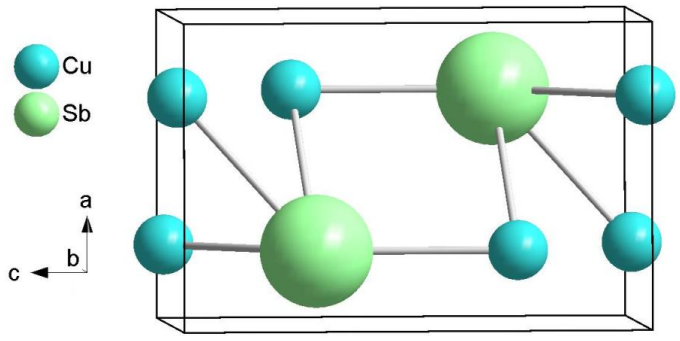

Figure 1-26: Unit cell of Cu_2Sb

The structure can be described in terms of edge-sharing $SbCu_9$ monocapped tetragonal antiprisms, as shown in Figure 1-27.[51]

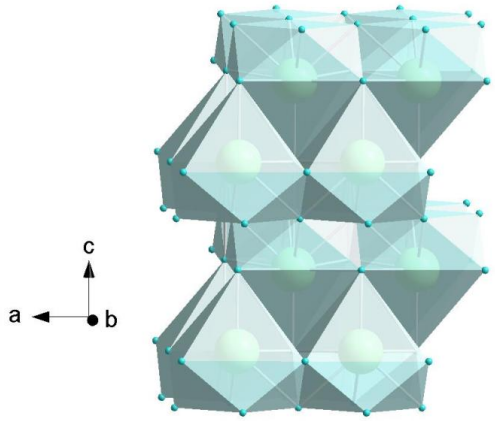

Figure 1-27: Polyhedral representation of Cu_2Sb

The structure can also be described in terms of layers of atoms on two distinct sites (2*a* and 2*c* Wyckoff positions). Copper atoms are located on the 2*a* and 2*c* sites, and antimony atoms are located only on the 2*c* site; ordering of the copper and antimony atoms over the 2*c* site is observed. These atoms located on the 2*c* sites are arranged in a 'corrugated' double layer, where the atom types alternate in all directions.[51] This double layer is sandwiched by two square planar layers of copper atoms located on the 2*a* site (Figure 1-28). The copper atoms in the double layer (2*c*) are displaced very slightly towards the atoms in the all-copper plane (2*a*) leading to the buckling of the layer.[52]

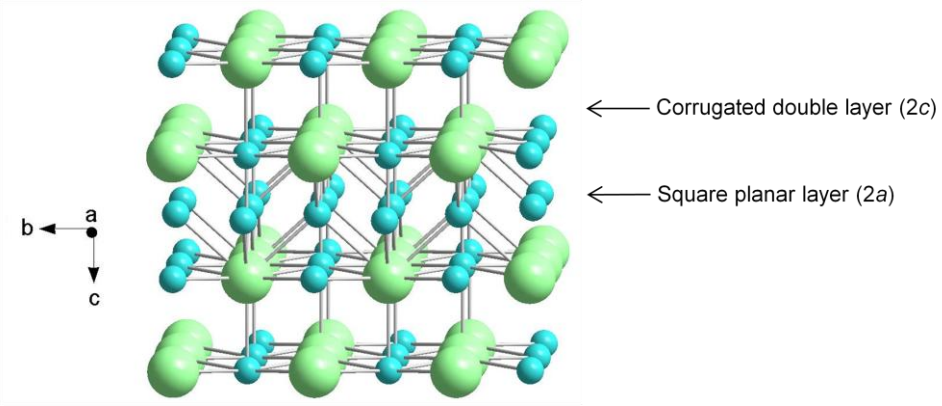

Figure 1-28: Layer structure of Cu_2Sb

The bonding in Cu_2Sb was determined by Vitkina *et al*. to be predominantly covalent.[53] Vitkina *et al.* also deduced that the Cu-Cu bond is the strongest in this phase.

1.3.4.2 La_2Sb Structure

La_2Sb crystallises in the tetragonal space group *I*4/*mmm*. The unit cell is shown in Figure 1-29.

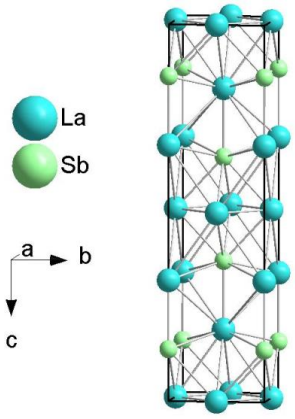

Figure 1-29: Unit cell of La_2Sb

The La_2Sb structure is related to the Cu_2Sb structure, and like Cu_2Sb it possesses two metal sites and one antimony site. La(1) and La(2) occupy the 4*c* and 4*e* Wyckoff positions, respectively, and Sb occupies the 4*e* Wyckoff position;[52] ordering of the lanthanum and antimony atoms over the 4*e* site is observed. La(1) atoms have eight nearest neighbours, positioned at the midpoints of an imaginary distorted cube surrounding the lanthanum atom. Four of these neighbours are antimony atoms, at a distance of 3.27 Å, and the remaining four neighbours are other La(1) atoms, at a distance of 3.39 Å. There are four next nearest neighbours of La(2) atoms at a distance of 3.98 Å, giving rise to a total coordination number of 12. This coordination can be seen in Figure 1-30.

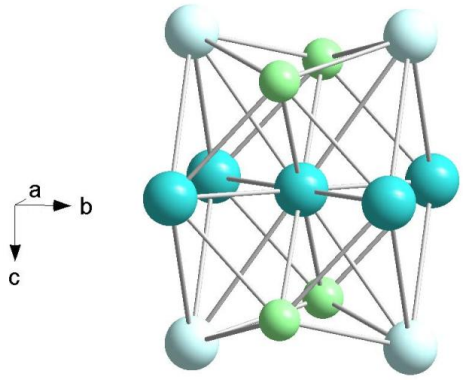

Figure 1-30: Coordination around La(1) in the La_2Sb structure. Pale blue spheres represent the next nearest neighbours [La(2)]

The La(2) atoms are coordinated by five Sb atoms positioned at the corners of a square pyramid.[52] This square pyramid of Sb atoms is also found in the Cu_2Sb structure. The distance to the Sb atom at the vertex is slightly longer than the distance to the Sb atoms at the base of the pyramid. The next nearest neighbours form a square antiprism built up of four La(1) atoms and four La(2) atoms. This gives rise to a total coordination number of 13 (Figure 1-31).

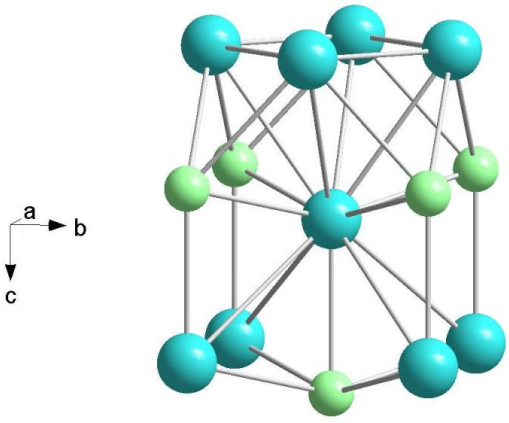

Figure 1-31: Coordination around La(2) in the La_2Sb structure

Each antimony atom is located at the centre of a mono-capped square antiprism of La(1) and La(2) atoms.[52] Like the Cu_2Sb structure, the La_2Sb structure is composed of a double layer of La(2) and Sb atoms on the 4*e* sites (2*c* in Cu_2Sb), sandwiched by a square planar layer of La(1) atoms on the 4*c* sites (2*a* in Cu_2Sb). However, there is a distinct difference

between the two structures. The La_2Sb structure is related to the Cu_2Sb structure by a reflection across a mirror plane perpendicular to the *c* axis (parallel to the all-metal layer).[52] Therefore, the atoms (La(2) and Sb) at either side of the all-metal layer in La_2Sb are related by a plane of symmetry running parallel to the all-metal layer, whereas the equivalent atoms in the Cu_2Sb structure are not. In addition, the metal atoms in the corrugated double layer of La_2Sb are displaced away from the all-metal layer, whereas the metal atoms in the Cu_2Sb structure are displaced towards the all-metal layer.

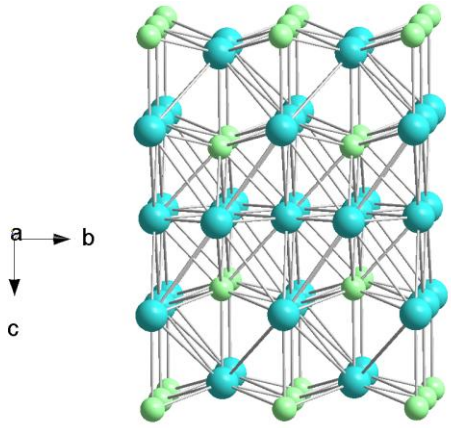

Figure 1-32: Layer structure of La_2Sb

The La_2Sb structure is adopted by Zr_2Sb.[33] Ti_2Sb adopts a distorted variant of the La_2Sb structure, and is therefore strictly a new structure type.[54] The distortion arises from a shortening of some of the Ti-Ti bonds in the square planar layer of Ti atoms. The diagonals of every other square are shortened, maintaining the rest as ideal squares. This distortion possibly occurs as a result of the smaller radius of titanium atoms compared to lanthanum atoms.

1.3.5 M_3Sb Stoichiometry

Binary transition metal antimonides with a 3:1 transition metal:antimony ratio adopt six different structure types. The most common of these are the Cr_3Si and Cu_3Ti structures. Other structure types that are commonly adopted by 3:1 transition metal antimonides include the Ni_3P, Cu_3Au, Fe_3Al and NaTl structures. However, these will not be discussed here. All structure types adopted by 3:1 transition metal antimonides are shown in Table 1-4.

Sc N/A	**Ti** Cr_3Si	**V** Cr_3Si	Cr N/A	**Mn** Cu_3Au	Fe N/A	Co N/A	**Ni** Fe_3Al	**Cu** Cu_3Ti	Zn N/A
Y N/A	Zr N/A	**Nb** Cr_3Si	Mo N/A	Tc N/A	Ru N/A	Rh N/A	**Pd** NaTl	**Ag** Cu_3Ti	Cd N/A
	Hf Ni_3P	**Ta** Cr_3Si	W N/A	Re N/A	Os N/A	Ir N/A	Pt N/A	Au N/A	Hg N/A

Table 1-4: Structure types adopted by 3:1 transition metal antimonides. N/A indicates that no 3:1 phase exists

1.3.5.1 Cr_3Si Structure

Cr_3Si adopts the cubic *β*-wolfram (tungsten) structure, and crystallises in the space group $Pm\bar{3}n$.[55] The structure comprises a *bcc* (body centred cubic) array of silicon atoms with chromium atoms sitting in pairs along each unit cell face.[56] In this arrangement, the chromium atoms form an icosahedron around the silicon atom at the centre of the unit cell (Figure 1-33).

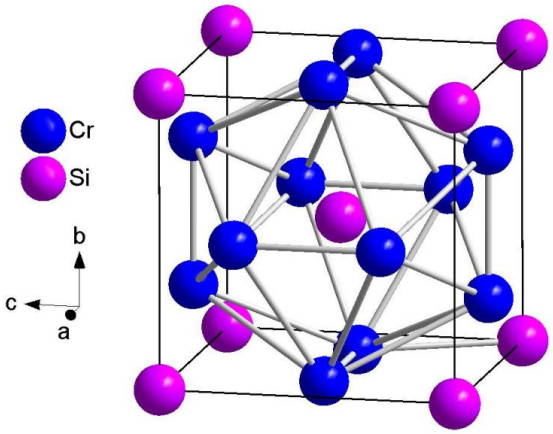

Figure 1-33: Unit cell of Cr_3Si

These $SiCr_{12}$ icosahedra share faces to form the complete structure (Figure 1-34).

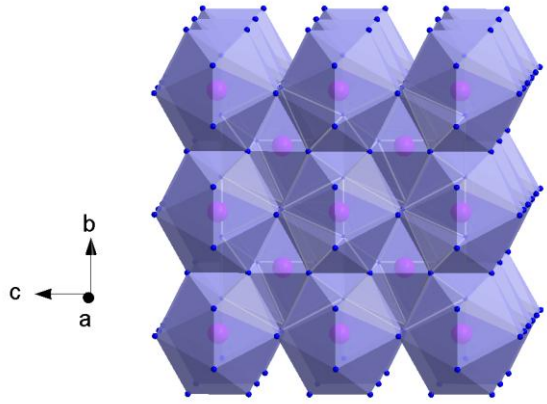

Figure 1-34: Face-sharing $SiCr_{12}$ icosahedra

The Cr_3Si structure is adopted by all of the Group 5 3:1 transition metal antimonides,[57,58,59] as well as Ti_3Sb.[60]

1.3.5.2 Cu_3Ti Structure

Cu_3Ti crystallises in the orthorhombic space group *Pmmn*. The unit cell is shown in Figure 1-35.

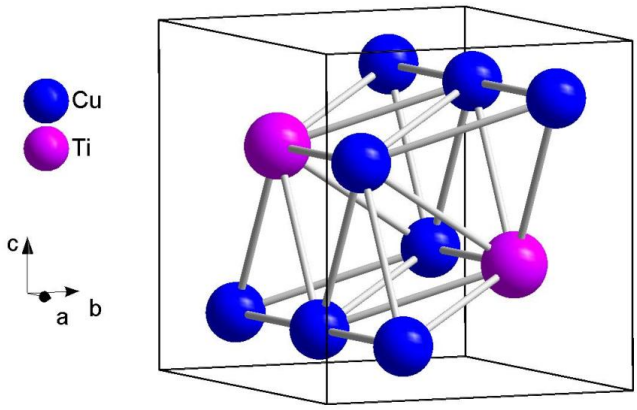

Figure 1-35: Unit cell of Cu_3Ti

The structure is an ordered variant, and therefore a superstructure, of hexagonal close packing.[56] This can be seen in Figure 1-36. It can also be described in terms of edge-sharing $TiCu_4$ square-based pyramids.[61]

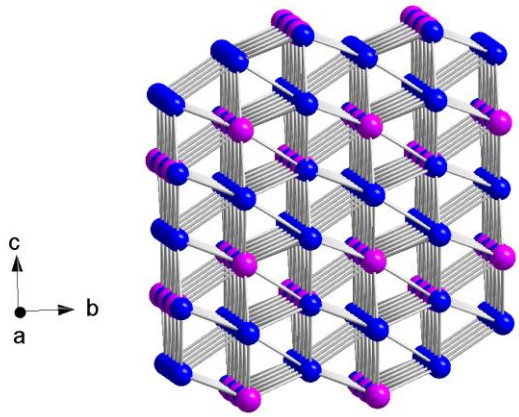

Figure 1-36: Structure of Cu_3Ti, showing an ordered variation of hexagonal close packing

The Cu_3Ti structure is adopted by Cu_3Sb and Ag_3Sb.[62,63]

1.3.6 Other Relevant Structures

1.3.6.1 Mo_3Sb_7

Mo_3Sb_7 adopts the Ir_3Ge_7 structure,[14] crystallising in the cubic space group $Im\bar{3}m$. Häussermann *et al.* provide a detailed description of the structure of Mo_3Sb_7, which is summarised below.[64] The Ir_3Ge_7-type structure is composed of atoms situated on three independent atomic positions, which are labelled T (12*e*), E1 (12*d*) and E2 (16*f*), with Mo atoms occupying the T site, and Sb atoms occupying the E sites. Two interpenetrating frameworks form the basis of the structure: the first is composed of T-centred square antiprisms, with E1 and E2 atoms at the vertices. Two of these square antiprisms share a square face forming a structure visually comparable to a 'barrel' (Figure 1-37), with the rotation angle between the two square antiprisms equal to 45°. This angle is the same for all compounds adopting this structure. E2 atoms are located at the junction between the two square antiprisms.

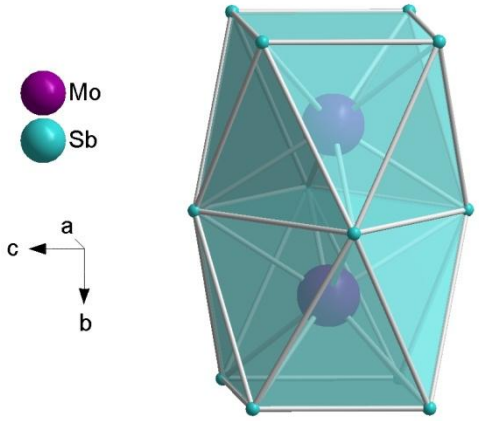

Figure 1-37: Face-sharing $MoSb_8$ square antiprisms, visually comparable to a 'barrel'. E2 atoms are located at the junction between the two square antiprisms

The 'barrels' are connected in such a way that an empty cube is formed as a junction between pairs of square antiprisms. The centres of these cubes are taken as the corners of the unit cell. This is section of the structure is shown in Figure 1-38.

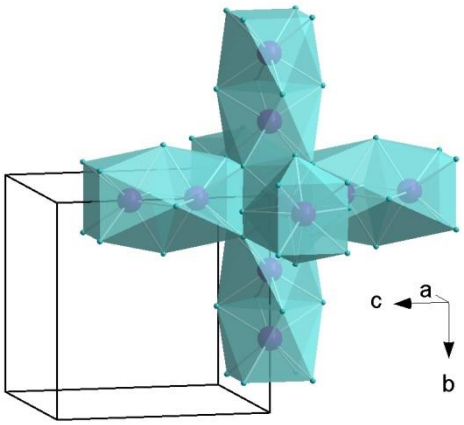

Figure 1-38: Four connected pairs of square antiprisms, emphasising the empty cubes formed at the corners of the unit cell

Repetition of the structure shown in Figure 1-38 leads to the formation of one framework. The second framework is equivalent to the first, and is generated by the body-centring translation imposed by the space group. The full structure of Mo_3Sb_7 displaying the two interpenetrating frameworks is shown in Figure 1-39.

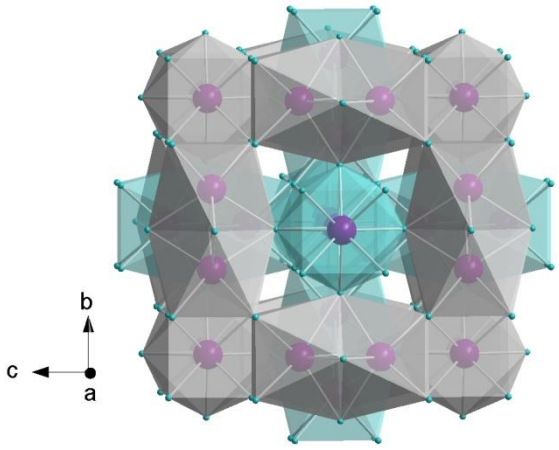

Figure 1-39: Structure of Mo_3Sb_7, emphasising the two equivalent interpenetrating frameworks

2.0 Experimental

2.1 Synthetic Methods

2.1.1 Reductive Synthesis

A reductive synthetic approach was used to prepare polycrystalline samples of intermetallic compounds and transition metal nitrides. Stoichiometric mixtures of metal oxides were intimately ground, pelletised and fired under a flow of dilute hydrogen: 10% hydrogen in argon was used for the synthesis of intermetallics, and 10% hydrogen in nitrogen was used for the synthesis of transition metal nitrides. In most cases, the initial firing was undertaken for 48 hours, and subsequent firings were undertaken for 24 hours each. In between firings, samples were re-ground and re-pelletised in order to maximise homogeneity. The furnaces were allowed to cool radiatively to room temperature. No special measures were implemented in order to prevent exposure to air upon removal of the samples from the furnace. A diagram of the furnace setup is shown in Figure 2-1.

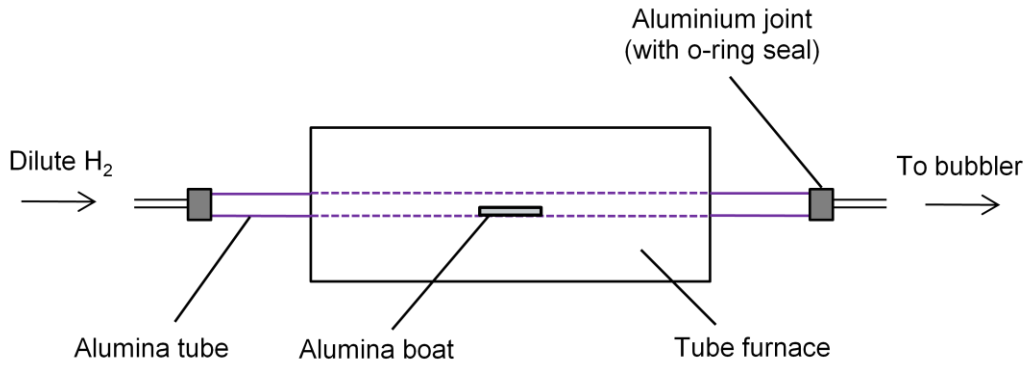

Figure 2-1: Reaction setup for the preparation of polycrystalline materials

2.1.2 Single Crystal Preparation

Single crystals of first row transition metal urea complexes were synthesised by the addition of the hydrated transition metal nitrate to urea in a 1:4 mole ratio, in a solvent comprising water and/or ethanol. The solvent was allowed to evaporate, allowing crystallisation of the desired complexes.

The crystals formed *via* this route were then fired in a tube furnace (setup outlined in Figure 2-1) under flowing 10% hydrogen in nitrogen at a temperature of 300 °C for 3 hours. The products were subsequently ground.

2.2 Structural Determination

2.2.1 Crystallography

2.2.1.1 Unit Cells and Crystal Systems

A unit cell is defined as the repeating unit of a crystal structure. It can be defined by the unit cell lengths, *a*, *b* and *c*, and the angles between the unit cell sides, *α*, *β*, and *γ* (Figure 2-2), but more correctly by the vectors **a**, **b** and **c**.

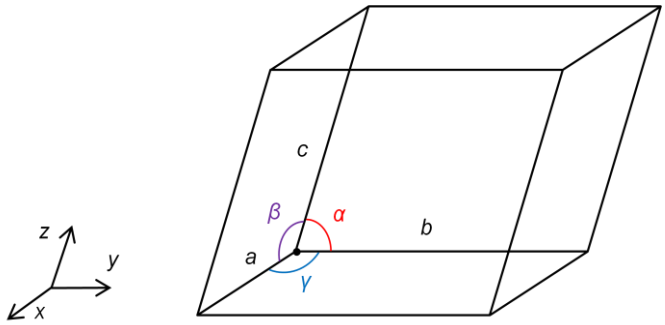

Figure 2-2: Schematic diagram of a unit cell

Atomic coordinates are specified in fractions of the unit cell lengths. An atom on x = ½, y = 0.268, z = ¼ will have a position related to the unit cell origin of a x ½, b x 0.268, c x ¼. The position of an atom can also be described in terms of a vector, **r**, relative to the origin of the unit cell:

$$\mathbf{r} = x\mathbf{a} + y\mathbf{b} + z\mathbf{c}$$

(Equation 2-1)

There are seven crystal systems, which are defined by the symmetry elements present. The symmetry elements place restrictions on the shape of the unit cell in a particular crystal system. The seven crystal systems and their essential symmetry elements and unit cell shapes are listed in Table 2-1.

Crystal system	Axial representation	Essential symmetry element
Cubic	$a = b = c$, $\alpha = \beta = \gamma = 90°$	Four 3-fold rotation axes
Tetragonal	$a = b \neq c$, $\alpha = \beta = \gamma = 90°$	One 4-fold rotation axis
Hexagonal	$a = b \neq c$, $\alpha = \beta = 90°$, $\gamma = 120°$	One 6-fold rotation axis
Trigonal	$a = b = c$, $\alpha = \beta = \gamma$	One 3-fold rotation axis
Orthorhombic	$a \neq b \neq c$, $\alpha = \beta = \gamma = 90°$	Three mutually $\perp$ 2-fold axes or mirror planes
Monoclinic	$a \neq b \neq c$, $\alpha = \gamma = 90°$, $\beta \neq 90°$	2-fold rotation axis or mirror plane
Triclinic	$a \neq b \neq c$, $\alpha \neq \beta \neq \gamma \neq 90°$	None

Table 2-1: Classification of the seven crystal systems

2.2.1.2 Lattice Types

A lattice is defined as a regular repeating array of points. Placing an atom or group of atoms, known as the 'basis', on each lattice point generates the crystal structure. There are four lattice types: primitive (*P*), body centred (*I*), face centred (*F*) and C-centred (*C*). In 1985 the International Union of Crystallography proposed guidelines for naming the different lattice types.[65] A side-centred unit cell was given the symbol *S*, derived from 'side centred' or *seitenflächenzentriert*. However, this has not been widely adopted, and the side centred lattice is more commonly called C-centred.

The primitive lattice contains one lattice point per unit cell. Each lattice point is related to others by unit translations along each of the unit cell axes, *a*, *b* and *c*. It is most commonly represented by one single lattice point at the centre of the unit cell, or alternatively as lattice points at each corner of the unit cell.

The body centred lattice can be viewed as a primitive lattice with an additional lattice point, which is related to the original by a translation of (½, ½, ½). There are therefore two lattice points in a body centred unit cell.

The face centred lattice can be viewed as a primitive lattice with three additional lattice points. These are related to the original lattice point by the translations (x, $y + ½$, $z + ½$), ($x + ½$, y, $z + ½$) and ($x + ½$, $y + ½$, z). There are therefore four lattice points in a face centred unit cell. The points in a face centred lattice can be thought of as equivalent to the atom packing in a cubic close packed (*ccp*) arrangement.

The *C*-centred lattice can be viewed as a primitive lattice with an additional lattice point at the centre of the *ab* face. This point is related to the original lattice point by a translation of (x + ½ , y + ½ , z). There are therefore two lattice points in a *C*-centred unit cell.

Useful pictorial representations of the four lattice types are shown in Figure 2-3.

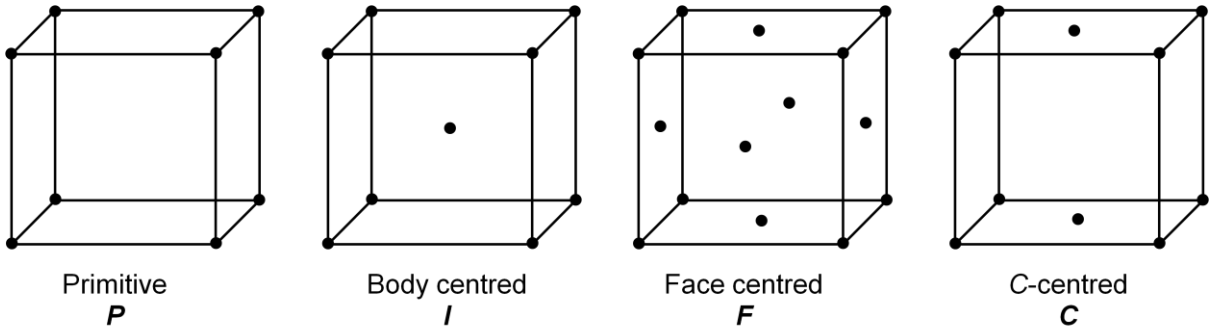

Figure 2-3: Schematic diagram of the four lattice types

The combination of the seven crystal systems with the four lattice types creates 14 Bravais lattices, which are classified in Table 2-2.

Crystal system	Bravais lattice
Cubic	*P, I, F*
Tetragonal	*P, I*
Orthorhombic	*P, I, F, C*
Hexagonal	*P*
Trigonal	*P*
Monoclinic	*P, C*
Triclinic	*P*

Table 2-2: Classification of the 14 Bravais lattices

2.2.1.3 Symmetry

Finite molecules possess only point symmetry elements, as these describe the symmetry immediately surrounding a point. The application of point symmetry elements on the 14 Bravais lattices generates 32 point groups. The subsequent addition of translational symmetry operations generates the 230 unique Space Groups. Point and translational symmetry operations are described below:

Point symmetry operations

Rotation: If after a rotation of 360°/*n*, all of the properties of the surrounding space remain unchanged, an *n*-fold rotation axis is present (symbol = *n i.e.* 1, 2, 3, 4, 6)

Reflection: A motif is replicated *via* reflection across a mirror plane to form a mirror image of the motif (symbol = *m*)

Rotoinversion: A rotoinversion combines a rotation of the order *n*, with an inversion through a point (symbol = $\bar{n}$ *i.e.* $\bar{1}$, $\bar{2}$, $\bar{3}$, $\bar{4}$, $\bar{6}$). The $\bar{2}$ axis is equivalent to a mirror plane perpendicular to it.

Translational symmetry operations

Screw axis: A screw axis is also known as a rototranslation axis, due to it having a rotational and translational component. A rotation of 360°/*n* is followed by a translation parallel to the rotation axis. The notation used to define screw axes has a subscript component (*m*) in addition to the symbol used for a rotation (*n*). *m*/*n* defines the fraction of the total translational distance covered by one whole screw operation. For example, a 4_1 screw axis indicates that the motif will undergo a 4-fold rotation (90°), followed by a translation of ¼ the length of the total translational distance.

Glide plane: A glide plane has a translational component and a mirror plane. A reflection across a plane is followed by a translation of ½ if the plane is parallel to a crystallographic axis. Diagonal glide planes bisect crystallographic axes across either the face or body of a unit cell. Their symbols are *n* and *d*, respectively. The *d* glide has a translation of ¼.

2.2.1.4 Miller Indices

Planes bisecting the crystallographic axes of a unit cell can be defined by the use of Miller indices (*hkl*). The lattice plane in question intercepts the *x*, *y* and *z* axes at 1/*h*, 1/*k* and 1/*l*, respectively. Miller indices can therefore be calculated by taking the reciprocal values of the unit cell intercepts. For example, a lattice plane intercepting the *x*, *y* and *z* axes at (½, ⅓, 1) would have Miller indices of (231).

2.2.2 X-ray Diffraction

X-rays interact with electrons and are therefore scattered in various directions by the electron clouds of atoms in a crystal. The interatomic distances in a crystal (~ 2 – 3 Å) are comparable to the wavelength of x-ray radiation (λ_{Cu} = 1.5418 Å) enabling the structures of crystalline materials to be probed.[66] X-ray diffraction experiments can be performed on polycrystalline materials in the case of x-ray powder diffraction, and single crystals in the case of single crystal x-ray diffraction. X-ray powder diffraction allows for the characterisation of a bulk sample, rather than one selected crystal as is the case with single crystal x-ray diffraction. X-ray powder diffraction is therefore useful when a sample may contain more than one phase. Single crystal x-ray diffraction is better for determining the absolute arrangement of atoms in a crystal, without the need for a structural model in advance. However, in a small number of cases structures have been solved using x-ray powder diffraction alone.[67] There are therefore obvious advantages and disadvantages to using each technique. It is important to note that structural characterisation of materials without long range order is rather difficult, although techniques employing the atomic pair distribution function (obtained from x-ray scattering data) have been developed to do this.[68]

2.2.2.1 Generation of X-ray Radiation

X-rays are generated in the x-ray tube by the bombardment of a copper target with high energy electrons. These high energy electrons are created *via* the acceleration of electrons by a potential difference of 40 kV. When electrons penetrate the target their velocity decreases as a result of many collisions, and the energy lost through this is converted into a continuous background of x-ray radiation. This is known as Bremsstrahlung radiation (Figure 2-4). A second mechanism for slowing electrons exists: an electron hitting the target with sufficient energy will eject an electron from one of the metal atom core orbitals. X-rays are emitted over a narrow energy range when this hole is filled by electron decay from a higher energy orbital. These x-rays are of high intensity, and can therefore be used in x-ray diffraction experiments. Kα radiation arises from a $2p \rightarrow 1s$ transition, and Kβ radiation from a $3p \rightarrow 1s$ transition. Kα radiation is more intense than Kβ radiation, and so is more frequently used in diffraction experiments. Two intense Kα peaks appear in the emission spectrum. These are known as Kα_1 and Kα_2; the energy difference between them

is small and so Kα_2 is only observed at high angles (Figure 2-4). The existence of a doublet is a result of the slightly different energies of the different spin states of the 2*p* electron in transition.

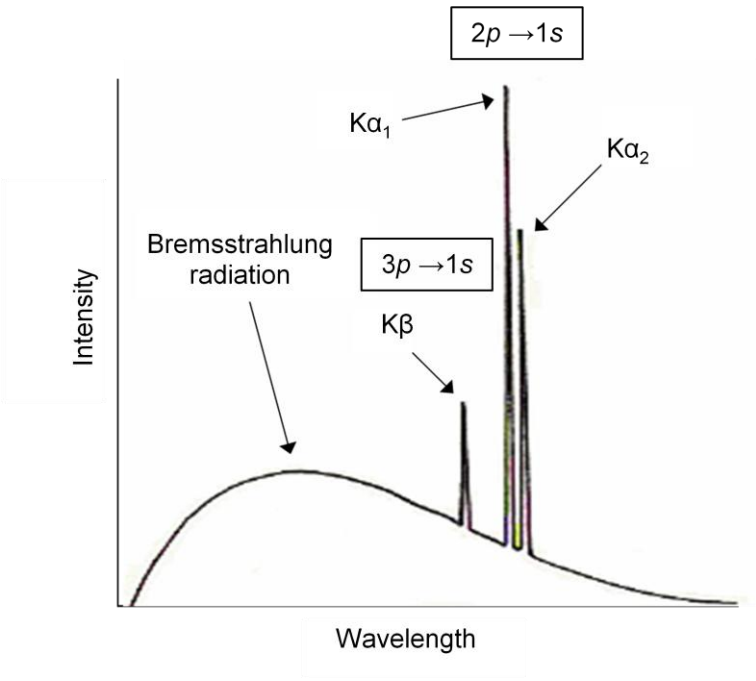

Figure 2-4: Schematic x-ray emission spectrum of copper

2.2.2.2 Bragg's Law

Scattering of x-rays by the atoms in a crystal can lead to interference maxima and minima. For constructive interference to occur, the incident and scattered waves must be in phase and Bragg's Law must be satisfied:

$$2d_{hkl}\sin\theta = n\lambda$$

(Equation 2-2)

where d_{hkl} = lattice spacing, θ = angle of incidence, n = order of diffraction and λ = wavelength.

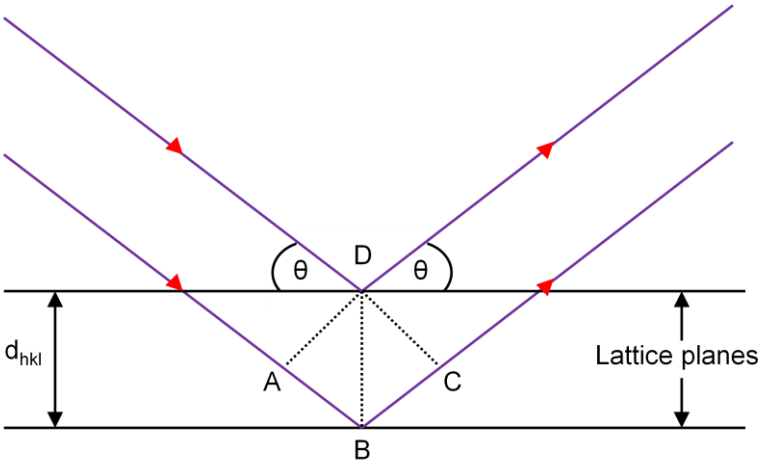

Figure 2-5: Bragg diffraction from a set of lattice planes

Bragg's Law states that the x-rays scattered from the points B and D will be in phase if the additional distance travelled by the second ray between AB and BC is an integral number of wavelengths *i.e. n* is an integer.

$$\text{Path difference} = AB + BC = 2d_{hkl} \sin\theta = n\lambda$$

(Equation 2-3)

The order of diffraction, *n*, is always taken to be 1 and the *hkl* values are adjusted accordingly. For example, second order diffraction from the (100) plane is equivalent to first order diffraction from the (200) plane.

As a consequence of Bragg diffraction some reflections will be systematically absent in certain lattice systems. Systematic absences arise from the presence of translational symmetry elements such as cell-centring, screw axes and glide planes. The existence or non-existence of systematic absences enables some conclusions about the lattice type and space group to be drawn.

The three-dimensional diffraction pattern of a crystal can be described using the reciprocal lattice. The reciprocal lattice is related to the direct lattice, and is defined in three dimensions by three vectors, **a***, **b*** and **c***. The directions of the vectors are perpendicular to the directions of the sides of the direct lattice unit cell.[69] Their lengths are the inverse of the perpendicular distance from the origin of the lattice to the sides of the direct lattice unit cell. For simplicity, the reciprocal lattice can be defined in two dimensions in terms of the

vectors **a*** and **b***. For square and rectangular plane lattices, the lengths of **a*** and **b*** are equal to 1/*a* and 1/*b*, respectively; for oblique and hexagonal plane lattices, they are equal to $1/d_{10}$ and $1/d_{01}$, respectively.[69] The reciprocal lattice provides a good method for visualising diffraction from crystal lattice planes.

2.2.2.3 Intensities of Diffracted X-rays

The intensity of a reflection from a set of (*hkl*) planes is dependent on several factors, including: (1) the Bragg angle of the diffracted x-rays; (2) the atomic scattering factors, which are a measure of the diffracting power of the atoms in question (discussed later); (3) the arrangement of the atoms in a crystal, also known as the structure factor (discussed later); (4) the temperature factors of the atoms and (5) the multiplicity of the reflection in powder diffraction (discussed in section 2.2.3.2).[69]

When the diffracted x-rays are recorded, individual wave amplitudes are retained as relative intensities, but the relative phases are lost. This is known as the 'Phase Problem'. Methods exist to solve this problem, and are described in later sections. Only the square magnitudes are recorded in a diffraction experiment. The relationship between the intensity and amplitude of a diffracted x-ray is given by:

$$I \propto |F|^2$$

(Equation 2-4)

where I = intensity and $|F|$ = amplitude.

Forming an image of the electron density from the diffraction pattern involves the summation of waves with their correct amplitudes ($|F|$) and phases (φ). They are related to the structure factor, F, by:[70]

$$F = |F|e^{i\varphi}$$

(Equation 2-5)

where $i^2 = -1$.

This relationship presented in Equation 2-5 is derived as follows:

In general, *F* is complex; the phase and amplitude of a wave can therefore be represented by the use of an Argand diagram, where the magnitude and direction can be replaced by a set of coordinates, A (on the real axis) and B (on the imaginary axis). This is shown in Figure 2-6.

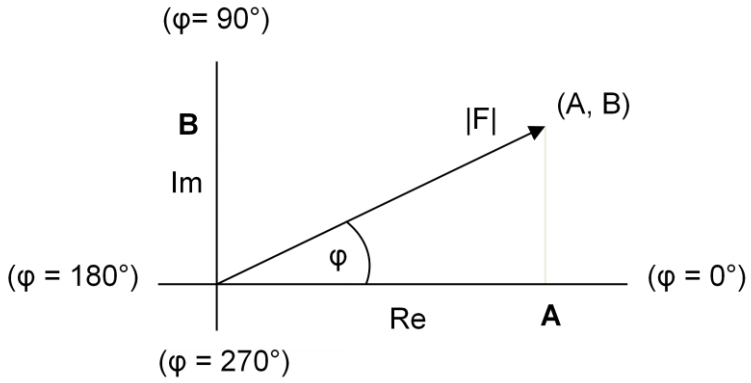

Figure 2-6: Argand diagram representing a wave with amplitude |*F*| and phase φ

A and B are related to the magnitude and phase of a wave by simple trigonometry:

$$A = |F| \cos \varphi$$

(Equation 2-6)

$$B = |F| \sin \varphi$$

(Equation 2-7)

$$\tan \varphi = B/A$$

(Equation 2-8)

The structure factor, *F*, is related to A and B by:

$$F = A + iB$$

(Equation 2-9)

By combining Equation 2-6, Equation 2-7 and Equation 2-9 the structure factor can be described as:

$$F = |F|\cos\varphi + i|F|\sin\varphi$$

(Equation 2-10)

This is equivalent to Equation 2-5 when considering a property of complex numbers whereby $e^{i\varphi} = \cos\varphi + i\sin\varphi$.

The combination of amplitude and phase for all atoms in the unit cell is represented by F_{hkl}, and is the Fourier transform of the electron density. When an atom is at rest, the Fourier transform takes the form:

$$F_{hkl} = \sum_j f_j \; exp\left[2\pi i\left(hx_j + ky_j + lz_j\right)\right]$$

(Equation 2-11)

where f_j is the scattering factor of atom j and x_j, y_j, z_j are the atomic coordinates.

As x-rays interact with electron clouds of atoms, the power of an individual atom to scatter x-rays (the atomic scattering factor) is related to the number of electrons (and therefore the number of protons) it contains. A heavy element such as lead (Z = 82) will therefore scatter more x-rays than a lighter element such as oxygen (Z = 8). The atomic scattering factor is angle dependent, decreasing as $\sin\theta/\lambda$ increases.[69] This effect is due to destructive interference occurring between waves scattered by the various regions of the atoms.[71] The larger the atom, the greater this effect becomes.

2.2.3 X-ray Powder Diffraction

2.2.3.1 Data Collection

A powder sample contains a vast number of crystallites, which randomly adopt a huge range of possible orientations. An x-ray beam will therefore be diffracted by a polycrystalline sample in all directions deemed possible by the Bragg equation. As a result, each lattice spacing in the crystal will give rise to a cone of diffraction. Powder diffractometers are therefore equipped with a detector (typically a Geiger-Muller tube or

scintillation counter) that is able to scan a wide area in order to detect diffraction cones. Powder diffraction patterns in this work were collected on a Siemens D5000 diffractometer operating with Cu Kα radiation in Bragg-Brentano geometry. A diagram of the setup is shown in Figure 2-7.

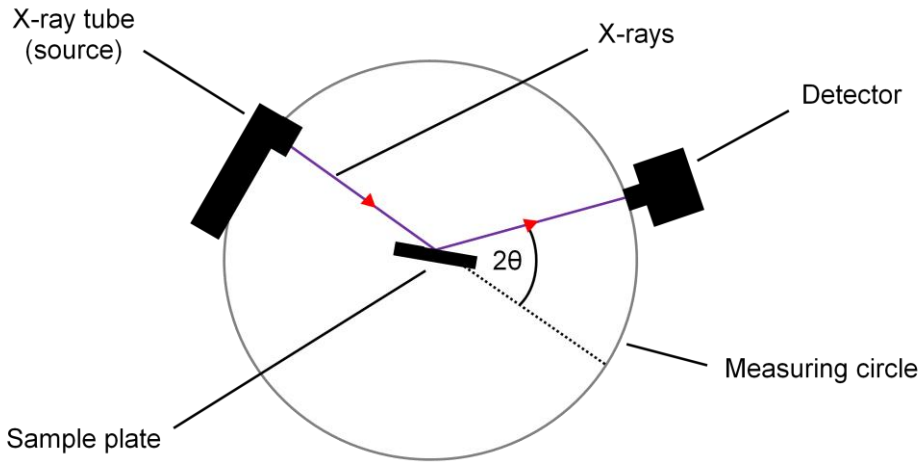

Figure 2-7: Schematic diagram of the Siemens D5000 diffractometer

The detector is scanned around the circumference of the measuring circle in order to detect Bragg reflections in specific 2θ ranges *e.g.* $5 \leq 2\theta/° \leq 120$. The data output is a 1-D diffraction pattern, where the intensity of the diffracted beam is plotted against the diffraction angle (2θ in °).

In this work, finely ground samples were mounted on a lightly greased glass sample mount and rotated at 15 revolutions per minute. In some cases a broad feature in the background centred on 20 – 25 $2\theta/°$ was observed. This was due to excessive grease present on the mounting. When this occurred a rough background was fitted manually and subtracted from the data. Diffraction patterns were recorded with a step size of 0.020°, over various ranges of 2θ, and with various counting times.

2.2.3.2 Rietveld Method

The Rietveld method is an invaluable technique used for obtaining structural information from powder diffraction data.[72] It is carried out using profile fitting software, in this case the GSAS suite of programs.[73] For Rietveld refinement, a model that closely resembles the observed data must first be calculated. Parameters of the model are then refined in order to

obtain the best fit of the model to the data. Hence, the intensity observed at the *i*th step, y_i, is compared with the corresponding intensity calculated *via* the model, y_{ci}. The model is refined using a least-squares process by minimising the residual, S_y:

$$S_y = \sum_i w_i (y_i - y_{ci})^2$$

(Equation 2-12)

where $w_i = 1/y_i$, y_i is the observed intensity at the *i*th step and y_{ci} is the calculated intensity at the *i*th step.[74]

The calculated intensity, y_{ci}, is dependent on several variables and is obtained from the equation:[74]

$$y_{ci} = s \sum_{hkl} L_{hkl} |F_{hkl}|^2 \phi(2\theta_i - 2\theta_{hkl}) P_{hkl} A + y_{bi}$$

(Equation 2-13)

where *s* is the scale factor; *hkl* are the Miller indices; L_{hkl} contains the Lorentz, polarisation and multiplicity factors; ϕ is the reflection profile function; P_{hkl} is the preferred orientation function; *A* is an absorption factor; F_{hkl} is the structure factor for the Bragg reflection corresponding to *hkl* and y_{bi} is the background intensity at the *i*th step.[74]

The variables presented in Equation 2-13 are discussed below:

Lorentz, polarisation and multiplicity factors, L_K: Bragg's Law implies that Bragg diffraction only occurs at discrete values of 2θ. However, Bragg diffraction actually occurs over a narrow range of 2θ values. This is taken into account using the Lorentz factor.[69] A polarisation factor must also be employed due to partial polarisation of the unpolarised incident x-rays, which produces an angle dependent reduction in intensity.[69] As mentioned earlier, powder diffraction results in a cone of diffraction, rather than single spots produced from single crystal diffraction. The intensities of individual reflections cannot therefore be measured independently. The intensities on a powder pattern are therefore greater than that of a single reflection by the reflection multiplicity.[69] This must be taken into account when determining a crystal structure from a powder pattern.

Reflection profile function, ϕ: Peak shapes observed in the experimental data are a function of both the sample and the diffractometer; for example, domain size and defects in terms of the sample, and radiation source, geometry and slit size in terms of the diffractometer.[75] The combination of these features can create a complicated peak shape, which requires a complicated profile function in order to model it accurately. Several profile functions are available, including the pseudo-Voigt function. This function is a result of an analytical convolution of Gaussian and Lorentzian components, with the ability to refine a mixing parameter which determines the fraction of each component.[74] It is the most widely used profile function for x-ray data, and is therefore employed in this work.

Preferred orientation function, P_K: Preferred orientation arises when the crystallites tend to arrange themselves in a specific orientation, usually determined by their morphology. For example, plate-like crystallites may prefer to orientate along one plane. This results in certain lattice planes diffracting more of the x-rays than others, and therefore results in an increase or decrease in the intensities of the affected reflections. A number of preferred orientation functions exist to model the distortion of the intensities, but were not employed in this work.

Absorption factor, A: Some x-rays are absorbed by the sample rather than diffracted; the degree of absorption is dependent on the sample thickness. This can lead to a reduction in the intensity of diffracted rays. Absorption corrections are available to model this but were not required in this work.

Structure factor, F_{hkl}: The structure factor is defined in section 2.2.2.3 and is given by:

$$F_{hkl} = \sum_j N_j f_j exp\left[2\pi i\left(hx_j + ky_j + lz_j\right)\right] exp\left[-M_j\right]$$

(Equation 2-14)

where F_{hkl} is the structure factor corresponding to a set of (hkl) planes; N_j is the site occupancy multiplier for the jth site (site occupancy divided by site multiplicity); f_j is the scattering factor of atom j; $i^2 = -1$; x_j, y_j and z_j are the positions of the jth atom in the unit cell;

$$M_j = 8\pi^2 \overline{u_s^2} \sin^2 \theta / \lambda^2$$

(Equation 2-15)

where $\overline{u_s^2}$ is the root-mean-square thermal (and random static) displacement of the *j*th atom parallel to the diffraction vector.[74]

Background intensity, y_{bi}: Scattering from the sample holder and in this case, the adhesive used to mount the sample, contributes to the background intensity. This intensity must be accounted for in the refinement in order to prevent it being modelled as Bragg intensity. There are three ways of obtaining the background intensity: (1) from a table of background intensities, (2) by linear interpolation between selected points in the pattern, and (3) by modelling it with a specified background function containing several refinable parameters.[74] In this case, the background was modelled using a shifted Chebyshev background function. However, other functions are also available.

The parameters refined in this work, and the order in which they were refined are as follows: background, lattice parameters, zero point correction, profile parameters, atomic positions of atoms on general positions and isotropic displacement parameters. The positions and isotropic displacement parameters of heavy atoms were refined before those of lighter atoms. In cases where refinement of the isotropic displacement parameters led to an unstable refinement the values were set to 0.025 $Å^2$ and not refined. In cases where refinement led to negative isotropic displacement parameters the values were set to zero and not refined. In addition, the peak cut-off points were set to 0.15% of the peak maximum in the process of the refinement.

The visual plot of the difference between the observed and calculated profiles is invaluable when assessing the quality of fit between the observed and calculated data. However, there are several numerical indicators also available to assess this, including:

$$R_p = \frac{\sum |y_i(\text{obs}) - y_i(\text{calc})|}{\sum y_i(\text{obs})}$$

(Equation 2-16)

where R_p = *R*-profile, y_i(obs) = observed intensity at *i*th step, y_i(calc) = calculated intensity at *i*th step;

$$R_{wp} = \left\{ \frac{\sum_i w_i \, [y_i(\text{obs}) - \, y_i(\text{calc})]^2}{\sum_i w_i \, [y_i(\text{obs})]^2} \right\}^{1/2}$$

(Equation 2-17)

where R_{wp} = *R*-weighted profile;

$$R_{exp} = \left[\frac{(N - P)}{\sum_i^N w_i \, y_i(\text{obs})^2} \right]^{1/2}$$

(Equation 2-18)

where R_{exp} = *R*-expected, N = number of profile points, P = number of refined parameters;

$$\chi^2 = \frac{R_{wp}}{R_{exp}}$$

(Equation 2-19)

$$R_F = \frac{\sum_{hkl} |F_{hkl}(\text{'obs'}) - \, F_{hkl}(\text{calc})|}{\sum_{hkl} |F_{hkl}(\text{'obs'})|}$$

(Equation 2-20)

where R_F = *R*-structure factor;

$$R_B = \frac{\sum_{hkl} |I_{hkl}(\text{'obs'}) - \, I_{hkl}(\text{calc})|}{\sum_{hkl} |I_{hkl}(\text{'obs'})|}$$

(Equation 2-21)

where R_B = *R*-Bragg factor.

In the expressions for R_F and R_B, the observed structure factor and intensity are in quotation marks because the Bragg intensity is not measured directly; the values are instead obtained by allocation of the total observed intensity in a 'scramble' of overlapping reflections to the individual reflections, according to the ratios of the intensities of the reflections in the calculated pattern.[74] R_F and R_B are therefore biased towards the structural model, but give an indication of the reliability of the structure.

The use of R_{wp} in assessing the quality of fit is useful, as the quantity to be minimised is the numerator in the equation. However, if the background is refined rather than subtracted both y_i(obs) and y_i(calc) will include the background contribution. This can produce misleadingly low R_{wp} values for samples with a high background contribution, as a significant part of the intensity is accounted for by the background function.[75] To enable direct comparison of *R*-values between refinements that have a refined background and refinements where a background subtraction has been carried out in this work, $R(F^2)$ was used as a numerical indicator of the quality of fit. The goodness of fit indicator, χ^2, was also used in this way. The value of $R(F^2)$ tends towards zero as the quality of fit improves; the value of χ^2, however, approaches unity.

2.2.4 Single Crystal X-ray Diffraction

2.2.4.1 Data Collection

The single crystal x-ray data were collected on a Stoe IPDS II diffractometer operating with Mo Kα radiation. The data were collected at 150 K; the crystals were cooled using an Oxford Instruments nitrogen cryostream. The general set up of a single crystal x-ray diffractometer equipped with an area detector is shown in Figure 2-8. A single crystal x-ray diffractometer equipped with an area detector has advantages over a diffractometer equipped with a point detector as more reflections can be recorded at once, reducing the time taken for data collection. In addition, weak reflections are more easily identified and the true symmetry of the crystal is therefore more easily determined.

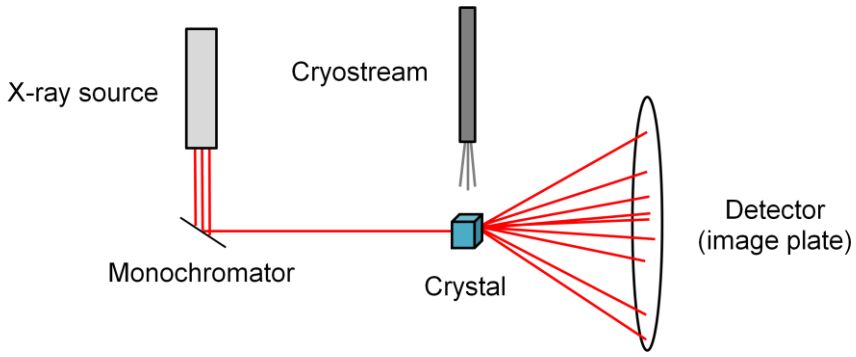

Figure 2-8: Schematic diagram of a single crystal x-ray diffractometer

X-rays of a single wavelength are first selected by diffracting the radiation from a single crystal of graphite cut along one face (crystal monochromator). The monochromatic x-rays are then directed at the crystal, which is cooled under a stream of nitrogen gas to reduce atomic vibrations due to thermal energy. The diffracted x-rays are recorded over several hours on a circular x-ray sensitive image plate, resulting in a picture of time-averaged electron density. The crystal is rotated through either one or more axes to ensure a high proportion of $I(h,k,l)$ values are included in the data collection. During the rotation, the crystal is held in certain orientations in order to collect frames of data, many of which are collected in any given experiment. The positions and intensities of the spots recorded on the frames are then used to determine the unit cell parameters and crystal structure.

2.2.4.2 Fourier Summation

To obtain an image of the electron density a Fourier summation (reverse Fourier transform) must be performed (the electron density is the reverse Fourier transform of the diffraction pattern). If the values of F_{hkl} are known for all reflections, performing a Fourier summation will allow determination of the crystal structure. The electron density at any point x, y, z is given by:

$$\rho_{xyz} = \frac{1}{V} \sum_{hkl} F_{hkl}\, exp[-2\pi i(hx + ky + lz)]$$

(Equation 2-22)

where ρ_{xyz} is the electron density at a point (x, y, z) in the unit cell and V is the unit cell volume.

The summation is performed over all values of h, k and l and at many different points (x,y,z) in order to show the variation of electron density in the unit cell. The structure factor has units of electrons, whereas the electron density has units of electrons per cubic angstrom. The term '$1/V$' is therefore required for unit consistency. If the amplitude $|F|$ and phase φ (and therefore the structure factor F) of each reflection was known, a map of the electron density could be easily computed using the Fourier summation. However, as the phase information is missing, the phases must be calculated either from a trial structure, or

by purely analytical methods. These methods include ‘direct methods’ and the Patterson method, and are discussed in the following sections.

2.2.4.3 Structure Solution

The crystal structure can be solved by several methods, including ‘direct methods’ or the Patterson method. However, there are restrictions to each method: structure solution by direct methods requires reasonably accurate knowledge of the chemical composition of the crystal for the structure solution to be successful, and the Patterson method requires the presence of heavy atoms in the structure for the structure solution to be successful. ‘Direct methods’ were used to solve the crystal structures described in this work, due to the absence of heavy atoms in the materials synthesised. SHELXL-97 was used to refine the structures within WinGX.[76] Both methods of structure solution are described in more detail in the following sections.

2.2.4.3.1 Direct Methods

The term ‘direct methods’ applies to a collection of structure solution methods which attempt to directly solve the phase problem by the use of phase relationships based on the observed intensities. These methods rely on the fact that the intensities and phases are not independent: they are linked by the electron density, and the electron density in a crystal cannot be negative.[70] These conditions give rise to constraints on the values which the phases of related reflections can take. For direct methods to be a viable means of structure solution, knowledge of the chemical composition of the crystal must be reasonably accurate.

2.2.4.3.2 Patterson Method

The Patterson method ignores the phase problem, and uses only $|F_{hkl}|^2$ values to solve the structure.[70] The summation in Patterson space (u, v, w) creates a map of interatomic vectors, and is given by:

$$P_{uvw} = \frac{1}{V}\sum_{hkl}|F_{hkl}|^2 \cos[2\pi(hu + kv + lw)]$$

(Equation 2-23)

Each peak in the Patterson map will have a height proportional to the product of the scattering factors of the atoms whose separation it represents. The build up of a Patterson map may be visualised by moving each interatomic vector to the cell origin, without changing its direction. This is a consequence of recombining only the intensities and ignoring the phases; information about lateral position is missing.

Patterson methods can be used to locate several atoms in the unit cell which are significantly heavier than the others (the *heavy atom method*). For example, vectors between heavy atoms related by symmetry often lie in special positions, making them easily recognisable. Patterson methods can also be used to locate a group of atoms which have a known arrangement, such that their intramolecular vectors can be easily calculated (the *Patterson search method*).

2.3 Physical Measurements

2.3.1 SQUID Magnetometry

A Quantum Design MPMS 5000 SQUID magnetometer was used to collect magnetic data on certain samples. The magnetometer consists of a superconducting magnet, which allows the production of large magnetic fields; superconducting detection coils, which couple inductively to the sample; and a superconducting quantum interference device (SQUID), amongst other components. A measurement is performed by moving the sample through the superconducting detection coils. The magnetic moment of the sample induces an electric current in the coils. A change of magnetic flux in the coils produces a proportional change in the current in the detection circuit. This change in current produces a change in the SQUID output voltage, as the device essentially functions as a current to voltage converter. The output voltage is proportional to the magnetic moment of the sample.

2.3.1.1 Magnetism

There are several different types of magnetic behaviour that a material can possess. Discrete metal centres, such as those in solution, can possess one of two types of magnetism: diamagnetism or paramagnetism. Diamagnetism occurs as a result of paired electron spins, and is therefore a property of all materials. However, it is overpowered if

other magnetic effects are present. For a material to be paramagnetic it must possess unpaired electrons, which are aligned at random (Figure 2-9).

In the solid state, the close proximity of metal centres can allow other cooperative magnetic effects to occur. These include ferromagnetism, antiferromagnetism and ferrimagnetism. In a ferromagnetic material, the unpaired electrons are arranged with their spins aligned parallel. There is therefore a net magnetic moment. In an antiferromagnetic material, the unpaired electrons are arranged with their spins aligned antiparallel. The magnetic moment produced by the alignment of electron spins is therefore cancelled out. In a ferrimagnetic material, the electron spins are aligned antiparallel, but the magnetic moment of up-spin electrons is of a different magnitude to that of down-spin electrons. This results in a net magnetic moment. The alignment of electron spins in these magnetic effects is depicted in Figure 2-9.

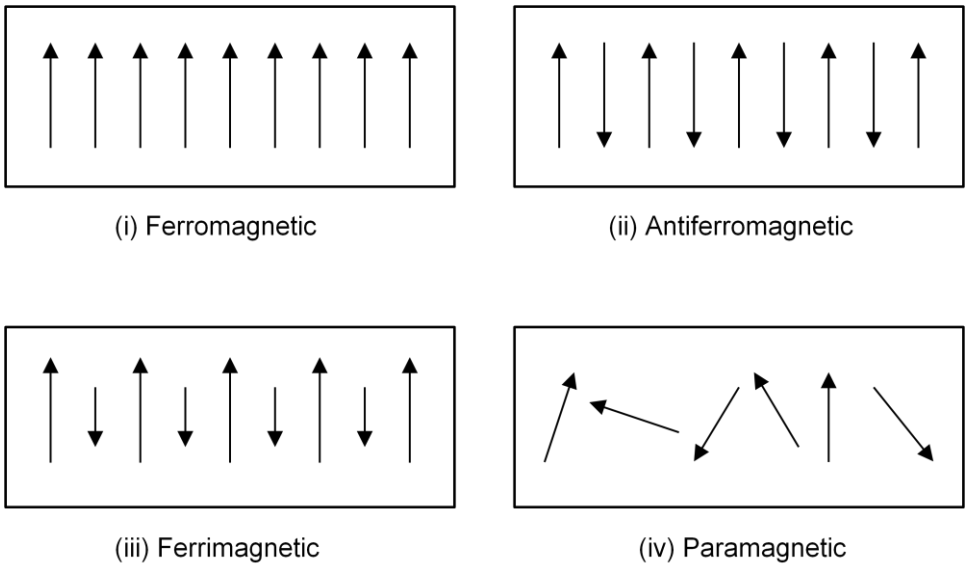

Figure 2-9: Alignment of electron spins in a (i) ferromagnetic, (ii) antiferromagnetic, (iii) ferrimagnetic and (iv) paramagnetic material

2.3.1.1.1 Curie and Curie-Weiss Laws

Many paramagnetic substances obey the Curie law, which states that magnetic susceptibility is inversely proportional to temperature:

$$\chi = \frac{C}{T}$$

(Equation 2-24)

where χ = magnetic susceptibility, C = Curie constant and T = absolute temperature.

The Curie law applies when there is no spontaneous interaction between adjacent unpaired electrons. The electrons tend to align at low temperatures in the presence of a magnetic field, but with increasing temperature, and therefore increasing thermal energy, the spins become randomly orientated. A plot of χ against T for a paramagnetic material is shown in Figure 2-10.

At high temperatures, ferromagnetic and antiferromagnetic materials lose their magnetic ordering and become paramagnets. The temperature at which this transition occurs is individual for each material, and is called the Curie temperature, T_C, for ferromagnetic materials, and the Néel temperature, T_N, for antiferromagnetic materials. When there is spontaneous interaction between adjacent electron spins (at low temperatures this may be attributed to ferromagnetic or antiferromagnetic behaviour), a better fit to the high temperature paramagnetic behaviour is provided by the Curie-Weiss law:

$$\chi = \frac{C}{T + \theta}$$

(Equation 2-25)

where θ = Weiss constant.

The inverse Curie-Weiss law is as follows:

$$\frac{1}{\chi} = \frac{T}{C} + \frac{\theta}{C}$$

(Equation 2-26)

A plot of χ^{-1} against T will have a gradient equal to C^{-1} and an intercept equal to θ/C, according to the inverse Curie-Weiss law. Figure 2-10 shows a plot of χ^{-1} against T for a paramagnet obeying the Curie law, and ferromagnetic and antiferromagnetic materials obeying the Curie-Weiss law.

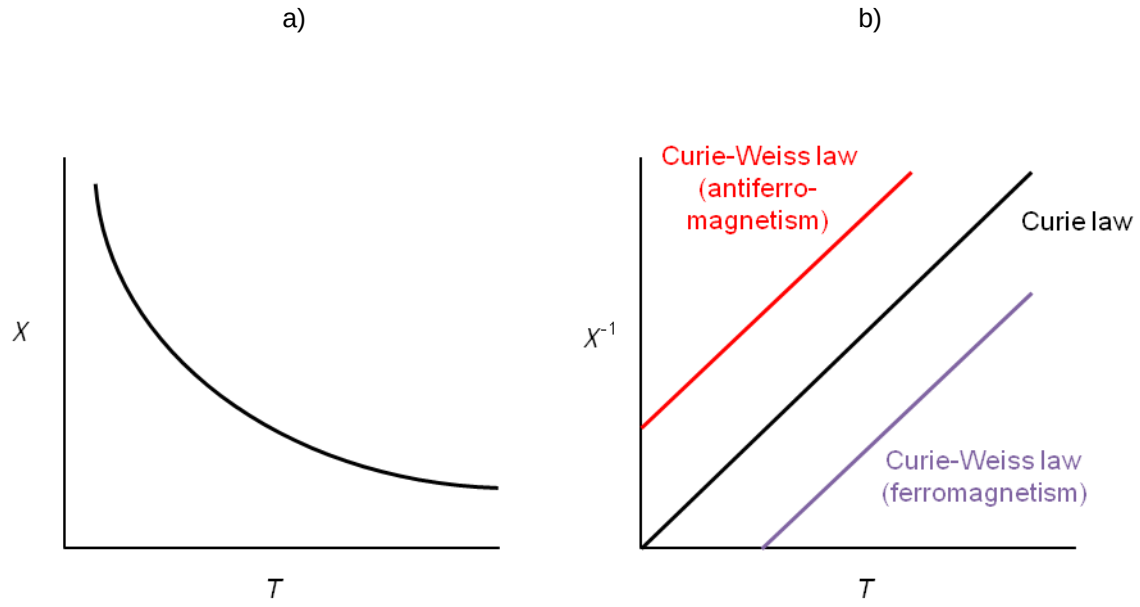

Figure 2-10: A plot of (a) χ against T for a paramagnetic material, and (b) χ^{-1} against T for a paramagnetic material obeying the Curie law, and ferromagnetic and antiferromagnetic materials obeying the Curie-Weiss law

At temperatures below T_C and T_N, deviation from Curie-Weiss behaviour occurs.

2.3.1.1.2 Pauli Paramagnetism

Pauli paramagnetism is a weak magnetic effect induced in some substances by the application of a magnetic field. If the electron spins in the substance are parallel to the applied field, the electrons go to a lower energy state. If the electron spins are antiparallel to the applied field, it is energetically favourable for the electrons to go to a higher energy state and change spin. This produces an imbalance of electron spins aligned with and against the field, giving rise to a net magnetic moment. Pauli paramagnetism is temperature independent, but is dependent on magnetic field strength.

3.0 First Steps: Binary Intermetallics

3.1 Transition Metal Nitrides: Background to the Method

Transition metal nitrides are interesting and technologically important materials. Some of their useful properties include hardness,[77] electrical[78] and thermal[79] conductivity, superconductivity[80] and magnetism.[81] In terms of bonding, transition metal nitrides tend to fall broadly into two categories. In the first category, bonding is similar to that in oxides, in that there is significant ionic or covalent character (*e.g.* Ca_3N_2). In the second category, the bonding is more similar to that present in carbides, in that metallic bonding predominates, with nitrogen atoms present in interstitial positions within the metal array (*e.g.* HfN, TiN, CrN). Traditional synthesis of nitrides involves the reaction of metals with nitrogen or ammonia at very high temperatures. CrN, for example, can be prepared by reacting chromium metal with nitrogen.[82] However, nitrides are generally difficult to synthesise under nitrogen due to the high bond energy of N_2 (941 kJ mol^{-1}).[83] The limited success of this method has resulted in attention being turned to the development of lower temperature routes. The synthesis of nitrides by reacting metal oxides with gaseous ammonia is carried out at lower temperatures, but these are still relatively high. VN, for example, can be prepared by reacting vanadium oxide with ammonia at 850 °C.[84] A new synthetic route to interstitial ternary nitrides was recently developed by Prior *et al*., involving the reduction of mixed metal oxides under 10% hydrogen in nitrogen.[85] The route was employed in the synthesis of ternary and quaternary metal nitrides adopting the filled β-manganese structure and the η-carbide structure. An example of a typical reaction equation is given below:

$$2\ NiO + 3\ MoO_3 \xrightarrow{10\%\ H_2\ in\ N_2} Ni_2Mo_3N + 11\ H_2O$$

The water produced as a by-product in the reaction is blown away by the flow of the gas through the furnace. The filled β-manganese compounds prepared in this way include Ni_2Mo_3N, Co_2Mo_3N (impure), and the solid solutions $Ni_{2-x}M_xMo_3N$ (M = Co, Pd),[85] $Fe_{2-x}M_xMo_3N$ (M = Ni, Pd, Pt)[86] and $Fe_{2-x}Rh_xMo_3N$.[87] The η-carbide compounds prepared in this way include the common η-carbides Fe_3Mo_3N and Co_3Mo_3N,[85] the solid solution of Fe in Co_3Mo_3N ($Co_{3-x}Fe_xMo_3N$),[88] and the ordered quaternary η-carbide Ni_2GaMo_3N.[88]

The reduction-nitridation method employed for the synthesis of η-carbide and filled β-manganese nitrides developed by Prior *et al.*[85] was adapted by Baker *et al.* for the synthesis of the germanide, $FeMo_4Ge_3$, as shown below: [89]

$$Fe_2O_3 + 8\ MoO_3 + 6\ GeO_2 \xrightarrow{10\%\ H_2\ in\ Ar} 2\ FeMo_4Ge_3 + 14½\ H_2O$$

Synthesis of the germanide was undertaken by reducing mixed metal oxides under 10% hydrogen in argon, rather than 10% hydrogen in nitrogen which was used to prepare the nitrides. The application of the reductive synthetic route to the synthesis of the germanide demonstrated that the route can be applied to other systems. The application of the route to the synthesis of antimonides, bismuthides and other germanides was therefore proposed. This chapter therefore comprises preliminary work that was carried out to assess the viability of the reductive synthetic route for the synthesis of binary antimonides, bismuthides and germanides. Known compositions were largely chosen as initial target compounds. The ease of reduction of the starting metal oxides was taken into account when planning which compositions to pursue. Preliminary experiments revealed that most of the starting materials reduced easily between 400 and 500 °C. Most reactions were therefore carried out within this temperature range.

3.2 Antimonides

The synthesis of binary antimonides of iron through to zinc in the first row of the *d*-block of the Periodic Table was attempted, as well as some binary antimonides of second and third row elements, including those of molybdenum and tungsten. An example of a reaction equation is given below:

$$2\ Co_3O_4 + 9\ Sb_2O_3 \xrightarrow{10\%\ H_2\ in\ Ar} 6\ CoSb_3 + 35\ H_2O$$

3.2.1 Iron Antimonides

The Fe-Sb system contains two intermetallic phases: ε-FeSb and $FeSb_2$.[90] The ε-FeSb phase is non-stoichiometric and metal-rich, with the atomic percentage of antimony in the phase ranging from 40-47%.[90] ε-FeSb melts congruently; there has been some disagreement regarding the specific melting point, but it has been agreed that the melting point at 42 at.%

Sb is 1019 °C.[90,91] In contrast, $FeSb_2$ is stoichiometric and forms peritectically at 738 °C.[90] The attempted synthesis of ε-FeSb and $FeSb_2$ is outlined in the following sections.

3.2.1.1 ε-FeSb

Stoichiometric amounts of iron(III) oxide and antimony(III) oxide were heated at 425 °C (48 hours), 450 °C (24 hours) and once more at 450 °C (24 hours). X-ray powder diffraction patterns were recorded after both reactions at 450 °C over the range $5 \leq 2\theta/° \leq 70$, with a counting time of 1.0 s per step.

Analysis of the x-ray diffraction patterns revealed that the predominant phase formed after the first reaction at 450 °C was the intermediate oxide, $FeSb_2O_4$. Both starting reagents were also present in the sample, in addition to elemental antimony. The second reaction at 450 °C resulted in the reduction of some of the $FeSb_2O_4$ to $FeSb_2$. Secondary phases present included $FeSb_2O_4$, elemental antimony and iron(II,III) oxide. At no stage in the reaction was the 1:1 phase ε-FeSb present. The formation of $FeSb_2$ rather than ε-FeSb suggests that the reductive synthesis of $FeSb_2$ is more energetically favourable than the reductive synthesis of ε-FeSb. In addition, the tendency towards non-stoichiometry in ε-FeSb may have made the reaction less favourable, given that stoichiometric amounts of starting metal oxides were used. The reductive synthesis of pure $FeSb_2$ was also attempted, and is outlined in the following section.

3.2.1.2 $FeSb_2$

Stoichiometric amounts of iron(III) oxide and antimony(III) oxide were heated at 425 °C (48 hours), 450 °C (24 hours), 475 °C (24 hours) and finally at 500 °C (24 hours). X-ray powder diffraction patterns were recorded after reaction at 450 °C, 475 °C and 500 °C, over the range $5 \leq 2\theta/° \leq 70$, with a counting time of 1.0 s per step.

Analysis of the x-ray diffraction patterns revealed that the predominant phase formed after reaction at 450 °C was the intermediate oxide, $FeSb_2O_4$. This was not unexpected, due to the formation of $FeSb_2O_4$ in the reaction performed in order to synthesise ε-FeSb. Secondary phases in the sample included antimony(III) oxide and elemental antimony. It is possible that a small amount of iron(III) oxide was also present in the sample at this stage. However, the data were of relatively low intensity, resulting in difficulty in the

identification of very minor phases in the sample. Reaction at 475 °C yielded $FeSb_2$, with impurities of antimony(III) oxide, elemental antimony and iron(II,III) oxide. The presence of iron(II,III) oxide after this reaction further implied the presence of iron(III) oxide after reaction at 450 °C. The final reaction, which was carried out at 500 °C, was performed in an attempt to reduce the metal oxides still remaining in the sample. However, it proved difficult to reduce the remaining iron(II,III) oxide at this temperature. The final product contained a mixture of $FeSb_2$, elemental antimony and iron(II,III) oxide. It was clear after studying the results of this reaction, and others described in later sections, that the formation of elemental antimony prevented subsequent synthesis of the desired phases; once elemental antimony had formed, it did not participate further in the reaction.

A three-phase Rietveld refinement was carried out after reaction at 500 °C using the structure published by Chumak *et al.* as the initial model for $FeSb_2$.[92] Attempts to refine isotropic displacement parameters resulted in negative values. These were therefore set to zero in the final refinement. The weight fractions of antimony and iron(II,III) oxide were not substantial, with values equal to 0.160(5) and 0.06(1), respectively. Data from the refinement are given in Table 3-1. The Rietveld fit is shown in Figure 3-1.

$FeSb_2$	Refined values			Literature values[92]		
Space group		*Pnnm*				
Structure type		$FeAs_2$				
a / Å		5.8300(7)			5.823(1)	
b / Å		6.5378(8)			6.523(1)	
c / Å		3.1998(3)			3.194(1)	
V / Å^3		121.96(4)			121.32(5)	
Atomic positions	***x***	***y***	***z***	***x***	***y***	***z***
Fe (4*g*)	0	0	0	0	0	0
Sb (2*a*)	0.1880(6)	0.6451(6)	0	0.1882(1)	0.6437(1)	0
Isotropic displacement parameters / Å^2	**Fe**		**Sb**			
	0		0			
R(F^2)		0.1842				
χ^2		1.339				

Table 3-1: Rietveld refinement data for $FeSb_2$

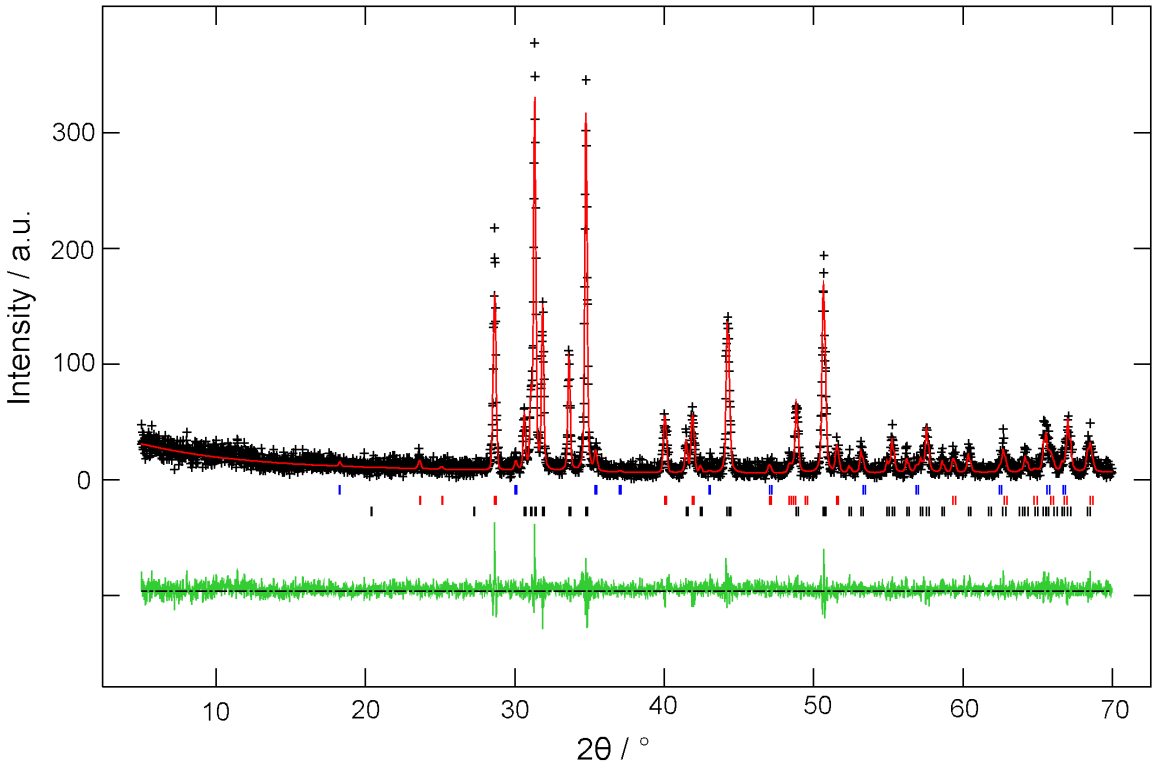

Figure 3-1: Observed (black), calculated (red) and difference (green) x-ray powder diffraction profiles for $FeSb_2$. Lower tick marks indicate positions of allowed reflections for $FeSb_2$. Middle tick marks indicate positions of allowed reflections for Sb. Upper tick marks indicate positions of allowed reflections for Fe_3O_4

The Rietveld fit demonstrates that the reaction produced a mixture of $FeSb_2$, elemental antimony and Fe_3O_4. The reaction appears to occur *via* the reduction of iron(III) oxide and antimony(III) oxide to the intermediate oxide, $FeSb_2O_4$, and subsequently *via* the reduction of $FeSb_2O_4$ to $FeSb_2$. The structures adopted by $FeSb_2O_4$ and $FeSb_2$ are the Pb_3O_4 structure and the $FeAs_2$ (compressed marcasite) structure, respectively. The two structures are shown in Figure 3-2 in order to highlight the relationships between them, and subsequently propose a mechanism for the reduction of $FeSb_2O_4$ to $FeSb_2$.

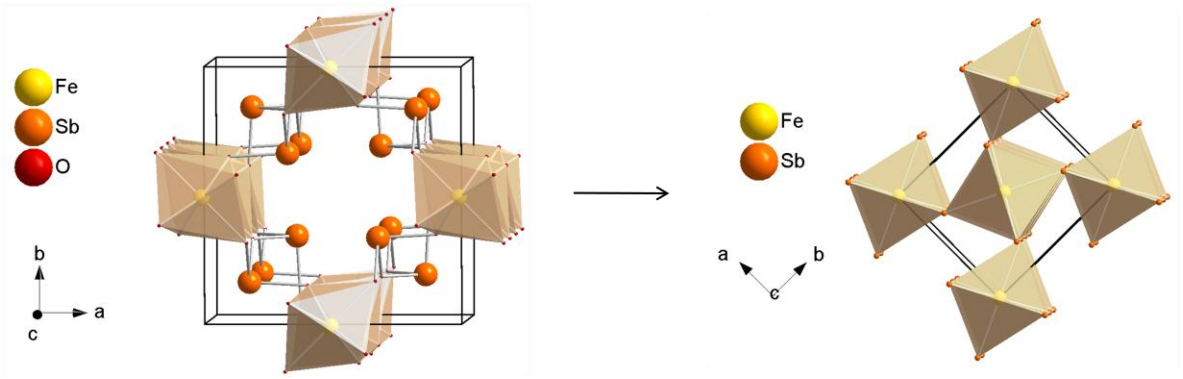

Figure 3-2: Structure of $FeSb_2O_4$ (left) with chains of edge-sharing octahedra and $FeSb_2$ (right) with chains of edge- and corner-sharing octahedra

Reduction of $FeSb_2O_4$ to $FeSb_2$ could occur *via* the migration of antimony atoms in $FeSb_2O_4$ to form $FeSb_6$ octahedra as oxygen is removed from the structure. The migration of antimony atoms would enable closer approach of the octahedra, and would also allow an extra iron atom to be introduced into the centre of the unit cell.

It is unlikely that $FeSb_2$ could be formed as a pure phase using this synthetic route, due to the different temperatures at which iron(II,III) oxide and antimony(III) oxide reduce.

3.2.2 Cobalt Antimonides

The Co-Sb system contains three intermetallic phases: CoSb, $CoSb_2$ and $CoSb_3$.[93] CoSb melts congruently at 1215 °C.[94] $CoSb_2$ and $CoSb_3$ both form through peritectic reactions: L + CoSb ↔ $CoSb_2$ (929 °C) and L + $CoSb_2$ ↔ $CoSb_3$ (873 °C).[94] As mentioned in section 1.3.1.1, CoSb exists over a broad range of composition, in both cobalt-rich and antimony-rich phases; cobalt vacancies occur in the antimony-rich compositions, and in the cobalt-rich compositions interstitial cobalt atoms are found at the centres of the trigonal bipyramids formed from antimony atoms[93] (2*d* Wyckoff position with coordinates (⅓, ⅔, ¾)). A pictorial representation of this is given in Figure 3-3.

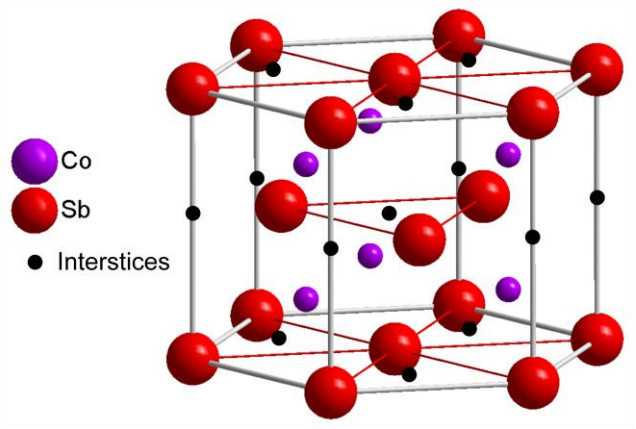

Figure 3-3: Diagram showing the interstitial sites present at the centres of the trigonal bipyramids formed from antimony atoms in CoSb

Complete filling of the interstitial sites in CoSb would result in the 'filled' NiAs structure, more commonly known as the Ni_2In-type structure.[93] The difference between the diffraction pattern of unfilled CoSb and the diffraction pattern of CoSb when an atom is put onto the 2*d* Wyckoff position with an occupancy of one is highlighted in Figure 3-4. According to Zhang *et al*., CoSb can also exist in a stoichiometric form.[93]

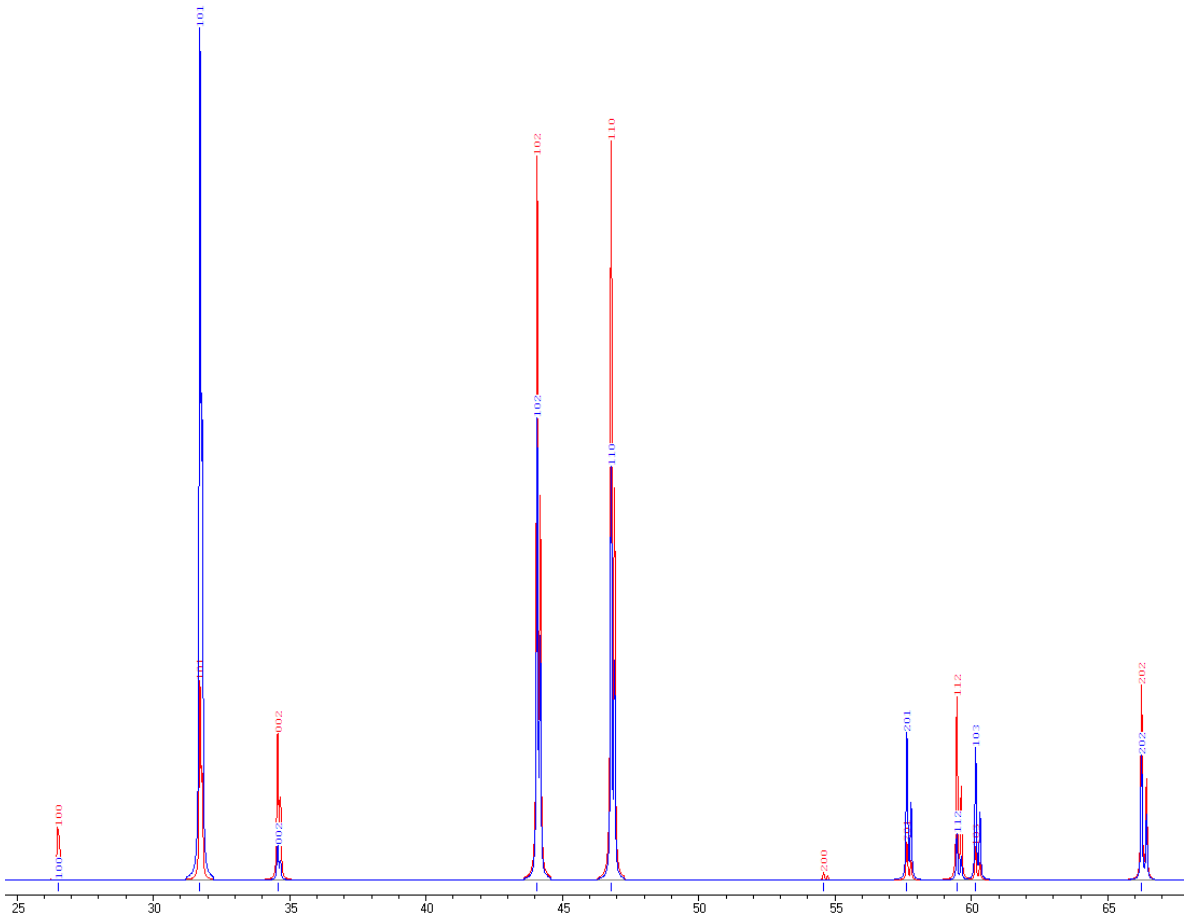

Figure 3-4: Diagram highlighting the difference in the diffraction pattern of unfilled CoSb (blue) and the diffraction pattern of CoSb when an atom is placed on the 2*d* Wyckoff position with an occupancy equal to one (red)

The most marked difference in the patterns shown in Figure 3-4 is the difference in intensity of the (101), (102) and (110) reflections between the filled and unfilled phases.

Skutterudite compounds, and $CoSb_3$ in particular, are well-known thermoelectric materials.[95] The empty octants within the unit cell can be filled with loosely bound atoms, which are able to 'rattle'. This rattling lowers the thermal conductivity of the material, leading to an increase in its thermoelectric power. A representation of 'filled' $CoSb_3$ is shown in Figure 3-5.

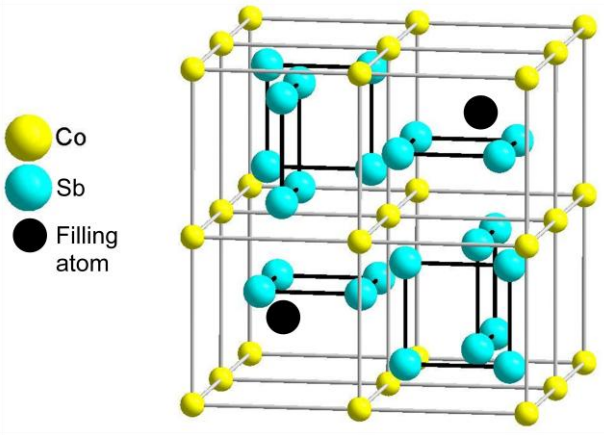

Figure 3-5: Representation of 'filled' $CoSb_3$

Filled skutterudite materials have the formula RM_4X_{12}, where R is the filling atom (most often a heavy element, such as a rare earth),[95] M is Co, Rh or Ir, and X is Sb, As or P. Examples of filling atoms include lanthanum,[96] barium,[97] indium,[98] ytterbium[99] and tin.[100] Double-filled skutterudite materials have also been shown to exhibit excellent thermoelectric properties.[101]

Doping skutterudites has also proved useful in enhancing the thermoelectric power: transition metal site dopants have included nickel[102] and iron;[103] metalloid site dopants have included tin[104] and tellurium.[105]

Although $CoSb_3$ is classed as an intermetallic, and there is therefore no strict representation of the bonding within the compound, a model has been proposed according to Kleinke.[106] The model assumes that the planar Sb_4 rectangles share electrons, as the distances between them are comparable to the lengths of Sb-Sb single bonds. Reduction of the Sb atoms by the Co atoms gives each Sb atom an extra electron. Each Sb atom therefore has six valence electrons. Each atom is bonded to two others, enabling all Sb atoms to achieve the octet. This results in the formation of Sb_4^{4-} units, which are able to form a neutral compound when the oxidation state of cobalt is taken to be +3.

The attempted synthesis of CoSb, $CoSb_2$ and $CoSb_3$ is outlined in the following sections.

3.2.2.1 CoSb

Stoichiometric amounts of cobalt(II, III) oxide and antimony(III) oxide were heated at 425 °C (48 hours) and subsequently at 450 °C (24 hours). An x-ray powder diffraction pattern was recorded after the final reaction over the range $5 \leq 2\theta/° \leq 120$, with a counting time of 9.3 s per step.

Analysis of the x-ray diffraction pattern indicated that the product was predominantly CoSb, but contained very small amounts of impurities of cobalt and antimony. A three-phase Rietveld refinement was carried out using the structure published by Terzieff *et al.* as the initial model for CoSb.[107] A background subtraction was performed in order to remove the background contribution from the greased sample mount. The weight fractions of cobalt and antimony were determined to be 0.005(1) and 0.0057(5), respectively. This reaction therefore demonstrated the ability to synthesise CoSb to a high degree of purity using this synthetic route. Data from the refinement are given in Table 3-2. The Rietveld fit is shown in Figure 3-6.

CoSb	Refined values			Literature values[107]		
Space group	$P6_3/mmc$					
Structure type	NiAs					
a / Å	3.8906(1)			3.900		
c / Å	5.1875(2)			5.172		
V / Å^3	68.002(5)			68.13		
Atomic positions	***x***	***y***	***z***	***x***	***y***	***z***
Co (2*a*)	0	0	0	0	0	0
Sb (2*c*)	⅓	⅔	¼	⅓	⅔	¼
Isotropic displacement parameters / Å^2	**Co**		**Sb**			
	0.031(1)		0.0238(6)			
R(F^2)	0.1367					
χ^2	7.986					

Table 3-2: Rietveld refinement data for CoSb

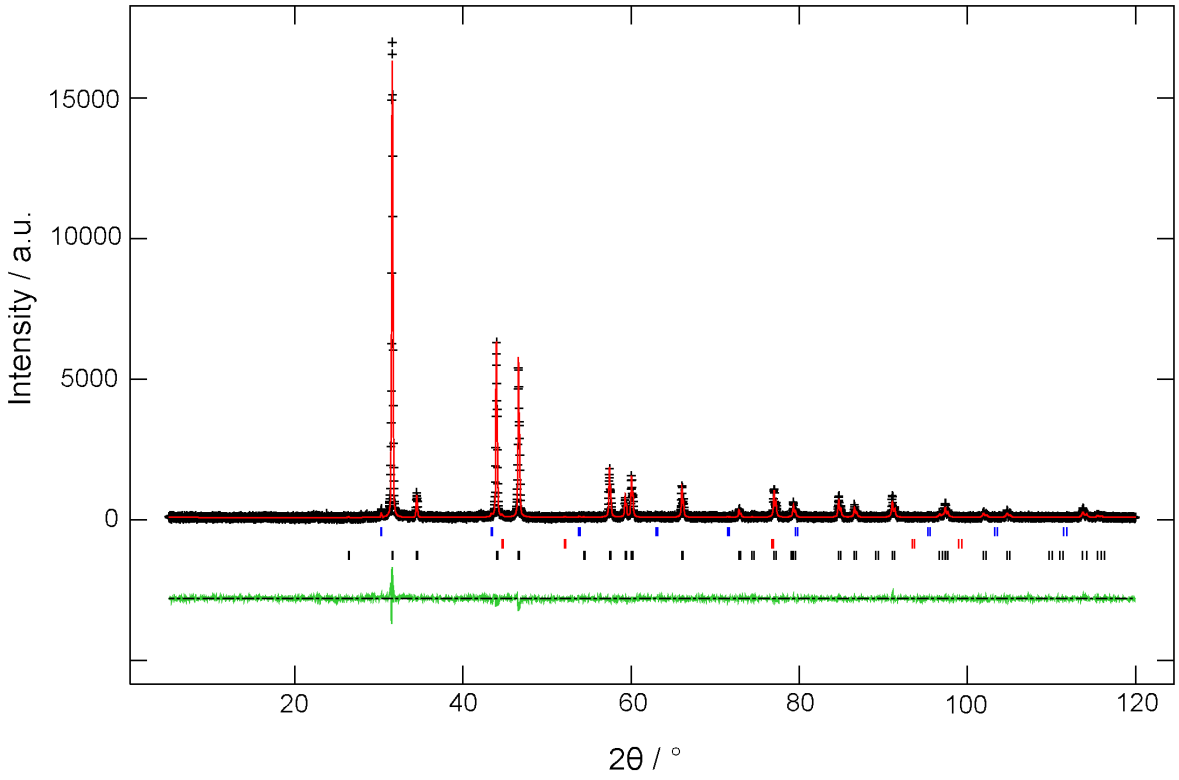

Figure 3-6: Observed (black), calculated (red) and difference (green) x-ray powder diffraction profiles for CoSb. Lower tick marks indicate positions of allowed reflections for CoSb. Middle tick marks indicate positions of allowed reflections for Co. Upper tick marks indicate positions of allowed reflections for Sb

The Rietveld fit demonstrates that the reaction produced a mixture dominated by CoSb, with very small amounts of elemental cobalt and elemental antimony. The presence of negligible amounts of elemental cobalt and antimony in the product suggests that the starting metal oxides were over-reduced to a small extent, forming their respective metallic elements, rather than CoSb. There is no evidence for non-stoichiometry in the cobalt antimonide prepared here; reflection intensities correspond to the unfilled phase rather than the filled phase (section 3.2.2).

3.2.2.2 $CoSb_2$

Stoichiometric amounts of cobalt(II, III) oxide and antimony(III) oxide were heated at 425 °C (48 hours) and subsequently at 450 °C (24 hours). An x-ray powder diffraction

pattern was recorded after the final reaction over the range $5 \leq 2\theta/° \leq 70$, with a counting time of 1.0 s per step.

Analysis of the x-ray diffraction pattern revealed that the product was predominantly $CoSb_2$, but contained a small scale impurity of $CoSb_3$. A two-phase Rietveld refinement was carried out using the structure published by Kjekshus as the initial model for $CoSb_2$.[45] Refinement of the isotropic displacement parameter of the antimony atom located on (0.349, 0.359, 0.169) caused the refinement to diverge. The value was therefore set to 0.025 $Å^2$ and not refined. The weight fraction of $CoSb_3$ was calculated to be 0.178(9). Data from the refinement are given in Table 3-3. The Rietveld fit is shown in Figure 3-7.

$CoSb_2$	Refined values			Literature values[45]		
Space group		$P2_1/c$				
Structure type		$CoSb_2$				
a / Å		6.504(1)			6.5077(3)	
b / Å		6.385(1)			6.3879(4)	
c / Å		6.537(1)			6.5430(3)	
V / $Å^3$		240.41(9)			240.91(2)	
Atomic positions	***x***	***y***	***z***	***x***	***y***	***z***
Co (4*e*)	0.26(1)	0.00(1)	0.26(1)	0.27	0	0.28
Sb(1) (4*e*)	0.349(3)	0.359(5)	0.169(2)	0.354	0.359	0.168
Sb(2) (4*e*)	0.148(3)	0.641(5)	0.367(2)	0.162	0.638	0.368
Isotropic displacement parameters / $Å^2$	**Co**	**Sb(1)**	**Sb(2)**			
	0.035(8)	0.025	0.032(7)			
R(F^2)		0.1547				
χ^2		1.172				

Table 3-3: Rietveld refinement data for $CoSb_2$

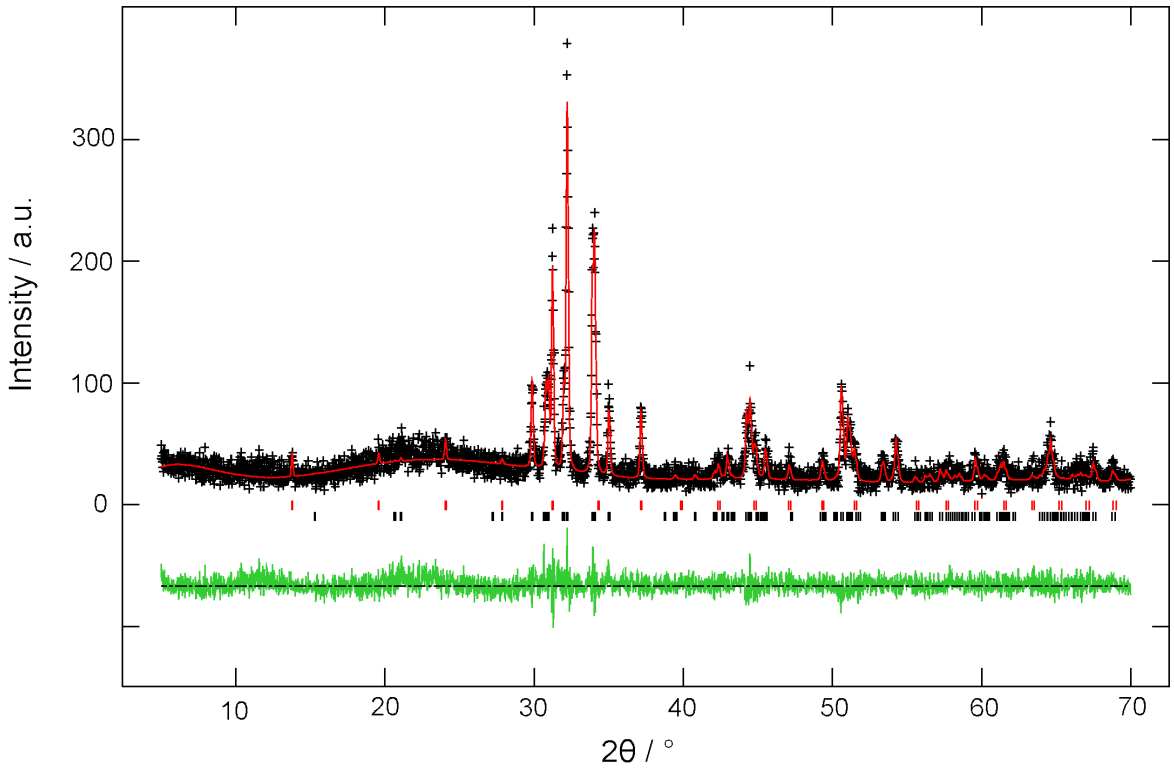

Figure 3-7: Observed (black), calculated (red) and difference (green) x-ray powder diffraction profiles for $CoSb_2$. Lower tick marks indicate positions of allowed reflections for $CoSb_2$. Upper tick marks indicate positions of allowed reflections for $CoSb_3$

The Rietveld fit demonstrates that this reaction produced a mixture of $CoSb_2$ and $CoSb_3$. The presence of $CoSb_3$ in the final product is unexpected, as the stoichiometric ratio of the starting reagents (1:2 Co:Sb) does not allow for a cobalt deficiency. It is possible that a small amount of a poorly crystalline cobalt-based compound is present in the sample, and is therefore not detected in the diffraction pattern. The broad hump in the pattern located at approximately 18-27 2θ/° is a result of the presence of excess grease on the sample mount, not a poorly crystalline impurity. The formation of $CoSb_3$ may be a result of a difference in stability between the two stoichiometries.

3.2.2.3 $CoSb_3$

Stoichiometric amounts of cobalt(II, III) oxide and antimony(III) oxide were heated at 425 °C (48 hours), 450 °C (24 hours) and once more at 450 °C (24 hours). X-ray powder

diffraction patterns were recorded after the first and second reaction at 450 °C, over the range $5 \leq 2\theta/° \leq 120$, with a counting time of 9.3 s per step.

Analysis of the x-ray diffraction pattern recorded after the first firing at 450 °C indicated that $CoSb_3$ had formed in high purity. A very small impurity peak was present in the pattern at approximately 30° 2θ. It is possible that this could be attributed to the antimony oxide, Sb_6O_{13}, and could therefore be a result of insufficient reduction. However, the peak is too small to state this conclusively. A second firing was carried out at the same temperature in order to increase crystallinity and induce reduction of Sb_6O_{13}. However, the reflection attributed to Sb_6O_{13} was still present in the final product. Rietveld refinement was carried out using the structure published by Xue *et al.* as the initial model for $CoSb_3$.[108] A background subtraction was performed in order to remove the background contribution from the greased sample mount. Data from the refinement are given in Table 3-4. Although R(F^2) and χ^2 are high, there is an outstanding visual fit to the observed data as shown in Figure 3-8.

$CoSb_3$	Refined values			Literature values[108]		
Space group		$Im\bar{3}$				
Structure type		$CoAs_3$				
a / Å		9.0366(2)			9.035(2)	
V / Å^3		737.92(5)			737.5(3)	
Atomic positions	***x***	***y***	***z***	***x***	***y***	***z***
Co (8*c*)	¼	¼	¼	¼	¼	¼
Sb (24*g*)	0	0.3358(2)	0.1582(2)	0	0.3354(2)	0.1583(3)
Isotropic displacement parameters / Å^2	**Co**		**Sb**			
	0.028(2)		0.0284(5)			
R(F^2)		0.2369				
χ^2		9.276				

Table 3-4: Rietveld refinement data for $CoSb_3$

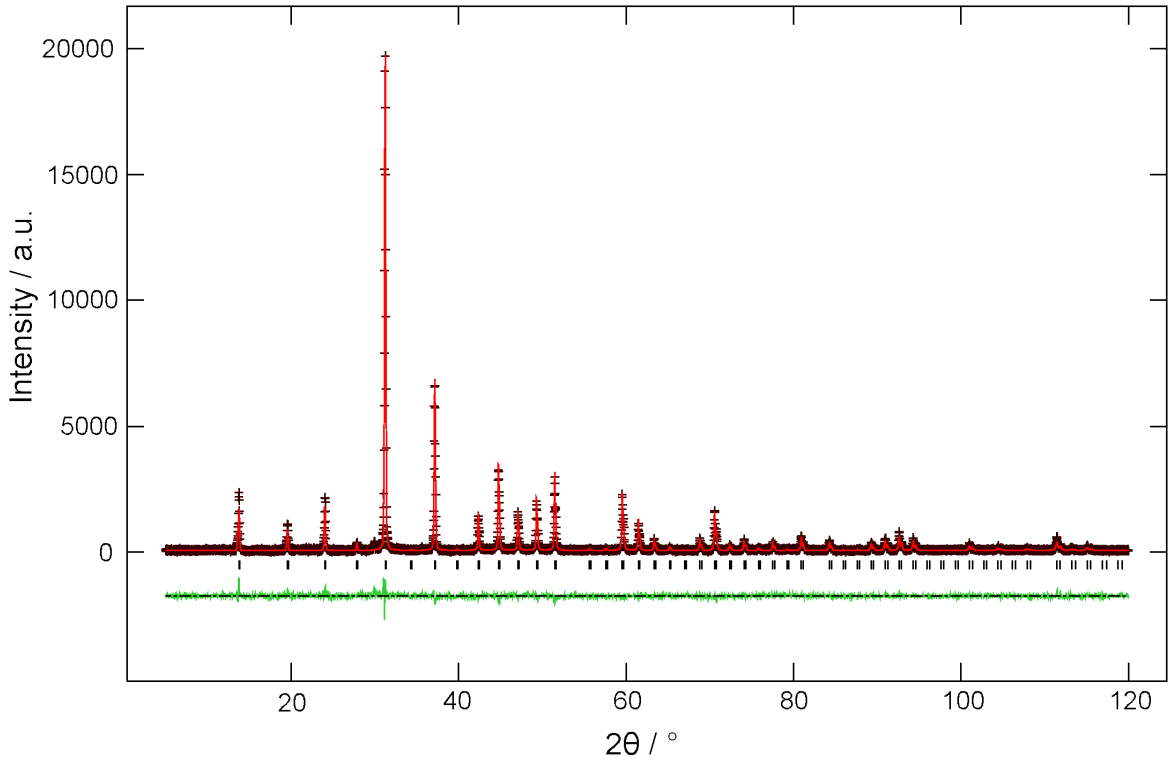

Figure 3-8: Observed (black), calculated (red) and difference (green) x-ray powder diffraction profiles for $CoSb_3$. Tick marks indicate positions of allowed reflections

The Rietveld fit demonstrates that this reaction produced high purity $CoSb_3$. The relative ease of synthesis of $CoSb_3$ in high purity coupled with the existence of $CoSb_3$ in the product of the reaction carried out to prepare $CoSb_2$ suggests that $CoSb_3$ is rather stable and is a thermodynamically favoured product in this system.

3.2.3 Nickel Antimonides

Nickel antimonides exist in four known stoichiometries: NiSb, $NiSb_2$, Ni_3Sb and Ni_5Sb_2.[94] NiSb and Ni_5Sb_2 melt congruently at 1147 and 1161 °C, respectively.[94] Ni_5Sb_2 is only stable at higher temperatures. $NiSb_2$ forms *via* a peritectic reaction at 621 °C: $NiSb + L \leftrightarrow NiSb_2$.[94] As in the case of CoSb, NiSb exists over a broad compositional range; various ranges have been reported, but most are in the range 46-54 at.% Sb.[23,109,110,111] The attempted synthesis of NiSb and $NiSb_2$ is outlined in the following sections.

3.2.3.1 NiSb

Stoichiometric amounts of nickel(II) oxide and antimony(III) oxide were heated at 425 °C (48 hours), 450 °C (24 hours) and once more at 450 °C (24 hours). X-ray powder diffraction patterns were recorded after all reactions over the range $5 \leq 2\theta/° \leq 120$, with a counting time of 9.3 s per step.

Analysis of the x-ray diffraction pattern recorded after the final reaction indicated that NiSb formed in high purity. Rietveld refinement was carried out using the structure published by Le Clanche *et al.* as the initial model.[112] Data from the refinement are given in Table 3-5. The Rietveld fit is shown in Figure 3-9.

NiSb	Refined values			Literature values[112]		
Space group	$P6_3/mmc$					
Structure type	NiAs					
a / Å	3.94523(4)			3.946(1)		
c / Å	5.14243(7)			5.148(1)		
V / Å^3	69.318(2)			69.42		
Atomic positions	***x***	***y***	***z***	***x***	***y***	***z***
Ni (2*a*)	0	0	0	0	0	0
Sb (2*c*)	⅓	⅔	¼	⅓	⅔	¼
Isotropic displacement parameters / Å^2	**Ni**		**Sb**			
	0.0181(5)		0.0148(2)			
R(F^2)	0.0968					
χ^2	2.905					

Table 3-5: Rietveld refinement data for NiSb

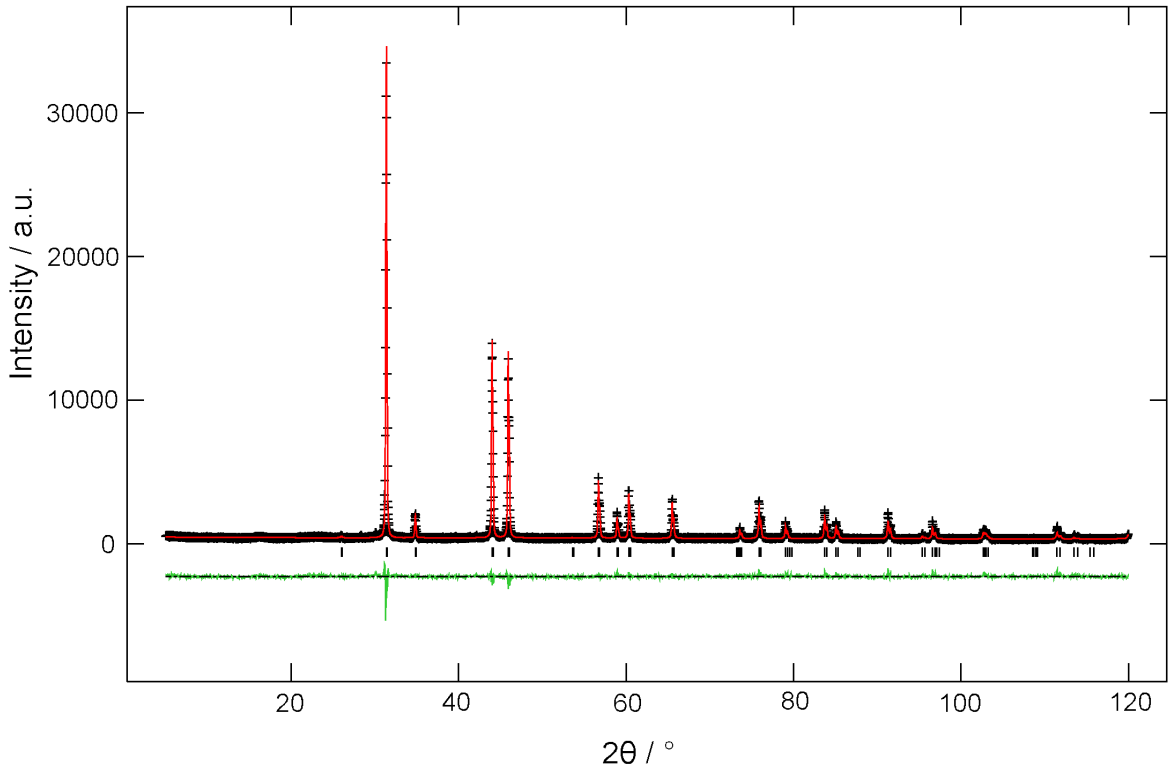

Figure 3-9: Observed (black), calculated (red) and difference (green) x-ray powder diffraction profiles for NiSb. Tick marks indicate positions of allowed reflections

The Rietveld fit demonstrates that high purity NiSb can be prepared using this synthetic route.

3.2.3.2 $NiSb_2$

Stoichiometric amounts of nickel(II) oxide and antimony(III) oxide were heated at 425 °C (48 hours), 450 °C (24 hours), 475 °C (24 hours) and once more at 475 °C (24 hours). X-ray powder diffraction patterns were recorded after reaction at 450 °C, and after both reactions at 475 °C, over the range $5 \leq 2\theta/° \leq 70$, with a counting time of 1.0 s per step.

It is interesting to note that NiSb, rather than $NiSb_2$, formed in the initial stages of the reaction (after reaction at 450 °C). Antimony(III) oxide was still present at this stage of the reaction. This is not unexpected when the stoichiometric ratio of the starting reagents is taken into account. The formation of $NiSb_2$ began during reaction at 475 °C, and was accompanied by significant amounts of NiSb and antimony(III) oxide, with respective weight fractions equal to 0.405(5) and 0.244(5). The final reaction at 475 °C resulted in a

mixture of $NiSb_2$ and NiSb, with respective weight fractions equal to 0.832(3) and 0.167(3). The presence of NiSb and absence of antimony(III) oxide at this stage indicated that a small amount of antimony had been lost from the reaction. It is likely that the relatively high temperatures used to form $NiSb_2$ vapourised a small amount of antimony in the furnace.

A prior reaction carried out in order to synthesise $NiSb_2$ was performed using the same heating regime as that described above, with the exception that the final reaction was carried out at 500 °C rather than 475 °C. The relative amount of NiSb formed in this reaction (weight fraction 0.188(4)) was greater than that formed in the reaction described above. This suggests that lowering the final reaction temperature further may result in a higher purity phase of $NiSb_2$.

A two-phase Rietveld refinement was carried out after reaction at 475 °C using the structure published by Kjekshus *et al.* as the initial model for $NiSb_2$.[113] Attempts to refine the isotropic displacement parameters of the atoms resulted in divergence. They were therefore set to 0.025 $Å^2$ in the final refinement. Data from the refinement are given in Table 3-6. The Rietveld fit is shown in Figure 3-10.

$NiSb_2$	Refined values			Literature values[113]		
Space group		*Pnnm*				
Structure type		Marcasite				
a / Å		5.1860(4)			5.1837(6)	
b / Å		6.3192(5)			6.318(1)	
c / Å		3.8398(3)			3.8408(6)	
V / $Å^3$		125.83(2)			114.01	
Atomic positions	***x***	***y***	***z***	***x***	***y***	***z***
Ni (2*a*)	0	0	0	0	0	0
Sb (4*g*)	0.2176(5)	0.3581(5)	0	0.219(1)	0.3593(8)	0
Isotropic displacement parameters / $Å^2$	**Ni**		**Sb**			
	0.025		0.025			
R(F^2)		0.1181				
χ^2		1.279				

Table 3-6: Rietveld refinement data for $NiSb_2$

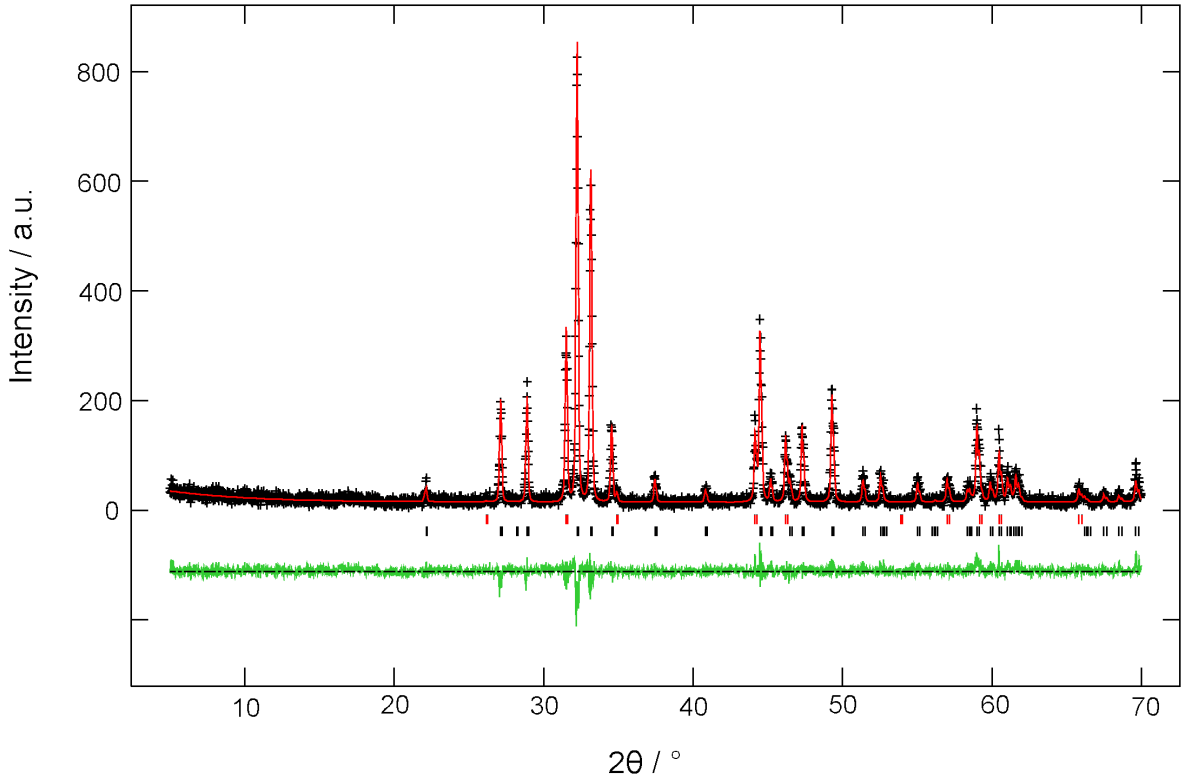

Figure 3-10: Observed (black), calculated (red) and difference (green) x-ray powder diffraction profiles for $NiSb_2$. Lower tick marks indicate positions of allowed reflections for $NiSb_2$. Upper tick marks indicate positions of allowed reflections for NiSb

3.2.4 Copper Antimonides

Copper antimonides exist in four known stoichiometries: Cu_2Sb, Cu_3Sb, $Cu_{10}Sb_3$ (also described as $Cu_{3.3}Sb$) and $Cu_{11}Sb_3$. No antimony-rich compositions are known. $Cu_{10}Sb_3$ was originally thought to crystallise in the space group $P\bar{3}$.[62] This has since been revised to the space group $P6_3/m$.[114]

The attempted synthesis of the metal-rich compositions plus the unknown composition "CuSb" is outlined in the following sections.

3.2.4.1 "CuSb"

A copper antimonide with a Cu:Sb ratio of 1:1 is currently unknown. However, an attempt at synthesising this composition is outlined below.

Stoichiometric amounts of copper(II) oxide and antimony(III) oxide were heated at 450 °C (48 hours) and subsequently fired once more at the same temperature (24 hours). An x-ray powder diffraction pattern was recorded after the final reaction over the range $5 \leq 2\theta/° \leq 70$, with a counting time of 1.0 s per step.

Analysis of the x-ray diffraction pattern indicated that the predominant phase formed after the final reaction at 450 °C was Cu_2Sb. Minor phases of elemental antimony and antimony(III) oxide were also present, due to the stoichiometry of the starting reagents. No other phases were present in the diffraction pattern, indicating that the synthesis of a new phase with the composition CuSb was unsuccessful.

3.2.4.2 Cu_2Sb

Stoichiometric amounts of copper(II) oxide and antimony(III) oxide were heated at 400 °C (48 hours) and subsequently at 425 °C (24 hours). An x-ray powder diffraction pattern was recorded after the final reaction over the range $5 \leq 2\theta/° \leq 120$, with a counting time of 9.3 s per step.

Analysis of the x-ray diffraction pattern indicated that high purity Cu_2Sb had formed after the final reaction. Very small impurity peaks, most obvious in the range $25 \leq 2\theta/° \leq 45$, were also present in the pattern, but were too small to enable identification of the impurity phases. Rietveld refinement was carried out using the structure published by Nuss and Jansen as the initial model.[115] Data from the refinement are given in Table 3-7. The Rietveld fit is shown in Figure 3-11.

Cu_2Sb	Refined values			Literature values[115]		
Space group	*Pnmm*					
Structure type	*Anti*-PbFCl					
a / Å	4.00302(7)			4.0021(4)		
c / Å	6.1058(1)			6.1038(8)		
V / Å^3	97.840(5)			97.76(2)		
Atomic positions	***x***	***y***	***z***	***x***	***y***	***z***
Cu(1) (2*a*)	¾	¼	0	¾	¼	0
Cu(2) (2*c*)	¼	¼	0.2717(3)	¼	¼	0.2725(1)
Sb (2*c*)	¼	¼	0.7033(2)	¼	¼	0.70287(5)

Isotropic displacement parameters / Å^2	**Cu(1)**	**Cu(2)**	**Sb**	**Cu(1)**	**Cu(2)**	**Sb**
	0.0292(6)	0.0314(7)	0.0220(4)	0.0133(2)	0.0154(2)	0.0115(2)
R(F^2)		0.1085				
χ^2		2.509				

Table 3-7: Rietveld refinement data for Cu_2Sb

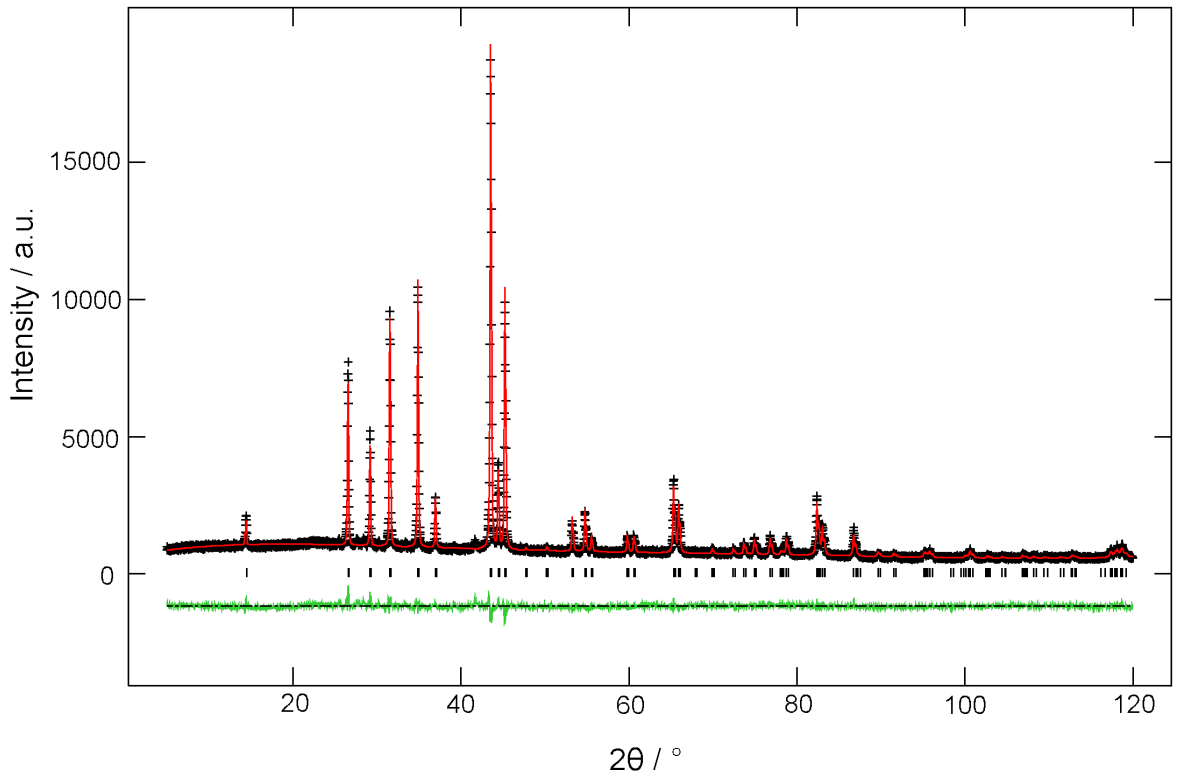

Figure 3-11: Observed (black), calculated (red) and difference (green) x-ray powder diffraction profiles for Cu_2Sb. Tick marks indicate positions of allowed reflections

The Rietveld fit demonstrates that this reaction produced high purity Cu_2Sb.

3.2.4.3 Cu_3Sb

Stoichiometric amounts of copper(II) oxide and antimony(III) oxide were heated at 400 °C (48 hours) and subsequently at 425 °C (24 hours). An x-ray powder diffraction pattern was recorded after the final reaction over the range $5 \leq 2\theta/° \leq 70$, with a counting time of 1.0 s per step.

Analysis of the diffraction pattern revealed that a mixture of Cu_3Sb and Cu_2Sb had formed in the reaction, with weight fractions equal to 0.645(6) and 0.355(6). Small impurity peaks were also present in the pattern, which were unable to be identified. Rietveld refinement was carried out using the structure published by Günzel and Schubert as the initial model for Cu_3Sb.[62] The overlap of some impurity reflections with reflections corresponding to Cu_3Sb made it difficult to refine the profile parameters of Cu_3Sb. The Gaussian and Lorentzian components of the profile were therefore fixed at sensible values and not refined. Only a limited refinement of the structure of Cu_3Sb was possible because of the poor quality of the data. Data obtained from the refinement are given in Table 3-8. The Rietveld fit is shown in Figure 3-12.

Cu_3Sb	Refined values			Literature values[62]		
Space group		*Pmmn*				
Structure type		Cu_3Ti				
a / Å		4.3327(5)			4.3440	
b / Å		5.501(1)			5.4930	
c / Å		4.757(1)			4.7580	
V / Å^3		113.37(3)			113.53	
Atomic positions	***x***	***y***	***z***	***x***	***y***	***z***
Cu(1) (8*g*)	¼	¾	0.178(3)	¼	¾	0.18000
Cu(1) (4*f*)	¾	0	0.33700	¾	0	0.33700
Sb (8*g*)	¼	¼	0.171(2)	¼	¼	0.17000
Isotropic displacement parameters / Å^2	**Cu(1)**	**Cu(1)**	**Sb**			
	0.025	0.025	0.025			
R(F^2)		0.0854				
χ^2		1.411				

Table 3-8: Rietveld refinement data for Cu_3Sb

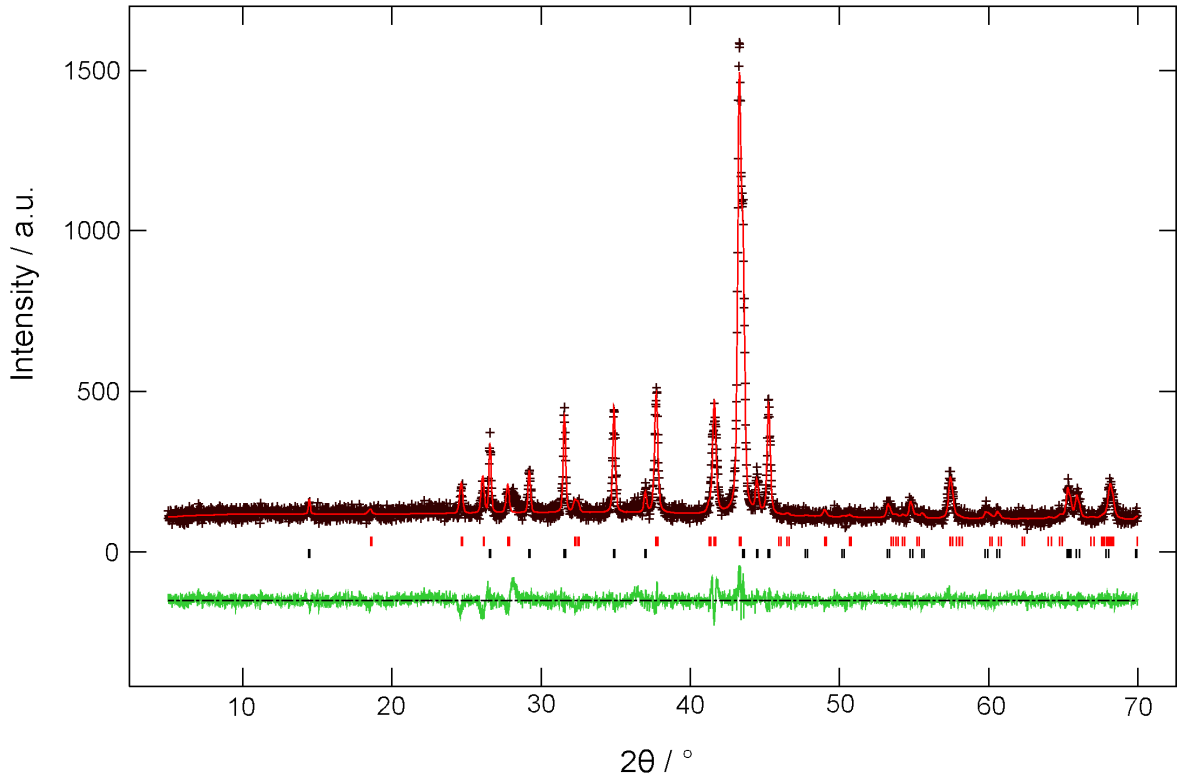

Figure 3-12: Observed (black), calculated (red) and difference (green) x-ray powder diffraction profiles for Cu_3Sb. Lower tick marks indicate positions of allowed reflections for Cu_2Sb. Upper tick marks indicate positions of allowed reflections for Cu_3Sb

The Rietveld fit conclusively demonstrates the presence of Cu_3Sb with an impurity of Cu_2Sb. The presence of Cu_2Sb in the final product is unexpected, as the stoichiometric ratio of the starting reagents (3:1 Cu:Sb) does not allow for a copper deficiency. It is likely that the impurity in the sample is therefore copper-based. The formation of Cu_2Sb may be a result of a difference in stability between the two stoichiometries; it is likely that Cu_2Sb is the more thermodynamically favoured product under these conditions.

3.2.4.4 $Cu_{10}Sb_3$ and $Cu_{11}Sb_3$

Stoichiometric amounts of copper(II) oxide and antimony(III) oxide were heated at 425 °C (48 hours) and once more at 425 °C (24 hours) in an attempt to form $Cu_{10}Sb_3$ and $Cu_{11}Sb_3$. X-ray powder diffraction patterns were recorded after the final reaction over the range $5 \leq 2\theta/° \leq 70$, with a counting time of 1.0 s per step.

Analysis of the diffraction patterns revealed that in both cases a mixture of Cu-Sb phases had formed, but did not possess the desired 10:3 or 11:3 stoichiometries.

3.2.4.5 Cu_4Sb

A new phase with the apparent stoichiometry Cu_4Sb has been synthesised by heating stoichiometric amounts of copper(II) oxide and antimony(III) oxide at 425 °C (48 hours) and subsequently at 450 °C (24 hours). An x-ray powder diffraction pattern was recorded after the final reaction over the range $5 \leq 2\theta/° \leq 120$, with a counting time of 9.3 s per step.

Inductively coupled plasma mass spectrometry (ICP-MS) studies revealed the ratio of Cu:Sb in the system was 3.790:1, which is close to the expected 4:1 stoichiometry.

$Cu_{10}Sb_3$ and $Cu_{11}Sb_3$ are both based on an *hcp* array with some antimony included. Neither model provides a good fit to the observed data. However, peaks in the diffraction pattern can be indexed in the space group *Pmmn*, with a model derived from *hcp* Mg. The diffraction pattern for Cu_4Sb was similar to that of *hcp* Mg, but had an extra unindexed reflection. The hexagonal cell was reset to an orthorhombic cell in the space group *Cmcm* with lattice parameters a = 2.74, b = 4.7458 and c = 4.33 Å. The C-centring was removed by resetting to *Pmnm*. The b axis was then doubled in order to index the extra reflection, and the space group was reset to the standard setting *Pmmn*, resulting in the final lattice parameters a = 2.7423(2), b = 4.3249(2) and c = 9.4835(9) Å. Fractional occupancies were constrained in a 4:1 Cu:Sb ratio. The model gives a reasonable fit to the data, as shown in the Rietveld fit in Figure 3-13.

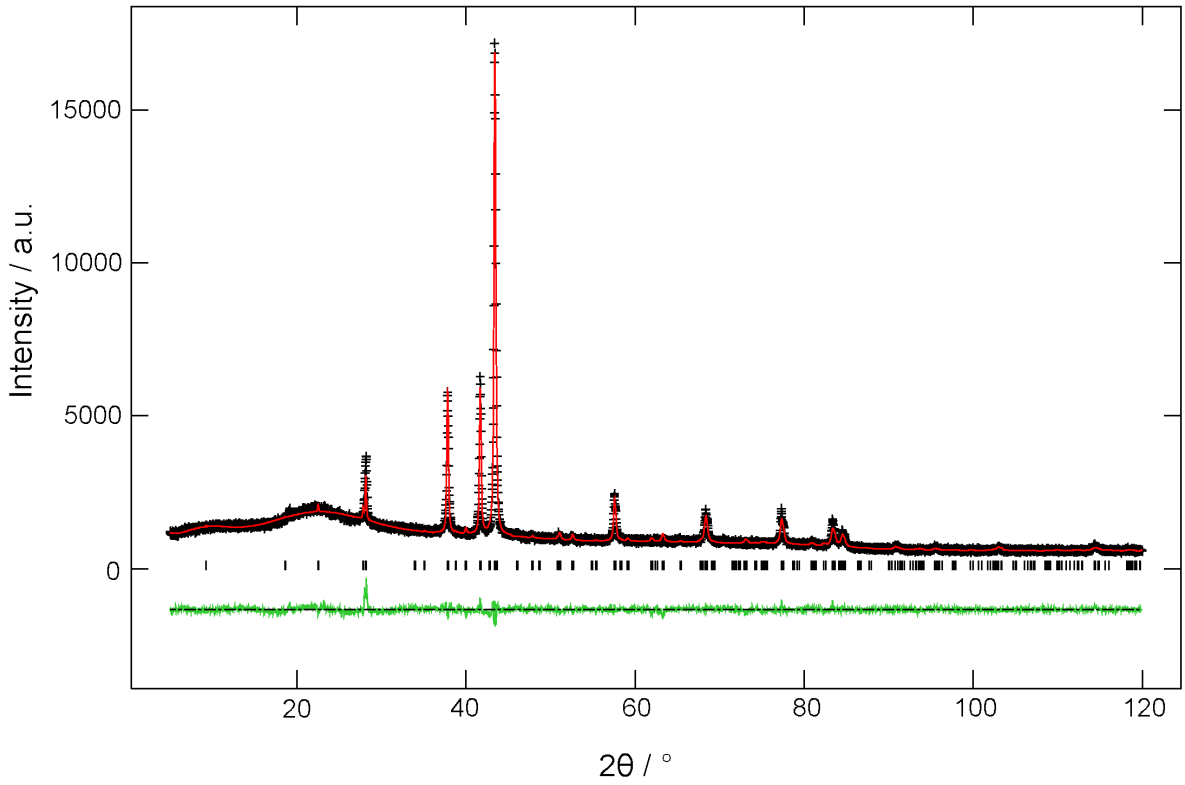

Figure 3-13: Observed (black), calculated (red) and difference (green) x-ray powder diffraction profiles for Cu_4Sb. Tick marks indicate positions of allowed reflections

The simplicity of the pattern suggests the presence of a single phase. To obtain an accurate crystal structure of this phase, it is possible that crystals could be grown from the melt.

3.2.5 Zinc Antimonides

Zinc antimonides exist in two main stoichiometries: ZnSb and the thermoelectric composition, Zn_4Sb_3.[29] A preliminary experiment carried out to synthesise ZnSb (outlined below) revealed that the temperatures at which ZnO and Sb_2O_3 reduce are significantly different. This caused problems in the synthesis of ZnSb, and so no further syntheses of zinc antimonides were explored.

3.2.5.1 ZnSb

Stoichiometric amounts of zinc(II) oxide and antimony(III) oxide were heated at 450 °C (48 hours) and subsequently heated once more at the same temperature (24 hours). An

x-ray powder diffraction pattern was recorded after the final reaction over the range $5 \leq 2\theta/° \leq 70$, with a counting time of 1.0 s per step.

Analysis of the x-ray diffraction pattern revealed that zinc(II) oxide remained in the sample after the final reaction. However, all of the antimony(III) oxide had been reduced to elemental antimony. This is likely to be a consequence of the significantly different temperatures at which the starting metal oxides reduce: the reduction of antimony(III) oxide occurs at a much lower temperature than the reduction of zinc(II) oxide. ZnSb and other zinc antimonides are therefore inaccessible *via* this synthetic route.

3.2.6 Molybdenum Antimonides

Mo_3Sb_7 is the only known molybdenum antimonide, and crystallises in the Ir_3Ge_7-type structure, as mentioned in section 1.3.6.1. The attempted synthesis of Mo_3Sb_7 is outlined in the following section.

3.2.6.1 Mo_3Sb_7

Stoichiometric amounts of molybdenum(VI) oxide and antimony(III) oxide were heated at 425 °C (48 hours), 450 °C (24 hours), 475 °C (24 hours) and finally at 520 °C (24 hours). Preliminary experiments revealed that this heating regime gave rise to the optimum amount of Mo_3Sb_7. An x-ray powder diffraction pattern was recorded after the final reaction over the range $5 \leq 2\theta/° \leq 70$, with a counting time of 1.0 s per step.

Analysis of the x-ray diffraction pattern indicated that the predominant phase formed after reaction at 520 °C was Mo_3Sb_7, with impurities of molybdenum(IV) oxide and antimony. The presence of these impurities is likely to be a result of the different temperatures at which molybdenum(IV) oxide and antimony(III) oxide reduce: antimony(III) oxide reduces at approximately 400 °C; molybdenum(VI) oxide reduces to molybdenum(IV) oxide quite easily at this temperature. However, the reduction of molybdenum(IV) oxide only occurs above approximately 600 °C. Performing this reaction at a higher temperature than 600 °C leads to the reduction of antimony(III) oxide occurring too quickly, therefore forming elemental antimony. However, performing the reaction at a lower temperature (*e.g.* 450 °C) reduces antimony(III) oxide at a reasonable rate, but will not reduce molybdenum(IV) oxide. Mo_3Sb_7 therefore appears to be inaccessible in pure form *via* this synthetic route.

A three-phase Rietveld refinement was carried out using the structure published by Jensen *et al.* as the initial model for Mo_3Sb_7.[116] Attempts to refine isotropic displacement parameters resulted in negative values. These were therefore set to zero in the final refinement. The weight fractions of molybdenum(IV) oxide and antimony were calculated to be 0.21(1) and 0.04(1), respectively. Data from the refinement are given in Table 3-9. The Rietveld fit is shown in Figure 3-14.

Mo_3Sb_7	Refined values			Literature values[116]		
Space group		$Im\bar{3}m$				
Structure type		Ir_3Ge_7				
a / Å		9.5744(3)			9.5713(8)	
V / Å^3		877.69(8)			876.8(1)	
Atomic positions	***x***	***y***	***z***	***x***	***y***	***z***
Mo (12*e*)	0.3425(8)	0	0	0.343(1)	0	0
Sb(1) (12*d*)	¼	0	½	¼	0	½
Sb(2) (16*f*)	0.1620(3)	0.1620(3)	0.1620(3)	0.1624(4)	0.1624(4)	0.1624(4)
Isotropic displacement parameters / Å^2	**Mo**	**Sb(1)**	**Sb(2)**			
	0	0	0			
R(F^2)		0.1070				
χ^2		1.446				

Table 3-9: Rietveld refinement data for Mo_3Sb_7

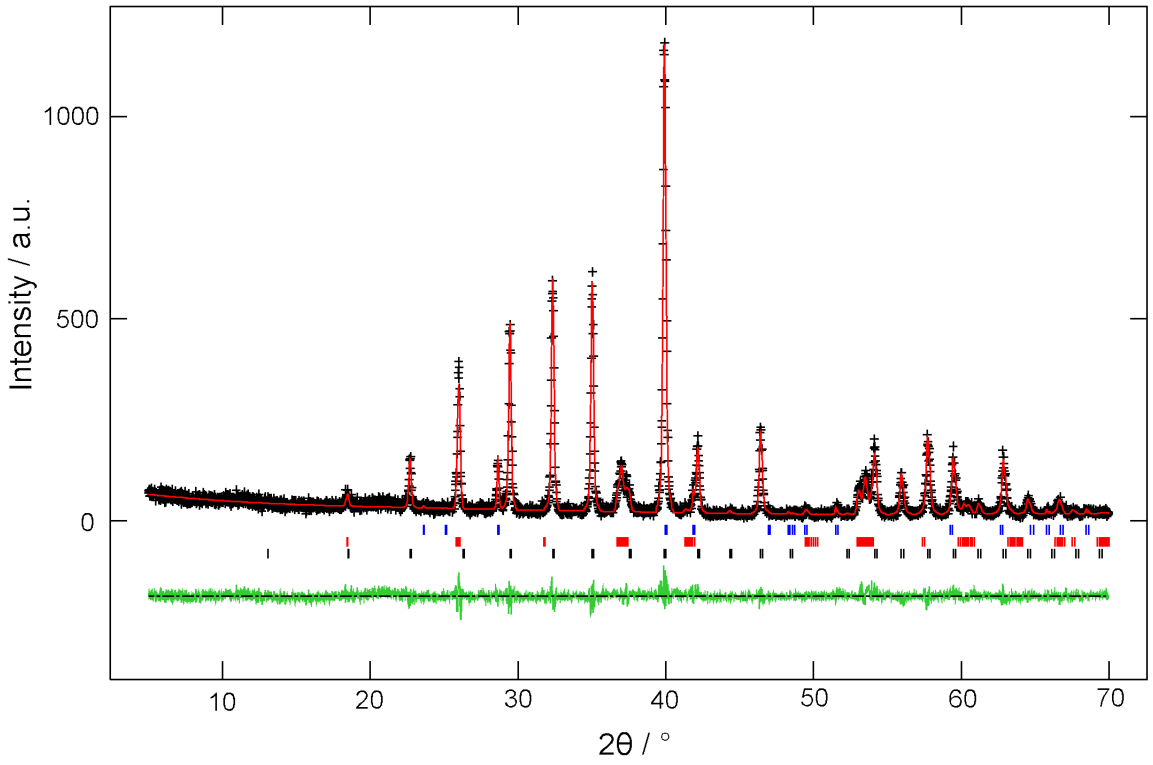

Figure 3-14: Observed (black), calculated (red) and difference (green) x-ray powder diffraction profiles for Mo_3Sb_7. Lower tick marks indicate positions of allowed reflections for Mo_3Sb_7. Middle tick marks indicate positions of allowed reflections for MoO_2. Upper tick marks indicate positions of allowed reflections for Sb

3.2.7 Tungsten Antimonides

There are no known tungsten antimonides. However, given that Mo_3Sb_7 is a known phase, and tungsten is in the same group of the Periodic Table as molybdenum and has a similar size as a result of the lanthanide contraction, the synthesis of the stoichiometrically equivalent tungsten antimonide, W_3Sb_7, was attempted and is described in the following section.

3.2.7.1 W_3Sb_7

Stoichiometric amounts of tungsten(VI) oxide and antimony(III) oxide were heated at 425 °C (48 hours), 450 °C (24 hours), once more at 450 °C (24 hours) and finally at 550 °C (24 hours). X-ray powder diffraction patterns were recorded after reaction at 425 °C, after

the second reaction at 450 °C, and after reaction at 550 °C, over the range $5 \leq 2\theta/° \leq 70$, with a counting time of 1.0 s per step.

Analysis of the x-ray diffraction patterns indicated that after the first reaction the starting reagents were still present in the sample. Subsequent reactions were performed at higher temperatures in order to try to induce reduction of the metal oxides. After two reactions at 450 °C the starting reagents were still present in the sample. However, some antimony(III) oxide had been reduced to elemental antimony. Despite this, a final reaction was carried out at 550 °C to establish whether a tungsten-antimony phase could be synthesised. This reaction resulted in the reduction of tungsten(VI) oxide to tungsten(IV) oxide, and the reduction of the remaining antimony(III) oxide to elemental antimony. This reaction demonstrated that a tungsten-antimony phase cannot be synthesised under these conditions. However, it is interesting to note that the oxidation state of the tungsten in the final tungsten oxide phase was the same as that of the molybdenum in the final molybdenum oxide phase in the corresponding reaction carried out to synthesise Mo_3Sb_7.

3.2.8 Tin Antimonides

The only binary tin antimonide known to exist is SnSb. Reductive synthesis of this composition is described below.

3.2.8.1 SnSb

The structure of SnSb has been a subject of controversy since its discovery by Osawa in 1927.[117] Osawa described the structure as primitive cubic with *a* equal to approximately 3.05 Å. Subsequent studies on the structure have described it as adopting the NaCl structure with *a* equal to approximately 6.13 Å,[118,119] and also as rhombohedral with *a* equal to approximately 6.13 Å, and α_{rho} equal to approximately 89.6°.[120,121,122] In 1970, Nikolaeva *et al.* discovered that SnSb occurs in nature as the mineral *stistaite*, but described its structure in a different way to all previous publications: the structure was described as body centred cubic with *a* equal to approximately 4.15 Å.[123] Rose later reported that the structure of *stistaite* was rhombohedral,[124] which was in agreement with the rhombohedral structures published from the synthesised samples of SnSb.[120,121,122] In response to the conflicting reports on the structure of SnSb, Norén *et al.* have recently definitively studied the

structure.[125] Their study confirmed rhombohedral, although very close to cubic symmetry for the average structure, which was virtually the same as the primitive cubic structure reported by Osawa.[117] The x-ray scattering factors of Sn and Sb are very similar as they are adjacent in the Periodic Table. Ordering of Sn and Sb within the structure is therefore difficult to detect in the absence of synchrotron data. Norén *et al.* therefore included synchrotron data in their study, revealing the presence of satellite reflections indicative of an incommensurate structure in the diffraction pattern.[125] The presence of these satellite reflections was attributed to ordering of Sn and Sb within the structure.

Stoichiometric amounts of tin(II) oxide and antimony(III) oxide were heated at 400 °C (48 hours) and subsequently at 425 °C (24 hours). An x-ray powder diffraction pattern was recorded after the final reaction over the range $5 \leq 2\theta/° \leq 70$, with a counting time of 1.0 s per step.

Analysis of the x-ray diffraction pattern revealed that SnSb had formed in high purity. Due to the unavailability of synchrotron data, Rietveld refinement was carried out using the average rhombohedral structure of SnSb described by Norén *et al.*[125] The isotropic displacement parameters of the two atoms were constrained to be equal due to both atoms occupying the same crystallographic site. Data from the refinement are given in Table 3-10. The Rietveld fit is shown in Figure 3-15 and demonstrates the formation of high purity SnSb.

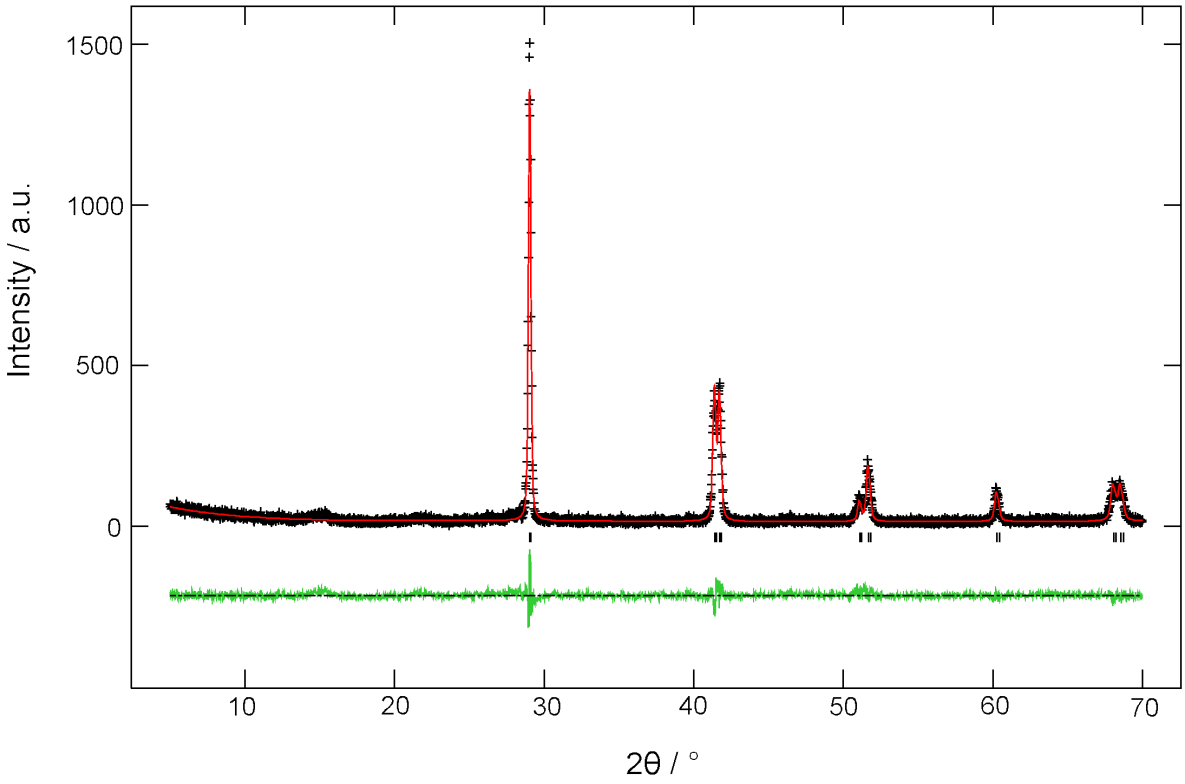

Figure 3-15: Observed (black), calculated (red) and difference (green) x-ray powder diffraction profiles for SnSb. Tick marks indicate positions of allowed reflections

SnSb	Refined values			Literature values[125]		
Space group	$R\bar{3}m$					
Structure type	Distorted α-Po					
a / Å	4.3182(4)			4.3251(4)		
c / Å	5.3518(6)			5.3376(6)		
V / Å^3	86.42(2)			86.47		
Atomic positions	***x***	***y***	***z***	***x***	***y***	***z***
Sn (3*a*)	0	0	0	0	0	0
Sb (3*a*)	0	0	0	0	0	0
Isotropic displacement parameters / Å^2	**Sn**		**Sb**			
	0.008(1)		0.008(1)			
Fractional occupancies	**Sn**		**Sb**			
	0.5		0.5			
R(F^2)	0.0959					
χ^2	1.605					

Table 3-10: Rietveld refinement data for SnSb

3.3 Germanides

The reductive synthetic route was relatively successful in synthesising binary metal antimonides. The method was therefore applied to the synthesis of other systems, including binary germanides of elements in the first row of the *d*-block of the Periodic Table (from Fe to Cu).

3.3.1 Iron Germanides

Iron germanides exist in several known compositions including FeGe, Fe_3Ge and Fe_5Ge_3. The attempted synthesis of each of these compositions is outlined in the following sections.

3.3.1.1 FeGe

Stoichiometric amounts of iron(III) oxide and germanium(IV) oxide were heated at 800 °C (12 hours) and subsequently at 950 °C (24 hours). An x-ray powder diffraction pattern was recorded after the final reaction over the range $5 \leq 2\theta/° \leq 70$, with a counting time of 1.0 s per step.

Analysis of the x-ray diffraction pattern indicated that a mixture of Fe_3Ge and Fe_5Ge_3 had formed. Rietveld refinement was carried out using the structure of Fe_3Ge published by Turbil *et al.*[126] and the structure of Fe_5Ge_3 published by Yasukochi *et al.*[127] The peak shape of Fe_3Ge was not modelled well, and isotropic displacement parameters in both phases did not refine well. However, the refinement allowed identification of the two phases present. Data obtained from the refinement are given in Table 3-11 and Table 3-12 for Fe_3Ge and Fe_5Ge_3, respectively. The Rietveld fit is shown in Figure 3-16.

Fe_3Ge	Refined values			Literature values[126]		
Space group		$P6_3/mmc$				
Structure type		$AuCu_3$				
a / Å		5.174(1)			5.169	
c / Å		4.225(1)			4.222	
V / Å^3		97.96(5)			97.69	
Atomic positions	***x***	***y***	***z***	***x***	***y***	***z***
Fe (6*h*)	0.833(2)	0.665(4)	¼	0.839	0.678	¼
Ge (2*c*)	⅓	⅔	¼	⅓	⅔	¼
Isotropic displacement parameters / Å^2	**Fe**		**Ge**			
	0.025		0.025			
R(F^2)		0.2461				
χ^2		1.661				

Table 3-11: Rietveld refinement data for Fe_3Ge

Fe_5Ge_3	Refined values			Literature values[127]		
Space group		$P6_3/mmc$				
Structure type		Ir_3Si_2				
a / Å		4.0180(7)			4.021	
c / Å		5.016(1)			5.027	
V / Å^3		70.13(3)			70.39	
Atomic positions	***x***	***y***	***z***	***x***	***y***	***z***
Fe(1) (2*a*)	0	0	0	0	0	0
Ge (2*c*)	⅓	⅔	¼	⅓	⅔	¼
Fe(2) (2*d*)	⅓	⅔	¾	⅓	⅔	¾
Isotropic displacement parameters / Å^2	**Fe(1)**	**Ge**	**Fe(2)**			
	0	0	0			
Fractional occupancies	**Fe(1)**	**Ge**	**Fe(2)**	**Fe(1)**	**Ge**	**Fe(2)**
	1	1	0.665	1	1	0.665
R(F^2)		0.2461				
χ^2		1.661				

Table 3-12: Rietveld refinement data for Fe_5Ge_3

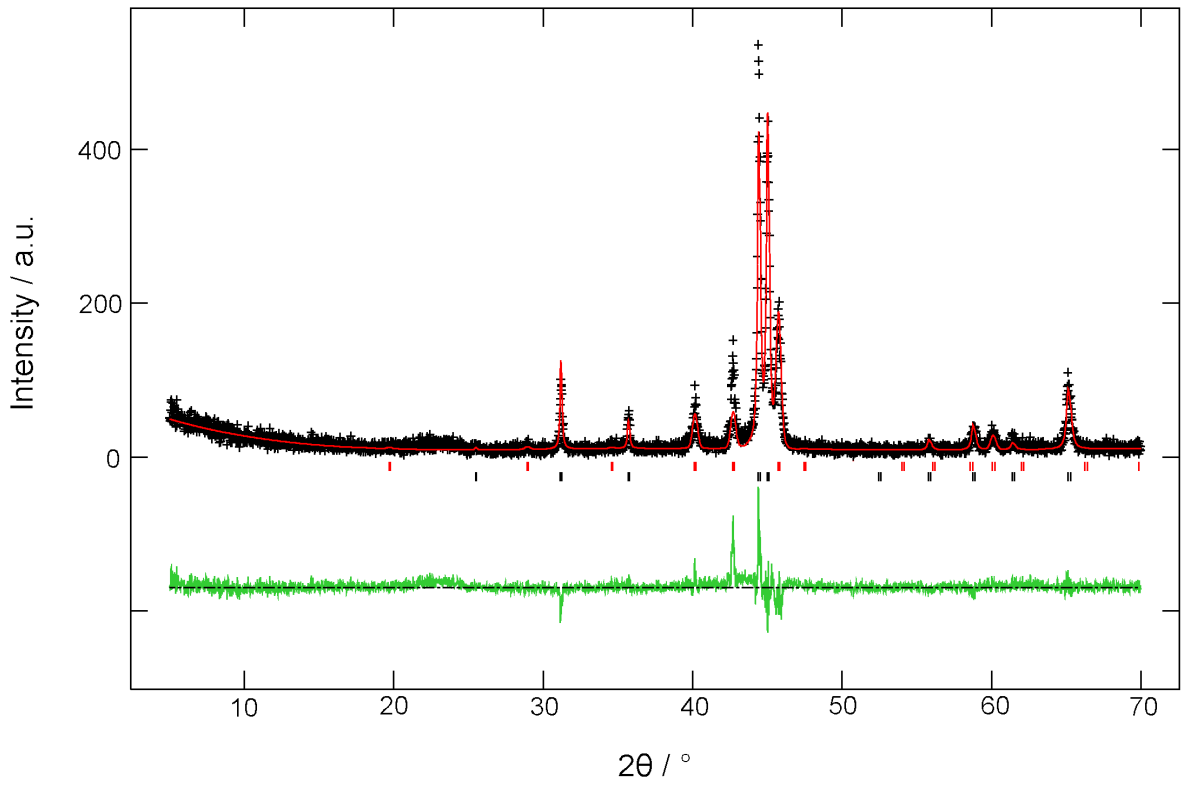

Figure 3-16: Observed (black), calculated (red) and difference (green) x-ray powder diffraction profiles for 'FeGe'. Lower tick marks indicate positions of allowed reflections for Fe_5Ge_3. Upper tick marks indicate positions of allowed reflections for Fe_3Ge

The Rietveld fit demonstrates that this reaction can be used to produce binary metal germanides, in this case a mixture of Fe_5Ge_3 and Fe_3Ge.

3.3.1.2 Fe_3Ge and Fe_5Ge_3

Stoichiometric amounts of iron(III) oxide and germanium(IV) oxide were heated at 800 °C (12 hours) and subsequently at 950 °C (24 hours) in order to prepare pure phases of Fe_3Ge and Fe_5Ge_3. X-ray powder diffraction patterns were recorded after the final reaction over the range $5 \leq 2\theta/° \leq 70$, with a counting time of 1.0 s. Analysis of the patterns indicated that mixtures of Fe_3Ge and Fe_5Ge_3 had formed in both cases. It is interesting that a mixture of these two compositions formed in every attempt to synthesise iron germanides. The synthesis of pure iron germanides has not been possible using this synthetic route.

3.3.2 Cobalt Germanides

Cobalt germanides exist in four main stoichiometries: CoGe, $CoGe_2$, Co_2Ge and Co_5Ge_7. The attempted synthesis of two cobalt germanides, CoGe and Co_2Ge, is described in the following section.

3.3.2.1 CoGe and Co_2Ge

Stoichiometric amounts of cobalt(II,III) oxide and germanium(IV) oxide were heated at 800 °C (12 hours) and subsequently at 950 °C (24 hours). X-ray powder diffraction patterns were recorded after the final reaction over the range $5 \leq 2\theta/° \leq 70$, with a counting time of 1.0 s per step. The highest intensity recorded for the reflections in both patterns was 360, compared to the background which had an intensity of approximately 120. The signal:noise ratio of the patterns was therefore poor, rendering identification of the phases difficult. However, it can be stated with certainty that the 1:1 cobalt germanide, CoGe, and the 2:1 germanide, Co_2Ge, were not present in the product of either reaction.

3.3.3 Nickel Germanides

Nickel germanides exist as several compositions including NiGe, $NiGe_2$, Ni_2Ge and Ni_3Ge. The attempted synthesis of NiGe and Ni_3Ge is described in the following section.

3.3.3.1 NiGe and Ni_3Ge

Stoichiometric amounts of nickel(II) oxide and germanium(IV) oxide were heated at 800 °C (12 hours) and subsequently at 950 °C (24 hours). The second reaction gave rise to a metallic-like “globule” in the case of NiGe, and a metallic-like pellet in the case of Ni_3Ge. It was presumed that both reactions had therefore formed mixtures dominated by the presence of elemental nickel.

3.3.4 Copper Germanides

Copper germanides exist in two known stoichiometries: Cu_3Ge and Cu_5Ge_2. The attempted synthesis of Cu_3Ge is described in the following section.

3.3.4.1 Cu_3Ge

Stoichiometric amounts of copper(II) oxide and germanium(IV) oxide were heated at 800 °C (12 hours). This gave rise to metallic-like "globules", which were presumed to consist mainly of elemental copper.

3.4 Bismuthides

The reductive synthetic route was also applied to the synthesis of transition metal bismuthides. The synthesis of bismuthides of iron through to zinc in the first row of the *d*-block of the Periodic Table was attempted.

3.4.1 Iron, Cobalt and Zinc Bismuthides

There are no known iron, cobalt or zinc bismuthides. Starting reagents were therefore reacted in a 1:1 ratio to determine if any new compositions could be synthesised.

Stoichiometric amounts of iron(III) oxide, cobalt(II,III) oxide or zinc(II) oxide were reacted with bismuth(III) oxide by heating at 400 °C (48 hours). After the reaction the pellets remained mainly intact, although a silvery metallic-like "globule" was adhered onto the pellet surfaces. Due to this, x-ray powder diffraction patterns of the products were not recorded. It was presumed that the "globule" was elemental bismuth, and that the remaining pellets contained a mixture of iron, cobalt or zinc oxides.

3.4.2 Nickel Bismuthides

Nickel bismuthides exist in two known stoichiometries: NiBi and $NiBi_3$. Several forms of NiBi have been reported: Hägg and Funke[128] and Feschotte and Rosset[129] both reported that NiBi synthesised from melting of the elements is disordered and crystallises in a simple NiAs-type structure, over a narrow range of composition. Ruck has since reported that NiBi synthesised by chemical vapour transport adopts a superstructure of the $InNi_2$-type (filled NiAs structure) in the space group $F12/m1$.[130] In this structure, the nickel atoms are spread over the octahedral and trigonal bipyramidal interstices within a *hcp* arrangement of bismuth atoms. $NiBi_3$ adopts the $RhBi_3$ structure and crystallises in the space group *Pnma*.[131] The attempted synthesis of both compositions is described in the following sections.

3.4.2.1 NiBi

Stoichiometric amounts of nickel(II) oxide and bismuth(III) oxide were heated at 425 °C (48 hours) and once more at 425 °C (24 hours). An x-ray powder diffraction pattern was recorded after the final reaction over the range $5 \leq 2\theta/° \leq 70$, with a counting time of 1.0 s per step.

Analysis of the x-ray diffraction pattern revealed that the form of NiBi reported by Ruck had formed in high purity.[130] Rietveld refinement was carried out using the structure published by Ruck as the initial model.[130] Refinement of the isotropic displacement parameters of the atoms caused the refinement to diverge. They were therefore set to 0.005 $Å^2$ and not refined. Data obtained from the refinement are given in Table 3-13. The Rietveld fit is shown in Figure 3-17.

NiBi	Refined values			Literature values[130]		
Space group	*F*12/*m*1 (no. 12)					
Structure type	Superstructure of $InNi_2$					
a / Å	14.083(1)			14.124(1)		
b / Å	8.1570(5)			8.1621(6)		
c / Å	21.399(1)			21.429(2)		
β / °	90.130(5)			90.00		
V / $Å^3$	2458.3(4)			2470.4(3)		
Atomic positions	***x***	***y***	***z***	***x***	***y***	***z***
Bi(1) (16*j*)	0.421(2)	0.232(3)	0.062(1)	0.42464(3)	0.22588(4)	0.06242(5)
Bi(2) (8*i*)	0.153(2)	½	0.063(2)	0.15021(5)	½	0.06301(9)
Bi(3) (8*i*)	0.167(3)	0	0.064(2)	0.16737(5)	0	0.06334(9)
Bi(4) (16*j*)	0.080(2)	0.257(5)	0.185(1)	0.07889(4)	0.2599(2)	0.18731(5)
Bi(5) (8*i*)	0.340(3)	0	0.189(2)	0.3411(1)	0	0.18817(6)
Bi(6) (8*i*)	0.334(3)	½	0.189(2)	0.3343(1)	½	0.18875(6)
Ni(1) (4*a*)	0	0	0	0	0	0
Ni(2) (8*e*)	¼	¼	0	¼	¼	0
Ni(3) (8*i*)	-0.024(7)	0	0.120(6)	-0.0019(2)	0	0.1236(2)
Ni(4) (16*j*)	0.263(6)	0.26(1)	0.126(5)	0.25063(9)	0.2546(8)	0.12499(9)
Ni(5) (8*i*)	0.00(1)	0	0.248(6)	0.0025(2)	0	0.2479(2)
Ni(6) (8*h*)	¼	0.25(2)	¼	¼	0.2442(1)	¼
Ni(7) (8*i*)	0.310(6)	½	0.043(4)	0.3333(1)	½	0.0619(3)
Ni(8) (8*i*)	0.17(1)	0	0.18(1)	0.1666(3)	0	0.1857(3)

R(F^2)	0.1442
χ^2	2.849

Table 3-13: Rietveld refinement data for NiBi

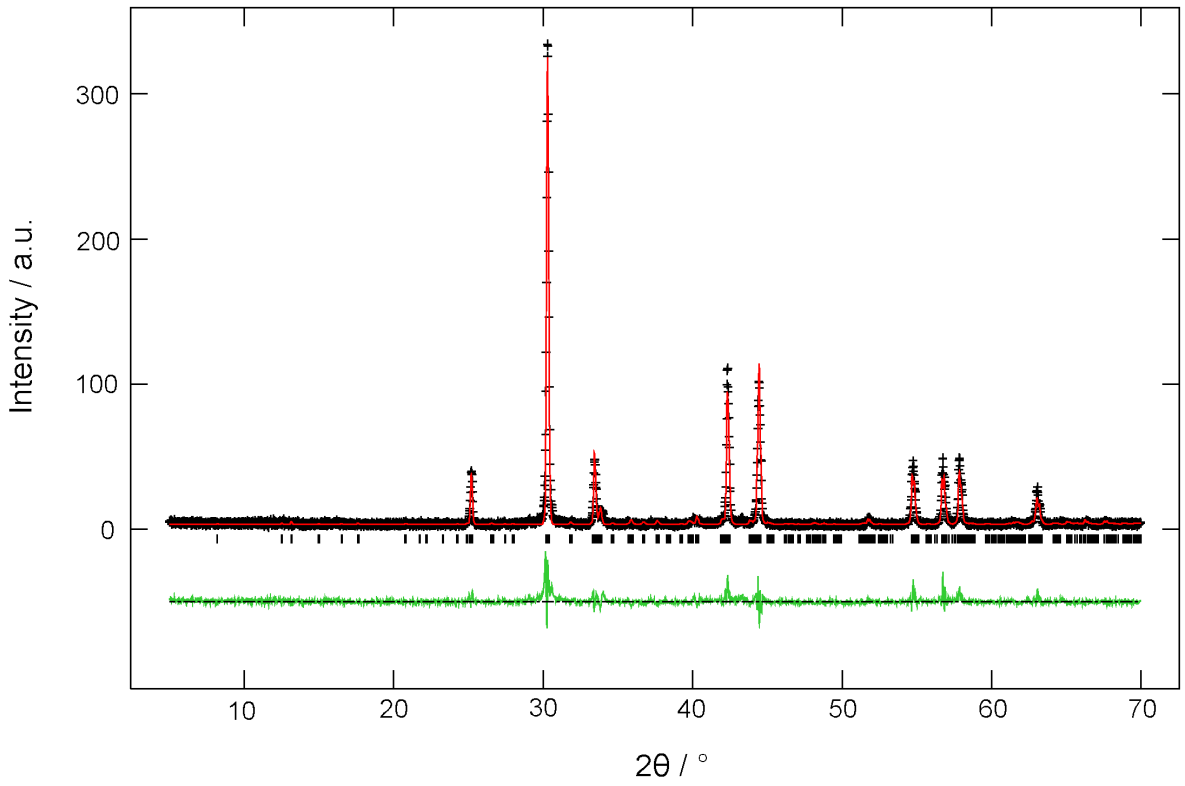

Figure 3-17: Observed (black), calculated (red) and difference (green) x-ray powder diffraction profiles for NiBi. Tick marks indicate positions of allowed reflections

The Rietveld fit demonstrates that the fit of the structural model to the data is relatively poor. In addition, the R(F^2) value of 0.1442 and the χ^2 value of 2.849 indicate a modest fit. However, the fit gives good evidence for the presence of a compound with a structure close to that described by Ruck, suggestive of the presence of NiBi.

3.4.2.2 $NiBi_3$

Stoichiometric amounts of nickel(II) oxide and bismuth(III) oxide were heated at 425 °C (48 hours) and once more at 425 °C (24 hours). An x-ray powder diffraction pattern was recorded after the final reaction, over the range $5 \leq 2\theta/° \leq 70$, with a counting time of 1.0 s per step.

Analysis of the x-ray diffraction pattern indicated that $NiBi_3$ had formed, as well as elemental bismuth, suggesting the initial temperature of the reaction was perhaps too high. The respective weight fractions of $NiBi_3$ and Bi were 0.768(4) and 0.232(4). Rietveld refinement was carried out using the structure published by Ruck and Söehnel as the initial model for $NiBi_3$.[131] Data obtained from the refinement are given in Table 3-14. The Rietveld fit is shown in Figure 3-18.

$NiBi_3$	Refined values			Literature values[131]		
Space group		*Pnma*				
Structure type		$RhBi_3$				
a / Å		8.8819(9)			8.8796(7)	
b / Å		4.1001(4)			4.0997(3)	
c / Å		11.486(1)			11.478(1)	
V / Å^3		418.3(1)			417.84(6)	
Atomic positions	***x***	***y***	***z***	***x***	***y***	***z***
Bi(1) (4*c*)	0.4135(9)	¼	0.1804(5)	0.4114(1)	¼	0.17901(6)
Bi(2) (4*c*)	0.2988(6)	¼	0.8909(6)	0.2981(1)	¼	0.88968(8)
Bi(3) (4*c*)	0.385(1)	¼	0.5967(7)	0.3820(1)	¼	0.59301(7)
Ni (4*c*)	0.106(3)	¼	0.517(2)	0.0897(3)	¼	0.5193(2)
Isotropic displacement parameters / Å^2	**Bi(1)**	**Bi(2)**	**Bi(3)**	**Ni**		
	0.016(3)	0.01(3)	0.042(4)	0.011(7)		
R(F^2)		0.1238				
χ^2		1.626				

Table 3-14: Rietveld refinement data for $NiBi_3$

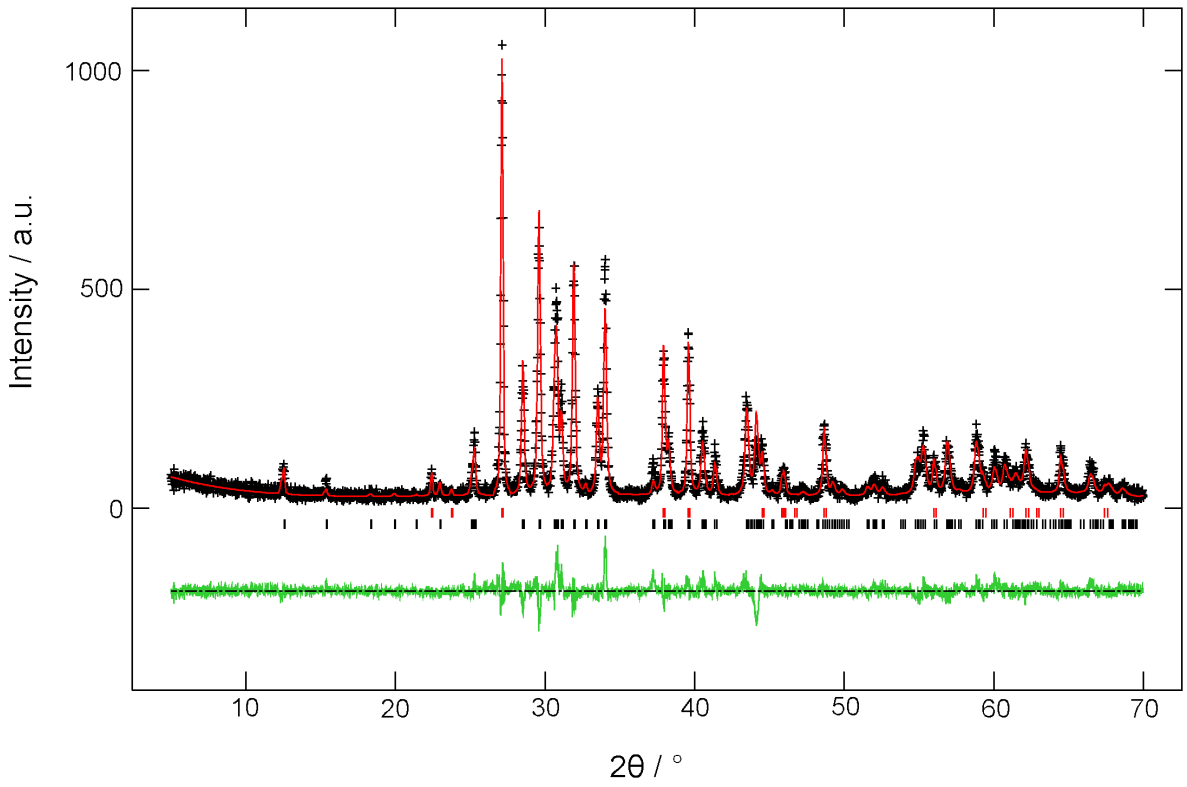

Figure 3-18: Observed (black), calculated (red) and difference (green) x-ray powder diffraction profiles for $NiBi_3$. Lower tick marks indicate positions of allowed reflections for $NiBi_3$. Upper tick marks indicate positions of allowed reflections for Bi

The Rietveld fit demonstrates that this reaction produced a mixture of $NiBi_3$ and elemental bismuth. Given that elemental bismuth formed in this reaction, it is likely that the starting metal oxides reduced too quickly. Performing this reaction at a lower temperature may therefore reduce the amount of bismuth in the product or perhaps eliminate it completely. This may, however, cause problems with the adequate reduction of nickel oxide.

3.4.3 Copper Bismuthides

Copper bismuthides exist in only the known 1:1 composition, CuBi. The attempted synthesis of this phase is described in the following section.

Stoichiometric amounts of copper(II) oxide and bismuth(III) oxide were heated at 400 °C (48 hours) and subsequently at 425 °C (24 hours). An x-ray powder diffraction pattern was recorded after the final reaction over the range $5 \leq 2\theta/° \leq 70$, with a counting time of 1.0 s per step.

Analysis of the x-ray diffraction pattern revealed that both metal oxides had reduced to their corresponding elemental metals. Performing the reaction at a lower temperature, decreasing the rate of reduction of the metal oxides, may prove successful in preparing CuBi.

3.5 Reaction Mechanism

The mechanism of the reductive synthesis of nitrides has been previously explored: ammonia was detected in the outflow gas of a reduction-nitridation reaction, suggesting that nitride formation may be the result of reaction with ammonia.[132] A similar test was therefore required to determine whether SbH_3 is involved in the reductive synthesis of antimonides. Gutzeit's test allows for the detection of arsine (AsH_3) or stibine (SbH_3) by the use of silver nitrate or mercury(II) chloride.[133] A more sensitive adaptation of this test is carried out using gold chloride,[133] and is described below.

The outflow gas of a reaction carried out to form NiSb was bubbled through an aqueous solution of $HAuCl_4$, which had been previously neutralised with sodium hydroxide. No change was observed in the solution over the course of the reaction. A control experiment was carried out in order to determine that SbH_3 could be positively detected using this test, where Sb_2O_3 was reacted with concentrated hydrochloric acid in the presence of zinc powder. The gas produced in this reaction resulted in the yellow neutralised $HAuCl_4$ solution turning deep brown/black, suggesting the presence of SbH_3. This test therefore suggested that SbH_3 is not a by-product of the reductive synthesis of antimonides, and does not play a role in the mechanism of the reaction.

3.6 Scope of the Method

The work described in this chapter demonstrated that the reductive synthetic route outlined in section 2.1.1 could be applied to the synthesis of a variety of binary metal antimonides. High purity antimonides synthesised include NiSb, CoSb, $CoSb_3$, Cu_2Sb and SnSb. The route also led to the synthesis of other binary antimonides containing various amounts of impurities. These antimonides included ε-FeSb, $FeSb_2$, $NiSb_2$, $CoSb_2$ and Mo_3Sb_7. Solid solutions and substitutions in NiSb, CoSb, $CoSb_3$ and Cu_2Sb producing ternary antimonides are described in later chapters.

The synthesis of germanides *via* this synthetic route was not as successful. Germanides of cobalt, nickel and copper were inaccessible. The temperatures at which these reactions were undertaken appeared to be too high: reduction of the metal oxides occurred too quickly leading to the formation of elemental metals. Carrying out these reactions at lower temperatures may solve this problem, although germanium(IV) oxide reduces at a relatively high temperature. The iron germanides, Fe_3Ge and Fe_5Ge_3, formed at the reaction temperatures employed, although they were not accessible as pure phases. No further work on the synthesis of germanides using this synthetic route was therefore carried out.

The success of the reductive synthetic route towards the synthesis of metal bismuthides was also limited. Iron, cobalt, zinc and copper bismuthides were inaccessible. Reactions carried out to form these compounds generally led to the formation of elemental bismuth, suggesting the temperatures at which the reactions were carried out were too high. Carrying out these reactions at lower temperatures may solve this problem, although this may prevent the other metal oxides from reducing sufficiently. However, the nickel bismuthide, NiBi, was formed in high purity. $NiBi_3$ was also synthesised, but with an impurity of elemental bismuth; lowering the reaction temperature may prove to be useful in obtaining a pure phase.

As discussed in this chapter, the reductive synthetic route has one main limitation: the difference in ease of reduction of certain starting metal oxides. There are several metal oxides which reduce at a similar temperature to Sb_2O_3. These include Co_3O_4, CuO, Fe_2O_3, NiO and SnO. Antimonides containing cobalt, copper, iron, nickel and tin were therefore relatively easy to prepare. $CoSb_3$ and Cu_2Sb appeared to be very stable compounds, forming as impurities in many other reactions. The molybdenum antimonide, Mo_3Sb_7, was not accessible as a pure phase due to the difference in reduction temperature of MoO_2 and Sb_2O_3. Zinc antimonides were also inaccessible due to the difference in ease of reduction of ZnO and Sb_2O_3. The synthesis of germanides was, on the whole, problematic, as GeO_2 reduces at a higher temperature than most of the starting metal oxides used. Conversely, the synthesis of bismuthides was problematic for a different reason: Bi_2O_3 reduces at a *lower* temperature than most of the starting metal oxides. In addition, there are few binary metal bismuthides already reported.

A general rule of thumb may be used in order to determine how easily a metal oxide will be reduced using this synthetic method. Oxides containing metal cations which have standard reduction potentials that are greater than approximately −0.7 V tend to reduce easily under these reaction conditions. Some standard reduction potentials are given in Table 3-15 to demonstrate this. [134,135]

Element	Reduction equation	E^o / V	Reduction equation	E^o / V
Zr	$Zr^{4+} + 4e^- \rightarrow Zr$	−1.70		
Ti	$Ti^{3+} + e^- \rightarrow Ti^{2+}$	−0.37	$Ti^{2+} + 2e^- \rightarrow Ti$	−1.63
Mn	$Mn^{3+} + e^- \rightarrow Mn^{2+}$	+1.5	$Mn^{2+} + 2e^- \rightarrow Mn$	−1.18
V	$V^{3+} + e^- \rightarrow V^{2+}$	−0.255	$V^{2+} + 2e^- \rightarrow V$	−1.13
Nb	$Nb^{3+} + 3e^- \rightarrow Nb$	−1.1		
Zn	$Zn^{2+} + 2e^- \rightarrow Zn$	−0.7626		
Fe	$Fe^{3+} + e^- \rightarrow Fe^{2+}$	+0.771	$Fe^{2+} + 2e^- \rightarrow Fe$	−0.44
Cd	$Cd^{2+} + 2e^- \rightarrow Cd$	−0.4025		
Co	$Co^{3+} + e^- \rightarrow Co^{2+}$	+1.92	$Co^{2+} + 2e^- \rightarrow Co$	−0.277
Ni	$Ni^{2+} + 2e^- \rightarrow Ni$	−0.236		
Sn	$Sn^{4+} + 2e^- \rightarrow Sn^{2+}$	+0.15	$Sn^{2+} + 2e^- \rightarrow Sn$	−0.136
Cu	$Cu^{2+} + 2e^- \rightarrow Cu$	+0.340		
Rh	$Rh^{3+} + 3e^- \rightarrow Rh$	+0.76		
Ag	$Ag^{+} + e^- \rightarrow Ag$	+0.7991		
Pd	$Pd^{2+} + 2e^- \rightarrow Pd$	+0.915		
Au	$Au^{3+} + 3e^- \rightarrow Au$	+1.52		

Table 3-15: Standard reduction potentials (E^o) of a selection of elements in acidic solution. The dashed line represents an approximate cut-off point for feasibility of reduction using this synthetic method: elements above the line are generally not reducible

Cu^{2+}, Ni^{2+}, Co^{3+} and Co^{2+} all have standard reduction potentials greater than −0.7 V, and reactions described in this chapter have demonstrated that CuO, NiO and Co_3O_4 are easily reduced using this method. The standard reduction potentials of Zn^{2+} and Mn^{2+} are less than −0.7 V, and reactions described in this chapter have demonstrated that ZnO is not easily reduced using this method. Reactions with MnO were not carried out due to the very negative standard reduction potential of Mn^{2+}. Mn^{2+} is likely to be difficult to reduce as a result of the relatively stable electron configuration of the d^5 ion. A set of M^{3+}/M and

M^{2+}/M reduction potentials in acidic solution were plotted by Phillips and Williams, and demonstrates this rule of thumb more clearly.[136] The plot is shown in Figure 3-19, with a line superimposed at approximately −0.7 V.

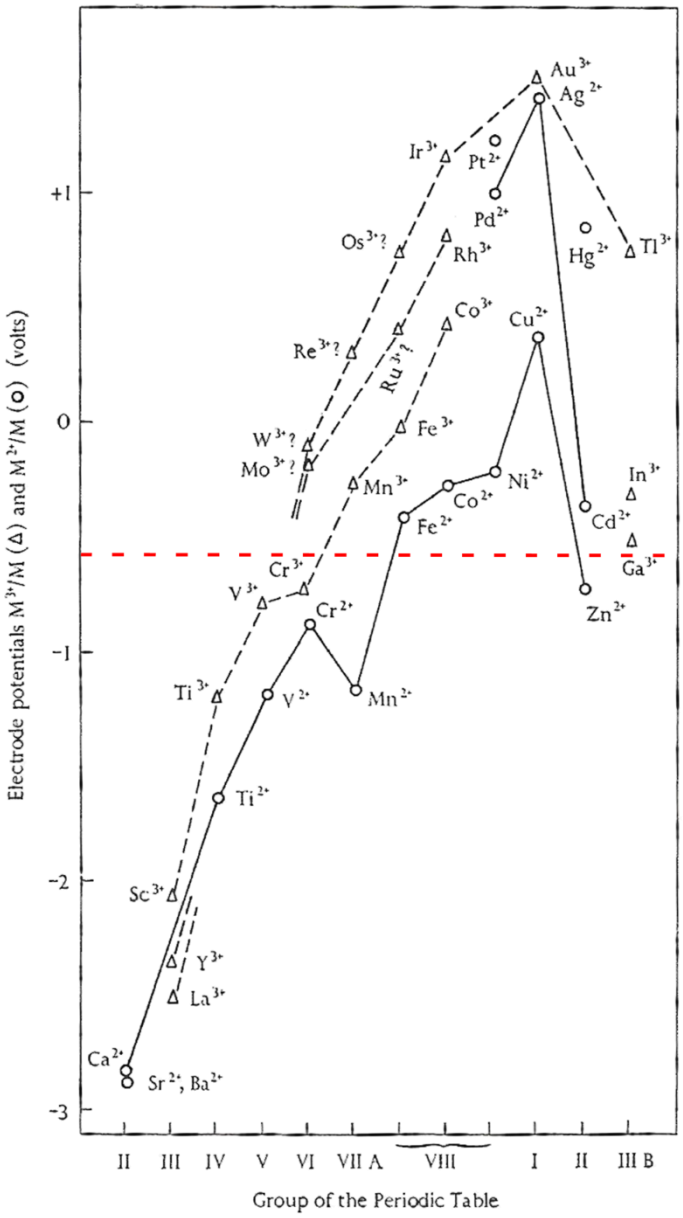

Figure 3-19: M^{3+}/M and M^{2+}/M potentials for the transition elements in acidic solution. Reductions above the red line are likely to be feasible using this synthetic route, whereas those below the line are not likely to be feasible using this synthetic route

The synthetic route reported here has similarities to a synthetic route reported by Gopalakrishnan *et al.*[137] where binary antimonides including $NiSb_2$, $CoSb_2$ and $CoSb_3$ were

synthesised by reduction of the oxide precursors, $NiSb_2O_6$, $CoSb_2O_6$ and $CoSb_3O_9$, respectively, at temperatures of 400 – 650 °C. Similar reaction temperatures were employed in work described in this chapter. However, the method reported here does not require the synthesis of precursors, is not restricted by the stoichiometry of the starting reagents and is applicable to the synthesis of ternary systems (as demonstrated in later chapters). The reductive synthetic route described here therefore has advantages when compared to the method of Gopalakrishnan *et al*.[137]

4.0 Substitutions in Compounds Crystallising with the Nickel Arsenide Structure

4.1 Antimonides

The reductive synthesis of CoSb and NiSb described in Sections 3.2.2.1 and 3.2.3.1 was readily accomplished and was carried out at temperatures of 425 – 450 °C. Given that both compounds crystallise with the nickel arsenide structure, and that nickel and cobalt are similar in size, the solid solution $Co_{1-x}Ni_xSb$ could be expected to form. Two brief accounts of the existence of this series have been reported elsewhere, but give little or no details on the synthesis or lattice parameters of the compositions.[94,138] This chapter describes work carried out on the synthesis of the solid solution and discusses relationships between lattice parameters and composition. In addition, bond lengths and angles are examined. Work is also described on the substitution of other similarly sized transition metals (Fe, Cu) for cobalt and nickel in CoSb and NiSb, respectively. Only one of these compositions ($Ni_{0.5}Cu_{0.5}Sb$) has been reported previously.[139] However, FeSb also adopts the nickel arsenide structure, and therefore a solid solution of Fe in CoSb and NiSb could be expected to form.

4.1.1 Introduction of Ni into CoSb ($Co_{1-x}Ni_xSb$)

Stoichiometric amounts of cobalt(II,III) oxide, nickel(II) oxide and antimony(III) oxide were heated at 425 °C (48 hours), 450 °C (24 hours), 450 °C (24 hours) for a second time, and finally at 500 °C (24 hours) in order to prepare the series $Co_{1-x}Ni_xSb$ ($0.1 \leq x \leq 0.9$), with x increasing in increments of 0.1. X-ray powder diffraction patterns were recorded after both reactions at 450 °C and after reaction at 500 °C over the range $5 \leq 2\theta/° \leq 70$, with a counting time of 1.0 s per step.

Analysis of the x-ray diffraction patterns revealed that a single phase adopting the nickel arsenide structure had formed in each case after the first reaction at 450 °C. Subsequent reactions at 450 °C and 500 °C were performed in order to increase product crystallinity. Rietveld refinement was carried out for all compositions in the series after reaction at 500 °C using the structure of CoSb as the initial model,[107] with atom occupancies altered according to the composition dictated by the stoichiometry of the starting materials.

Isotropic displacement parameters of nickel and cobalt were constrained to be equal due to both atoms occupying the same crystallographic site. The Rietveld fit obtained for the middle member of the series, $Co_{0.5}Ni_{0.5}Sb$, is shown in Figure 4-1.

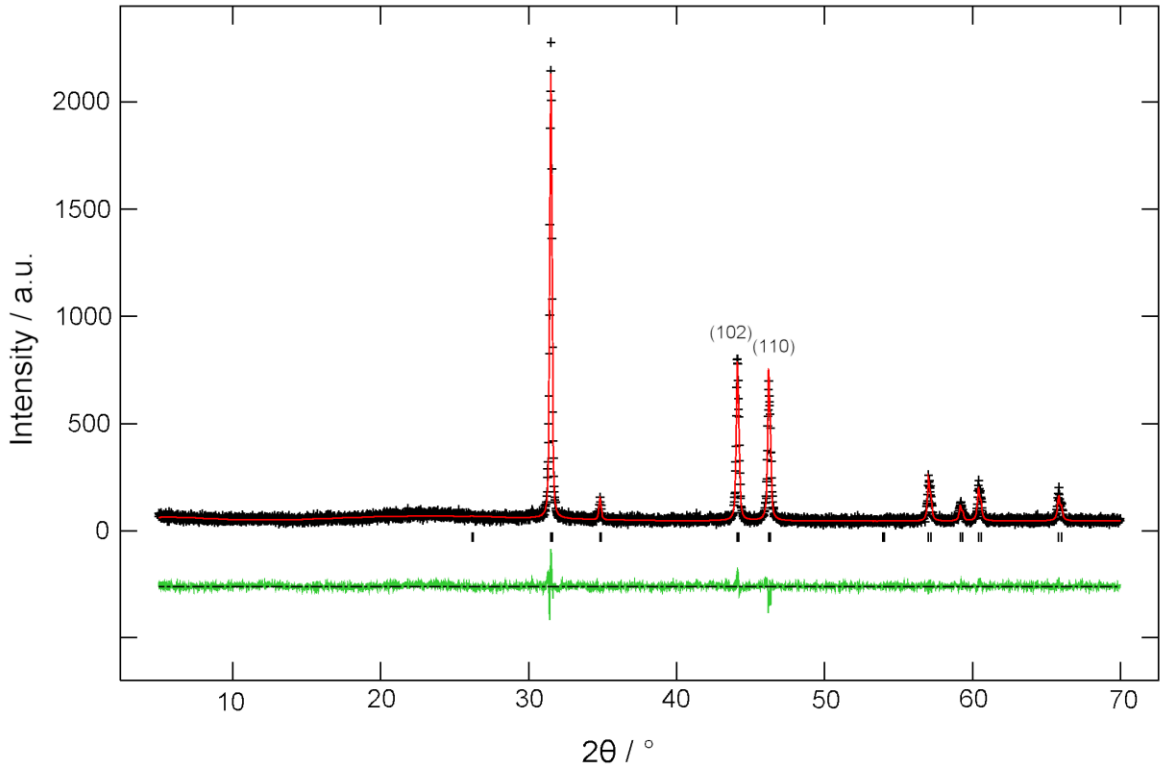

Figure 4-1: Observed (black), calculated (red) and difference (green) x-ray powder diffraction profiles for $Co_{0.5}Ni_{0.5}Sb$. Tick marks indicate positions of allowed reflections

Upon close inspection of the Rietveld fit, a small difference in intensity of the calculated (102) and (110) reflections to the observed data is apparent. This mismatch is present to some degree in all compositions in the series except the end members. It was proposed that this difference in intensity might be due to ordering of cobalt and nickel within the structure. A similar compound, $Ni_{0.5}Cu_{0.5}Sb$, is ordered (discussed later) and adopts the space group $P\bar{3}m1$. A pattern was therefore simulated with nickel and cobalt fully ordered in $P\bar{3}m1$, but displayed an almost negligible change in the intensities of these two peaks, as a result of the very similar x-ray scattering factors of nickel and cobalt. The position of the antimony atom was refined in $P\bar{3}m1$, but this resulted in divergence. This suggested that the antimony atom should not be located on a general position (z = ~0.27), and the model was therefore incorrect. It is therefore likely that the metal atoms are disordered. In addition,

many examples of disordered cobalt and nickel alloy systems have been reported in the literature, such as $CoNiAs_2$, CoNiZr, CoNiGe and $Co_{0.5}Ni_{0.5}Te_2$.[140,141,142,143]

A second possible cause for the mismatch could be preferred orientation of the hexagonal rod-like crystallites. However, if this was the case, a mismatch in intensity of the (102) and (110) reflections would be expected to be observed in the end members of the series as well.

The potential non-stoichiometry of the NiAs-type phases was also considered when attempting to determine the cause of the mismatch. However, as depicted in Figure 3-4 in section 3.2.2, introducing cobalt onto the 2*d* Wyckoff position increases the intensity of the (102) and (110) reflections, but does not create the mismatch observed in this series. In addition, lowering the occupancy of cobalt on the 2*a* Wyckoff position, and therefore creating cobalt vacancies, does not generate a mismatch in intensity of the two peaks in question. The mismatch is therefore not due to non-stoichiometry in the series.

Full width at half maximum values for each phase were calculated for the (102) reflection located at approximately 44° 2θ. Examination shows there is little change in full width at half maximum across the series, strongly suggesting the presence of single phase products. Selected crystal data for all compositions in the series are given in the Appendix. Crystal data from the refinement of $Co_{0.5}Ni_{0.5}Sb$ are given in Table 4-1.

$Co_{0.5}Ni_{0.5}Sb$				
Atomic positions and occupancies	***x***	***y***	***z***	**Occupancy**
Co (2*a*)	0	0	0	0.5
Ni (2*a*)	0	0	0	0.5
Sb (2*c*)	⅓	⅔	¼	1
Isotropic displacement parameters / Å^2	**Co**	**Ni**		**Sb**
	0.027(2)	0.027(2)		0.028(2)
R(F^2)		0.0581		
χ^2		1.278		

Table 4-1: Selected crystal data from the refinement of $Co_{0.5}Ni_{0.5}Sb$

Unit cell data obtained from Rietveld refinement of all compositions in the series are given in Table 4-2.

Composition	x	a / Å	c / Å	V / Å^3	M-Sb bond length / Å	Sb-Sb bond length / Å
CoSb	0	3.8906(1)	5.1875(2)	68.002(5)	2.59374(9)	3.43120(8)
$Co_{0.9}Ni_{0.1}Sb$	0.1	3.8974(4)	5.1766(5)	68.10(2)	2.5958(2)	3.4296(2)
$Co_{0.8}Ni_{0.2}Sb$	0.2	3.9034(4)	5.1651(5)	68.16(1)	2.5974(3)	3.4276(3)
$Co_{0.7}Ni_{0.3}Sb$	0.3	3.9094(4)	5.1563(5)	68.25(2)	2.5993(3)	3.4266(4)
$Co_{0.6}Ni_{0.4}Sb$	0.4	3.9167(2)	5.1488(4)	68.40(1)	2.6020(2)	3.4265(2)
$Co_{0.5}Ni_{0.5}Sb$	0.5	3.9215(3)	5.1424(4)	68.49(1)	2.6036(2)	3.4260(3)
$Co_{0.4}Ni_{0.6}Sb$	0.6	3.9270(3)	5.1413(5)	68.66(2)	2.6062(2)	3.4276(2)
$Co_{0.3}Ni_{0.7}Sb$	0.7	3.9291(2)	5.1388(3)	68.70(1)	2.6070(1)	3.4275(2)
$Co_{0.2}Ni_{0.8}Sb$	0.8	3.9323(2)	5.1395(3)	68.83(1)	2.6087(2)	3.4290(2)
$Co_{0.1}Ni_{0.9}Sb$	0.9	3.9352(3)	5.1411(4)	68.95(1)	2.6103(2)	3.4307(3)
NiSb	1.0	3.94523(4)	5.14243(7)	69.318(2)	2.61554(2)	3.43503(3)

Table 4-2: Unit cell data and bond lengths for the series $Co_{1-x}Ni_xSb$

Graphical representations of the unit cell data given in Table 4-2 were prepared and are shown in the following figures.

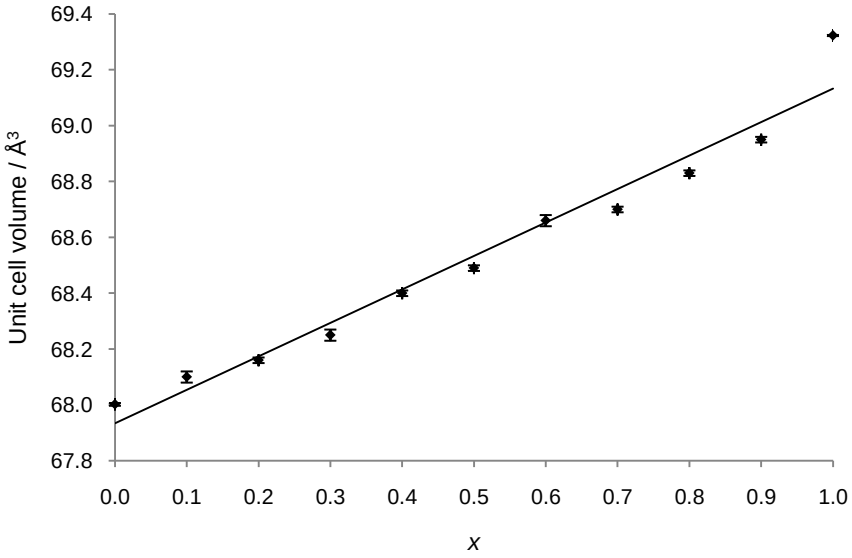

Figure 4-2: Plot of unit cell volume against composition (x) for the series $Co_{1-x}Ni_xSb$

Figure 4-2 demonstrates the variation in unit cell volume with composition. In this plot the unit cell volume increases in a linear fashion as more nickel is introduced into the structure. The increase in unit cell volume across the series is expected given that the unit cell volume

of NiSb (69.323(2) Å^3) is greater than that of CoSb (68.002(5) Å^3). The weighted mean lengths of the metal-metal distances in *hcp* cobalt and *ccp* nickel are 2.5013 Å[144] and 2.4883 Å,[145] respectively. The unit cell volume of NiSb would therefore be expected to be smaller than the unit cell volume of CoSb, and the unit cell volume of the compositions in the series would therefore be expected to decrease as more nickel is introduced into the structure. However, there are examples in the literature of isostructural cobalt and nickel intermetallic compounds where the Ni-Ni distances are longer than the Co-Co distances. For example, the length of the Ni-Ni distance in $NiTe_2$ is 3.8480 Å,[143] whereas the length of the Co-Co distance in $CoTe_2$ is 3.8040 Å.[143] Also, the length of the Ni-Ni distance in NiGa is 2.8860 Å,[146] whereas the length of the Co-Co distance in CoGa is 2.8833(2) Å.[147] Another example exists in nickel and cobalt germanides adopting the $InNi_2$ structure: the length of the Ni-Ni distance in Ni_2Ge is 2.5180 Å, whereas the length of the Co-Co distance in Co_2Ge is 2.502(1) Å.[142] The linear relationship observed between the unit cell volume and composition in the $Co_{1-x}Ni_xSb$ series obeys Vegard's Law[148] and therefore indicates full miscibility of NiSb in CoSb.

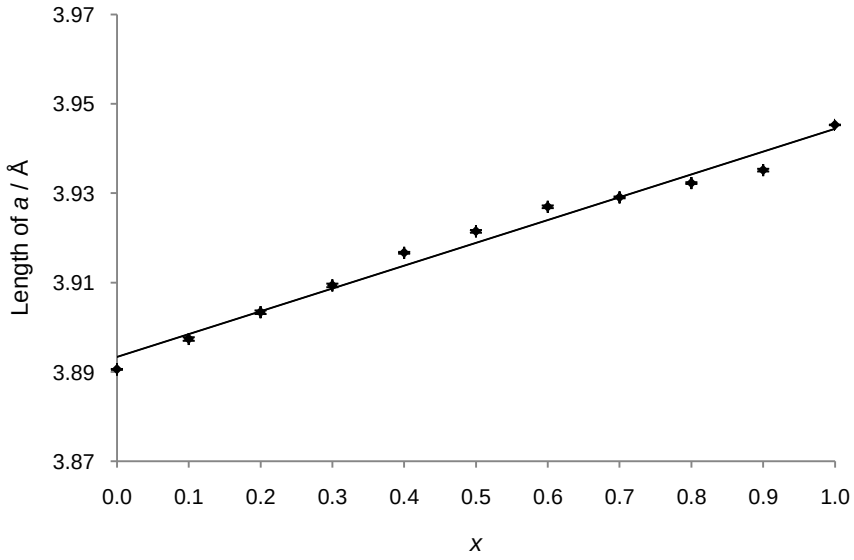

Figure 4-3: Plot of unit cell length *a* against composition (*x*) for the series $Co_{1-x}Ni_xSb$

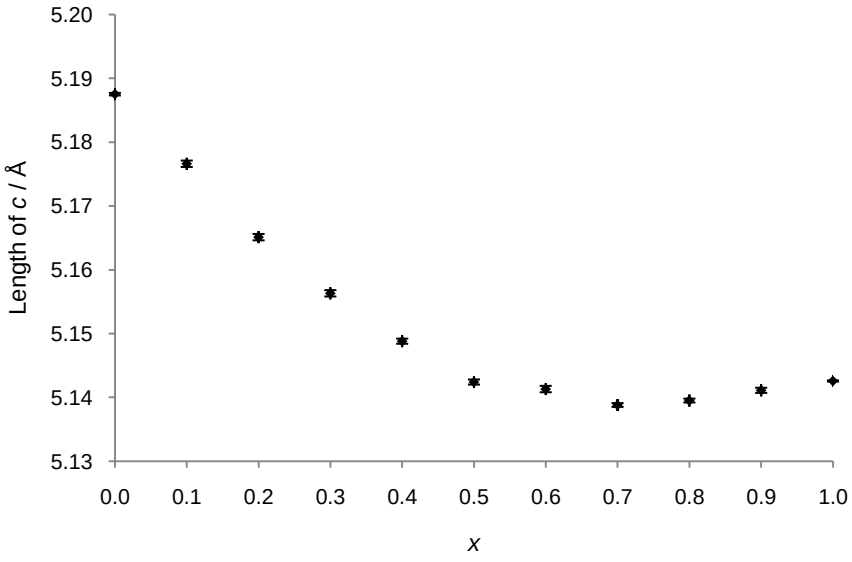

Figure 4-4: Plot of unit cell length *c* against composition (*x*) for the series $Co_{1-x}Ni_xSb$

Figure 4-3 and Figure 4-4 demonstrate the variation in unit cell lengths *a* and *c* with composition, respectively. Figure 4-3 demonstrates that the unit cell length *a* increases in an almost linear fashion as more nickel is introduced into the structure. However, a distinctly different trend is observed between the unit cell length *c* and composition: the unit cell length *c* decreases in an almost linear fashion as *x* is increased from zero to 0.5. At values of *x* greater than 0.5 the value of *c* is almost constant. The increase in *a* across the series is expected given that the length of *a* in NiSb (3.94532(6) Å) is greater than that in CoSb (3.8906(1) Å). The general decrease in the length of *c* across the series is also expected given that the length of *c* in NiSb (5.14257(9) Å) is shorter than that in CoSb (5.1875(2) Å). An increase in *a* and a general decrease in *c* across the series demonstrates that the expansion of the unit cell is anisotropic. The relationships between the unit cell parameters *a* and *c* and composition are discussed in more detail later in the section.

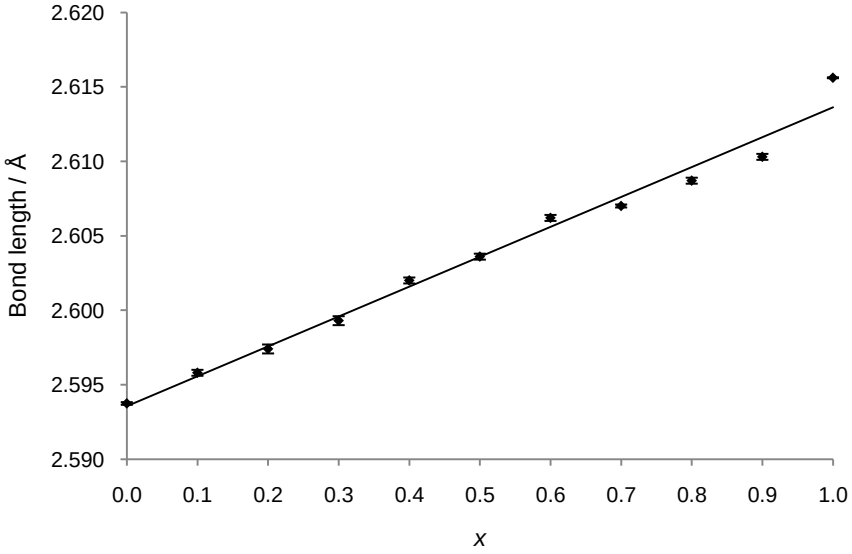

Figure 4-5: Plot of M-Sb bond length against composition (x) for the series $Co_{1-x}Ni_xSb$

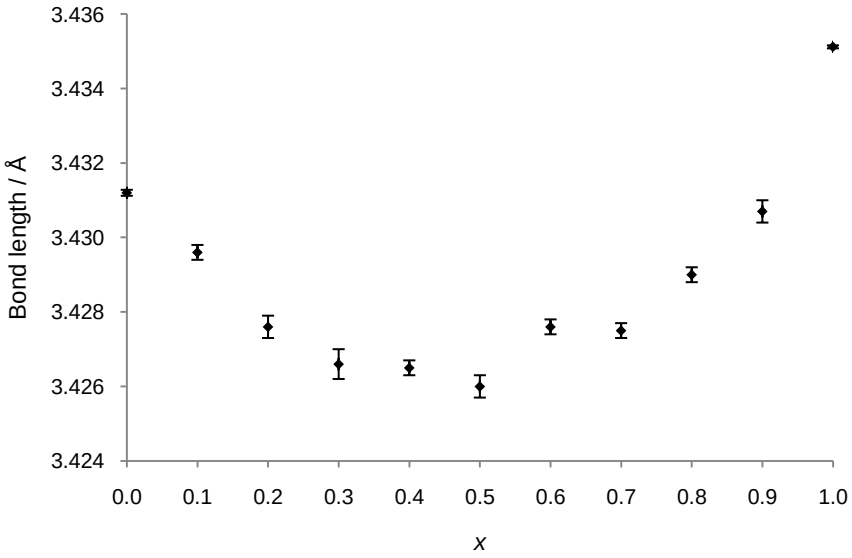

Figure 4-6: Plot of Sb-Sb bond length against composition (x) for the series $Co_{1-x}Ni_xSb$

Figure 4-5 and Figure 4-6 demonstrate the variation in M-Sb and Sb-Sb bond lengths with composition, respectively. Figure 4-5 displays a linear increase in the M-Sb bond length as more nickel is introduced into the structure. This is unexpected when considering the relative lengths of the metal-metal distances in the elements (as mentioned earlier),[144,145]

but is less surprising when considering that Ni-Ni distances are longer than Co-Co distances in some other intermetallic compounds.[142,143,146,147]

The relationship between the Sb-Sb bond length and composition shown in Figure 4-6 is not linear, and a general decrease or increase in the length of the bond is not observed. Instead, the Sb-Sb bond length varies smoothly across the series, and reaches a minimum (3.4260(3) Å) at the composition $Co_{0.5}Ni_{0.5}Sb$. The strongest Sb-Sb interaction is therefore present in the middle member of the solid solution series. However, the Sb-Sb distance in $Co_{0.5}Ni_{0.5}Sb$ is considerably longer than the Sb-Sb distance in elemental antimony recorded at 298 K (2.9082(5) Å),[149] suggesting the Sb-Sb interaction in $Co_{0.5}Ni_{0.5}Sb$ is comparatively weak.

The M-Sb and Sb-Sb bond lengths were calculated using the following expressions, where $d_{M\text{-}Sb}$ is the M-Sb bond length and $d_{Sb\text{-}Sb}$ is the Sb-Sb bond length:

$$d_{M-Sb} = \sqrt{\frac{a^2}{3} + \frac{c^2}{16}}$$

(Equation 4-1)

$$d_{Sb-Sb} = \sqrt{\frac{a^2}{3} + \frac{c^2}{4}}$$

(Equation 4-2)

Equation 4-1 and Equation 4-2 can be rearranged to give expressions for the lengths of *a* and *c* in terms of the M-Sb and Sb-Sb bond lengths, as depicted in Equation 4-3 and Equation 4-4:

$$a = \sqrt{4d_{M-Sb}^2 - d_{Sb-Sb}^2}$$

(Equation 4-3)

$$c = \sqrt{\frac{16}{3}(d_{Sb-Sb}^2 - d_{M-Sb}^2)}$$

(Equation 4-4)

Equation 4-3 demonstrates that the length of *a* is four times more dependent on the square of the length of the M-Sb bond than it is on the square of the length of the Sb-Sb bond. This may explain why the length of *a* increases in a linear fashion when plotted against composition. Equation 4-4 demonstrates that the length of *c* is equally dependent on the squares of the M-Sb and Sb-Sb bond lengths. This may explain why the length of *c* decreases until $x = 0.5$, and remains almost constant above 0.5. The relationship between Sb-Sb bond length and composition is not well understood. The minimum bond length occurs at $x = 0.5$; it is likely that this is a result of electronic effects, arising from the filling of a band with significant 5*p* character at the Fermi energy. A potential scenario explaining the observed relationship could be that in CoSb there is an empty or under half-full Sb-derived band, in NiSb there is a full or over half-full band, and in $Co_{0.5}Ni_{0.5}Sb$ the band is exactly half-full. Calculation of density of states diagrams may provide a greater insight into the reasons behind the observed trend in Sb-Sb bond length, by allowing identification of the origin of the states at the Fermi level. This is likely to be relatively easy to perform for the end members of the series. However, calculation of density of states diagrams for the intermediate compositions is likely to be much more difficult due to the potential disorder of cobalt and nickel. Time has not allowed for this to be investigated, and it is therefore a clear target for further work.

The likelihood that the minimum in Sb-Sb bond length observed in the $Co_{1-x}Ni_xSb$ series is due to an electronic effect is increased when considering the M-Sb-M-Sb plane outlined in black in Figure 4-7.

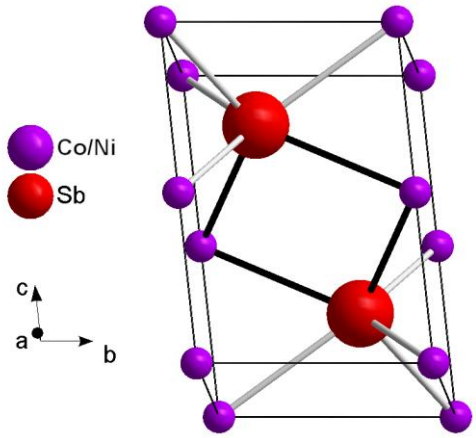

Figure 4-7: Representation of the M-Sb-M-Sb plane in $Co_{1-x}Ni_xSb$

As the M-Sb bond length increases in a linear fashion across the series, the distance between the two antimony atoms in Figure 4-7 would also be expected to increase if the geometry of the plane was retained. As the Sb-Sb bond length does not increase across the series, the M-Sb-M-Sb plane must distort in order to accommodate a shorter Sb-Sb bond. It is therefore likely that shortening of the Sb-Sb bond is favourable, and is a result of a stable electronic configuration. The lattice parameters *a* and *c* are dependent on the M-Sb and Sb-Sb bond lengths: distortion of the plane results in a longer *a* axis and a shorter *c* axis. The Sb-M-Sb angle was determined for each composition in the series. A plot demonstrating the variation in the bond angle with increasing nickel content is shown in Figure 4-8.

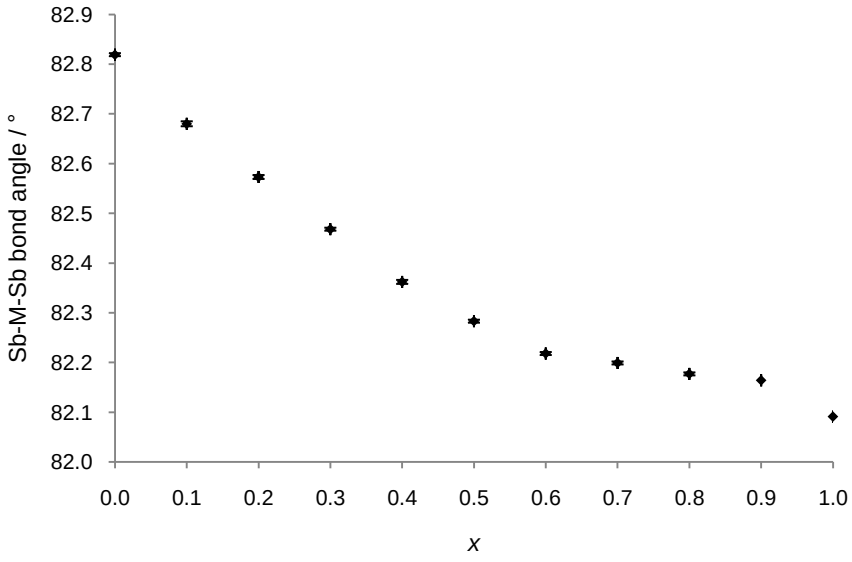

Figure 4-8: Plot of Sb-M-Sb angle against composition (x) for the series $Co_{1-x}Ni_xSb$

Figure 4-8 displays a general decrease in the Sb-M-Sb angle as more nickel is introduced into the structure. The rate of change between $x = 0$ and $x = 0.5$ is greater than the rate of change later on in the series. This confirms that the M-Sb-M-Sb plane shown in Figure 4-7 must distort in order to accommodate a shorter Sb-Sb bond between $x = 0$ and $x = 0.5$. The bond angle continues to decrease after $x = 0.5$ as, although the Sb-Sb bond length is increasing, the M-Sb bond length is also increasing. The net result is a smaller incremental decrease in the Sb-M-Sb bond angle as the value of x is increased from $x = 0.5$ onwards.

4.1.2 Introduction of Cu into CoSb ($Co_{1-x}Cu_xSb$)

Stoichiometric amounts of cobalt(II,III) oxide, copper(II) oxide and antimony(III) oxide were heated at 425 °C (48 hours) and subsequently at 450 °C (24 hours) in order to prepare the series $Co_{1-x}Cu_xSb$ ($0.1 \leq x \leq 0.6$), with x increasing in increments of 0.1. X-ray powder diffraction patterns were recorded after the final reaction over the range $5 \leq 2\theta/° \leq 70$, with a counting time of 1.0 s per step.

Analysis of the x-ray diffraction pattern recorded for $Co_{0.9}Cu_{0.1}Sb$ revealed that a single NiAs-type phase formed in the reaction. A very small reflection attributed to an impurity was also present at approximately 30° 2θ, which could not be identified. In all other compositions in the series an NiAs-type phase was present, in addition to various amounts

of Cu_2Sb and $CoSb_2$. The formation of Cu_2Sb in this reaction is not surprising as it tends to form readily under the reaction conditions. The weight fractions of each phase in each composition were calculated and are given in Table 4-3.

Composition	*x*	NiAs-type	$CoSb_2$	Cu_2Sb
CoSb	0	1	0	0
$Co_{0.9}Cu_{0.1}Sb$	0.1	1	0	0
$Co_{0.8}Cu_{0.2}Sb$	0.2	0.825	0.080(7)	0.095(9)
$Co_{0.7}Cu_{0.3}Sb$	0.3	0.662	0.188(9)	0.149(5)
$Co_{0.6}Cu_{0.4}Sb$	0.4	0.478	0.276(8)	0.25(1)
$Co_{0.5}Cu_{0.5}Sb$	0.5	0.261	0.363(8)	0.376(8)
$Co_{0.4}Cu_{0.6}Sb$	0.6	0.10	0.46(2)	0.43(2)

Table 4-3: Weight fractions of the NiAs-type phase, $CoSb_2$ and Cu_2Sb in the series $Co_{1-x}Cu_xSb$

The weight fractions of each phase were plotted as a function of composition in Figure 4-9.

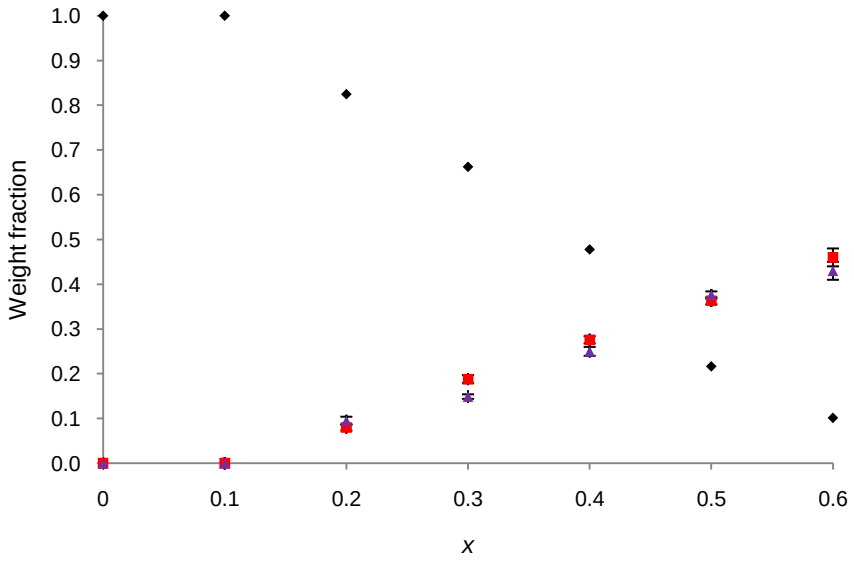

Figure 4-9: Plot of the weight fractions of the NiAs-type phase (black diamonds), $CoSb_2$ (red squares) and Cu_2Sb (purple triangles) against composition (*x*) for the series $Co_{1-x}Cu_xSb$

Figure 4-9 demonstrates a clear relationship between the relative amounts of each phase in each composition. It is clear that at values of *x* greater than 0.1, the weight fraction of the

NiAs-type phase decreases in a linear fashion. This is coupled with the linear increase in weight fraction of both $CoSb_2$ and Cu_2Sb.

Rietveld refinement was carried out for all compositions in the series using the structure of CoSb as the initial model for the NiAs-type phase,[107] with the fractional occupancies changed according to the composition dictated by the stoichiometry of the starting materials. Unit cell data obtained from the refinement are given in Table 4-4.

Composition	x	a / Å	c / Å	V / Å^3	R(F^2)
CoSb	0	3.8906(1)	5.1875(2)	68.002(5)	0.1367
$Co_{0.9}Cu_{0.1}Sb$	0.1	3.9146(3)	5.1746(4)	68.67(1)	0.0422
$Co_{0.8}Cu_{0.2}Sb$	0.2	3.9191(3)	5.1723(4)	68.80(1)	0.2182
$Co_{0.7}Cu_{0.3}Sb$	0.3	3.9166(3)	5.1703(4)	68.68(1)	0.1982
$Co_{0.6}Cu_{0.4}Sb$	0.4	3.9151(4)	5.1677(7)	68.60(2)	0.1081
$Co_{0.5}Cu_{0.5}Sb$	0.5	3.9154(5)	5.1671(7)	68.60(2)	0.0760
$Co_{0.4}Cu_{0.6}Sb$	0.6	3.9144(7)	5.167(1)	68.56(3)	0.0969

Table 4-4: Unit cell data for the series $Co_{1-x}Cu_xSb$

Graphical representations of the unit cell data given in Table 4-4 were prepared and are given in the following figures.

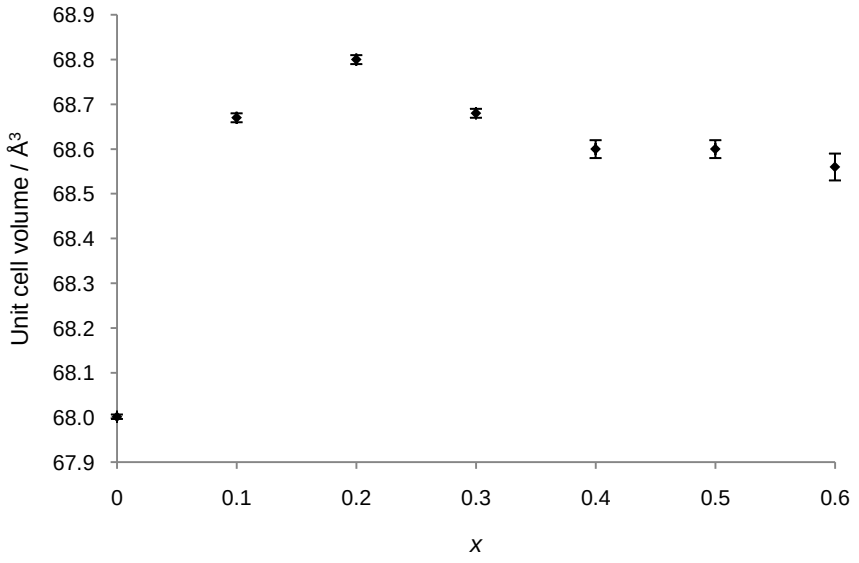

Figure 4-10: Plot of unit cell volume against composition (x) for the series $Co_{1-x}Cu_xSb$

Figure 4-10 demonstrates an increase in the unit cell volume between $x = 0$ and $x = 0.2$, suggesting that some copper has been introduced into the structure in the reactions performed to prepare $Co_{0.9}Cu_{0.1}Sb$ and $Co_{0.8}Cu_{0.2}Sb$. The presence of only a very small unidentifiable impurity in $Co_{0.9}Cu_{0.1}Sb$ suggests that almost all (if not all) of the copper has been substituted in place of cobalt. The variation in unit cell volume between CoSb and $Co_{0.9}Cu_{0.1}Sb$ is large; the variation in unit cell volume between $Co_{0.9}Cu_{0.1}Sb$ and '$Co_{0.8}Cu_{0.2}Sb$' is much smaller. This suggests that the full amount of copper has not been substituted in place of cobalt in the reaction carried out to prepare $Co_{0.8}Cu_{0.2}Sb$, which is not surprising given that Cu_2Sb also formed as an impurity in this sample. The limit of solubility of Cu in CoSb therefore lies between 0.1 and 0.2. The use of better quality data may enable refinement of the fractional occupancies. However, the similar x-ray scattering factors of cobalt and copper may prevent this. Neutron diffraction data may therefore be more useful in determining the exact limit of solubility in this system. A rough estimate of the limit of solubility can be obtained by extrapolating a linear trendline between the points at $x = 0$ and $x = 0.1$ to a point where it coincides with the unit cell volume where $x = 0.2$. Reading off the x-axis value gives an estimate for the solubility limit ($x \approx 0.12$).

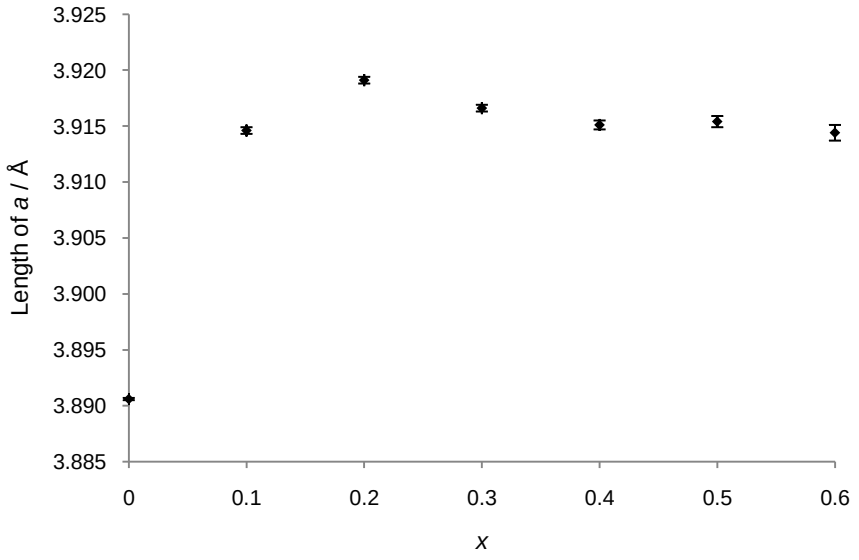

Figure 4-11: Plot of unit cell length *a* against composition (*x*) for the series $Co_{1-x}Cu_xSb$

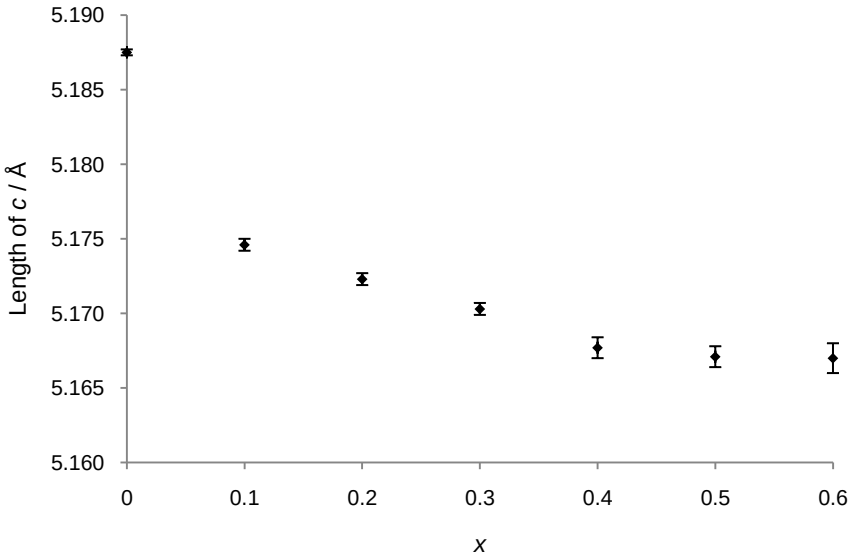

Figure 4-12: Plot of unit cell length *c* against composition (*x*) for the series $Co_{1-x}Cu_xSb$

Figure 4-11 and Figure 4-12 demonstrate similar changes in lattice parameters between $x = 0$ and $x = 0.2$ as those observed in Figure 4-10. However, the length of *a* increases as copper is introduced into the structure, whereas the length of *c* decreases as copper is introduced into the structure. This trend of an increase in *a* and a decrease in *c* across the series was also observed in the $Co_{1-x}Ni_xSb$ solid solution.

It is important to note that the lattice parameters of Cu_2Sb present in the compositions with $x = 0.2$ to 0.6 were not significantly different, suggesting that no amount of cobalt had been introduced into the Cu_2Sb structure.

4.1.3 Introduction of Cu into NiSb ($Ni_{1-x}Cu_xSb$)

Stoichiometric amounts of nickel(II) oxide, copper(II) oxide and antimony(III) oxide were heated at 425 °C (48 hours), 450 °C (24 hours) and once more at 450 °C (24 hours) in order to prepare the series $Ni_{1-x}Cu_xSb$ ($0.1 \leq x \leq 0.9$), with *x* increasing in increments of 0.1. X-ray powder diffraction patterns were recorded after the final reaction over the range $5 \leq 2\theta/° \leq 70$, with a counting time of 1.0 s per step.

Analysis of the x-ray diffraction patterns indicated that in the compositions where $0.1 \leq x \leq 0.4$ a single NiAs-type phase was present. The composition where $x = 0.5$ was

recently discovered to occur in nature as the mineral *Zlatogorite*.[150] This study established that $Ni_{0.5}Cu_{0.5}Sb$ crystallises in the space group $P\bar{3}m1$. There are two metal positions in $P\bar{3}m1$; ordering of the two metal atoms in the structure is therefore allowed. The unit cell of $Ni_{0.5}Cu_{0.5}Sb$ is shown in Figure 4-13 and demonstrates the ordering of nickel and copper within the structure.

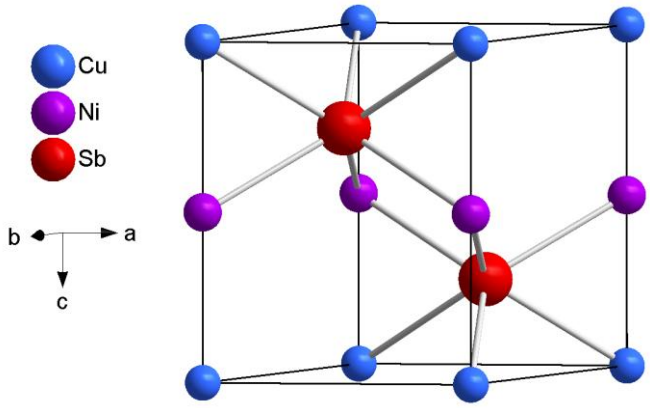

Figure 4-13: Unit cell of $Ni_{0.5}Cu_{0.5}Sb$, demonstrating ordering of the nickel and copper atoms within the structure

The nickel arsenide structure can be described in terms of $NiAs_6$ octahedra, which share edges in the *ab* plane and faces in the *c* direction. In $Ni_{0.5}Cu_{0.5}Sb$, equivalent octahedra (*e.g.* two Cu-centred octahedra) share edges in the *ab* plane, and non-equivalent octahedra (*e.g.* a Cu-centred octahedron and an Ni-centred octahedron) share faces in the *c* direction. This is illustrated in Figure 4-14.

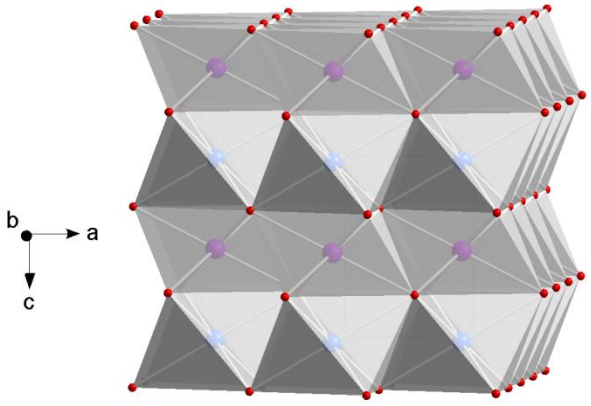

Figure 4-14: Polyhedral representation of $Ni_{0.5}Cu_{0.5}Sb$, demonstrating the edge-connectivity of equivalent octahedra and face-connectivity of non-equivalent octahedra

In compounds adopting the nickel arsenide structure in $P6_3/mmc$, the antimony atom is located on (⅓, ⅔, ¼). In compounds crystallising in $P\bar{3}m1$, the antimony atom is no longer located on a special position; it is instead located on the 2*d* Wyckoff position with coordinates (⅓, ⅔, *z*), where *z* in $Ni_{0.5}Cu_{0.5}Sb$ is approximately 0.27. This results in different Ni-Sb and Cu-Sb distances: in $Ni_{0.5}Cu_{0.5}Sb$ the average length of the Ni-Sb bond is 2.6198 Å, and the average length of the Cu-Sb bond is 2.7201 Å.[150] Table 4-5 provides information on the Wyckoff positions and atomic coordinates in NiSb ($P6_3/mmc$) and $Ni_{0.5}Cu_{0.5}Sb$ ($P\bar{3}m1$) for direct comparison between the two space groups.

$P6_3/mmc$					$P\bar{3}m1$				
Atom	Wyckoff	*x*	*y*	*z*	Atom	Wyckoff	*x*	*y*	*z*
Ni	2*a*	0	0	0	Cu	1*a*	0	0	0
Sb	2*c*	⅓	⅔	¼	Ni	1*b*	0	0	½
					Sb	2*d*	⅓	⅔	0.27

Table 4-5: Comparison between atomic positions in NiSb ($P6_3/mmc$) and $Ni_{0.5}Cu_{0.5}Sb$ ($P\bar{3}m1$)

According to the literature, $Ni_{0.5}Cu_{0.5}Sb$ has not been previously obtained synthetically. Attempted synthesis of this phase resulted in the formation of what appeared at first glance to be an NiAs-type phase; small reflections attributed to impurities were also present in the diffraction pattern. Fingerprinting of the peak positions suggested that the impurities were small amounts of Cu_2Sb and Sb_2O_3. Rietveld refinement was carried out in the space group

$P\bar{3}m1$ using the structure published by Kabalov and Sokolova as the initial model.[150] Isotropic displacement parameters of nickel and copper were constrained to be equal in order to prevent the introduction of an extra degree of freedom into the refinement, and therefore biasing the results towards $P\bar{3}m1$ rather than $P6_3/mmc$. Addition of Cu_2Sb and Sb_2O_3 into the refinement caused divergence. Previous identification of the impurities in the sample as Cu_2Sb and Sb_2O_3 was therefore not conclusive. However, it is clear from the Rietveld fit shown in Figure 4-15 that the relative amounts of the impurities are small and therefore relatively insignificant. Data obtained from the refinement are given in Table 4-6.

$Ni_{0.5}Cu_{0.5}Sb$	Refined values			Literature values[150]		
Space group		$P\bar{3}m1$				
a / Å		4.0482(3)			4.0510(2)	
c / Å		5.1322(4)			5.1382(4)	
V / Å^3		72.84(1)			73.02	
Atomic positions	***x***	***y***	***z***	***x***	***y***	***z***
Ni (1*b*)	0	0	½	0	0	½
Cu (1*a*)	0	0	0	0	0	0
Sb (2*d*)	⅓	⅔	0.271(1)	⅓	⅔	0.2703
Isotropic displacement parameters / Å^2	**Ni**	**Cu**	**Sb**			
	0.009(2)	0.009(2)	0.007(2)			
R(F^2)		0.1825				
χ^2		2.605				

Table 4-6: Rietveld refinement data for $Ni_{0.5}Cu_{0.5}Sb$

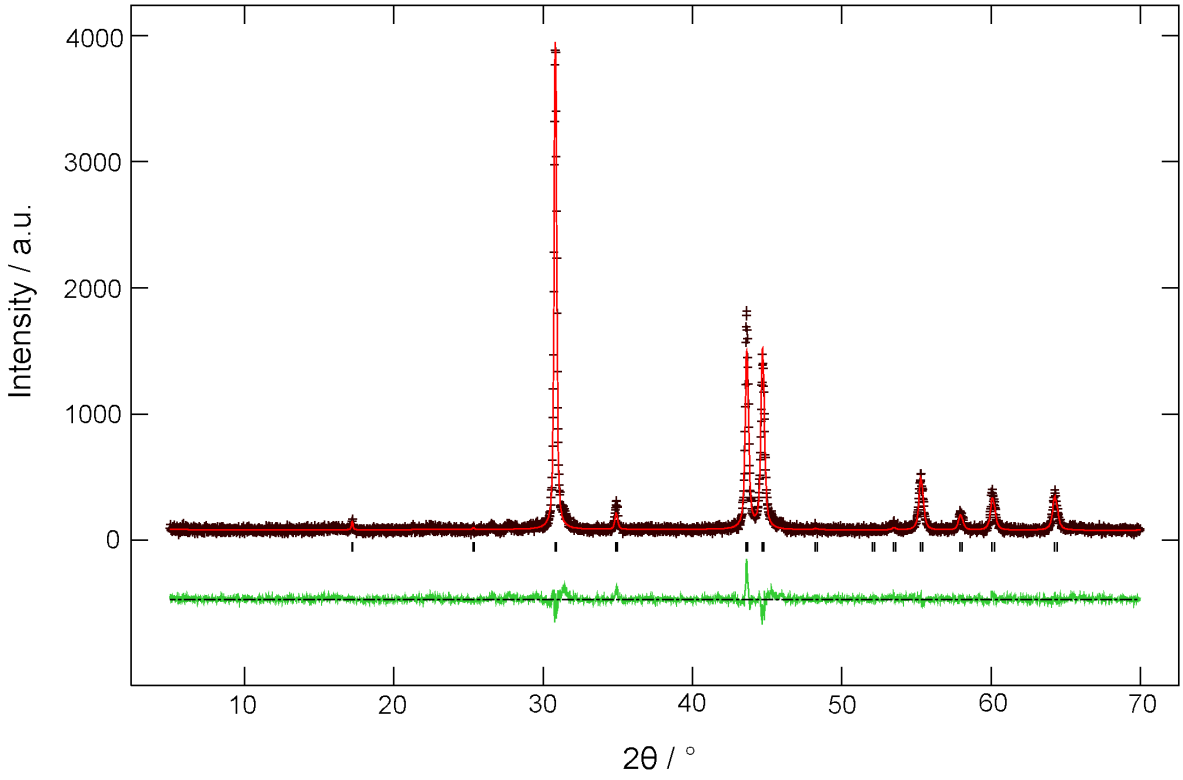

Figure 4-15: Observed (black), calculated (red) and difference (green) x-ray powder diffraction profiles for $Ni_{0.5}Cu_{0.5}Sb$. Tick marks indicate positions of allowed reflections

A clear mismatch in the intensity of the (102) reflection located at approximately 43° 2θ is apparent from the Rietveld fit shown in Figure 4-15; the model is under-calculating the intensity for this reflection. Refinement of the structure of $Ni_{0.5}Cu_{0.5}Sb$ was therefore also carried out in $P6_3/mmc$ to ensure the metal atoms were not disordered. Refinement of the isotropic displacement parameters of the atoms in $P6_3/mmc$ resulted in abnormally high parameters for the two metals disordered over the 2*a* Wyckoff position. This, in conjuction with the refined atomic position of the antimony atom (z = 0.271(1)), therefore suggested that the nickel and copper atoms in $Ni_{0.5}Cu_{0.5}Sb$ are ordered.

An NiAs-type phase also formed in compositions where $0.6 \leq x \leq 0.9$; various amounts of Cu_2Sb, Sb_2O_3 and elemental antimony were also present in these samples. Rietveld refinement was carried out for all compositions using the structure of NiSb as the initial model,[112] with atom occupancies changed according to the composition dictated by the stoichiometry of the starting materials. The weight fractions of each phase in each composition were calculated and are given in Table 4-7.

Composition	*x*	NiAs-type	Cu_2Sb	Sb_2O_3	Sb
NiSb	0	1	0	0	0
$Ni_{0.9}Cu_{0.1}Sb$	0.1	1	0	0	0
$Ni_{0.8}Cu_{0.2}Sb$	0.2	1	0	0	0
$Ni_{0.7}Cu_{0.3}Sb$	0.3	1	0	0	0
$Ni_{0.6}Cu_{0.4}Sb$	0.4	1	0	0	0
$Ni_{0.5}Cu_{0.5}Sb$	0.5	1*	0	0	0
$Ni_{0.4}Cu_{0.6}Sb$	0.6	0.82973	0.165(5)	0.0055(7)	0
$Ni_{0.3}Cu_{0.7}Sb$	0.7	0.71146	0.224(4)	0.0031(3)	0.061(2)
$Ni_{0.2}Cu_{0.8}Sb$	0.8	0.45262	0.388(7)	0.0041(8)	0.156(4)
$Ni_{0.1}Cu_{0.9}Sb$	0.9	0.21626	0.547(8)	0.0037(5)	0.233(6)

Table 4-7: Weight fractions of the NiAs-type phase, Cu_2Sb, Sb_2O_3 and Sb in the series $Ni_{1-x}Cu_xSb$. * denotes the presence of small amounts of unidentifiable impurities

The weight fractions of each phase were plotted as a function of composition in Figure 4-16.

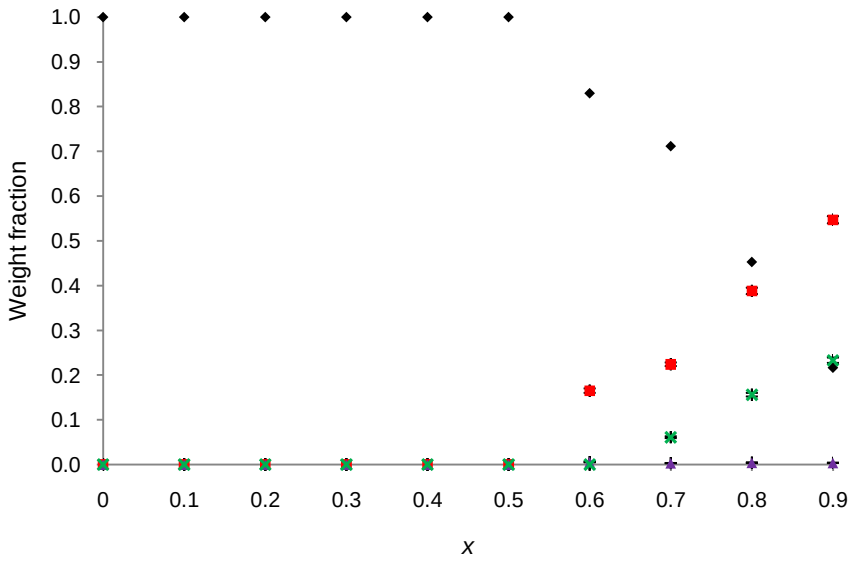

Figure 4-16: Plot of the weight fractions of the NiAs-type phase (black diamonds), Cu_2Sb (red squares), Sb_2O_3 (purple triangles) and Sb (green crosses) against composition (*x*) for the series $Ni_{1-x}Cu_xSb$

Figure 4-16 displays a clear relationship between the relative amounts of each phase in each composition. It is clear that at values of *x* between 0.5 and 1.0, the weight fraction of the NiAs-type phase decreases in an almost linear fashion. This is coupled with the almost

linear increase in weight fraction of Cu_2Sb and Sb. Very small amounts of Sb_2O_3 are present in phases with x equal to or greater than 0.7, although this is not apparent on a plot of this scale.

Given that refinement of the structure of $Ni_{0.5}Cu_{0.5}Sb$ in $P\bar{3}m1$ resulted in a z_{Sb} value of 0.271(1) and it therefore appeared to be ordered, it is likely that $Ni_{0.6}Cu_{0.4}Sb$ and $Ni_{0.7}Cu_{0.3}Sb$ are also ordered given that copper dominates the 1*a* Wyckoff position in $P\bar{3}m1$ in both compositions (site occupancy = 0.8 and 0.6 for $Ni_{0.6}Cu_{0.4}Sb$ and $Ni_{0.7}Cu_{0.3}Sb$, respectively). Rietveld refinement of both compositions was therefore carried out in both $P6_3/mmc$ and $P\bar{3}m1$ in order to determine order or disorder. Visually, there did not appear to be a difference between the two fits. However, in $P\bar{3}m1$ z refined to 0.265(1) and 0.261(2) in $Ni_{0.6}Cu_{0.4}Sb$ and $Ni_{0.7}Cu_{0.3}Sb$, respectively, suggesting the metals in these compositions are ordered.

Chemical intuition and the ordering of the metal atoms in $Ni_{0.7}Cu_{0.3}Sb$ suggest that the metal atoms in $Ni_{0.8}Cu_{0.2}Sb$ and $Ni_{0.9}Cu_{0.1}Sb$ should be ordered. Both compositions were refined in both $P6_3/mmc$ and $P\bar{3}m1$ in order to determine order or disorder. Refining the value of z_{Sb} in $P\bar{3}m1$ resulted in divergence of the refinement. When z_{Sb} was set to ¼, and subsequently refined, the value of z_{Sb} refined to ¼ within one standard deviation. This suggested that the metals in $Ni_{0.8}Cu_{0.2}Sb$ and $Ni_{0.9}Cu_{0.1}Sb$ are disordered over the one crystallographic site. However, this cannot be stated conclusively given the very small amounts of copper in the structures (x = 0.1 and 0.2), and therefore the very small expected deviations from z_{Sb} = ¼ in the ordered structure. Data reported for these compositions are therefore from refinements carried out in $P6_3/mmc$.

Full width at half maximum values for compositions where $0.1 \leq x \leq 0.5$ were calculated for the (102) reflection located at approximately 43° 2θ. Examination shows there is little change in full width at half maximum across the series, strongly suggesting the presence of single phase products. $R(F^2)$ values for the series were all in the range 0.0643 to 0.0805, demonstrating good fits to the observed data.

Unit cell data obtained from the refinements are given in Table 4-8. Two bond lengths are quoted for compositions where x = 0.3, 0.4 and 0.5 as their ordered structures result in the

calculation of the Ni(1)-Sb (1*b* Wyckoff) and Ni(2)/Cu-Sb (1*a* Wyckoff) distances, rather than an average metal-antimony distance calculated for disordered structures. The general position of the antimony atom in the ordered structure also results in two Sb-Sb bond lengths, which are also quoted in the table.

Composition	x	a / Å	c / Å	V / Å^3	M-Sb bond length / Å	Sb-Sb bond length / Å
NiSb	0	3.94523(4)	5.14243(7)	69.318(2)	2.61554(2)	3.43503(3)
$Ni_{0.9}Cu_{0.1}Sb$	0.1	3.9443(2)	5.1381(3)	68.94(1)	2.6108(1)	3.4289(2)
$Ni_{0.8}Cu_{0.2}Sb$	0.2	3.9707(3)	5.1269(4)	70.00(1)	2.6265(1)	3.4390(2)
$Ni_{0.7}Cu_{0.3}Sb$	0.3	3.9966(3)	5.1292(4)	70.95(1)	2.612(4)* / 2.669(4)^	3.36(1) / 3.54(1)
$Ni_{0.6}Cu_{0.4}Sb$	0.4	4.0190(3)	5.1313(5)	71.78(1)	2.615(3)* / 2.689(3)^	3.34(1) / 3.58(1)
$Ni_{0.5}Cu_{0.5}Sb$	0.5	4.0482(3)	5.1322(4)	72.84(1)	2.615(2)* / 2.721(3)^	3.312(7)
$Ni_{0.4}Cu_{0.6}Sb$	0.6	4.0656(3)	5.1278(5)	73.40(1)	2.6745(2)	3.4761(2)
$Ni_{0.3}Cu_{0.7}Sb$	0.7	4.0777(3)	5.1275(5)	73.84(2)	2.6806(2)	3.4807(2)
$Ni_{0.2}Cu_{0.8}Sb$	0.8	4.0704(3)	5.1270(6)	73.57(2)	2.6769(2)	3.4777(3)
$Ni_{0.1}Cu_{0.9}Sb$	0.9	4.0688(7)	5.126(1)	73.50(3)	2.6760(4)	3.4769(5)

Table 4-8: Unit cell data and bond lengths for the series $Ni_{1-x}Cu_xSb$. Two bond lengths are quoted for compositions where x = 0.3, 0.4 and 0.5 as their ordered structures result in the calculation of the Ni(1)-Sb distance (1*b* Wyckoff) (*) and the Ni(2)/Cu-Sb distance (1*a* Wyckoff) (^), rather than an average metal-antimony distance as is calculated for disordered structures

Isotropic displacement parameters obtained in refinements in $P6_3/mmc$ for all compositions in the series (except x = 0.3, 0.4 and 0.5) were in an acceptable range, further suggesting that copper and nickel atoms in these compositions are disordered over the one crystallographic site (2*a* Wyckoff).

Graphical representations of the unit cell data given in Table 4-8 were prepared and are given in the following figures.

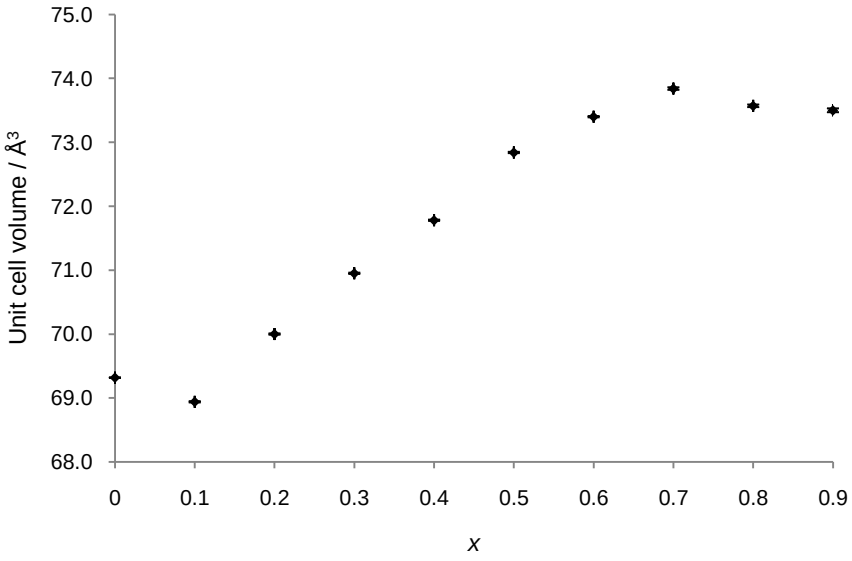

Figure 4-17: Plot of unit cell volume against composition (x) for the series $Ni_{1-x}Cu_xSb$

Figure 4-17 demonstrates the variation in unit cell volume with composition (x). The initial decrease in unit cell volume between $x = 0$ and $x = 0.1$ is unexpected. However, at values where $0.1 \leq x \leq 0.5$, there is a linear relationship between the unit cell volume and composition, suggesting compositions in this range were synthesised successfully. At values of x greater than 0.5, the unit cell volume remains relatively constant; this is expected given that compositions where $0.6 \leq x \leq 0.9$ contain impurities. This suggests that the limit of solubility of Cu in NiSb is $x = 0.5$. However, the presence of small amounts of impurities in the sample containing the phase $Ni_{0.5}Cu_{0.5}Sb$ indicates that the amount of copper in the structure is between $x = 0.4$ and $x = 0.5$.

It is important to note that the lattice parameters of Cu_2Sb present in the compositions where $x = 0.6$ to 0.9 were not significantly different, suggesting that no amount of nickel had been introduced into the Cu_2Sb structure.

Plots demonstrating the variation in M-Sb and Sb-Sb bond lengths with composition are shown below.

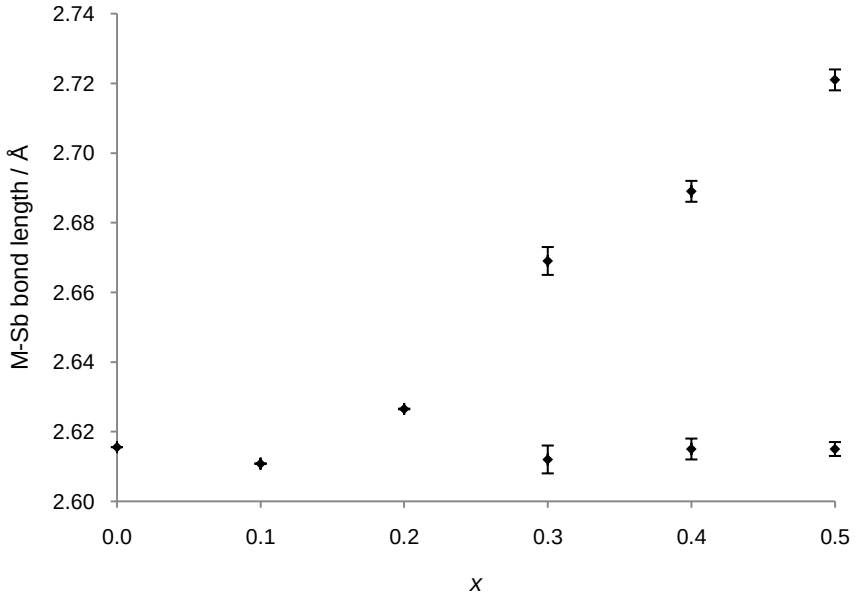

Figure 4-18: Plot of M-Sb bond length against composition (x) for the series $Ni_{1-x}Cu_xSb$. Two bond lengths are given for compositions where x = 0.3, 0.4 and 0.5 as their ordered structures result in two different bond lengths

Figure 4-18 displays an overall increase in the M-Sb bond length between x = 0 and x = 0.2. The Cu-Cu distance in *ccp* copper (2.5548 Å)[151] is larger than the Ni-Ni distance in *ccp* nickel (2.4883 Å),[145] which explains this increase in bond length across the series. At values of x between 0.3 and 0.5 both the Ni(1)-Sb (1*b* Wyckoff) and the Ni(2)/Cu-Sb (1*a* Wyckoff) bond lengths are given; the Ni(1)-Sb bond is the shorter of the two. The length of the Ni(1)-Sb bond stays relatively constant as x is increased; copper is not introduced onto this site, and so the bond length remains the same. The Ni(2)/Cu-Sb bond length increases in an almost linear fashion. The larger atomic radius of copper is likely to be responsible for this trend.

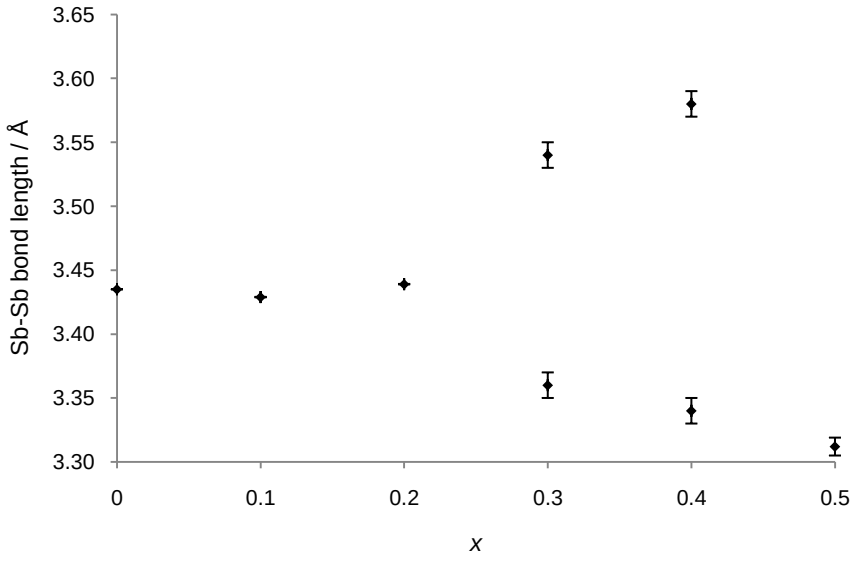

Figure 4-19: Plot of Sb-Sb bond length against composition (x) for the series $Ni_{1-x}Cu_xSb$. Two bond lengths are given for compositions where x = 0.3 and 0.4 as their ordered structures result in two different bond lengths

Figure 4-19 demonstrates the variation in Sb-Sb bond lengths with composition. Two different Sb-Sb bond lengths arise for compositions refined in $P\bar{3}m1$, as the antimony atoms are located at approximately z = 0.27 and 0.73 in the unit cell. The Sb-Sb distance between two antimony atoms in one unit cell will therefore be shorter than the Sb-Sb distance in NiSb, for example, where the antimony atoms are located at ¼ and ¾ in the unit cell. The second distance in compounds refined in $P\bar{3}m1$ is attributed to the Sb-Sb distance between an antimony atom in one unit cell and an antimony atom in a neighbouring unit cell. This distance will be longer than the Sb-Sb distance in NiSb.

4.1.4 Introduction of Fe into CoSb ($Co_{1-x}Fe_xSb$)

Stoichiometric amounts of cobalt(II,III) oxide, iron(III) oxide and antimony(III) oxide were heated at 425 °C (48 hours) and subsequently at 450 °C (24 hours) in order to prepare the series $Co_{1-x}Fe_xSb$ ($0.1 \leq x \leq 0.9$), with x increasing in increments of 0.1. X-ray powder diffraction patterns were recorded after the final reaction over the range $5 \leq 2\theta/° \leq 70$, with a counting time of 1.0 s per step.

Analysis of the x-ray diffraction patterns indicated that in the compositions where $0.1 \leq x \leq 0.8$ an NiAs-type phase had formed. However, all compositions except $Co_{0.9}Fe_{0.1}Sb$ also contained other phases. Peaks attributed to impurities present in compositions where x = 0.1 and 0.2 were too small to enable identification. $CoSb_2$ was present as an impurity in compositions where x = 0.3, 0.4 and 0.5. The presence of impurities indicated that not all of the iron had been substituted in place of cobalt in the solid solution. Compositions where $x \geq 0.6$ contained mixtures of iron and cobalt antimonides in various proportions, with some still also containing unreacted Fe_2O_3. The diffraction patterns contained many overlapping reflections, therefore making refinement of the peak shapes very difficult, even when constraining profile parameters in each phase. For this reason unit cell data on these compositions have not been included in this discussion. The weight fractions of phases present in compositions where $x \leq 0.5$ are given in Table 4-9.

Composition	x	NiAs-type	$CoSb_2$
CoSb	0	1	0
$Co_{0.9}Fe_{0.1}Sb$	0.1	1*	0
$Co_{0.8}Fe_{0.2}Sb$	0.2	1*	0
$Co_{0.7}Fe_{0.3}Sb$	0.3	0.928	0.072(9)
$Co_{0.6}Fe_{0.4}Sb$	0.4	0.785	0.215(9)
$Co_{0.5}Fe_{0.5}Sb$	0.5	0.67	0.33(1)

Table 4-9: Weight fractions of the NiAs-type phase and $CoSb_2$ in the series $Co_{1-x}Fe_xSb$. * denotes the presence of small amounts of unidentifiable impurities

The weight fractions of each phase were plotted as a function of composition in Figure 4-20.

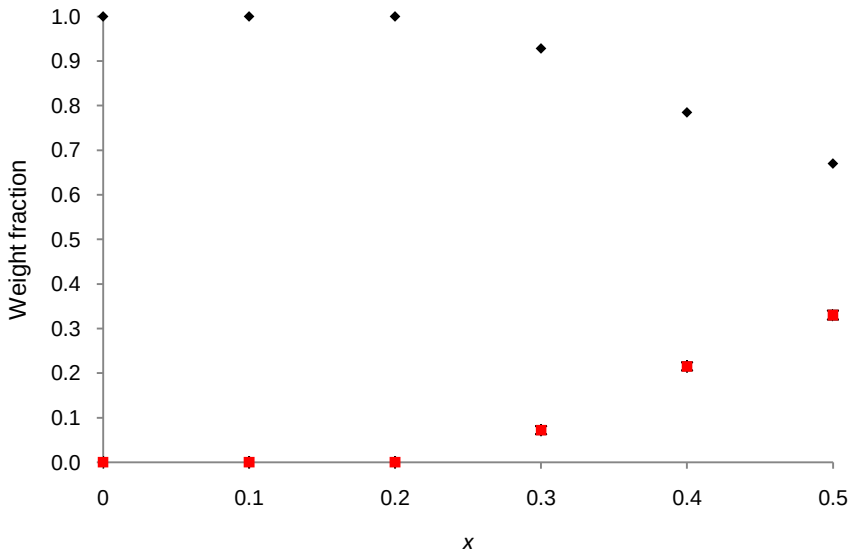

Figure 4-20: Plot of the weight fractions of the NiAs-type phase (black diamonds) and $CoSb_2$ (red squares) against composition (x) for the series $Co_{1-x}Fe_xSb$

Figure 4-20 illustrates the linear increase in the amount of $CoSb_2$ in the sample and the linear decrease in the amount of the NiAs-type phase from $x = 0.3$ onwards.

Rietveld refinement was carried out for all compositions in the series using the structure of CoSb as the initial model for the NiAs-type phase,[107] with atom occupancies changed according to the composition dictated by the stoichiometry of the starting materials. Unit cell data obtained from the refinement are given in Table 4-10. The Rietveld fit for $Co_{0.6}Fe_{0.4}Sb$ is shown in Figure 4-21.

Composition	x	a / Å	c / Å	V / Å^3
CoSb	0	3.8906(1)	5.1875(2)	68.002(5)
$Co_{0.9}Fe_{0.1}Sb$	0.1	3.9033(5)	5.1704(8)	68.22(2)
$Co_{0.8}Fe_{0.2}Sb$	0.2	3.926(1)	5.158(2)	68.85(6)
$Co_{0.7}Fe_{0.3}Sb$	0.3	3.9461(7)	5.146(1)	69.40(3)
$Co_{0.6}Fe_{0.4}Sb$	0.4	3.9599(8)	5.138(1)	69.78(4)
$Co_{0.5}Fe_{0.5}Sb$	0.5	3.990(2)	5.129(2)	70.72(7)

Table 4-10: Unit cell data for the series $Co_{1-x}Fe_xSb$

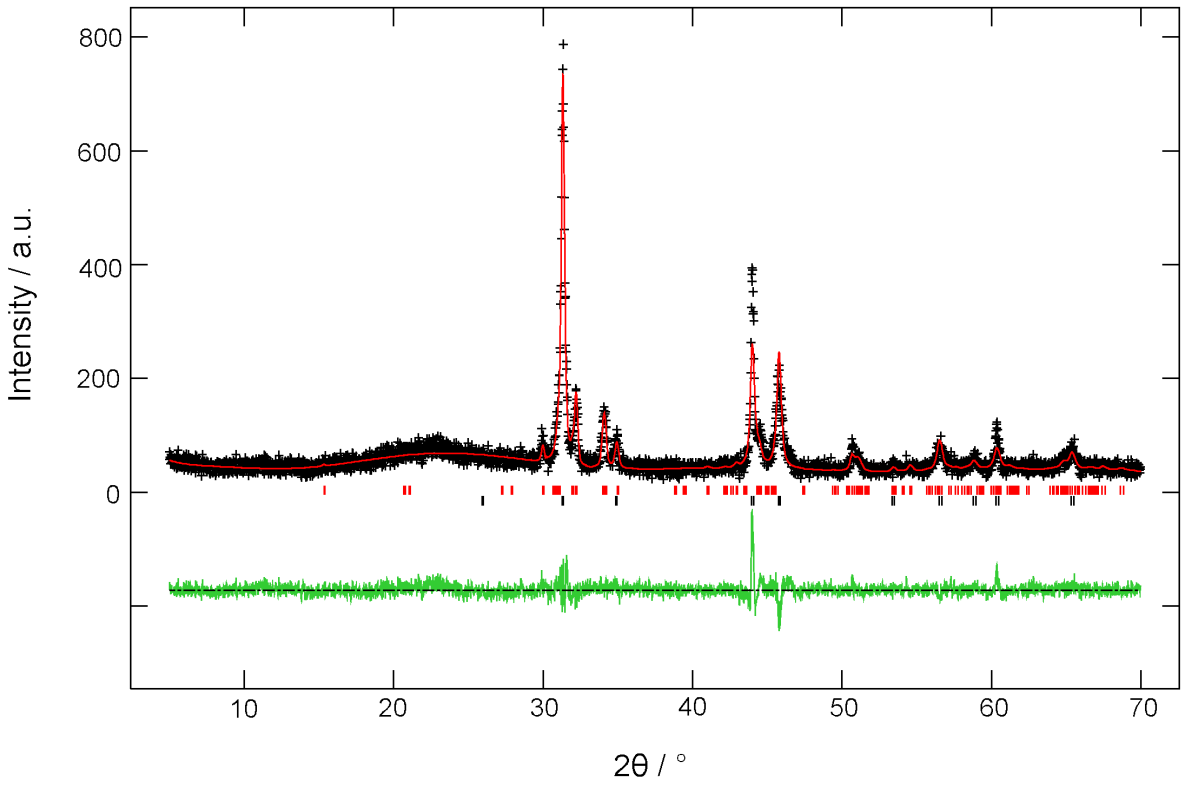

Figure 4-21: Observed (black), calculated (red) and difference (green) x-ray powder diffraction profiles for $Co_{0.6}Fe_{0.4}Sb$. Lower tick marks indicate positions of allowed reflections for the NiAs-type phase. Upper tick marks indicate positions of allowed reflections for $CoSb_2$

In Figure 4-21 and all other diffraction patterns recorded for this series there is a very large difference in intensity between the recorded (102) intensity (located at approximately 43° 2θ) and the modelled intensity. This is not accounted for by non-stoichiometry of the NiAs-type phase.

Graphical representations of the unit cell data given in Table 4-10 were prepared and are shown in the following figures.

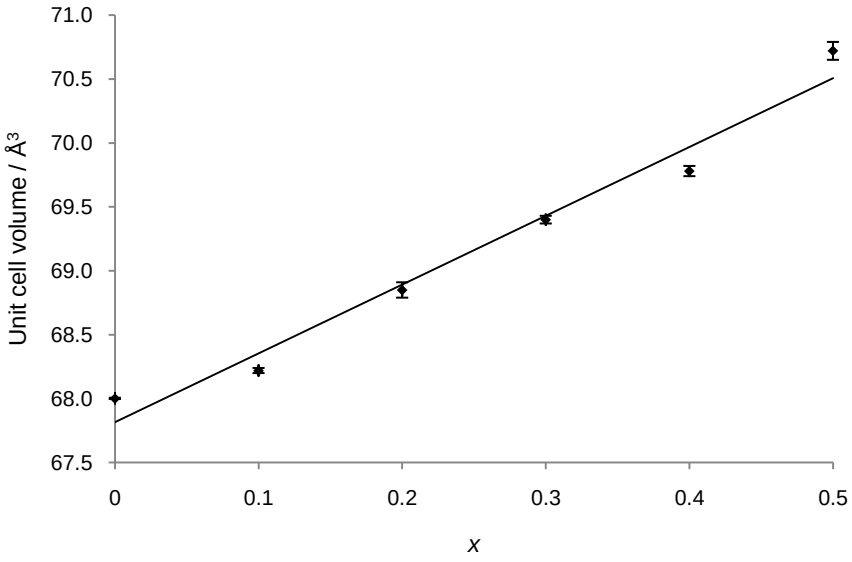

Figure 4-22: Plot of unit cell volume against composition (x) for the series $Co_{1-x}Fe_xSb$

Figure 4-22 displays an increasing linear trend between the unit cell volume and composition. Given that compositions from $x = 0.2$ onwards are impure this linear increase in unit cell volume is unexpected; the unit cell volume would be expected to increase in smaller increments as the value of x increased. However, the linear variation in unit cell volume with increasing iron in the reaction mixture demonstrates that iron may be introduced into CoSb, which is not unexpected given that FeSb also adopts the nickel arsenide structure. The presence of impurities in the products would ordinarily suggest that the full amount of iron introduced into the system has not been introduced into the CoSb structure. However, there are no identifiable iron-containing impurities in the system; only $CoSb_2$ could be identified as an impurity. It is possible that a poorly crystalline iron-containing phase is present and is therefore not detected in the diffraction pattern. The lattice parameters of the $CoSb_2$-type phase in the compositions do not vary across the series, indicating that iron has not been introduced into the $CoSb_2$ structure.

Refinement of the fractional occupancies in the $Co_{1-x}Fe_xSb$ series may provide a conclusive reason for the linear variation observed between the unit cell volume and iron content. However, as the x-ray scattering factors of cobalt and iron are very similar, this is not possible to achieve with x-ray data. Neutron diffraction data may therefore prove more useful.

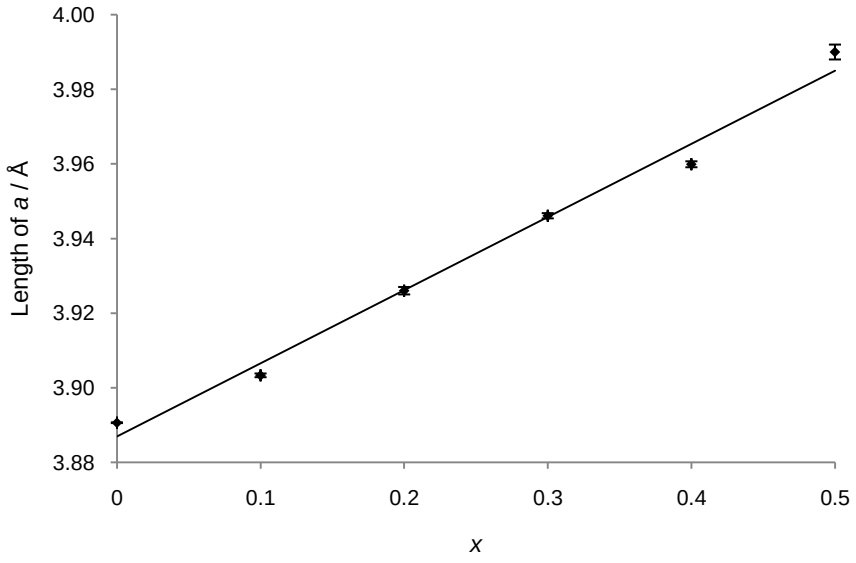

Figure 4-23: Plot of unit cell length *a* against composition (*x*) for the series $Co_{1-x}Fe_xSb$

Figure 4-23 displays an almost linear increasing relationship between the length of *a* and the composition. A similar trend is observed in the $Co_{1-x}Ni_xSb$ series.

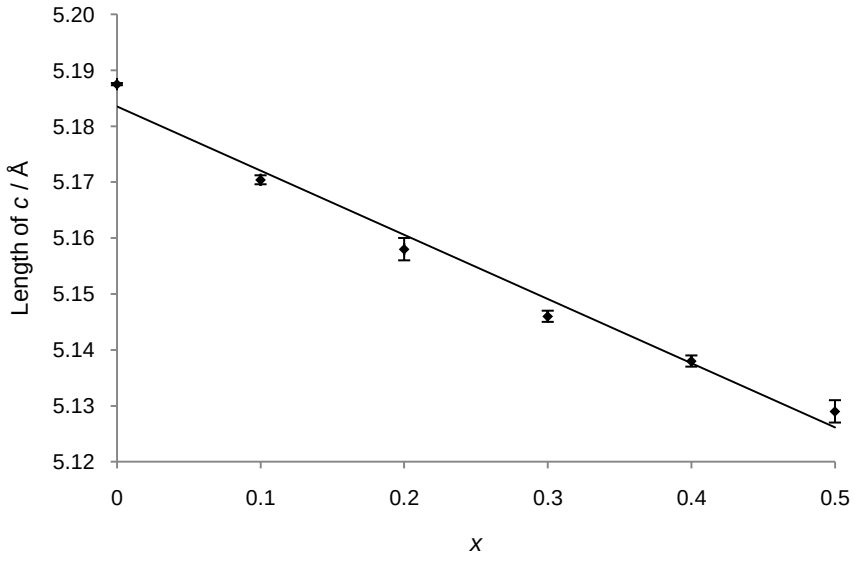

Figure 4-24: Plot of unit cell length *c* against composition (*x*) for the series $Co_{1-x}Fe_xSb$

Figure 4-24 displays an almost linear decreasing relationship between the length of *c* and composition. A similar trend is observed in the $Co_{1-x}Ni_xSb$ series.

Figure 4-23 and Figure 4-24 both suggest that iron has been introduced into the CoSb structure. This is surprising given that impurities were present in compositions from $x = 0.2$ onwards. In addition, there is no evidence for non-stoichiometry in the NiAs-type phases, and the lattice parameters of the $CoSb_2$-type phase do not change across the series. This suggests that a poorly crystalline iron-containing impurity must be present in the samples.

4.2 Tellurides

The application of the reductive synthetic route to other ternary systems was proposed. Given that binary 1:1 cobalt and nickel tellurides adopt the NiAs structure,[152] the synthesis of solid solutions in the Co-Sb-Te and Ni-Sb-Te systems was attempted. Compositions where $x = 0.5$ have been previously reported for both of these series.[107,153] In addition, the synthesis of solid solutions in the Ni-Co-Te system was also attempted, as well as the substitution of other similarly sized transition metals in place of cobalt and nickel in CoTe and NiTe, respectively. Synthesis of the composition $Ni_{0.5}Co_{0.5}Te$ has been reported previously.[143] However, it appears that no other solid solutions in the Ni-Co-Te system have been reported. The synthesis of all other compositions attempted has not been previously reported in the literature.

4.2.1 Metalloid Site Substitutions

4.2.1.1 Introduction of Te into CoSb ($CoSb_{1-x}Te_x$)

Stoichiometric amounts of copper(II) oxide, antimony(III) oxide and tellurium(IV) oxide were heated at 450 °C (48 hours), 450 °C (24 hours) for a second and third time, and finally at 500 °C (24 hours) in order to prepare the series $CoSb_{1-x}Te_x$ ($0.25 \leq x \leq 0.75$), with x increasing in increments of 0.25. X-ray powder diffraction patterns were recorded after the second reaction at 450 °C and after the final reaction, over the range $5 \leq 2\theta/° \leq 70$, with a counting time of 1.0 s per step.

Analysis of the x-ray diffraction patterns revealed that an NiAs-type phase had formed in each case. However, the (102) and (103) reflections in the patterns were abnormally wide. Full width at half maximum values for the (102) reflection were in the range 0.3549 to 0.6405. These values are considerably larger than those of the (110) reflection which was in the range 0.2400 to 0.3229. The large width of the reflections led to unsuccessful Rietveld

refinement of the structures. However, the widths of these reflections decreased as the amount of antimony in the structure was increased. This is explained when considering that the (102) and (103) reflections differ the most in 2θ value between CoTe and CoSb (Figure 4-25). It is likely that the poor resolution of these reflections is therefore due to the sample containing a range of compositions between CoSb and CoTe. The peak widths did not change between the second and final firings, suggesting that further heating would not result in the synthesis of a single phase. However, heating the samples at a significantly higher temperature may form a single phase, if decomposition does not occur.

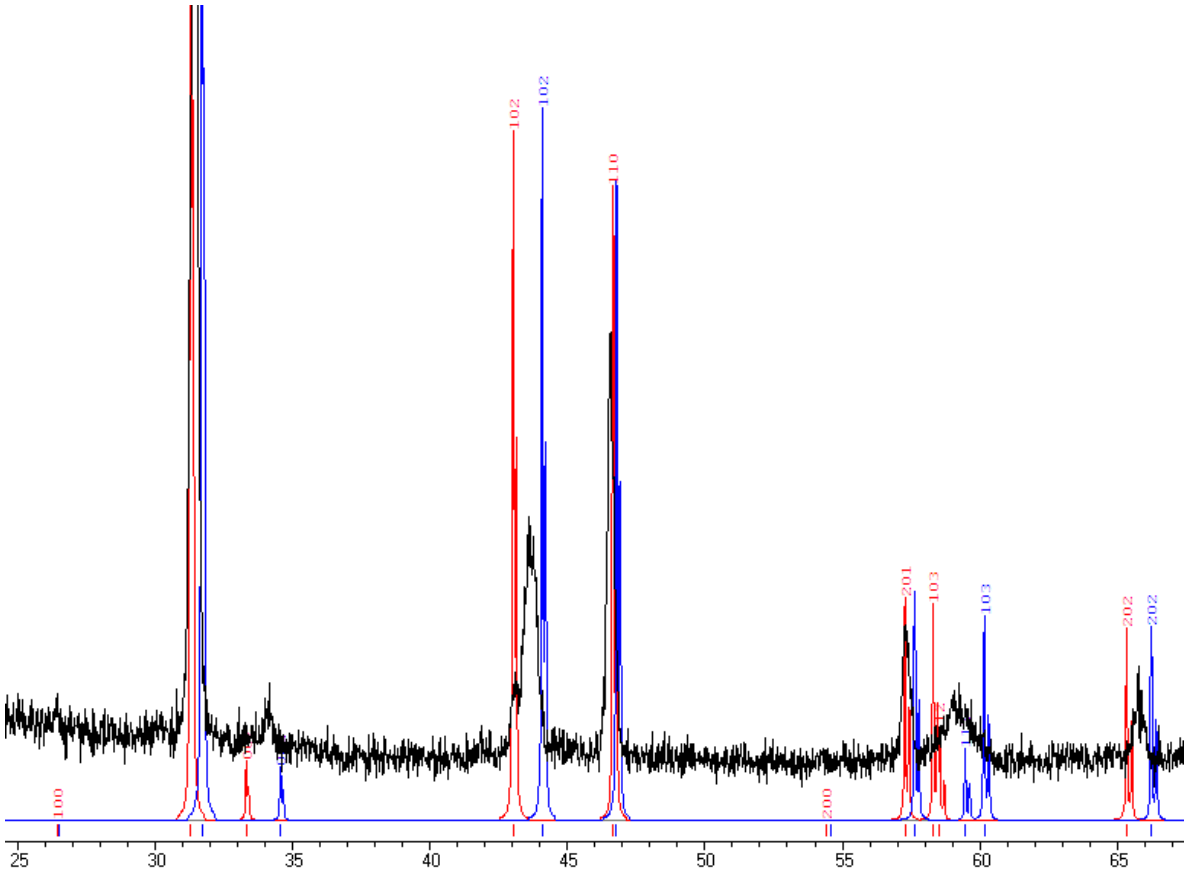

Figure 4-25: Diffraction pattern of '$CoSb_{0.5}Te_{0.5}$' compared with database patterns of CoSb (blue) and CoTe (red). The large differences in 2θ of the (102) and (103) reflections between CoSb and CoTe are clear

The range of composition produced in this reaction could be a result of inadequate mixing of the starting materials. More frequent grindings of the reagents (*e.g.* every 12 hours) may

prove successful in producing a single phase. The use of acetone when grinding, or the use of machinery such as a ball mill may also facilitate improved mixing.

4.2.1.2 Introduction of Te into NiSb ($NiSb_{1-x}Te_x$)

Stoichiometric amounts of nickel(II) oxide, antimony(III) oxide and tellurium(IV) oxide were heated at 450 °C (48 hours), 450 °C (24 hours) for a second and third time, and finally at 500 °C (24 hours) in order to prepare the series $NiSb_{1-x}Te_x$ ($0.25 \leq x \leq 0.75$), with x increasing in increments of 0.25. X-ray powder diffraction patterns were recorded after all reactions over the range $5 \leq 2\theta/° \leq 70$, with a counting time of 1.0 s per step.

Analysis of the x-ray diffraction patterns revealed that an NiAs-type phase had formed in each case. However, the (102) and (103) reflections in the patterns were abnormally wide, in a similar way to that observed in the $CoSb_{1-x}Te_x$ series. Full width at half maximum values for the (102) reflection were in the range 0.3740 to 0.5903. These values are considerably larger than those of the (110) reflection which was in the range 0.2271 to 0.2931. The large widths led to unsuccessful Rietveld refinement of the structures. The (102) and (103) reflections differ the most in 2θ value between NiTe and NiSb. This is comparable to the difference in 2θ values of the (102) and (103) reflections observed in CoTe and CoSb mentioned in the previous section. It is therefore likely that the large width of these reflections is due to the sample containing a range of compositions between NiSb and NiTe. The peak widths did not change between the second and final firings, suggesting that further heating would not result in the synthesis of a single phase. However, heating the samples at a significantly higher temperature may form a single phase, if decomposition does not occur. The range of composition produced in this reaction could be a result of inadequate mixing of the starting materials. More frequent grindings of the reagents (*e.g.* every 12 hours) may prove successful in producing a single phase. The use of acetone when grinding, or the use of machinery such as a ball mill may also facilitate improved mixing.

4.2.2 Transition Metal Site Substitutions

4.2.2.1 Introduction of Ni into CoTe ($Co_{1-x}Ni_xTe$)

Stoichiometric amounts of cobalt(II,III) oxide, nickel(II) oxide and tellurium(IV) oxide were heated at 425 °C (48 hours) and subsequently at 450 °C (24 hours) on three separate occasions in order to prepare the series $Co_{1-x}Ni_xTe$ ($0.25 \leq x \leq 0.75$), with x increasing in increments of 0.25. X-ray powder diffraction patterns were recorded after all reactions over the range $5 \leq 2\theta/° \leq 70$, with a counting time of 1.0 s per step.

Analysis of the x-ray diffraction patterns revealed that an NiAs-type phase had formed in each reaction. However, in the composition where x = 0.75 the nickel telluride $Ni_{2.88}Te_2$ had also formed (weight fraction 0.126(4)) after the initial reaction carried out at 425 °C. Further firings were undertaken to eliminate this phase, but did not alter the product composition. The other compositions in the series were also heated again in an attempt to increase product crystallinity. Rietveld refinement was carried out for all compositions in the series after the final reaction using the structure of NiTe published by Kamat Dalal and Keer as the initial model for the NiAs-type phase.[154] The initial model used for the structure of $Ni_{2.88}Te_2$ was that published by Gulay and Olekseyuk.[155] The Rietveld fit obtained for $Ni_{0.5}Co_{0.5}Te$ is shown in Figure 4-26. Unit cell data obtained from the refinements are given in Table 4-11.

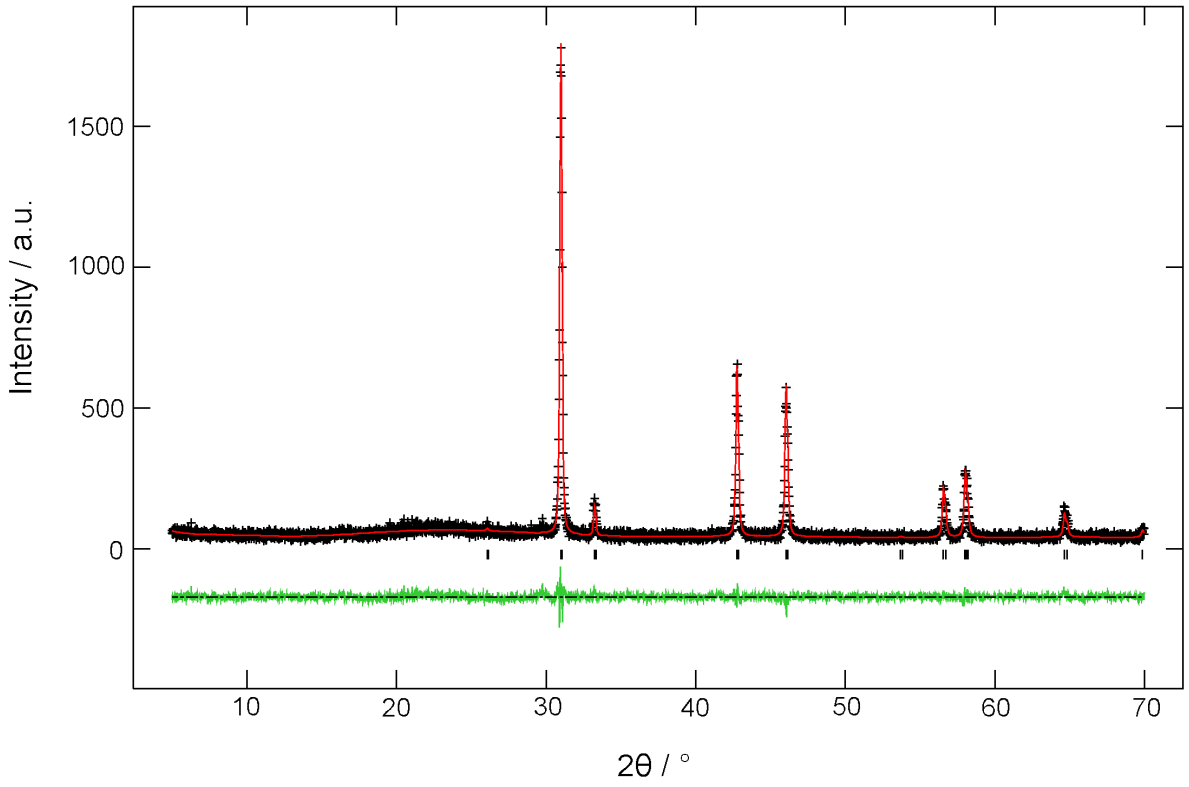

Figure 4-26: Observed (black), calculated (red) and difference (green) x-ray powder diffraction profiles for $Co_{0.5}Ni_{0.5}Te$. Tick marks indicate positions of allowed reflections

Composition	*x*	*a* / Å	*c* / Å	*V* / Å^3	M-Te bond length / Å	Te-Te bond length / Å
CoTe[143]	1	3.890	5.373	70.41	2.617	3.502
$Co_{0.75}Ni_{0.25}Te$	0.25	3.9086(3)	5.3787(5)	71.16(2)	2.6269(2)	3.5107(2)
$Co_{0.5}Ni_{0.5}Te$	0.50	3.9366(3)	5.3785(5)	72.18(2)	2.6408(2)	3.5210(2)
$Co_{0.25}Ni_{0.75}Te$	0.75	3.9515(3)	5.3742(5)	72.67(2)	2.6476(2)	3.5249(2)
NiTe[152]	1	3.965	5.358	72.95	2.652	3.524

Table 4-11: Unit cell data and bond lengths for the series $Co_{1-x}Ni_xTe$

Graphical representations of the unit cell data given in Table 4-11 were prepared and are given in the following figures.

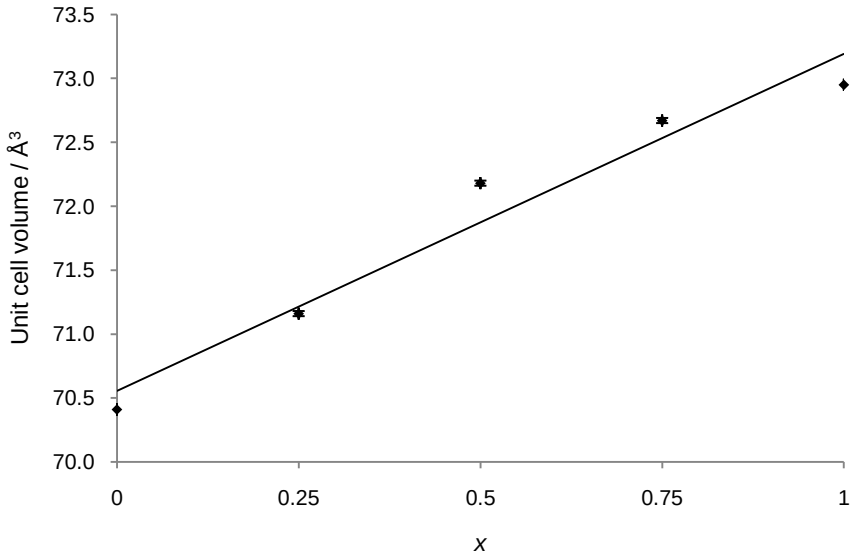

Figure 4-27: Plot of unit cell volume against composition (x) for the series $Co_{1-x}Ni_xTe$

Figure 4-27 demonstrates the variation in unit cell volume with composition. The unit cell volume increases in an almost linear fashion with increasing nickel content. A similar trend was observed in the $Co_{1-x}Ni_xSb$ series. This linear relationship suggests that the solid solution formed over the whole range of miscibility. However, there appears to be a miscibility gap which lies somewhere between $x = 0.5$ and $x = 1.0$, given that attempts to form $Co_{0.25}Ni_{0.75}Te$ did not result in a single phase product. Further experiments to determine the exact values of x where the two phases are immiscible could be performed.

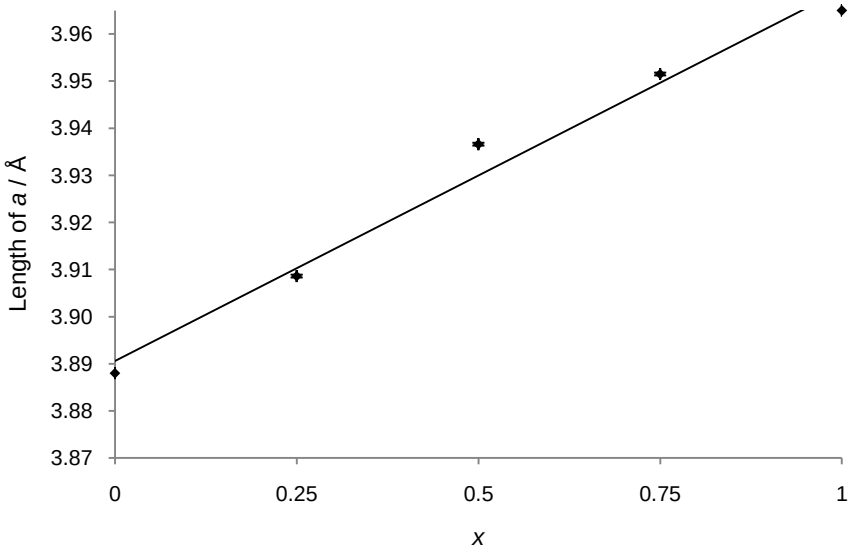

Figure 4-28: Plot of unit cell length *a* against composition (*x*) for the series $Co_{1-x}Ni_xTe$

Figure 4-28 demonstrates the variation in unit cell length *a* with composition. The unit cell length *a* increases in a linear fashion with increasing nickel content; a similar trend is observed in the series $Co_{1-x}Ni_xSb$.

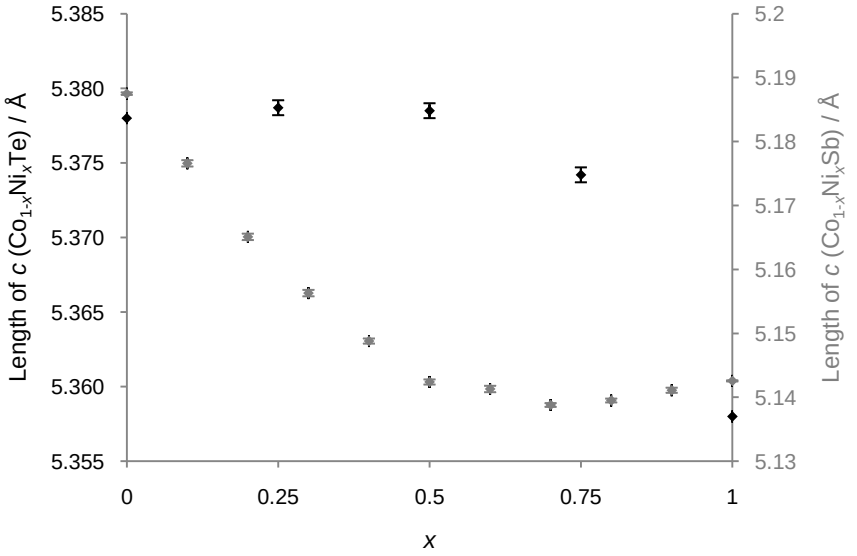

Figure 4-29: Plot of unit cell length *c* against composition (*x*) for the series $Co_{1-x}Ni_xTe$. The plot of unit cell length *c* against composition (*x*) for the series $Co_{1-x}Ni_xSb$ is plotted on the secondary axis and shown in grey for comparison

Figure 4-29 demonstrates the variation in unit cell length *c* with composition. The unit cell length *c* stays constant between $x = 0$ and $x = 0.5$. Between $x = 0.5$ and $x = 1$ the length of *c* decreases. This is a distinctly different trend from that observed in the $Co_{1-x}Ni_xSb$ series; in this series, the length of *c* decreases between values of $x = 0$ and 0.5, and stays relatively constant at values of *x* between 0.5 and 1.0.

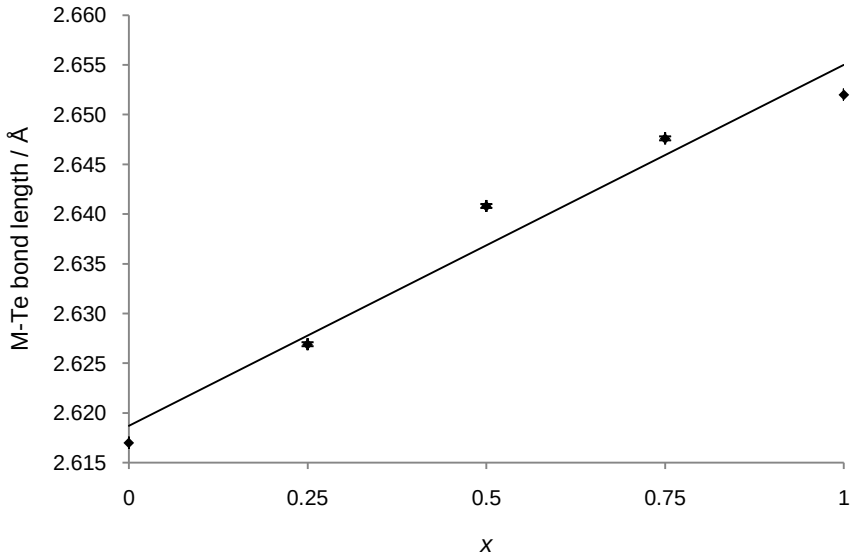

Figure 4-30: Plot of the M-Te bond length against composition (*x*) for the series $Co_{1-x}Ni_xTe$

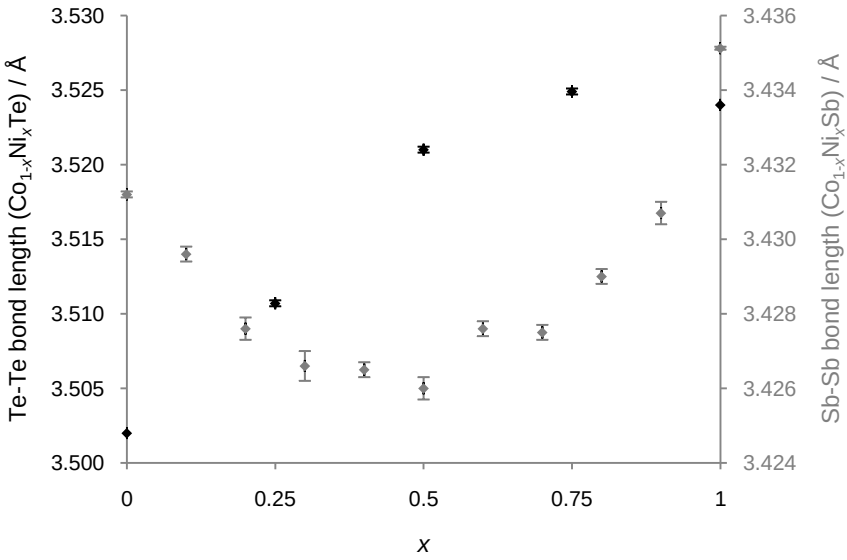

Figure 4-31: Plot of the Te-Te bond length against composition (x) for the series $Co_{1-x}Ni_xTe$. The plot of Sb-Sb bond length for the series $Co_{1-x}Ni_xSb$ is plotted on the secondary axis and shown in grey for comparison

Figure 4-30 and Figure 4-31 demonstrate the variation in M-Te and Te-Te bond lengths in the $Ni_{1-x}Co_xTe$ series with composition. The relationship between M-Te bond length and composition is similar to that observed between the M-Sb bond length and composition in the $Co_{1-x}Ni_xSb$ series: the M-Te bond length increases in a linear fashion with increasing nickel content.

The Te-Te bond length in the $Co_{1-x}Ni_xTe$ series initially increases in a linear fashion until $x = 0.5$, after which the length of the Te-Te bond stays almost constant. This relationship is not unexpected; as the unit cell volume increases, the Te-Te bond length increases. This trend is very different from that observed between the Sb-Sb bond length and composition in the $Co_{1-x}Ni_xSb$ series, where the Sb-Sb bond length initially decreases to a minimum of $x = 0.5$, and subsequently increases. The stark contrast in the metalloid-metalloid bond lengths between the two series is interesting, and is most probably the cause of the different relationships observed between the unit cell length c and composition in the two series. Electronic effects proposed to cause the smooth variation and minimum Sb-Sb bond length observed in the $Co_{1-x}Ni_xSb$ series are not applicable to the analogous telluride compositions.

4.2.2.2 Introduction of Cu into CoTe ($Co_{1-x}Cu_xTe$)

Stoichiometric amounts of cobalt(II,III) oxide, copper(II) oxide and tellurium(IV) oxide were heated at 450 °C (48 hours) and once more at 450 °C (24 hours) in order to prepare the series $Co_{1-x}Cu_xSb$ ($0.1 \leq x \leq 0.2$), with x increasing in increments of 0.1. X-ray powder diffraction patterns were recorded after the final reaction over the range $5 \leq 2\theta/° \leq 70$, with a counting time of 1.0 s per step.

Analysis of the x-ray diffraction patterns indicated that an NiAs-type phase had formed in both samples, in addition to small amounts of various copper tellurides. Rietveld refinement revealed that the lattice parameters of the NiAs-type phase were not significantly different from those of the binary phase CoTe. It can therefore be concluded that copper had not been introduced into the NiAs-type phases. This is not surprising given that CuTe does not crystallise in the NiAs structure. In addition, there have been no previous reports on the synthesis of any compositions in the series.

4.2.2.3 Introduction of Cu into NiTe ($Ni_{1-x}Cu_xTe$)

Stoichiometric amounts of nickel(II) oxide, copper(II) oxide and tellurium(IV) oxide were heated at 450 °C (48 hours) and once more at 450 °C (24 hours) in order to prepare the series $Ni_{1-x}Cu_xSb$ ($0.1 \leq x \leq 0.3$), with x increasing in increments of 0.1. X-ray powder diffraction patterns were recorded after the final reaction over the range $5 \leq 2\theta/° \leq 70$, with a counting time of 1.0 s per step.

Analysis of the x-ray diffraction patterns revealed that the predominant phase formed in each sample was the copper nickel telluride, $Cu_{1.45}Ni_{1.45}Te_2$. No NiAs-type phase was present in any of the samples. This is not unexpected given that CuTe does not crystallise in the NiAs structure. In addition, there have been no previous reports on the synthesis of any compositions in the series.

4.3 Summary

The synthesis of ternary compounds adopting the nickel arsenide structure has been described in this chapter. Ternary transition metal antimonides attempted include $Co_{1-x}Ni_xSb$, $Co_{1-x}Cu_xSb$, $Ni_{1-x}Cu_xSb$ and $Co_{1-x}Fe_xSb$. Only the series $Co_{1-x}Ni_xSb$ displayed

miscibility over the full range of *x*. The series $Ni_{1-x}Cu_xSb$ could be prepared pure with values of *x* up to 0.4; impurities formed when *x* was increased to 0.5. Only compositions where $x = 0.1$ could be synthesised in the $Co_{1-x}Cu_xSb$ and $Co_{1-x}Fe_xSb$ series. To complete this work, further work could include the synthesis of the series $Ni_{1-x}Fe_xSb$.

Ternary transition metal tellurides attempted include $Ni_{1-x}Co_xTe$, $CoSb_{1-x}Te_x$, $NiSb_{1-x}Te_x$, $Co_{1-x}Cu_xTe$ and $Ni_{1-x}Cu_xTe$. None of these series displayed full miscibility over the whole range of *x*. All compositions attempted in the $Ni_{1-x}Co_xTe$ series, apart from where $x = 0.75$, were synthesised in high purity. In both $CoSb_{1-x}Te_x$ and $NiSb_{1-x}Te_x$, NiAs-type phases formed over a range of composition. In $Co_{1-x}Cu_xTe$, NiAs-type phases formed, but were characterised as CoTe due to insignificant differences in lattice parameters. In $Ni_{1-x}Cu_xTe$, a copper nickel telluride formed of an undesired stoichiometry. The unsuccessful copper substitutions are not unexpected given that CuTe does not crystallise in the NiAs structure.

The most striking result in this chapter is the comparison of bond lengths within the $Co_{1-x}Ni_xSb$ and $Co_{1-x}Ni_xTe$ series. The expansion in unit cell volume as nickel is introduced into CoTe, accompanied by lengthening of the M-Te and Te-Te bonds, is expected. The same expansion in unit cell volume is observed in the $Co_{1-x}Ni_xSb$ series, but the variation in bond length is anisotropic: the M-Sb bond length increases across the series, whereas the Sb-Sb bond length initially decreases until $x = 0.5$, and subsequently increases. This could be due to electronic effects discussed earlier, which could be investigated by calculating density of states diagrams.

5.0 Substitutions in Compounds Crystallising with the Skutterudite ($CoAs_3$) Structure

The synthesis of $CoSb_3$ described in section 3.2.2.3 was easily accomplished at temperatures of 425-450 °C. The presence of $CoSb_3$ as an impurity in many other syntheses indicated it was relatively stable. The skutterudite ($CoAs_3$) structure is adopted by all of the Group 9 antimonides, including $CoSb_3$. Increasing the thermoelectric behaviour of skutterudite compounds by filling the empty octants in the structure with loosely bound atoms was described in section 3.2.2. Introducing dopants into the structure to increase the thermoelectric behaviour of the materials was also discussed in this section. This chapter of the thesis describes the attempted synthesis of solid solutions of $RhSb_3$ in $CoSb_3$ and $IrSb_3$ in $CoSb_3$ in an attempt to increase the thermoelectric behaviour of $CoSb_3$; it was proposed that the introduction of large scattering centres (Rh, Ir) into the structure may result in a decrease in the thermal conductivity. The synthesis of other substituted $CoSb_3$ series by introducing transition metals with similar sizes to cobalt, including copper and zinc, into the structure was also carried out. In addition, substitutions of tin and bismuth for antimony were performed, due to the close proximity of these elements in the Periodic Table.

5.1 Transition Metal Site Substitutions

5.1.1 Introduction of Rh into $CoSb_3$ ($Co_{1-x}Rh_xSb_3$)

The $Co_{1-x}Rh_xSb_3$ solid solution has been reported by Wojciechowski, although a miscibility gap was present between $x = 0.2$ and $x = 0.5$.[156] In addition, the presence of satellite reflections in the diffraction pattern of a sample outside of the miscibility gap ($x = 0.18$) was reported, indicating that compositions outside of the miscibility gap may not be pure. Wojciechowski used the traditional synthetic method used to prepare intermetallic compounds of melting elemental reagents to prepare the compositions.[156] It is therefore likely that the compositions in the miscibility gap crystallised as a mixture of phases, rather than as a solid solution. Synthesis of this series by avoiding melting may therefore prove successful in preparing the series over the full range of miscibility. Synthesis of part of the solid solution range ($0.1 \leq x \leq 0.3$) has been recently reported by Harnwunggmoung *et al.*,[157] although these phases contained $CoSb_2$ as an impurity. Synthesis of the $Co_{1-x}Rh_xSb_3$

solid solution over a wide range of composition and without a miscibility gap has therefore not been reported before. Attempted synthesis of the solid solution using the reductive synthetic route is detailed below.

Stoichiometric amounts of cobalt(II,III) oxide, rhodium(III) oxide and antimony(III) oxide were heated using various heating regimes as shown in Table 5-1 in order to prepare the series $Co_{1-x}Rh_xSb_3$ ($0.18 \leq x \leq 0.75$). X-ray powder diffraction patterns were recorded after almost all firings to monitor the progress of the reactions. The patterns were recorded over the range $5 \leq 2\theta/° \leq 70$ with a counting time of 1.0 s per step.

Composition	Firing 1 / °C	Firing 2 / °C	Firing 3 / °C	Firing 4 / °C	Firing 5 / °C	Firing 6 / °C	Firing 7 / °C	Firing 8 / °C	Firing 9 / °C
$Co_{0.82}Rh_{0.18}Sb_3$	425	450	450	500	550	600	600	600	-
$Co_{0.75}Rh_{0.25}Sb_3$	425	450	450	500	550	550	575	600	-
$Co_{0.625}Rh_{0.375}Sb_3$	425	450	450	500	550	600	600	600	-
$Co_{0.5}Rh_{0.5}Sb_3$	425	450	450	500	550	600	600	-	-
$Co_{0.375}Rh_{0.625}Sb_3$	425	450	450	500	550	600	600	600	600
$Co_{0.25}Rh_{0.75}Sb_3$	425	450	450	500	550	600	600	600	-

Table 5-1: Heating regimes for compositions in the $Co_{1-x}Rh_xSb_3$ series. The first firing for all compositions was undertaken for 48 h. All other firings were undertaken for 24 h

Analysis of the x-ray diffraction patterns revealed that in the initial stages of the reaction two separate skutterudite phases formed: a phase with lattice parameters similar to those of $RhSb_3$ (a = 9.2322(6) Å),[49] and another phase with lattice parameters similar to those of $CoSb_3$ (a = 9.0366(2) Å). The two phases will be referred to as the $RhSb_3$-rich phase and the $CoSb_3$-rich phase, and reasons for this will become clear later. Rietveld refinement was carried out for all compositions after most firings using initial models of $CoSb_3$[108] and $RhSb_3$.[49] Metal site occupancies were not refined. Isotropic displacement parameters of cobalt and rhodium were constrained to be equal due to both atoms occupying the same crystallographic site. Profile parameters of the two phases were constrained to be equal given that there were many overlapping reflections between the two skutterudite phases. The Rietveld fit for $Co_{0.5}Rh_{0.5}Sb_3$ is shown in Figure 5-1 and demonstrates the presence of two skutterudite phases after reaction at 450 °C.

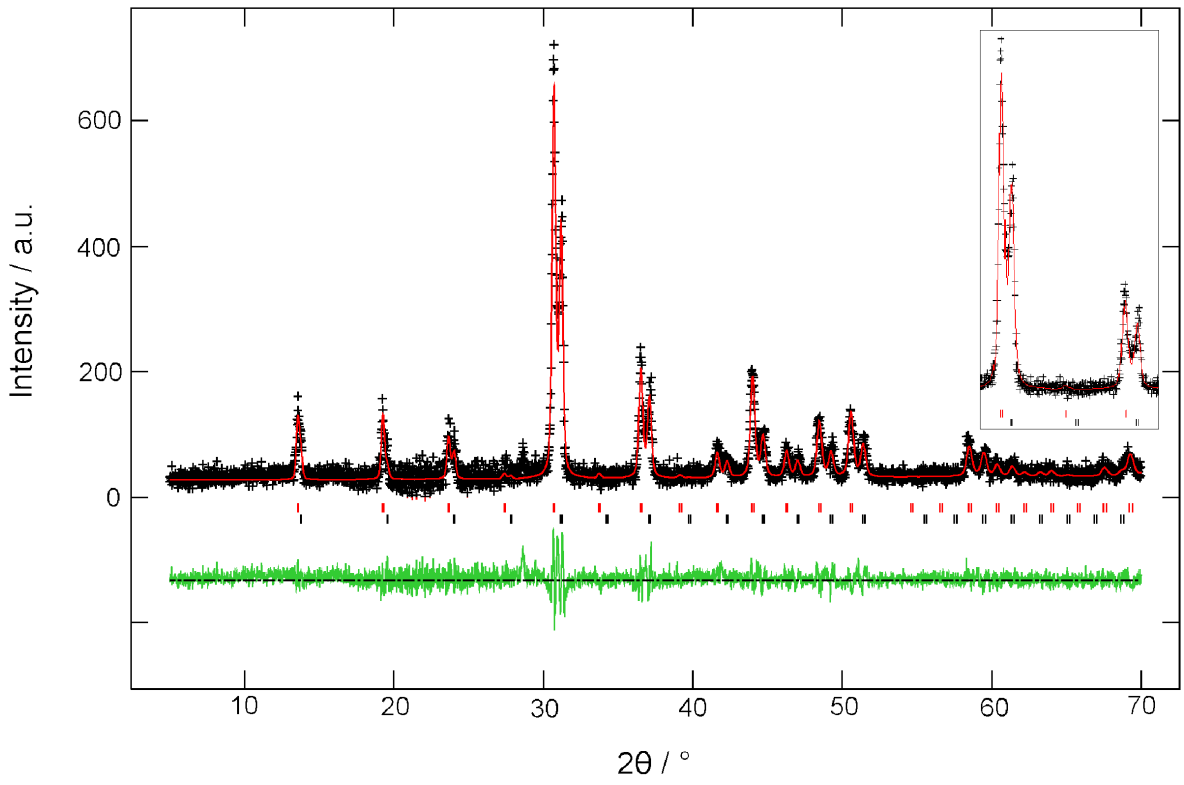

Figure 5-1: Observed (black), calculated (red) and difference (green) x-ray powder diffraction profiles for $Co_{0.5}Rh_{0.5}Sb_3$ after reaction at 450 °C. Lower tick marks indicate positions of allowed reflections for the $CoSb_3$-rich skutterudite phase. Upper tick marks indicate positions of allowed reflections for the $RhSb_3$-rich skutterudite phase. Inset shows an enlarged section of the pattern between approximately $29 \leq 2\theta/° \leq 38$, demonstrating more clearly the two-phase nature of the product

As the temperature of the reactions was increased the mixture approached a single phase product. The lattice parameters of the $RhSb_3$-rich phase gradually decreased and those of the $CoSb_3$-rich phase gradually increased until a single phase product was formed. This indicated that rhodium atoms were diffusing into the $CoSb_3$-rich phase, and cobalt atoms were diffusing into the $RhSb_3$-rich phase. The Rietveld fit for $Co_{0.5}Rh_{0.5}Sb_3$ obtained after the final reaction at 600 °C is shown in Figure 5-2, and demonstrates the single phase nature of the final product.

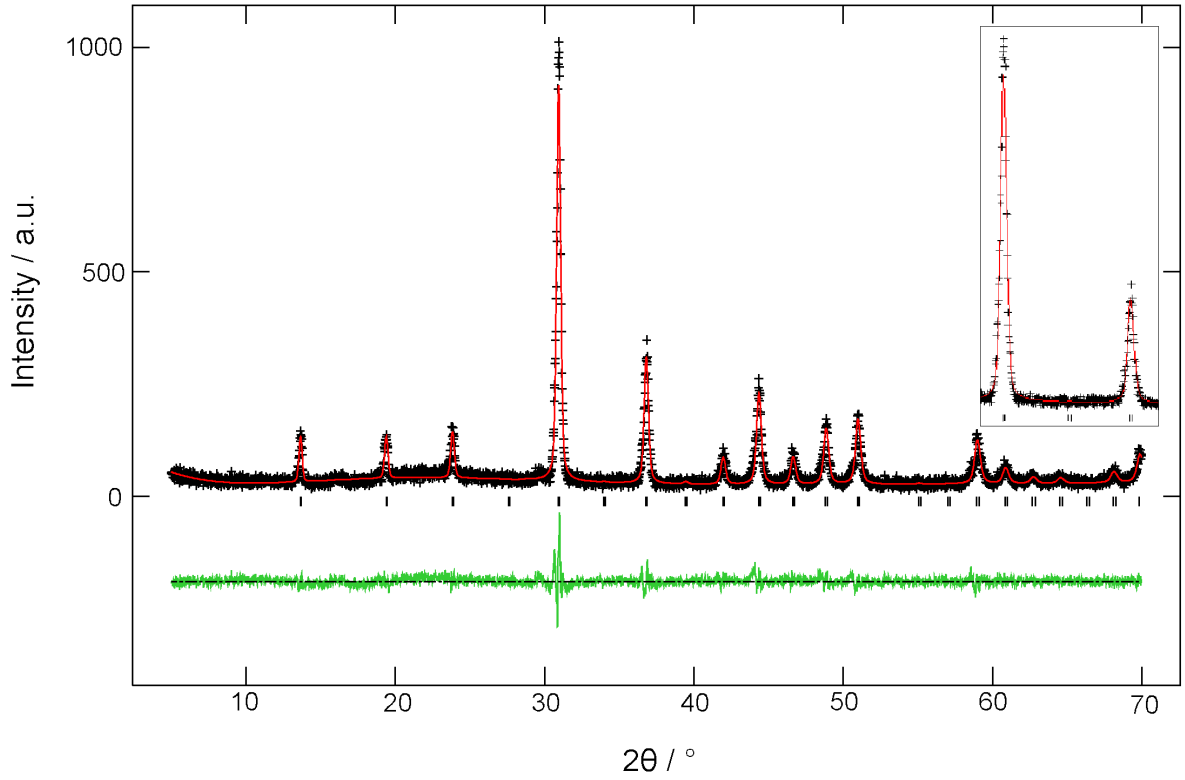

Figure 5-2: Observed (black), calculated (red) and difference (green) x-ray powder diffraction profiles for $Co_{0.5}Rh_{0.5}Sb_3$ after the final reaction at 600 °C. Tick marks indicate positions of allowed reflections. Inset shows an enlarged section of the pattern between approximately $29 \leq 2\theta/° \leq 38$, demonstrating more clearly the single phase nature of the product

No evidence for ordering of cobalt and rhodium in the structure was present in any composition. Selected data from the refinement of $Co_{0.5}Rh_{0.5}Sb_3$ are given in Table 5-2. Crystal data for all other compositions in the series are given in the Appendix.

$Co_{0.5}Rh_{0.5}Sb_3$				
Atomic positions and occupancies	***x***	***y***	***z***	**Occupancy**
Co (8*c*)	¼	¼	¼	0.5
Rh (8*c*)	¼	¼	¼	0.5
Sb (24*g*)	0	0.3361(3)	0.1551(4)	1
Isotropic displacement parameters / Å^2	**Co**	**Rh**		**Sb**
	0.018(3)	0.018(3)		0.019(2)
R(F^2)		0.0839		
χ^2		1.410		

Table 5-2: Selected crystal data from the refinement of $Co_{0.5}Rh_{0.5}Sb_3$

The lattice parameters of compositions with *x* equal to 0.25, 0.5 and 0.75 were monitored after almost every firing. They are given in the following tables and figures, which demonstrate the variation in lattice parameters with reaction progression.

Temperature / °C	*a* ($CoSb_3$-rich phase) / Å	*a* ($RhSb_3$-rich phase) / Å
425	-	-
450	9.039(1)	9.159(1)
450	9.041(2)	9.157(3)
500	9.040(4)	9.155(4)
550	9.047(2)	9.148(3)
550	9.055(2)	9.144(2)
575	9.062(2)	9.102(3)
600	9.074(2)	

Table 5-3: Table demonstrating the variation in the lattice parameters of the $CoSb_3$-rich and $RhSb_3$-rich phases with temperature for $Co_{0.75}Rh_{0.25}Sb_3$

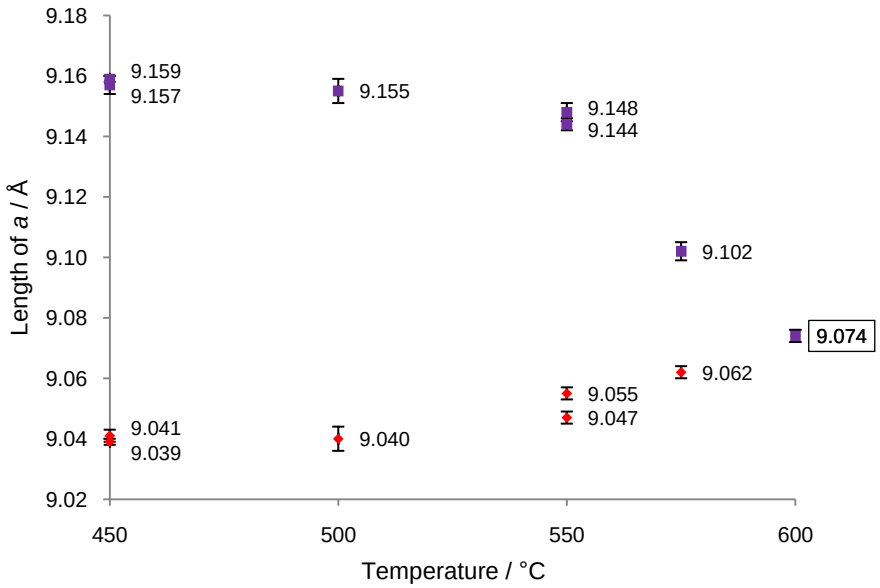

Figure 5-3: Plot demonstrating the variation in the length of *a* of the $CoSb_3$-rich (red) and $RhSb_3$-rich (purple) phases with temperature for $Co_{0.75}Rh_{0.25}Sb_3$

Table 5-3 and Figure 5-3 demonstrate the variation in the length of *a* in the $CoSb_3$-rich phase and the $RhSb_3$-rich phase with reaction progression in $Co_{0.75}Rh_{0.25}Sb_3$. The tendency of the lattice parameters to converge at a value (9.074(2) Å) almost equal to the length of *a*

in $CoSb_3$ plus one quarter of the difference between the lattice parameters of the end members (9.0855 Å) of the series is evident. This suggests that the lattice parameters are dependent on the composition, and that Vegard's law is therefore obeyed.[148]

Temperature / °C	*a* ($CoSb_3$-rich phase) / Å	*a* ($RhSb_3$-rich phase) / Å
425	-	-
450	-	-
450	9.056(3)	9.192(3)
500	9.055(2)	9.186(2)
550	9.076(5)	9.174(5)
600	-	-
600	9.122(2)	

Table 5-4: Table demonstrating the variation in lattice parameters of the $CoSb_3$-rich and $RhSb_3$-rich phases with temperature for $Co_{0.5}Rh_{0.5}Sb_3$

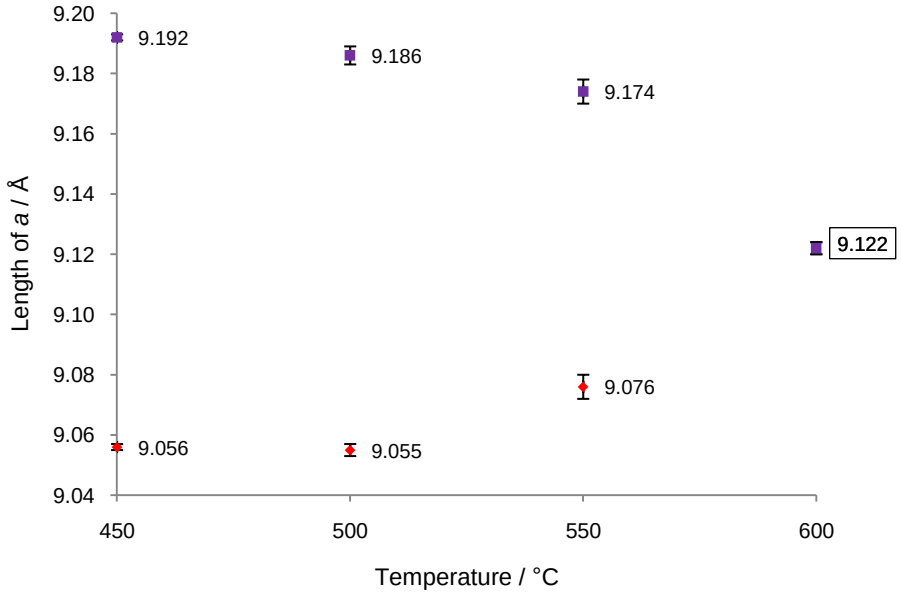

Figure 5-4: Plot demonstrating the variation in the length of *a* of the $CoSb_3$-rich (red) and $RhSb_3$-rich (purple) phases with temperature for $Co_{0.5}Rh_{0.5}Sb_3$

Table 5-4 and Figure 5-4 demonstrate the variation in the length of *a* in the $CoSb_3$-rich phase and the $RhSb_3$-rich phase with reaction progression in $Co_{0.5}Rh_{0.5}Sb_3$. The tendency of the lattice parameters to converge at a value (9.122(2) Å) almost equal to the length of *a* in $CoSb_3$ plus one half of the difference between the lattice parameters of the end members

(9.1344 Å) of the series is evident. This suggests that the lattice parameters are dependent on the composition, and that Vegard's law is therefore obeyed.[148]

Temperature / °C	*a* ($CoSb_3$-rich phase) / Å	*a* ($RhSb_3$-rich phase) / Å
425	-	-
450	-	-
450	9.053(1)	9.2164(8)
500	9.054(1)	9.213(1)
550	9.076(2)	9.1994(8)
600	9.151(2)	9.194(2)
600	9.166(2)	9.202(2)
600	9.175(1)	

Table 5-5: Table demonstrating the variation in lattice parameters of the $CoSb_3$-rich and $RhSb_3$-rich phases with temperature for $Co_{0.25}Rh_{0.75}Sb_3$

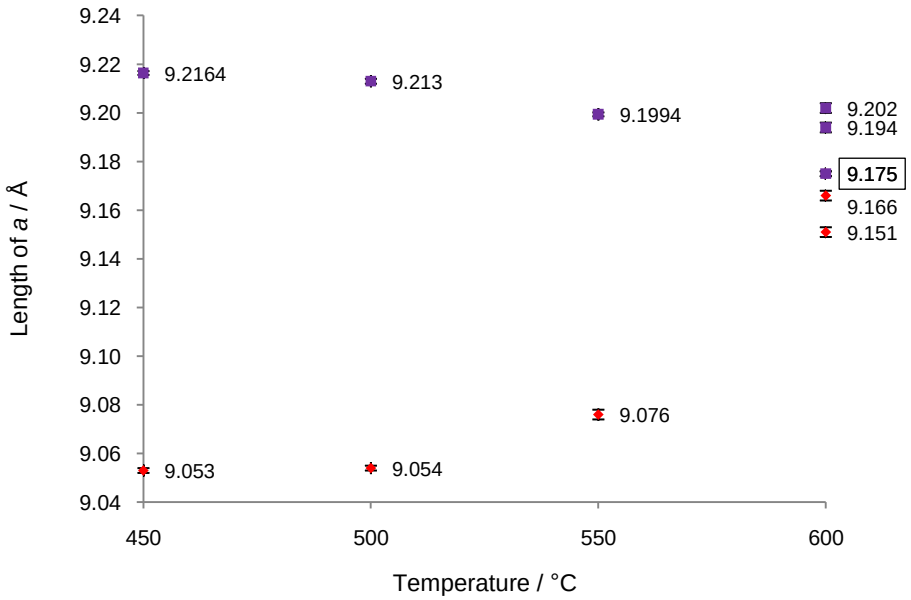

Figure 5-5: Plot demonstrating the variation in the length of *a* of the $CoSb_3$-rich (red) and $RhSb_3$-rich (purple) phases with temperature for $Co_{0.25}Rh_{0.75}Sb_3$

Table 5-5 and Figure 5-5 demonstrate the variation in the length of *a* in the $CoSb_3$-rich phase and the $RhSb_3$-rich phase with reaction progression in $Co_{0.25}Rh_{0.75}Sb_3$. The tendency of the lattice parameters to converge at a value (9.175(1) Å) almost equal to the length of *a* in $CoSb_3$ plus three quarters of the difference between the lattice parameters of the end

members (9.1833 Å) of the series is evident. This suggests that the lattice parameters are dependent on the composition, and that Vegard's law is therefore obeyed.[148]

Plots showing the variation in the length of *a* with reaction progression for all compositions monitored demonstrate the respective decrease and increase in the length of *a* of the $RhSb_3$-rich and $CoSb_3$-rich phases with reaction progression. Final lattice parameters for the single skutterudite phase formed in each composition are given in Table 5-6.

Composition	*x*	*a* / Å	*V* / Å^3
$CoSb_3$	0	9.0366(2)	737.92(5)
$Co_{0.82}Rh_{0.18}Sb_3$	0.18	9.066(1)	745.1(3)
$Co_{0.75}Rh_{0.25}Sb_3$	0.25	9.074(2)	747.1(4)
$Co_{0.625}Rh_{0.375}Sb_3$	0.375	9.1100(6)	756.1(2)
$Co_{0.5}Rh_{0.5}Sb_3$	0.5	9.122(2)	759.0(5)
$Co_{0.375}Rh_{0.625}Sb_3$	0.625	9.148(1)	765.6(3)
$Co_{0.25}Rh_{0.75}Sb_3$	0.75	9.175(1)	772.4(3)

Table 5-6: Unit cell data for the $Co_{1-x}Rh_xSb_3$ series

The data given in Table 5-6 are shown graphically in Figure 5-6, which visually demonstrates the variation in unit cell volume with composition in the $Co_{1-x}Rh_xSb_3$ series.

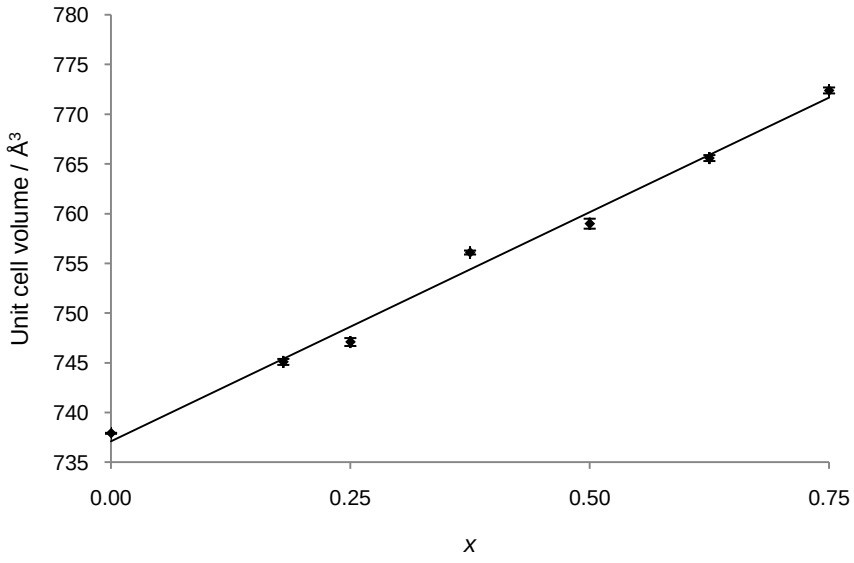

Figure 5-6: Plot of unit cell volume against composition (*x*) for the $Co_{1-x}Rh_xSb_3$ series

Figure 5-6 shows that there is a linear relationship between the unit cell volume and composition in the $Co_{1-x}Rh_xSb_3$ solid solution. This linear increase in unit cell volume with increasing rhodium content obeys Vegard's Law,[148] and therefore demonstrates the successful synthesis of the $Co_{1-x}Rh_xSb_3$ solid solution without a miscibility gap in the range examined ($0.18 \leq x \leq 0.75$). The composition where $x = 0.18$ lies almost exactly on the linear trendline. This, in addition to the absence of satellite reflections in the diffraction pattern (shown in Figure 5-7) suggests that the reductive synthesis of this composition allows for the production of a single phase compound, unlike the synthetic route employed by Wojciechowski.[156]

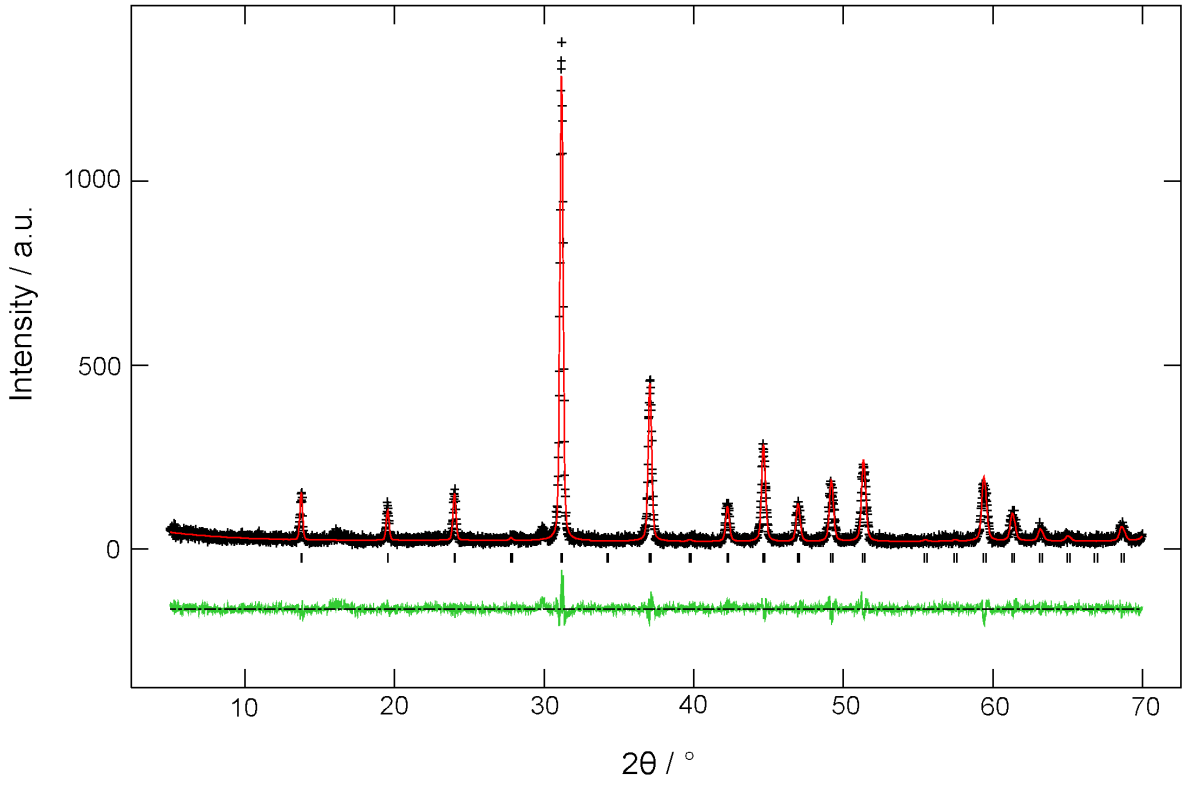

Figure 5-7: Observed (black), calculated (red) and difference (green) x-ray powder diffraction profiles for $Co_{0.82}Rh_{0.18}Sb_3$. Tick marks indicate positions of allowed reflections

In summary, the $Co_{1-x}Rh_xSb_3$ solid solution has been synthesised over the range $0.18 \leq x \leq 0.75$, without evidence of a miscibility gap. This is in stark contrast to the results presented by Wojciechowski,[156] and demonstrates that the miscibility gap reported was a result of the synthetic method used. Measurements of the thermoelectric power of the compositions in this series should be carried out in order to determine whether the

introduction of rhodium into $CoSb_3$ has resulted in an increase in the thermoelectric power, as predicted. However, time constraints and the lack of availability of equipment have prevented collection of these data prior to submission of this work. Measurements are currently underway at Heriot-Watt University, and a paper describing the synthesis of the series and the thermoelectric behaviour of the compositions is in preparation.

5.1.2 Introduction of Ir into $CoSb_3$ ($Co_{1-x}Ir_xSb_3$)

A brief report of the attempted synthesis of the solid solution of $IrSb_3$ in $CoSb_3$ has been published previously, although no x-ray diffraction patterns were included in the report.[158] In addition, only a partial solid solution was prepared: the existence of a miscibility gap between $x = 0.36$ and $x = 0.80$ was reported.[158] Although both $CoSb_3$ and $IrSb_3$ melt incongruently, the miscibility gap cannot be a result of this given that the synthetic method employed (hot pressing of elemental powders) did not involve melting of the materials. Given that the solid solution of $RhSb_3$ in $CoSb_3$ was relatively easy to prepare over the full range of miscibility, preparation of the solid solution of $IrSb_3$ in $CoSb_3$ is also likely to be easy to prepare, given that rhodium and iridium have relatively similar sizes as a result of the lanthanide contraction. Attempts at preparing the solid solution over the range $0.25 \leq x \leq 0.75$ using the reductive synthetic route are described below.

Stoichiometric amounts of cobalt(II,III) oxide, iridium(IV) oxide and antimony(III) oxide were heated using various heating regimes as shown in Table 5-7 in order to prepare the series $Co_{1-x}Ir_xSb_3$ ($0.25 \leq x \leq 0.75$), with x increasing in increments of 0.25. X-ray powder diffraction patterns were recorded after almost all firings to monitor the progress of the reactions. The patterns were recorded over the range $5 \leq 2\theta/° \leq 70$ with a counting time of 1.0 s per step. The composition $Co_{0.75}Ir_{0.25}Sb_3$ was prepared initially. This reaction was used as a 'test' to determine the ease of reduction of iridium(IV) oxide. The temperature between firings was therefore increased gradually. This set of reactions indicated that very little changed between temperatures of 425 and 550 °C. The heating regime for subsequent compositions in the series was then modified accordingly.

Composition	$Co_{0.75}Ir_{0.25}Sb_3$	$Co_{0.5}Ir_{0.5}Sb_3$	$Co_{0.25}Ir_{0.75}Sb_3$
Firing 1 / °C	425	400	400
Firing 2 / °C	450	550	550
Firing 3 / °C	450	600	600
Firing 4 / °C	500	600	600
Firing 5 / °C	550	650	650
Firing 6 / °C	600	650	650
Firing 7 / °C	650	725	700
Firing 8 / °C	700	750	-
Firing 9 / °C	750	-	-
Firing 10 / °C	750	-	-
Firing 11 / °C	750	-	-

Table 5-7: Heating regimes for compositions in the $Co_{1-x}Ir_xSb_3$ series. The first firing for all compositions was undertaken for 48 h. All other firings were undertaken for 24 h

For $Co_{0.75}Ir_{0.25}Sb_3$, reaction at 425 °C resulted in a mixture of two skutterudite phases, which were determined to be $CoSb_3$ and $IrSb_3$, in addition to a small amount of elemental antimony (3.6(4)% by weight). Reaction at higher temperature resulted in either sublimation or reaction of the antimony, and after reaction at 550 °C there was no elemental antimony remaining in the product. Lattice parameters of the skutterudite phases were not significantly different from those of $CoSb_3$ and $IrSb_3$ at this point. Reaction at higher temperature resulted in a slight increase in the lattice parameter of $CoSb_3$. By reaction at 750 °C the lattice parameter of the $CoSb_3$ phase had changed from 9.0365(7) (at 425 °C) to 9.0923(9) Å. However, the lattice parameter of $IrSb_3$ stayed relatively constant. This indicated that there was some diffusion of iridium into $CoSb_3$, but no diffusion of cobalt into $IrSb_3$. This was possibly accompanied by loss of antimony. A plot of lattice parameter against reaction progression is shown in Figure 5-8 to demonstrate this.

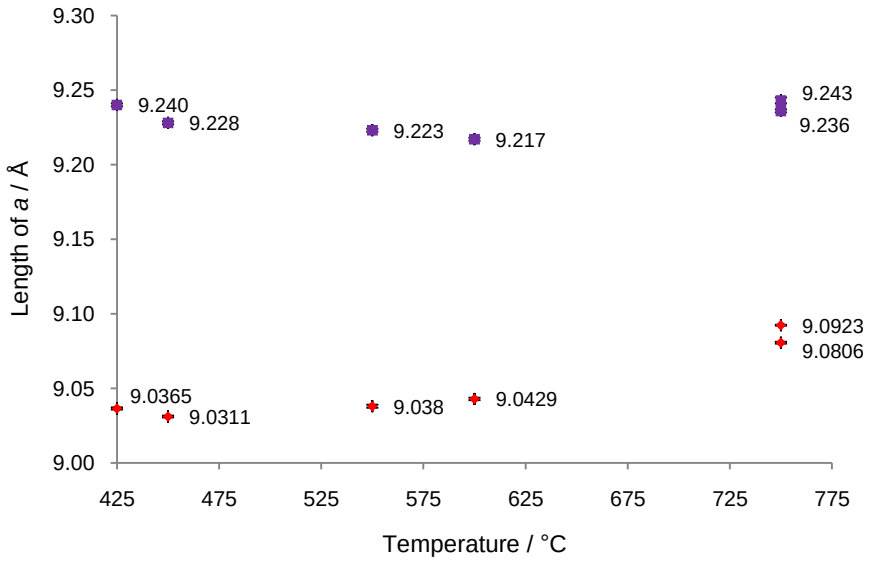

Figure 5-8: Plot demonstrating the variation in the length of *a* of the $CoSb_3$ (red) and $IrSb_3$ (purple) phases with temperature for $Co_{0.75}Ir_{0.25}Sb_3$

The temperature was not increased beyond 750 °C as after the second reaction at this temperature a small amount of $CoSb_2$ appeared in the diffraction pattern, indicating that $CoSb_3$ was not stable at this temperature. Consequently, it was not necessary to undertake further reactions. It can therefore be concluded that the solid solution with the composition $Co_{0.75}Ir_{0.25}Sb_3$ cannot be prepared using this synthetic route.

For the compositions $Co_{0.5}Ir_{0.5}Sb$ and $Co_{0.25}Ir_{0.75}Sb_3$, a similar progression in lattice parameters occurred: the lattice parameters of the $IrSb_3$-rich phase changed very little, whereas the lattice parameters of the $CoSb_3$-rich phase altered quite significantly. This is shown in Figure 5-9 for $Co_{0.5}Ir_{0.5}Sb_3$ and in Figure 5-10 for $Co_{0.25}Ir_{0.75}Sb_3$.

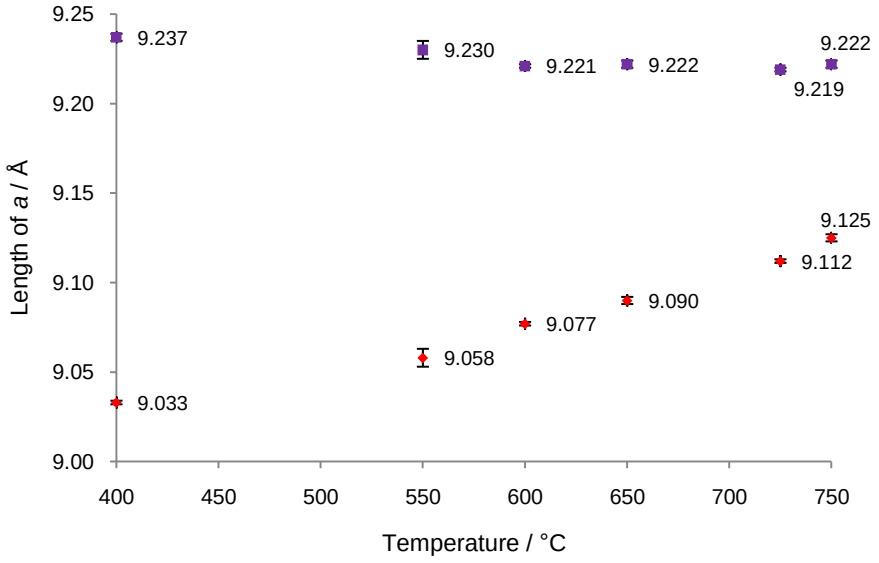

Figure 5-9: Plot demonstrating the variation in the length of *a* of the $CoSb_3$ (red) and $IrSb_3$ (purple) phases with temperature for $Co_{0.5}Ir_{0.5}Sb_3$

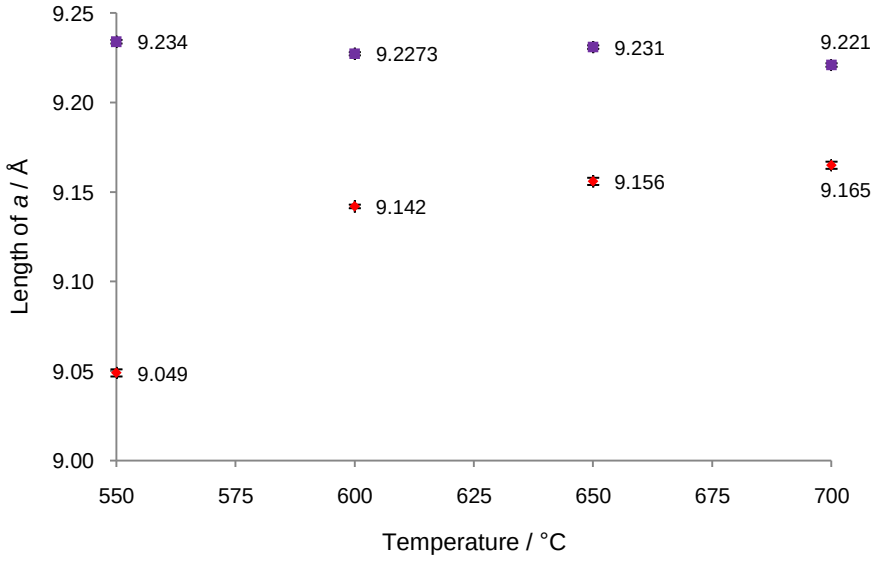

Figure 5-10: Plot demonstrating the variation in the length of *a* of the $CoSb_3$ (red) and $IrSb_3$ (purple) phases with temperature for $Co_{0.25}Ir_{0.75}Sb_3$

Using Vegard's law the amount of iridium introduced into the $CoSb_3$-rich phase in each composition can be calculated. The lattice parameter of $IrSb_3$ was required in order to do this, and so this was taken from the literature (9.2533 Å).[49] The calculated stoichiometries

of the $CoSb_3$-rich phase for compositions where x = 0.25, 0.5 and 0.75 were $Co_{0.74}Ir_{0.26}Sb_3$, $Co_{0.59}Ir_{0.41}Sb_3$ and $Co_{0.41}Ir_{0.59}Sb_3$, respectively. Calculation of the $Co_{0.74}Ir_{0.26}Sb_3$ stoichiometry for x = 0.25 suggests that this composition has been made pure. However, the presence of a small amount of $IrSb_3$ (4.3(3)% by weight) still remaining in the product indicates that this is not the case.

It is unexpected that diffusion of iridium atoms into $CoSb_3$ is observed, but diffusion of cobalt atoms into $IrSb_3$ is not observed. Given that cobalt atoms are smaller and lighter than iridium atoms, the reverse trend might be expected. The lack of diffusion of cobalt atoms into $IrSb_3$ appears to be the reason for the reluctance of formation of the solid solution. The formation of $Co_{1-x}Rh_xSb_3$ and the lack of formation of $Co_{1-x}Ir_xSb_3$ is likely to be a result of the difference in size between elemental rhodium and elemental iridium: although the lanthanide contraction results in similar atomic radii of elements in the second and third rows of the *d*-block, the Rh-Rh distance (2.5392 Å)[159] is slightly shorter than the Ir-Ir distance (2.7149 Å).[160] Shi *et al.* calculated phase diagrams for the then theoretical solid solutions of $RhSb_3$ and $IrSb_3$ in $CoSb_3$, and determined that the solubility of $RhSb_3$ and $IrSb_3$ in $CoSb_3$ would be very limited.[161] The work described here demonstrates that this is not the case. Although not carried out, syntheses undertaken at 450 °C strongly suggest that pure $IrSb_3$ could be prepared using this method. In terms of further work, the possibility of a solid solution of $IrSb_3$ in $RhSb_3$ could be explored, and according to Fleurial *et al.* this solid solution exists over the full range of miscibility.[162]

5.1.3 Introduction of Cu into $CoSb_3$ ($Co_{1-x}Cu_xSb_3$)

Stoichiometric amounts of cobalt(II,III) oxide, copper(II) oxide and antimony(III) oxide were heated at 425 °C (48 hours) and subsequently at 450 °C (24 hours) in order to prepare the series $Co_{1-x}Cu_xSb_3$ ($0.1 \leq x \leq 0.3$), with x increasing in increments of 0.1. X-ray powder diffraction patterns were recorded after the final reaction over the range $5 \leq 2\theta/° \leq 70$, with a counting time of 1.0 s per step.

Analysis of the x-ray diffraction patterns revealed that in each case various amounts of a skutterudite phase, Cu_2Sb and elemental antimony had formed. The lattice parameters of the skutterudite phases were not significantly different from those of $CoSb_3$, indicating that

copper had not been introduced into the $CoSb_3$ structure. This is not surprising when considering that $CuSb_3$ is not a known compound.

5.1.4 Introduction of Zn into $CoSb_3$ ($Co_{1-x}Zn_xSb_3$)

Stoichiometric amounts of cobalt(II,III) oxide, zinc(II) oxide and antimony(III) oxide were heated at 425 °C (48 hours) in order to prepare the series $Co_{1-x}Zn_xSb_3$ ($0.1 \leq x \leq 0.3$), with x increasing in increments of 0.1. X-ray powder diffraction patterns were recorded after the final reaction over the range $5 \leq 2\theta/° \leq 70$, with a counting time of 1.0 s per step.

Analysis of the x-ray diffraction patterns revealed that in each case various amounts of a skutterudite phase and elemental antimony had formed. In all cases the starting material zinc(II) oxide remained in the sample. The lattice parameters of the skutterudite phases were not significantly different from those of $CoSb_3$, indicating that zinc had not been introduced into the $CoSb_3$ structure. This is not surprising given that zinc(II) oxide is difficult to reduce (discussed in section 3.6).

5.2 Attempted Synthesis of the Isoelectronic Phase, $Fe_{0.5}Ni_{0.5}Sb_3$

$Fe_{0.5}Ni_{0.5}Sb_3$ is isoelectronic and isostructural with respect to $CoSb_3$. It was originally synthesised by Kjekshus and Rakke in 1970.[163] The attempted reductive synthesis of this phase is described below.

Stoichiometric amounts of iron(III) oxide, nickel(II) oxide and antimony(III) oxide were heated at 425 °C (48 hours) and subsequently at 450 °C (24 hours). An x-ray powder diffraction pattern was recorded after the final reaction over the range $5 \leq 2\theta/° \leq 70$, with a counting time of 1.0 s per step.

Analysis of the x-ray diffraction pattern revealed that no skutterudite phase had formed. The mixture contained many phases including various nickel antimonides, the oxide precursor to $FeSb_2$ ($FeSb_2O_4$), and unreacted Sb_2O_3. It is likely that a skutterudite phase did not form due to the facile synthesis of the reaction products, in particular NiSb.

5.3 Metalloid Site Substitutions

5.3.1 Introduction of Sn into $CoSb_3$ ($CoSb_{3-x}Sn_x$)

Stoichiometric amounts of cobalt(II,III) oxide, antimony(III) oxide and tin(II) oxide were heated at 425 °C (48 hours) and subsequently at 450 °C (24 hours) in order to prepare the series $CoSb_{3-x}Sn_x$ ($0.25 \leq x \leq 1$). X-ray powder diffraction patterns were recorded after the final reaction over the range $5 \leq 2\theta/° \leq 70$, with a counting time of 1.0 s per step.

Analysis of the diffraction patterns revealed that a skutterudite phase was present in each sample, in addition to various amounts of Co_2SnO_4 and other unidentifiable impurities. Rietveld refinement was carried out for all compositions using the structure of $CoSb_3$ published by Xue *et al.* as the initial model.[108] Unit cell data of the skutterudite phases obtained from the refinements are given in Table 5-8.

Composition	x	a / Å	V / Å^3
$CoSb_3$	0	9.0366(2)	737.92(5)
$CoSb_{2.75}Sn_{0.25}$	0.25	9.0440(6)	739.7(1)
$CoSb_{2.5}Sn_{0.5}$	0.5	9.0480(7)	740.7(2)
$CoSb_2Sn$	0.75	9.044(2)	739.8(5)

Table 5-8: Unit cell data for the $CoSb_{3-x}Sn_x$ series

The unit cell volume of the skutterudite phase was plotted against composition in Figure 5-11.

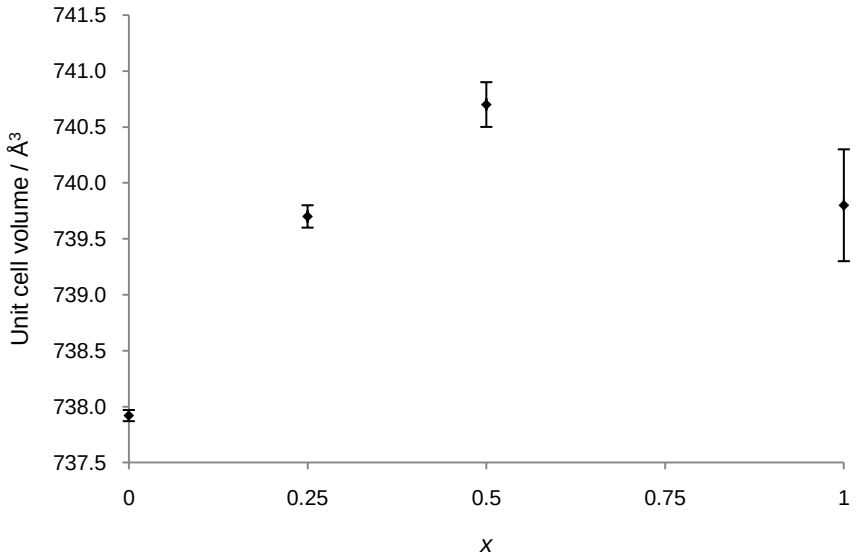

Figure 5-11: Plot of unit cell volume against composition (x) for the $CoSb_{3-x}Sn_x$ series

Figure 5-11 demonstrates an initial increase in unit cell volume as tin is introduced into the system. The point at $x = 1$ has a large standard deviation, and taking this into account, the unit cell volume differs very little between $x = 0.5$ and $x = 1$. Although the unit cell volume initially increases as x increases, the presence of impurities in the diffraction patterns suggests that the full amount of tin has not been introduced into the $CoSb_3$ structure.

The refinements were carried out with cobalt and antimony located on the 8*c* and 24*g* Wyckoff positions, respectively; tin was not included in the refinements. Given that the $CoSb_3$ structure has been "stuffed" with tin previously,[100] and no previous substitutions on the antimony site have been reported, it is difficult to say whether the tin is filling the empty octants in $CoSb_3$, or whether it has replaced some of the antimony in the structure. Fourier difference maps were therefore calculated, and demonstrated that there is no unmodelled electron density on the 2*a* site in $CoSb_3$ (0, 0, 0) where the tin atoms are located in the stuffed structure. It can therefore be concluded that tin has been introduced onto the antimony site in $CoSb_3$ rather than in the empty octants. However, it is not possible to state the degree of inclusion, given the similar x-ray scattering factors of tin and antimony. Neutron diffraction may prove more useful in determining the amount of tin introduced into the $CoSb_3$ structure.

5.3.2 Introduction of Bi into $CoSb_3$ ($CoSb_{3-x}Bi_x$)

Stoichiometric amounts of cobalt(II,III) oxide, antimony(III) oxide and bismuth(III) oxide were heated at 425 °C (48 hours) and subsequently at 450 °C (24 hours) in order to prepare the two compositions $CoSb_{2.5}Bi_{0.5}$ and $CoSb_2Bi$. X-ray powder diffraction patterns were recorded after the final reaction over the range $5 \leq 2\theta/° \leq 70$, with a counting time of 1.0 s per step.

Analysis of the x-ray diffraction patterns revealed that a mixture of a skutterudite phase, $CoSb_2$ and elemental bismuth had formed in the reaction carried out to form $CoSb_{2.5}Bi_{0.5}$. In the reaction carried out to prepare $CoSb_2Bi$, a mixture of $CoSb_2$ and elemental bismuth formed. It is likely that these reactions were unsuccessful due to the difference in size between bismuth and antimony, and also the ease of reduction of bismuth(III) oxide. Bismuth is in the same group of the Periodic Table as antimony, but lies one period below. Bismuth therefore has one extra *p*- and *d*-shell of electrons as well as an additional *f*-shell from the lanthanides, and therefore has a larger atomic radius. It is likely that the skutterudite structure cannot accommodate such a large atom in place of antimony.

5.4 Summary

In this chapter, synthesis of the $Co_{1-x}Rh_xSb_3$ and $Co_{1-x}Ir_xSb_3$ solid solutions has been described. In addition, the substitution of copper and zinc for cobalt was attempted, as well as the synthesis of the isoelectronic phase, $Fe_{0.5}Ni_{0.5}Sb_3$. Substitutions on the metalloid site were attempted with tin and bismuth.

The solid solution $Co_{1-x}Rh_xSb_3$ formed over the whole range of miscibility attempted ($0.18 \leq x \leq 0.75$). This series has not been reported over this range of miscibility previously. In contrast, the solid solution of $IrSb_3$ in $CoSb_3$ could not be prepared in high purity using this synthetic route. However, there is good evidence for $CoSb_3$ accepting Ir with concomitant growth in unit cell volume. Approximate compositions of the $CoSb_3$-rich phases obtained were $Co_{0.74}Ir_{0.26}Sb_3$, $Co_{0.59}Ir_{0.41}Sb_3$ and $Co_{0.41}Ir_{0.59}Sb_3$. It is likely that the formation of high purity $Co_{1-x}Rh_xSb_3$ and the lack of formation of high purity $Co_{1-x}Ir_xSb_3$ is a result of the larger atomic size of iridium with respect to rhodium.

Substitutions of copper and zinc for cobalt were not successful; lattice parameters of the skutterudite phase were not significantly different from those of $CoSb_3$. In addition, synthesis of the isoelectronic phase $Fe_{0.5}Ni_{0.5}Sb_3$ was unsuccessful.

Reactions carried out to introduce tin onto the antimony site in $CoSb_3$ were successful, although the amount of tin introduced into the structure is unknown. Attempts to introduce bismuth into the $CoSb_3$ structure were unsuccessful; it is likely that this was a result of the large size of bismuth, and the ease of reduction of bismuth(III) oxide.

6.0 Substitutions in Cu_2Sb

The synthesis of Cu_2Sb described in section 3.2.4.2 was easily accomplished at temperatures of 400 – 425 °C. Its presence as an impurity in many other syntheses indicated it was relatively stable. Substitutions in Cu_2Sb were attempted in order to prepare new phases in the Cu_2Sb system. Substitutions were carried out on both the transition metal site and the metalloid site, and included substituting manganese, iron, cobalt, nickel and silver for copper, and tellurium for antimony. The substitution of manganese for copper was attempted as Mn_2Sb (*anti*-PbFCl structure) is a known phase. Iron, cobalt and nickel were introduced into the structure due to their similar sizes with respect to copper. The introduction of silver in place of copper was attempted as silver has the same number of valence electrons as copper. Finally, the substitution of tellurium for antimony was carried out due to the similar sizes of the two metalloids.

6.1 Transition Metal Site Substitutions

6.1.1 Introduction of Mn into Cu_2Sb ($Cu_{2-x}Mn_xSb$)

Stoichiometric amounts of copper(II) oxide, manganese(II) nitrate tetrahydrate and antimony(III) oxide were heated at 425 °C (48 hours) and subsequently at 450 °C (24 hours) in order to form the compositions $Cu_{1.75}Mn_{0.25}Sb$ and $Cu_{1.5}Mn_{0.5}Sb$. X-ray powder diffraction patterns were recorded after the final reaction over the range $5 \leq 2\theta/° \leq 70$, with a counting time of 1.0 s per step.

Analysis of the diffraction patterns indicated that in both cases a mixture of Cu_2Sb, MnO and elemental antimony had formed. The lattice parameters of the Cu_2Sb-type phase were not significantly different from those of Cu_2Sb, indicating that manganese had not been introduced into the structure. The formation of MnO is likely to be a result of the d^5 electron configuration of the Mn^{2+} ion. It is likely that a solid solution of Mn_2Sb in Cu_2Sb could be formed using a route which avoids the reduction of MnO, as Mn_2Sb adopts the same structure,[51] although this solid solution has not been previously reported in the literature.

6.1.2 Introduction of Fe into Cu_2Sb ($Cu_{2-x}Fe_xSb$)

Stoichiometric amounts of copper(II) oxide, iron(III) oxide and antimony(III) oxide were heated at 425 °C (48 hours) and subsequently at 450 °C (24 hours) in order to prepare the compositions $Cu_{1.75}Fe_{0.25}Sb$ and CuFeSb. X-ray powder diffraction patterns were recorded after the final reaction over the range $5 \leq 2\theta/° \leq 70$, with a counting time of 1.0 s per step.

Analysis of the diffraction patterns indicated that a Cu_2Sb-type phase, various iron oxides and unreacted Sb_2O_3 were present in the product of the reaction carried out to prepare $Cu_{1.75}Fe_{0.25}Sb$. A mixture of a Cu_2Sb-type phase, FeSb, Fe_3O_4 and elemental antimony was present in the product of the reaction carried out to prepare CuFeSb. The lattice parameters of the Cu_2Sb-type phase formed in both reactions were not significantly different from those of Cu_2Sb, indicating that iron had not been introduced into the Cu_2Sb structure. However, it is possible that smaller amounts of iron (*e.g.* $x \leq 0.1$) may be able to be introduced into the Cu_2Sb structure, although there have been no previous reports of this in the literature. In addition, there is no known 2:1 iron antimonide which adopts the *anti*-PbFCl structure.

6.1.3 Introduction of Co into Cu_2Sb ($Cu_{2-x}Co_xSb$)

Stoichiometric amounts of copper(II) oxide, cobalt(II,III) oxide and antimony(III) oxide were heated at 425 °C (48 hours) and subsequently at 450 °C (24 hours) in order to prepare the series $Cu_{2-x}Co_xSb$ ($0.25 \leq x \leq 1$). X-ray powder diffraction patterns were recorded after the final reaction over the range $5 \leq 2\theta/° \leq 70$, with a counting time of 1.0 s per step.

Analysis of the diffraction patterns revealed that reactions carried out to prepare $Cu_{1.75}Co_{0.25}Sb$ and $Cu_{1.5}Co_{0.5}Sb$ formed a mixture of a Cu_2Sb-type phase, CoSb and Cu_4Sb (a new phase reported in section 3.2.4.5). The reaction carried out to prepare CuCoSb resulted in a mixture of a Cu_2Sb-type phase and elemental copper. The lattice parameters of the Cu_2Sb-type phase formed in all reactions were not significantly different to those of Cu_2Sb, indicating that cobalt had not been introduced into the Cu_2Sb structure. However, it is possible that smaller amounts of cobalt may be able to be introduced into the Cu_2Sb structure, although there have been no previous reports of this in the literature. In addition, there is no known 2:1 cobalt antimonide which adopts the *anti*-PbFCl structure.

6.1.4 Introduction of Ni into Cu_2Sb ($Cu_{2-x}Ni_xSb$)

Stoichiometric amounts of copper(II) oxide, nickel(II) oxide and antimony(III) oxide were heated at 425 °C (48 hours) and subsequently at 450 °C (24 hours) for values of x = 0.05 and 0.1; for values of x = 0.25, 0.5 and 0.75 the oxides were heated once more at 450 °C. X-ray powder diffraction patterns were recorded after the final reaction over the range $5 \leq 2\theta/° \leq 70$, with a counting time of 1.0 s per step.

Analysis of the diffraction patterns revealed that a Cu_2Sb-type phase had formed in all reactions except the reaction carried out to prepare CuNiSb. Impurities were present in all reaction products; some could not be identified; others were identified as the nickel arsenide NiSb and unreacted Sb_2O_3. In the reaction carried out to prepare CuNiSb, a mixture of NiSb and elemental copper formed. The weight fractions of each phase in each composition were calculated and are given in Table 6-1.

Composition	x	Cu_2Sb-type	NiSb	Sb_2O_3
$Cu_{1.95}Ni_{0.05}Sb$	0.05	1*	0	0
$Cu_{1.9}Ni_{0.1}Sb$	0.10	1*	0	0
$Cu_{1.75}Ni_{0.25}Sb$	0.25	0.949	0.042(2)	0.008
$Cu_{1.5}Ni_{0.5}Sb$	0.50	0.412	0.319(5)	0.268(7)

Table 6-1: Weight fractions of the Cu_2Sb-type phase, NiSb and Sb_2O_3 in the series $Cu_{2-x}Ni_xSb$. * denotes the presence of small amounts of unidentifiable impurities

Rietveld refinement was carried out for all compositions in the series except where x = 1, using the structure of Cu_2Sb published by Nuss and Jansen as the initial model.[115] Unit cell data obtained from the refinements are given in Table 6-2.

Composition	x	a / Å	c / Å	V / Å^3
Cu_2Sb	0	4.00302(7)	6.1058(1)	97.840(5)
$Cu_{1.95}Ni_{0.05}Sb$	0.05	3.9972(3)	6.0962(5)	97.40(2)
$Cu_{1.9}Ni_{0.1}Sb$	0.10	3.9967(3)	6.0943(6)	97.35(2)
$Cu_{1.75}Ni_{0.25}Sb$	0.25	3.9887(3)	6.0791(6)	96.72(2)
$Cu_{1.5}Ni_{0.5}Sb$	0.50	3.9885(4)	6.0780(8)	96.69(3)

Table 6-2: Unit cell data for the $Cu_{2-x}Ni_xSb$ series

Graphical representations of the unit cell data given in Table 6-2 were prepared and are given in the following figures.

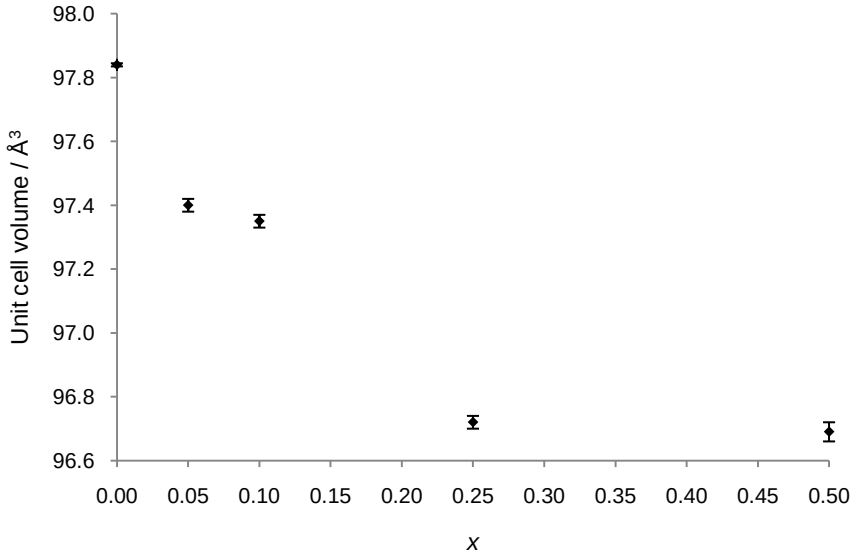

Figure 6-1: Plot of unit cell volume against composition (x) for the $Cu_{2-x}Ni_xSb$ series

Figure 6-1 demonstrates the variation in unit cell volume with composition. The unit cell volume decreases in a close to linear fashion up to $x = 0.25$. Between $x = 0.25$ and $x = 0.5$ the unit cell volume remains the same, within error. This suggests that the limit of solubility of nickel in Cu_2Sb is $x = 0.25$. However, none of the compositions in the series are pure. It is therefore likely that some nickel has been introduced into the structure, perhaps, for example, 80% of the amount introduced into the system. This would explain the decrease in unit cell volume, but also the presence of impurities. The limit of solubility of nickel in Cu_2Sb is therefore less than $x = 0.25$.

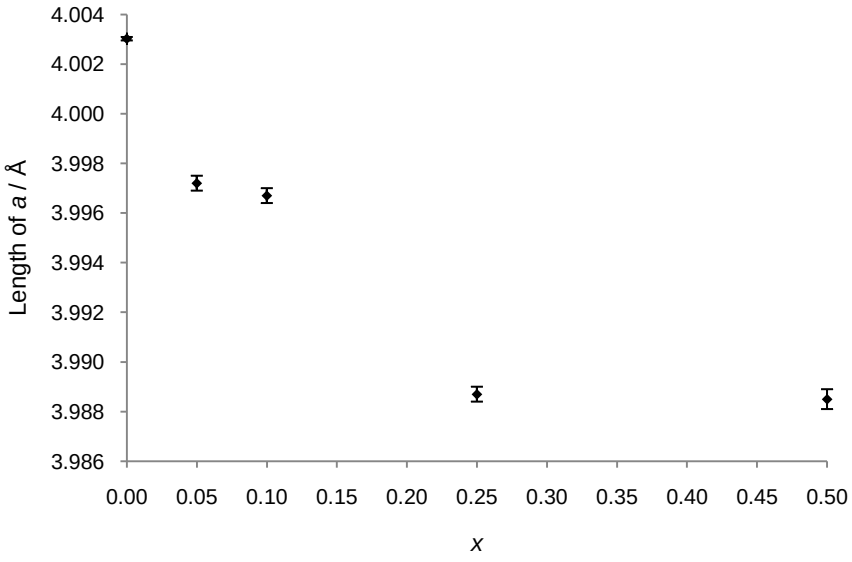

Figure 6-2: Plot of unit cell length *a* against composition (*x*) for the $Cu_{2-x}Ni_xSb$ series

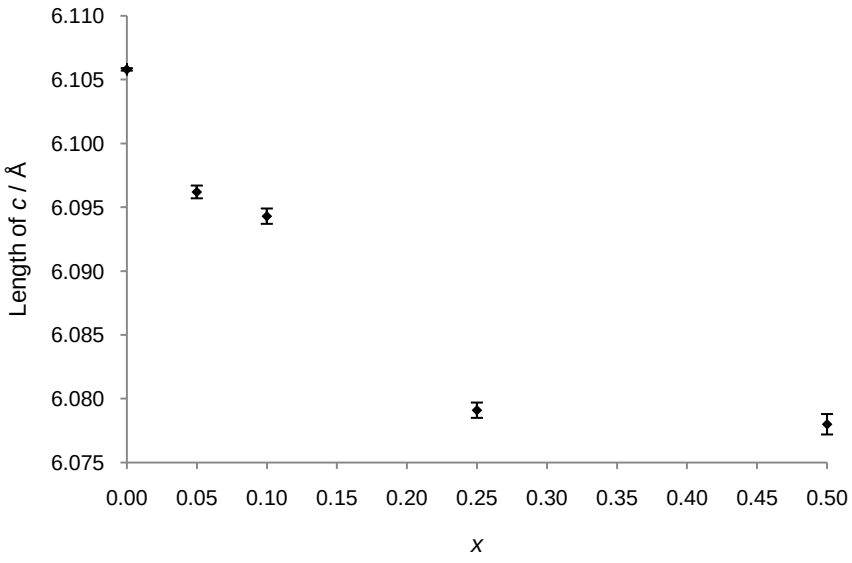

Figure 6-3: Plot of unit cell length *c* against composition (*x*) for the $Cu_{2-x}Ni_xSb$ series

Figure 6-2 and Figure 6-3 demonstrate the variation in unit cell length *a* and *c* with composition, respectively. Similar relationships are observed between the two unit cell lengths and composition to that observed between the unit cell volume and composition. The plots confirm that the limit of solubility in this system appears to be $x = 0.25$. However, due to the presence of impurities in the patterns the true value is less than this.

The difficulty in introducing nickel into the Cu_2Sb structure is likely to be a result of a small difference in size between copper and nickel. It is not likely to be caused by different electron counts, given that some nickel was able to be introduced into the structure.

6.1.5 Introduction of Ag into Cu_2Sb ($Cu_{2-x}Ag_xSb$)

Stoichiometric amounts of copper(II) oxide, silver(I) oxide and antimony(III) oxide were heated at 425 °C (48 hours) and subsequently at 450 °C (24 hours) in order to prepare the compositions $Cu_{1.9}Ag_{0.1}Sb$ and $Cu_{1.8}Ag_{0.2}Sb$. X-ray powder diffraction patterns were recorded after the final reaction over the range $5 \leq 2\theta/° \leq 70$, with a counting time of 1.0 s per step.

Analysis of the diffraction patterns revealed that a Cu_2Sb-type phase had formed in both reactions, in addition to impurities. The impurity present in the reaction carried out to prepare $Cu_{1.9}Ag_{0.1}Sb$ was not able to be identified. However, Ag_3Sb was identified as an impurity present in the reaction carried out to prepare $Cu_{1.8}Ag_{0.2}Sb$. The lattice parameters of the Cu_2Sb-phase in both compositions were not significantly different from those of Cu_2Sb, indicating that silver had not been introduced into the Cu_2Sb structure. This is not very surprising given that a binary silver antimonide with a copper to antimony ratio of 2:1 has not been reported before. In addition, silver is larger than copper; introduction of silver into the Cu_2Sb structure may therefore be unfavourable. However, the synthesis of Ag_3Sb as a by-product in the reaction suggests that this binary phase may be made pure. Further work on the synthesis of binary silver antimonides could therefore be carried out.

6.2 Metalloid Site Substitutions

6.2.1 Introduction of Te into Cu_2Sb ($Cu_2Sb_{1-x}Te_x$)

Stoichiometric amounts of copper(II) oxide, antimony(III) oxide and tellurium(IV) oxide were heated at 425 °C (48 hours) and subsequently at 450 °C (24 hours) in order to prepare the series $Cu_2Sb_{1-x}Te_x$ ($0.1 \leq x \leq 0.3$), with x increasing in increments of 0.1. X-ray powder diffraction patterns were recorded after the final reaction over the range $5 \leq 2\theta/° \leq 70$, with a counting time of 1.0 s per step.

Analysis of the diffraction patterns indicated that in each composition a mixture of a Cu_2Sb-type phase, $Cu_{2-x}Te$ and an unidentifiable impurity was present. The lattice parameters of the Cu_2Sb-type phase were not significantly different from those of Cu_2Sb, indicating that tellurium had not been introduced into the Cu_2Sb structure. This is not surprising given that this series has not been previously reported in the literature. In addition, the 2:1 copper telluride $Cu_{2-x}Te$ crystallises in a different structure to Cu_2Sb. It is likely that formation of this structure is more favourable than the introduction of tellurium into Cu_2Sb.

6.3 Summary

In this chapter, the attempted synthesis of series of substitutions in Cu_2Sb on both the transition metal site and the metalloid site has been described. Problems were encountered when attempting to introduce Mn into the Cu_2Sb structure due to the stability and therefore resistance to reduction of MnO under these conditions. Cobalt and iron were also unable to be introduced into the Cu_2Sb structure. It is likely that this was due to a difference in size between cobalt/iron and copper, or electronic reasons, as iron and cobalt have rather different numbers of valence electrons to copper. A small but unidentifiable amount of nickel was able to be introduced into Cu_2Sb. It is likely that this was a result of the similar size of nickel and copper; however, a small difference in size may have limited the amount introduced into the structure. Silver was not able to be introduced into Cu_2Sb. It is likely that this was a result of the large size of silver in relation to copper. The attempted substitution of antimony for tellurium was also unsuccessful. It is likely that this was a result of the stability of $Cu_{2-x}Te$.

7.0 Transition Metal Nitrides: η-Carbide and Filled β-Manganese Nitrides, and Precursor Routes to Binary Nitrides

Work described in this chapter focuses on attempts to expand new routes to η-carbide and filled β-manganese nitrides, and attempts to create new routes to binary transition metal nitrides. The need for new synthetic routes to transition metal nitrides was outlined in section 3.1. The traditional synthetic routes to nitrides were also explored in this section. Other synthetic routes that have been used to prepare η-carbide and filled β-manganese nitrides are discussed in the following sections, in addition to descriptions of these structure types. Most of the synthetic routes described in this chapter are based on the treatment of transition metal molybdates with ammonia.

7.1 η-Carbide Nitrides

7.1.1 η-Carbide Structure

The η-carbide structure, M_3T_3X (M, T = transition metals, X = small electronegative atom), is cubic and crystallises in the space group $Fd\bar{3}m$. Fe_3Mo_3N is an example of an interstitial nitride which crystallises in this structure.[85] The structure is generated by the filling of octahedral holes within the array of metal atoms in the Ti_2Ni structure,[164] with small electronegative atoms, such as carbon, nitrogen or oxygen. Filling of the octahedral holes increases the metallic bonding in the structure through the overlap of the non-metal 2*p* orbitals with the metal 3*d*/4*d* orbitals.[82] The η-carbide structure consists of two interpenetrating diamondoid subunits, one derived from M atoms and one derived from T_6X octahedra. M atoms are located on two sites: the 16*d* and 32*e* Wyckoff positions. M atoms situated on the 32*e* positions form tetrahedra, which are capped over each face by M atoms situated on the 16*d* positions, therefore forming supertetrahedra (Figure 7-1).

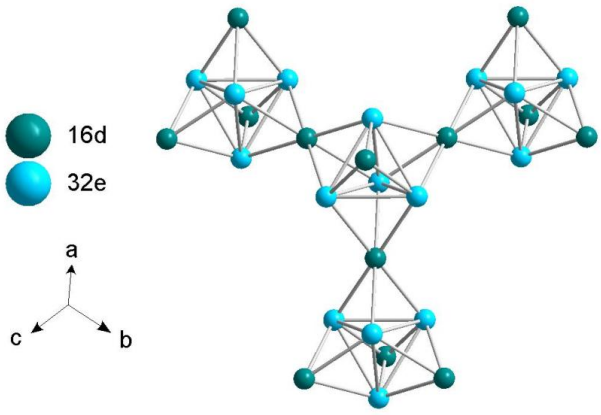

Figure 7-1: Supertetrahedra of M atoms (Fe in Fe_3Mo_3N) located on the 16*d* and 32*e* sites

The structure is therefore represented more accurately as $[M^{32e}{}_2M^{16d}]T_3X$. The supertetrahedra share vertices to form one of the diamondoid nets. A unit cell with only M atoms shown is given in Figure 7-2.

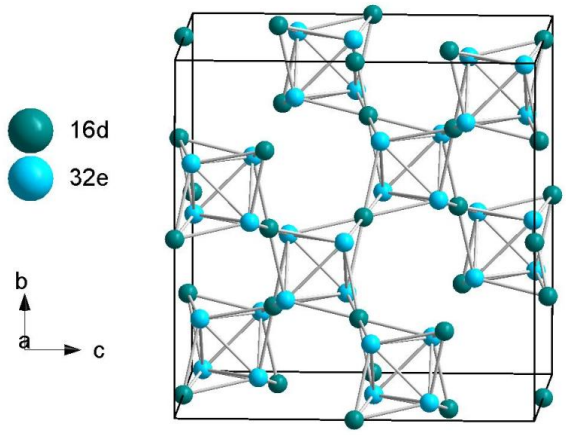

Figure 7-2: Unit cell of M atoms (Fe in Fe_3Mo_3N), highlighting the corner connectivity of the supertetrahedra

The second diamondoid net is formed by corner-sharing tetrahedral clusters, formed from groups of four corner-sharing T_6X octahedra, where T atoms are located on the 48*f* Wyckoff position and X atoms are located on the 16*c* Wyckoff position (Figure 7-3).

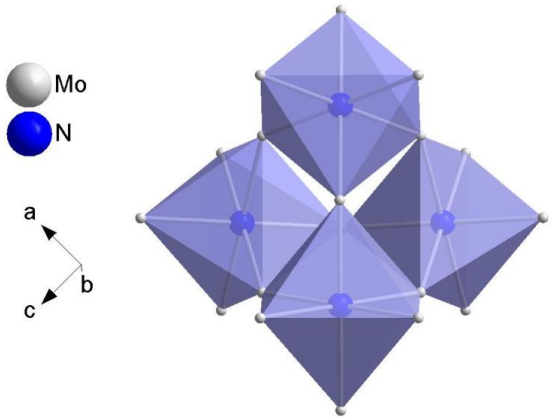

Figure 7-3: Tetrahedral cluster of T_6X (Mo_6N in Fe_3Mo_3N) octahedra

The two diamondoid nets are related to each other by a translation of (½, ½, ½), thereby completing the structure.

The η-carbide structure can also exist in a 6:6:1 stoichiometry, *e.g.* in Fe_6W_6C,[165] where the interstitial atoms are located on the 8*a* Wyckoff position rather than the 16*c* Wyckoff position.

7.1.1 Synthetic Routes

Solid state precursor reduction: Bem *et al*. discovered a relatively low temperature precursor route to the ternary nitride, Fe_3Mo_3N.[166] Synthesis was carried out *via* the reduction of the stoichiometric precursor, $FeMoO_4$, with ammonia gas at 800 °C for 12 hours. Replacing ammonia gas with 5% hydrogen in nitrogen also resulted in the synthesis of Fe_3Mo_3N. This route was expanded by Jackson *et al*. to include the synthesis of Co_3Mo_3N.[167] The same research group also synthesised Fe_3Mo_3N and Co_3Mo_3N by plasma nitridation of the oxide precursors, where ionised nitrogen gas was used as the nitriding species.[167]

Ammonolysis of chemically complexed precursors: Weil and Kumta prepared Fe_3Mo_3N and Co_3W_3N *via* the ammonolysis of metallo-organic precursors.[168,169] The precursors were prepared by the addition of a complexing agent (triethylamine in the case of Co_3W_3N, and ethanolamine in the case of Fe_3Mo_3N) to stoichiometric mixtures of the corresponding transition metal chlorides dissolved in acetonitrile. Evaporation of the solvent and

subsequent ammonolysis at 950 °C for 4 hours yielded ternary transition metal nitrides. Fe_3W_3N was subsequently prepared using the same method.[170]

Oxide precursors and urea: Gomathi developed a new route to Fe_3Mo_3N and Co_3Mo_3N by reacting transition metal molybdates with urea.[171] The oxide precursors $FeMoO_4$ and $CoMoO_4$ were reacted with urea in a 1:12 molar ratio under an atmosphere of nitrogen at 900 °C for 3 hours. It is thought that urea forms ammonia when heated, which is likely to be the nitriding species in this reaction.

7.2 Filled β-Manganese Nitrides

7.2.1 Filled β-Manganese Structure

The β-manganese structure, a high temperature form of elemental manganese, is cubic and adopts the space group $P4_132$. It is a complicated elemental structure, with 20 atoms present in the unit cell. The room temperature form of elemental manganese, known as α-manganese, is also complicated, with 58 atoms in the unit cell. In the β-manganese structure atoms are located on two sites: the Wyckoff 8*c* and 12*d* positions. Atoms on the 8*c* positions generate a (10,3)-a network of Mn atoms (Figure 7-4).

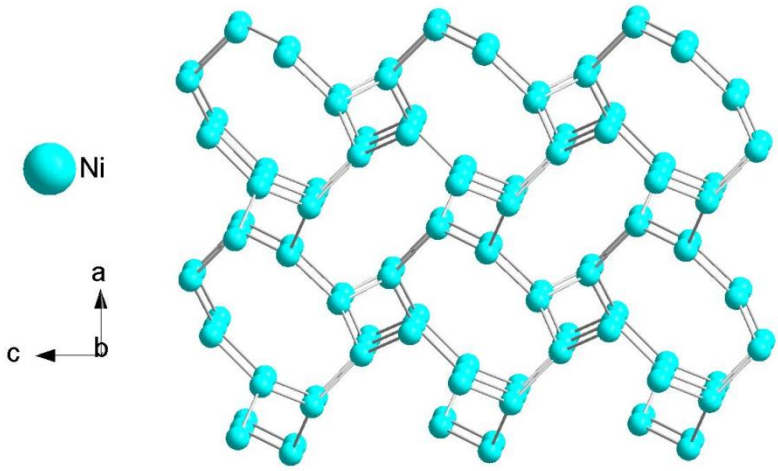

Figure 7-4: (10,3)-a network of Mn (Ni in Ni_2Mo_3N) atoms

The space within this network is filled by Mn atoms on the 12*d* sites, which form corner-sharing Mn_6 octahedra. This gives rise to the empirical formula M_2T_3, where M atoms are situated on the 8*c* sites, and T atoms are situated on the 12*d* sites. An

electronegative non-metal atom can be accommodated in an interstitial site, which lies at the centre of the T_6 octahedra. Filling of these sites with boron, carbon or nitrogen results in the *filled* β-manganese structure, M_2T_3X (M, T = transition metals, X = B, C, N). Ni_2Mo_3N is an example of an interstitial nitride which adopts this structure.[85]

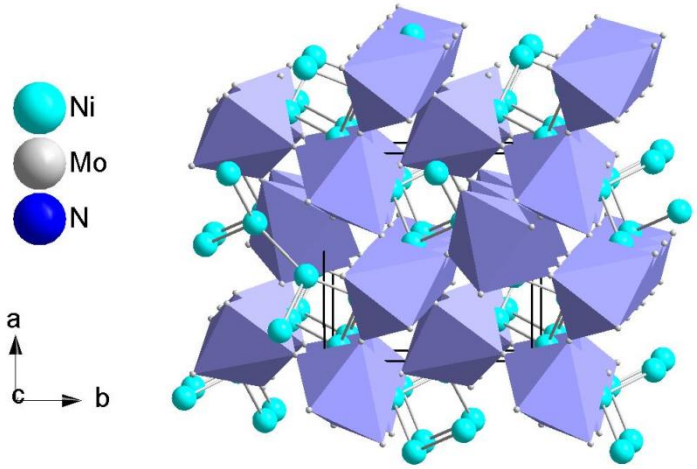

Figure 7-5: The filled β-manganese structure, M_2T_3X (Ni_2Mo_3N). Nitrogen atoms lie at the centres of the octahedra

7.2.1 Synthetic Routes

Ammonolysis of chemically complexed precursors: A very similar technique to that used to prepare η-carbide nitrides was used by Herle *et al.* to prepare the filled β-manganese nitride Ni_2Mo_3N.[172] The precursor was made by dissolving the corresponding metal chlorides in acetonitrile and complexing with triethylamine. The precursor was then reacted under flowing ammonia gas at 950 °C for 4 hours. The same group also attempted the synthesis of Ni_2Mo_3N *via* the reduction of $NiMoO_4$. This, however, resulted in a mixture of Ni_2Mo_3N and nickel metal, due to the difference in stoichiometry of the precursor and desired product. This mixture of Ni_2Mo_3N and nickel metal has been erroneously reported in the literature as Ni_3Mo_3N.[145,166,173,174] Ni_2W_3N was also synthesised *via* the ammonolysis of chemically complexed precursors.[175]

Freeze-dried precursors: Pt_2Mo_3N and $PtPdMo_3N$ have been prepared by the ammonolysis of amorphous precursors obtained by the freeze-drying of aqueous solutions of the appropriate metal salts: $(NH_4)_6Mo_7O_{24}.4H_2O$, $(NH_4)_2[PdCl_6]$ and $(NH_4)_2[PtCl_6]$.[176]

The individual salts were dissolved in water and added to each other in stoichiometric amounts. Drops of the solutions were then flash frozen by projection on liquid nitrogen and subsequently freeze-dried. The resulting amorphous powders were reacted in air at 600 °C for 12 hours, in order to induce crystallinity. The crystalline precursors were then reacted with ammonia gas at 900 °C for 12 hours. This method was also used to prepare Pd_2Mo_3N.[177]

Oxide precursors and urea: Ni_2Mo_3N was synthesised by Gomathi using the same route used for the synthesis of η-carbide nitrides.[171] However, due to the stoichiometry of the starting material ($NiMoO_4$), the resulting Ni_2Mo_3N was in admixture with nickel metal.

7.3 Synthesis of η-Carbide Nitrides *via* Reduction-Nitridation

Certain η-carbide nitrides have been shown to exhibit interesting magnetic behaviour. For example, Fe_3Mo_3N, Co_3Mo_3N and Ni_2GaMo_3N were determined to be Pauli paramagnets.[88] In addition, it was thought that some compositions of the solid solution $Fe_{3-x}Co_xMo_3N$ contained superparamagnetic clusters,[88] although the magnetic behaviour observed did not vary smoothly across the series. Ordering of metal atoms in compounds adopting the η-carbide structure is rare, although several cases are known where complete metal site ordering occurs. For example, Ni_2GaMo_3N was shown to exhibit full metal site ordering, with nickel atoms located exclusively on the 32*e* sites, and gallium atoms located exclusively on the 16*d* sites.[88] The complete ordering in Ni_2GaMo_3N was strongly suggested by x-ray diffraction, and confirmed by neutron diffraction. Ordering in the solid solution $Fe_{3-x}Co_xMo_3N$ was also determined by neutron diffraction due to the similar x-ray scattering factors of iron and cobalt; the compositions were shown to exhibit partial metal site ordering. It is likely that full ordering is not observed in this series given the very similar sizes of iron and cobalt. Prior and Battle concluded that the ordering in Ni_2GaMo_3N and the solid solution $Fe_{3-x}Co_xMo_3N$ must be determined by effects that (i) extend beyond the first coordination shell, or (ii) are a result of electronic factors.[88]

Initial work described here was carried out in order to test the reaction setup and verify that using the same synthetic method as Prior and Battle the same products could be formed. The filled β-manganese compound, Ni_2Mo_3N, and some germanium-substituted η-carbides

were therefore synthesised under the exact conditions reported by Prior and Battle. The synthesis of germanium-substituted η-carbide nitrides was attempted, given that germanium(IV) oxide was successfully reduced by Baker *et al*. when preparing the germanide, $FeMo_4Ge_3$,[89] and that the previous synthesis of the gallium-substituted η-carbide, Ni_2GaMo_3N, was successful (given that gallium atoms are similar in size to germanium atoms).[88] The magnetic behaviour of the germanium-substituted η-carbides was investigated due to the interesting magnetic behaviour exhibited by other η-carbide nitrides. When this work was carried out, reports of the existence of germanium-substituted η-carbide nitrides were not available in the literature. However, shortly after completion of this work a report was published on the synthesis of Co_2GeMo_3N.[178] In addition, work reported later on in this chapter on the synthesis of $Co_{2-x}Fe_xGeMo_3N$ and $Co_{2-x}Ni_xGeMo_3N$ was also published in the same paper.

7.3.1 M_2GeMo_3N (M = Fe, Co, Ni)

η-Carbide nitrides were prepared using the method reported by Prior and Battle.[88] Stoichiometric amounts of iron(III) oxide/cobalt(II,III) oxide/nickel(II) oxide, germanium(IV) oxide and molybdenum(VI) oxide were heated at 700 °C (48 hours), 750 °C (24 hours), 875 °C (24 hours), 975 °C (24 hours) and once more at 975 °C (24 hours). X-ray powder diffraction patterns were recorded after the final reaction over the range $5 \leq 2\theta/° \leq 120$, with a counting time of 9.3 s per step.

Analysis of the x-ray diffraction patterns indicated that an η-carbide phase was present in all samples, in addition to very small amounts of elemental molybdenum and/or $MoN_{0.46}$. Rietveld refinement was carried out for Fe_2GeMo_3N using the structure of Fe_3Mo_3N published by Jackson *et al*. as the initial model.[167] The structure of Co_3Mo_3N published by Jackson *et al*. was used as the initial model for Co_2GeMo_3N and Ni_2GeMo_3N.[167] The germanium atom was presumed to be located on the 16*d* iron site; subsequent refinement of disordered Fe/Co/Ni and Ge across the 16*d* and 32*e* sites indicated complete ordering. Previous work on a similar η-carbide series demonstrated that there was no evidence for the presence of molybdenum on either the 32*e* or 16*d* site.[88] It was therefore refined on the 48*f* Wyckoff position. Weight fractions of impurities in the compositions are given in Table 7-1.

Composition	Weight fraction of Mo	Weight fraction of $MoN_{0.46}$
Fe_2GeMo_3N	0.0041(2)	0.0064(2)
Co_2GeMo_3N	0.0044(6)	0.0068(6)
Ni_2GeMo_3N	-	0.0031(3)

Table 7-1: Weight fractions of Mo and $MoN_{0.46}$ in compositions in the M_2GeMo_3N (M = Fe, Co, Ni) series

The Rietveld fit for Ni_2GeMo_3N is shown in Figure 7-6. Rietveld refinement data for the η-carbide nitrides are given in Table 7-2, Table 7-3 and Table 7-4.

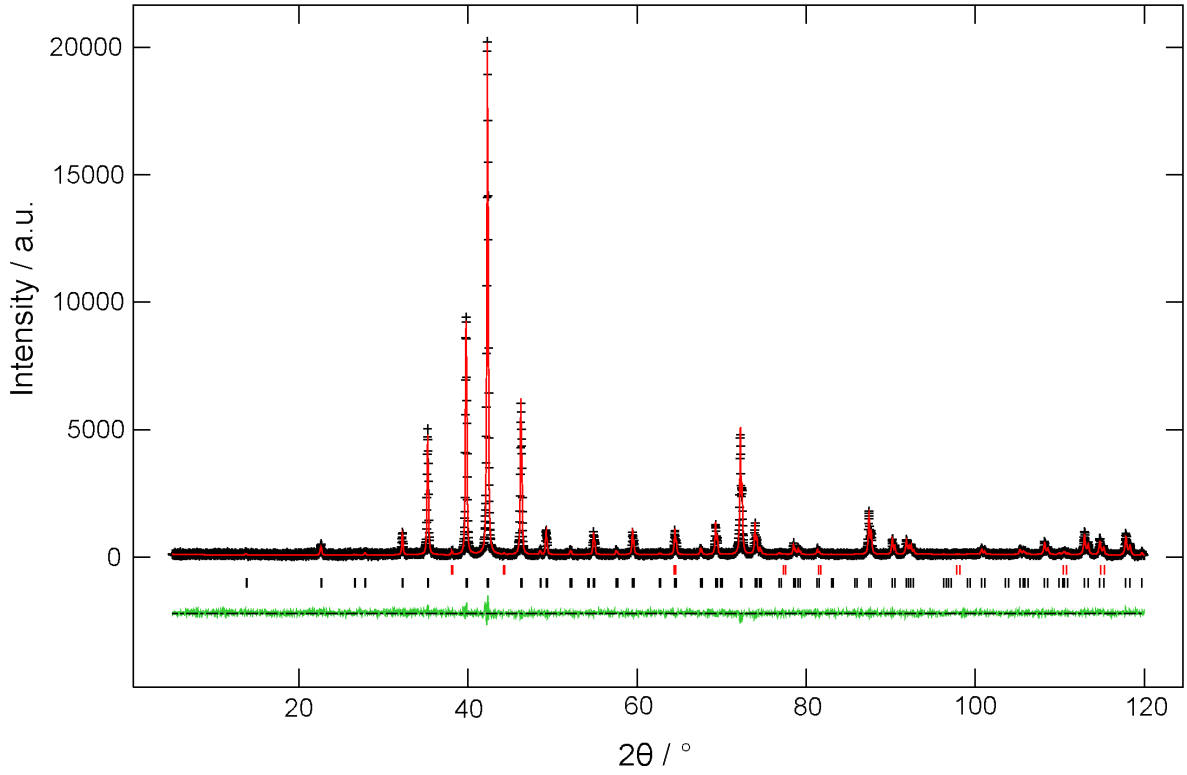

Figure 7-6: Observed (black), calculated (red) and difference (green) x-ray powder diffraction profiles for Ni_2GeMo_3N. Lower tick marks indicate positions of allowed reflections for Ni_2GeMo_3N. Upper tick marks indicate positions of allowed reflections for $MoN_{0.46}$

Fe_2GeMo_3N	Refined values		
Space group	$Fd\bar{3}m$		
Structure type	Fe_3W_3C (η-carbide)		
a / Å	11.1618(1)		
V / Å^3	1390.59(5)		
Atomic positions	***x***	***y***	***z***
Fe (32*e*)	0.29205(9)	0.29205(9)	0.29205(9)
Ge (16*d*)	½	½	½
Mo (48*f*)	0.31815(7)	⅛	⅛
N (16*c*)	0	0	0
Isotropic displacement parameters / Å^2	**Fe**	**Ge**	**Mo**
	0.0053(5)	0.0062(5)	0.0048(2)
R(F^2)	0.0376		
χ^2	4.028		

Table 7-2: Rietveld refinement data for Fe_2GeMo_3N

Co_2GeMo_3N	Refined values		
Space group	$Fd\bar{3}m$		
Structure type	Fe_3W_3C (η-carbide)		
a / Å	11.1014(2)		
V / Å^3	1368.14(7)		
Atomic positions	***x***	***y***	***z***
Co (32*e*)	0.2913(2)	0.2913(2)	0.2913(2)
Ge (16*d*)	½	½	½
Mo (48*f*)	0.3177(1)	⅛	⅛
N (16*c*)	0	0	0
Isotropic displacement parameters / Å^2	**Co**	**Ge**	**Mo**
	0.016(1)	0.015(1)	0.0115(4)
R(F^2)	0.0842		
χ^2	5.216		

Table 7-3: Rietveld refinement data for Co_2GeMo_3N

Ni_2GeMo_3N	Refined values		
Space group	$Fd\bar{3}m$		
Structure type	Fe_3W_3C (η-carbide)		
a / Å	11.0889(2)		
V / Å^3	1363.54(8)		
Atomic positions	***x***	***y***	***z***
Ni (32*e*)	0.2918(1)	0.2918(1)	0.2918(1)
Ge (16*d*)	½	½	½
Mo (48*f*)	0.3161(1)	⅛	⅛
N (16*c*)	0	0	0
Isotropic displacement parameters / Å^2	**Ni**	**Ge**	**Mo**
	0.0204(9)	0.0174(9)	0.0151(4)
R(F^2)	0.0618		
χ^2	7.672		

Table 7-4: Rietveld refinement data for Ni_2GeMo_3N

It is interesting that high purity Ni_2GeMo_3N and Ni_2GaMo_3N (reported by Prior and Battle) were synthesised given that Ni_3Mo_3N is not a known phase. In both of these compounds nickel atoms are located exclusively on the 32*e* site, and the germanium/gallium atoms are located exclusively on the 16*d* site. It is perhaps likely that Ni_2GeMo_3N and Ni_2GaMo_3N can be synthesised whereas Ni_3Mo_3N cannot is due to the difference in size between nickel atoms and germanium/gallium atoms. The Ni-Ni distance in *ccp* nickel is 2.5013 Å,[145] whereas the interatomic distances in elemental gallium (*Cmca*) and germanium ($Fd\bar{3}m$) are 2.4821 Å[179] and 2.4494 Å,[180] respectively. Germanium and gallium atoms are therefore smaller than nickel atoms; their presence on the smaller 16*d* site may therefore be more favourable than the presence of nickel on the 16*d* site (in 'Ni_3Mo_3N').

Fourier difference maps were calculated in order to verify the presence of nitrogen within the structures and are shown in Figure 7-7, Figure 7-8 and Figure 7-9. Contours were drawn at intervals of 0.20 e Å^{-3}.

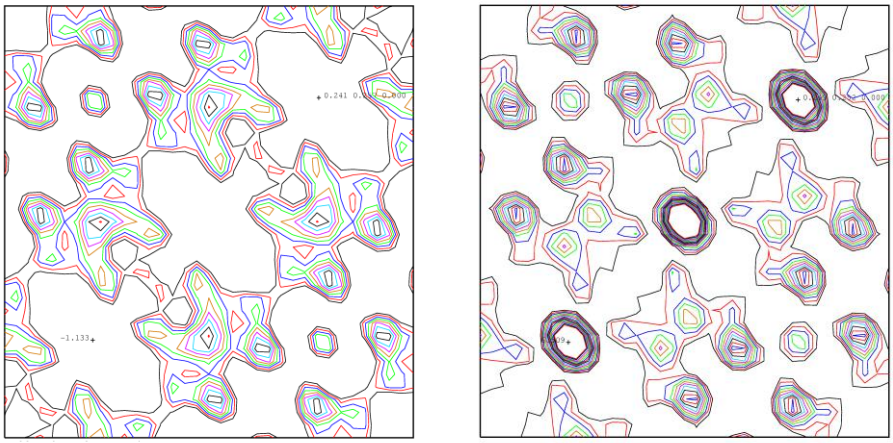

Figure 7-7: 2-D Fourier difference maps of Fe_2GeMo_3N through $z = 0$ with the nitrogen occupancy equal to one (left) and zero (right), with the limits $-\frac{1}{8} \leq x \leq \frac{3}{8}$ and $-\frac{1}{8} \leq y \leq 0$

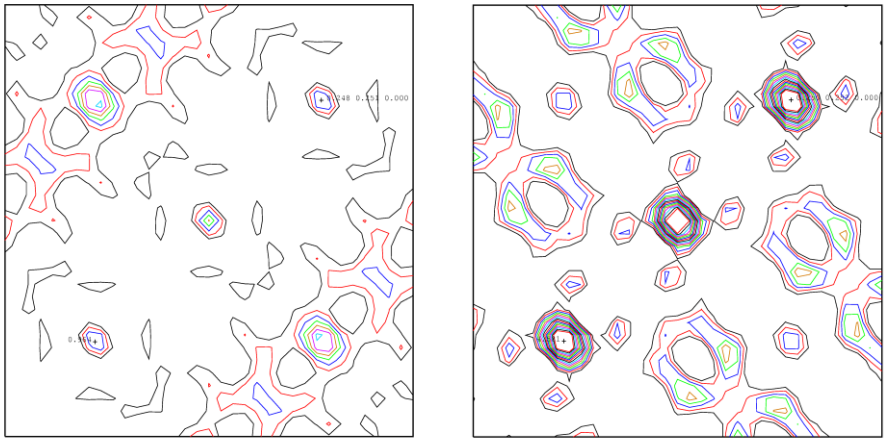

Figure 7-8: 2-D Fourier difference maps of Co_2GeMo_3N through $z = 0$ with the nitrogen occupancy set to one (left) and zero (right), with the limits $-\frac{1}{8} \leq x \leq \frac{3}{8}$ and $-\frac{1}{8} \leq y \leq 0$

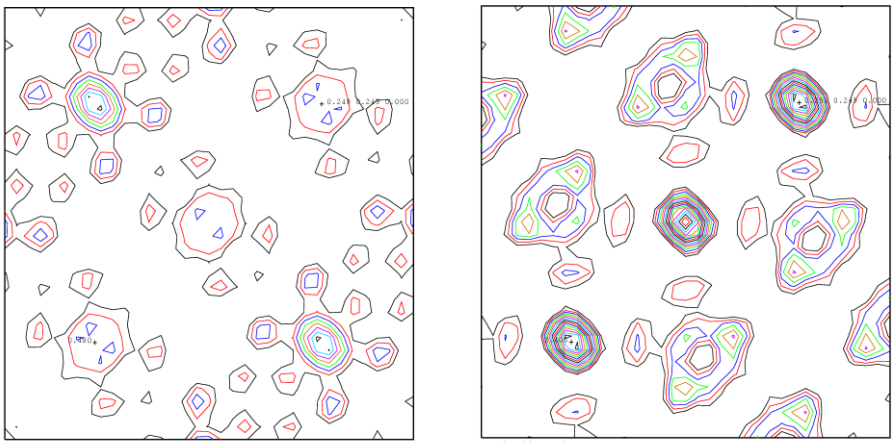

Figure 7-9: 2-D Fourier difference maps of Ni_2GeMo_3N through $z = 0$ with the nitrogen occupancy set to one (left) and zero (right), with the limits $-⅛ \leq x \leq ⅜$ and $-⅛ \leq y \leq 0$

The Fourier difference maps clearly demonstrate that nitrogen is present in all compositions, and is located on the 16*c* Wyckoff positions, indicated as three regions of electron density at (−¼, −¼, 0), (0, 0, 0) and (¼, ¼, 0). Fourier difference maps were also calculated through $z = ⅛$ in order to determine occupation of the 8*a* interstitial site. The maps calculated showed that the 8*a* site was not occupied in these η-carbide phases.

Mackay *et al.* developed a rule of thumb for the determination of occupation of either the 16*c* or 8*a* site by oxygen in oxides adopting the η-carbide structure, based on the atomic position of the atom located on the 48*f* (x, ⅛, ⅛) site.[181] Their rule stated that when $x > 0.3125$, the interstitial atom is preferentially located on the 8*a* site. However, this was shown by Jackson *et al.* not to be applicable to the η-carbide nitride, Fe_3Mo_3N.[167] Equivalent carbides were also shown to have their interstitial atoms located on the 16*c* site when $x > 0.3125$, breaching this rule of thumb. η-Carbide nitrides subsequently synthesised, including the $Fe_{3-x}Co_xMo_3N$ solid solution reported by Prior and Battle, were also shown to breach this rule,[88] in addition to Co_3Mo_3N, reported by Hunter *et al.*[182] Hunter *et al*. have therefore proposed that the bonding in and minimum energy structures adopted by η-carbide nitrides are more similar to carbides than to η-carbide oxides. The η-carbide nitrides prepared in this work support the conclusion that the rule of thumb suggested by Mackay *et al*. cannot be applied to η-carbide nitrides, given that the 16*c* sites are occupied by nitrogen when $0.3161 \leq x \leq 0.31815$.

Elemental (CHN) analysis was performed on each composition in order to determine the nitrogen content. The results are presented in Table 7-5.

Composition	Expected N content / %	Actual N content / %	Calculated stoichiometry
Fe_2GeMo_3N	2.88	2.66	$Fe_2GeMo_3N_{0.92}$
Co_2GeMo_3N	2.85	2.63	$Co_2GeMo_3N_{0.92}$
Ni_2GeMo_3N	2.85	2.65	$Ni_2GeMo_3N_{0.93}$

Table 7-5: Expected nitrogen content, actual nitrogen content and resulting stoichiometry for compositions in the series M_2GeMo_3N (M = Fe, Co, Ni)

Results presented in Table 7-5 indicate the presence of nitrogen in the η-carbide nitrides synthesised. The calculated stoichiometries also provide information on the site preference of the interstitial nitrogen: if nitrogen was present on only the 8*c* Wyckoff positions, the maximum amount of nitrogen in the compounds would be 0.5.

Magnetic susceptibility measurements were carried out using a Quantum Design MPMS 5000 SQUID magnetometer. The sample magnetisation was measured as a function of temperature over the range 5 – 300 K, in a field of 100 Oe for Fe_2GeMo_3N and Ni_2GeMo_3N, and 5000 Oe for Co_2GeMo_3N. Plots of magnetic susceptibility against temperature and inverse magnetic susceptibility against temperature were constructed and are shown in the following figures.

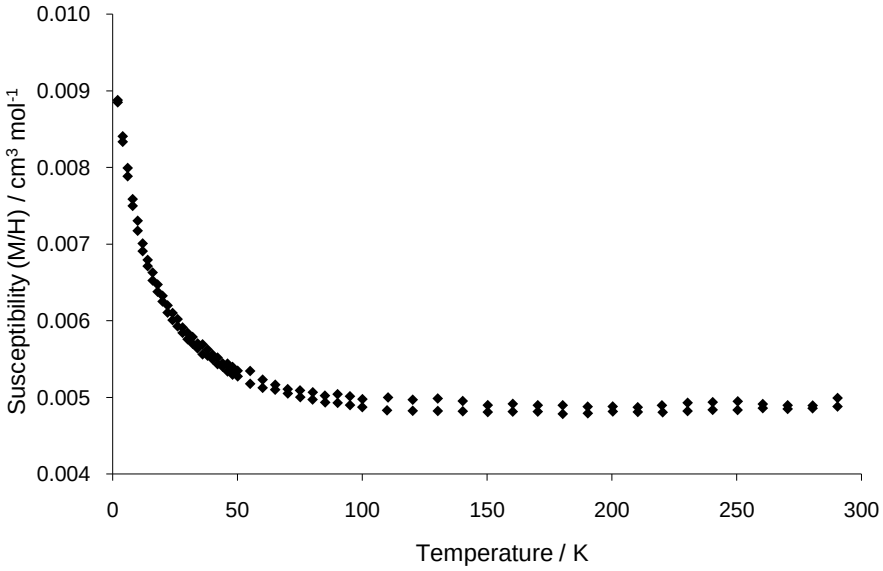

Figure 7-10: Plot of susceptibility (M/H) against temperature for Fe_2GeMo_3N

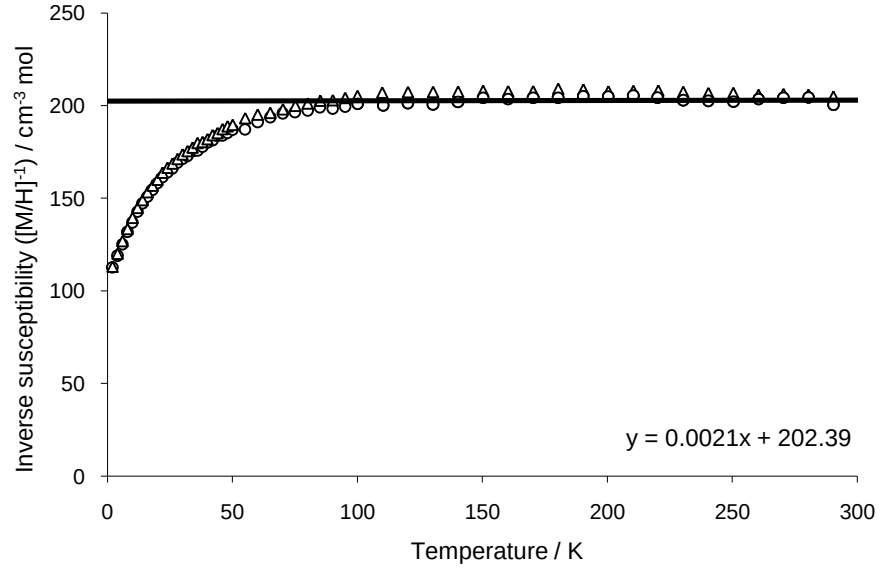

Figure 7-11: Plot of inverse susceptibility ($[M/H]^{-1}$) against temperature for Fe_2GeMo_3N

Figure 7-10 and Figure 7-11 suggest that Fe_2GeMo_3N is a Pauli paramagnet; at temperatures greater than approximately 100 K, the magnetic susceptibility and inverse susceptibility are both independent of temperature. The trendline on the plot of inverse susceptibility against temperature was therefore plotted from 100 K onwards.

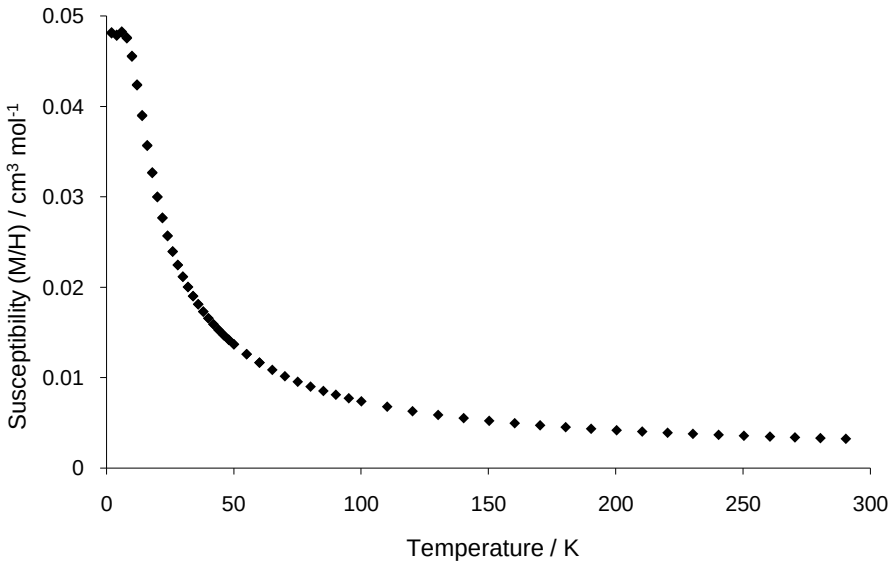

Figure 7-12: Plot of susceptibility (M/H) against temperature for Co_2GeMo_3N

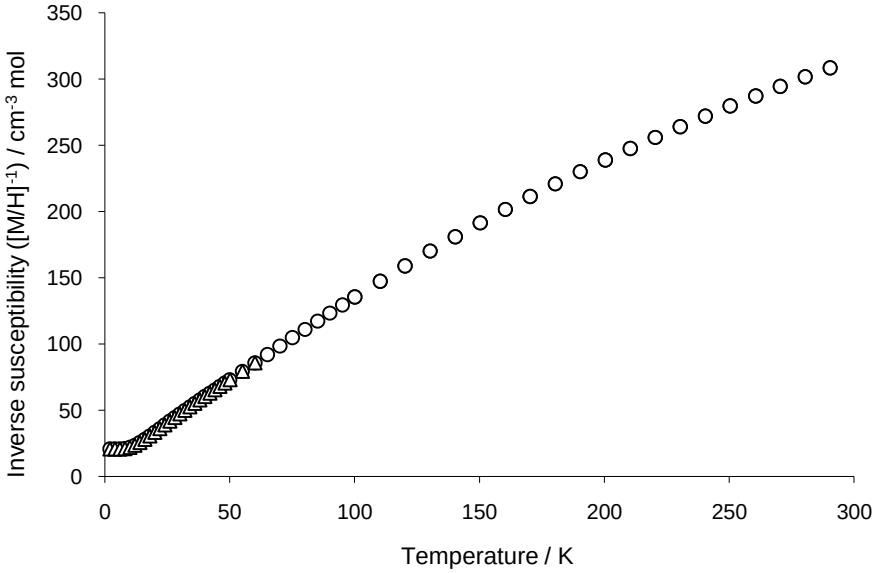

Figure 7-13: Plot of inverse susceptibility ($[M/H]^{-1}$) against temperature for Co_2GeMo_3N

Figure 7-13 suggests that Co_2GeMo_3N is a simple paramagnet given that the inverse susceptibility increases in an almost linear fashion, and extrapolation of the line beyond the deviation from linear behaviour observed at very low temperatures would likely reveal an intercept of the *y*-axis at the origin. It would therefore obey the Curie law. However, the deviation from linear behaviour at low temperature (also observed in Figure 7-12) suggests

that $Co_2Ge_3Mo_3N$ does not behave as a paramagnet at all temperatures. This deviation was also observed in Co_2GeMo_3N prepared by Sviridov *et al*. who concluded that this deviation was the result of a magnetic transition to a spin-glass state.[178] A spin-glass has an antiferromagnetic array of spins, which is disrupted by enforced ferromagnetic coupling.[66]

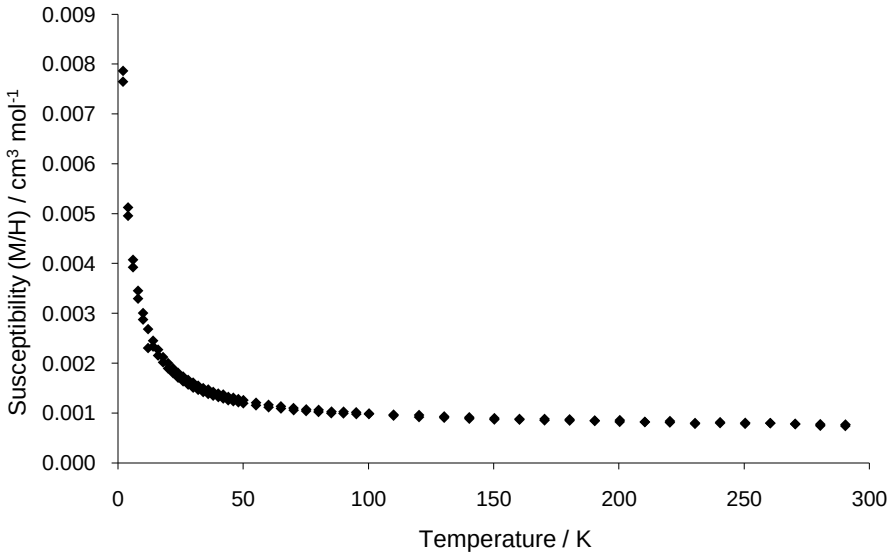

Figure 7-14: Plot of susceptibility (M/H) against temperature for Ni_2GeMo_3N

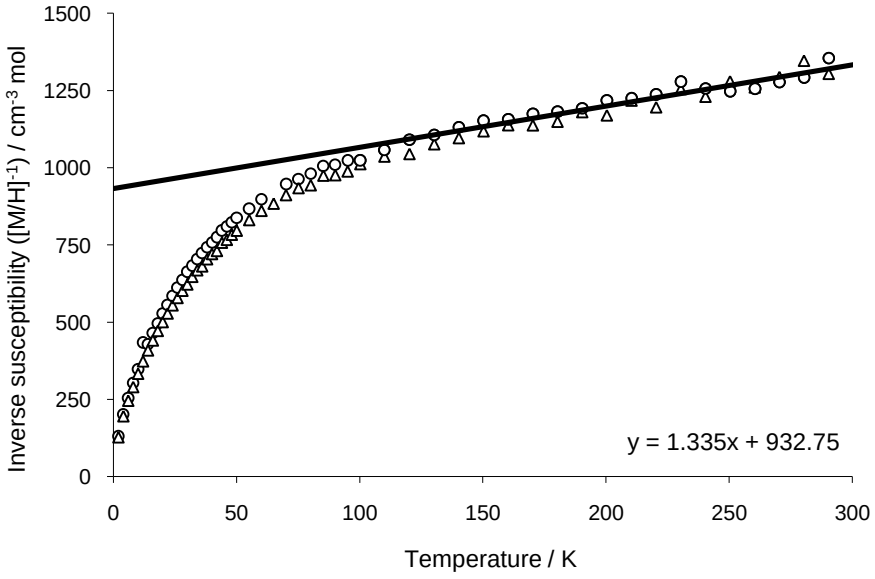

Figure 7-15: Plot of inverse susceptibility ($[M/H]^{-1}$) against temperature for Ni_2GeMo_3N

Figure 7-14 and Figure 7-15 suggest that Ni_2GeMo_3N is a Pauli paramagnet; at temperatures greater than approximately 100 K, the magnetic susceptibility and inverse susceptibility are almost independent of temperature. The trendline on the plot of inverse susceptibility against temperature was therefore plotted from 100 K onwards.

7.3.2 M_2GeMo_3 (M = Fe, Co, Ni)

In this series of reactions, attempts were made to synthesise the nitrogen-free analogues of the η-carbide series, M_2GeMo_3N, in order to determine whether nitrogen is necessary to stabilise compounds adopting the η-carbide structure in this series. The η-carbide structure is generated by the filling of octahedral holes within the Ti_2Ni structure. It was proposed that these reactions might therefore produce compounds with the Ti_2Ni structure *i.e.* η-carbide compounds with the octahedral holes left unfilled. It was thought that as the η-carbide nitrides were synthesised using 10% hydrogen in nitrogen, the synthesis of the unfilled compositions might be achieved using 10% hydrogen in argon.

Stoichiometric amounts of iron(III) oxide/cobalt(II,III) oxide/nickel(II) oxide, germanium(IV) oxide and molybdenum(VI) oxide were heated at 700 °C (48 hours), 750 °C (24 hours), 875 °C (24 hours), 975 °C (24 hours) and once more at 975 °C (24 hours). X-ray powder diffraction patterns were recorded after the final reaction over the range $5 \leq 2\theta/° \leq 70$, with a counting time of 1.0 s per step.

Analysis of the x-ray diffraction patterns revealed that each reaction had produced a mixture of products. The principal component of the product of the reaction carried out to prepare Fe_2GeMo_3 was Mo_3Ge. Other phases were difficult to identify. Products of the reaction carried out to prepare Co_2GeMo_3 were difficult to identify, but appeared to be elemental cobalt, Mo_3Ge and Co_5Ge_3. The products of the reaction carried out to prepare Ni_2GeMo_3 were also difficult to identify. However, there was no evidence for the presence of Mo_3Ge in the diffraction pattern. In no pattern was there evidence for the presence of a compound adopting the Ti_2Ni structure. This reaction demonstrated that the presence of 10% hydrogen in nitrogen is crucial to the formation of compounds in this system with a Ti_2Ni metal eutaxy.

7.3.3 η-Carbide Solid Solutions

The synthesis of solid solutions of the germanium-based η-carbides reported in section 7.3.1 was attempted, and is described in the following sections.

7.3.3.1 Introduction of Fe into Co_2GeMo_3N ($Co_{2-x}Fe_xGeMo_3N$)

Stoichiometric amounts of cobalt(II,III) oxide, iron(III) oxide, germanium(IV) oxide and molybdenum(VI) oxide were heated at 700 °C (48 hours), 750 °C (24 hours), 875 °C (24 hours), 975 °C (24 hours) and once more at 975 °C (24 hours) in order to prepare the series $Co_{2-x}Fe_xGeMo_3N$ ($0.1 \leq x \leq 0.3$), with x increasing in increments of 0.1. X-ray powder diffraction patterns were recorded after the final reaction over the range $5 \leq 2\theta/° \leq 70$, with a counting time of 1.0 s per step. An additional diffraction pattern was recorded over the range $5 \leq 2\theta/° \leq 120$, with a counting time of 9.3 s per step for the composition $Co_{1.7}Fe_{0.3}GeMo_3N$.

Analysis of the diffraction patterns revealed that an η-carbide phase had formed in each case. Very small amounts of elemental molybdenum were also present in each sample. Rietveld refinement was carried out for all compositions using the structure of Fe_3Mo_3N published by Jackson *et al*. as the initial model for the η-carbide phase.[167] The germanium atom was refined on the 16*d* Wyckoff position, and the iron and cobalt atoms were presumed to be disordered over the 32*e* Wyckoff position, given that ordering of these atoms cannot be determined by x-ray powder diffraction. The weight fractions of molybdenum present in each sample were determined to be 0.006(1), 0.008(1) and 0.0017(4) for $Co_{1.9}Fe_{0.1}GeMo_3N$, $Co_{1.8}Fe_{0.2}GeMo_3N$ and $Co_{1.7}Fe_{0.3}GeMo_3N$, respectively. The Rietveld fit for $Co_{1.7}Fe_{0.3}GeMo_3N$ is shown in Figure 7-16.

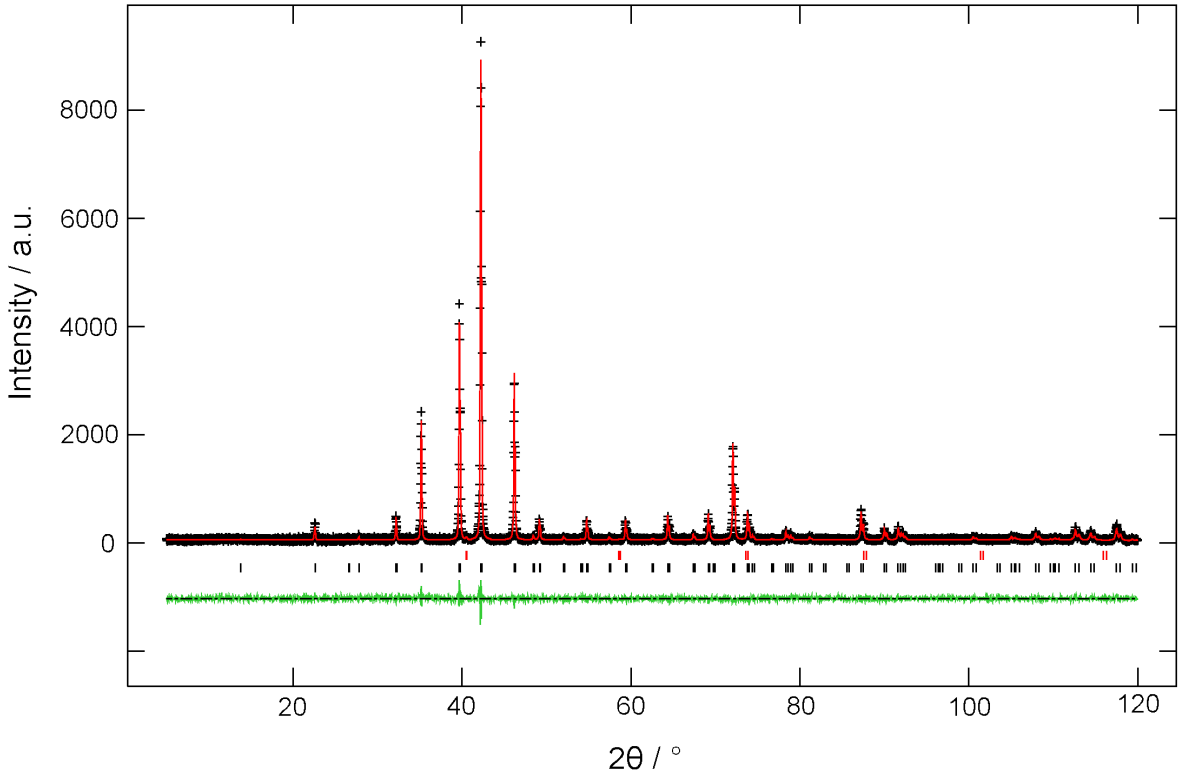

Figure 7-16: Observed (black), calculated (red) and difference (green) x-ray powder diffraction profiles for $Co_{1.7}Fe_{0.3}GeMo_3N$. Lower tick marks indicate positions of allowed reflections for $Co_{1.7}Fe_{0.3}GeMo_3N$. Upper tick marks indicate positions of allowed reflections for Mo

Unit cell data obtained from Rietveld refinement of all compositions in the series are given in Table 7-6.

Composition	x	a / Å	V / Å^3
Co_2GeMo_3N	0	11.1014(2)	1368.14(7)
$Co_{1.9}Fe_{0.1}GeMo_3N$	0.1	11.105(1)	1369.6(5)
$Co_{1.8}Fe_{0.2}GeMo_3N$	0.2	11.108(1)	1370.6(5)
$Co_{1.7}Fe_{0.3}GeMo_3N$	0.3	11.1093(2)	1371.08(8)

Table 7-6: Unit cell data for the $Co_{2-x}Fe_xGeMo_3N$ series

A plot of the unit cell volume against composition was constructed, and is shown in Figure 7-17.

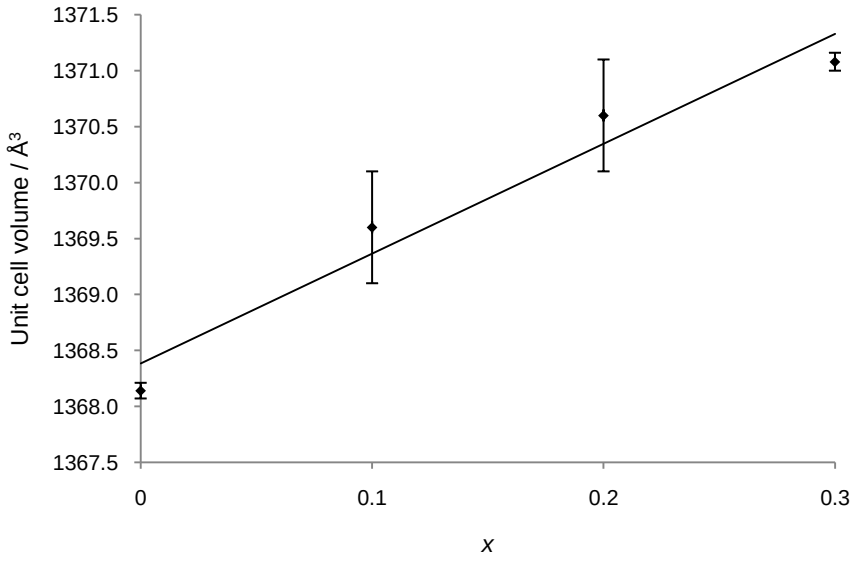

Figure 7-17: Plot of unit cell volume against composition (x) for the $Co_{2-x}Fe_xGeMo_3N$ series

Figure 7-17 demonstrates an almost linear increase in unit cell volume with increasing iron content. This is to be expected given that iron has a larger atomic size than cobalt. The relationship obeys Vegard's law,[148] demonstrating the successful synthesis of this solid solution over the range attempted ($0.1 \leq x \leq 0.3$).

Further compositions in this series could be synthesised to determine the limit of solubility of Fe_2GeMo_3N in Co_2GeMo_3N, although Sviridov *et al*. have already shown that the solid solution exists over the full range of composition.[178] Magnetic susceptibility measurements were also carried out by this research group; $Co_{0.5}Fe_{0.5}GeMo_3N$ was determined to have an antiferromagnetic arrangement of ferromagnetic Co_4 groups over the temperature range of 50 to 200 K.

7.3.3.2 Introduction of Ni into Co_2GeMo_3N ($Co_{2-x}Ni_xGeMo_3N$)

Stoichiometric amounts of cobalt(II,III) oxide, nickel(II) oxide, germanium(IV) oxide and molybdenum(VI) oxide were heated at 700 °C (48 hours), 750 °C (24 hours), 875 °C (24 hours), 975 °C (24 hours) and once more at 975 °C (24 hours) in order to prepare the series $Co_{2-x}Ni_xGeMo_3N$ ($0.1 \leq x \leq 0.3$), with x increasing in increments of 0.1. X-ray powder diffraction patterns were recorded after the final reaction over the range $5 \leq 2\theta/° \leq 70$, with a counting time of 1.0 s per step.

Analysis of the diffraction patterns indicated that an η-carbide phase had formed in each case. Very small amounts of elemental molybdenum were also present in each sample. Rietveld refinement was carried out for all compositions using the structure of Co_3Mo_3N published by Jackson *et al*. as the initial model for the η-carbide phase.[167] The germanium atom was refined on the 16*d* Wyckoff position, and the nickel and cobalt atoms were presumed to be disordered over the 32*e* Wyckoff position, given that ordering of the metal atoms cannot be determined by x-ray powder diffraction. The weight fractions of molybdenum present in each sample were determined to be 0.0040(8), 0.0052(8) and 0.0052(8) for $Co_{1.9}Ni_{0.1}GeMo_3N$, $Co_{1.8}Ni_{0.2}GeMo_3N$ and $Co_{1.7}Ni_{0.3}GeMo_3N$, respectively. The Rietveld fit for $Co_{1.7}Ni_{0.3}GeMo_3N$ is shown in Figure 7-18.

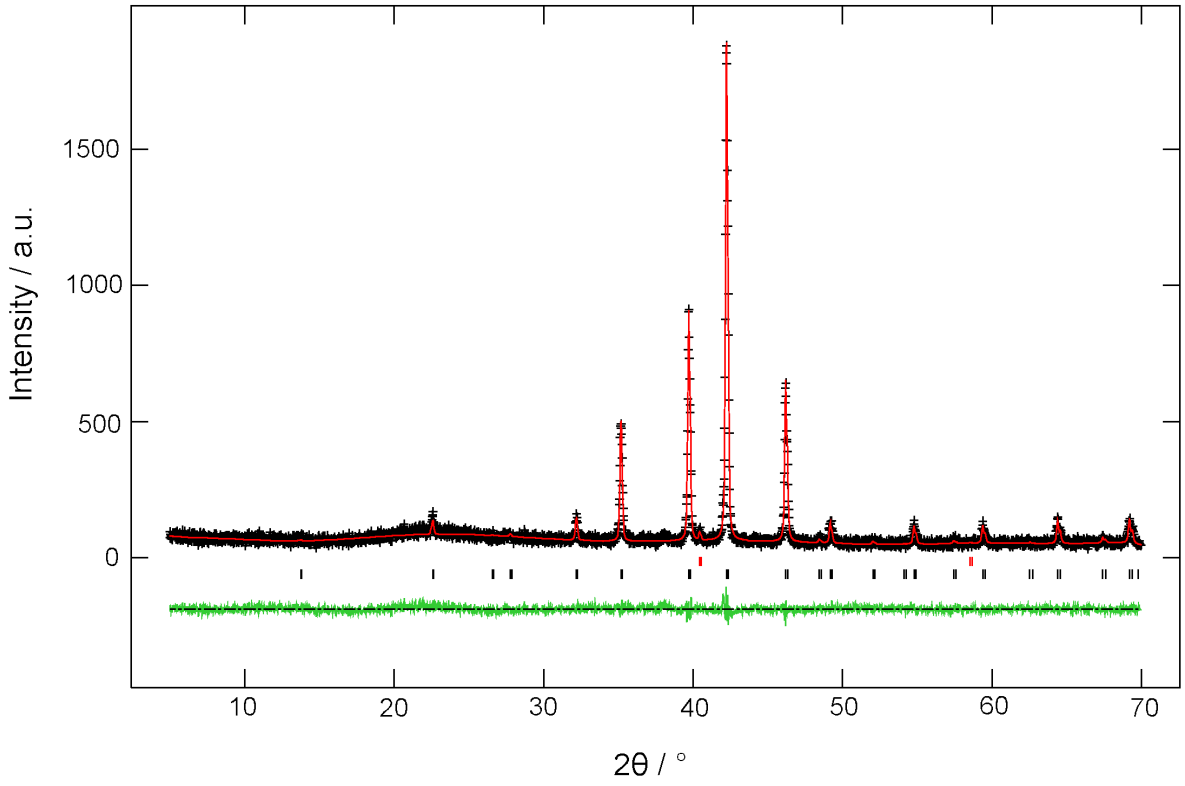

Figure 7-18: Observed (black), calculated (red) and difference (green) x-ray powder diffraction profiles for $Co_{1.7}Ni_{0.3}GeMo_3N$. Lower tick marks indicate positions of allowed reflections for $Co_{1.7}Ni_{0.3}GeMo_3N$. Upper tick marks indicate positions of allowed reflections for Mo

Unit cell data obtained from Rietveld refinement of all compositions in the series are given in Table 7-7.

Composition	x	a / Å	V / Å^3
Co_2GeMo_3N	0	11.1014(2)	1368.14(7)
$Co_{1.9}Fe_{0.1}GeMo_3N$	0.1	11.105(1)	1369.6(5)
$Co_{1.8}Fe_{0.2}GeMo_3N$	0.2	11.108(1)	1370.6(5)
$Co_{1.7}Fe_{0.3}GeMo_3N$	0.3	11.1093(2)	1371.08(8)

Table 7-7: Unit cell data for the $Co_{2-x}Ni_xGeMo_3N$ series

A plot of the unit cell volume against composition was constructed, and is shown in Figure 7-19.

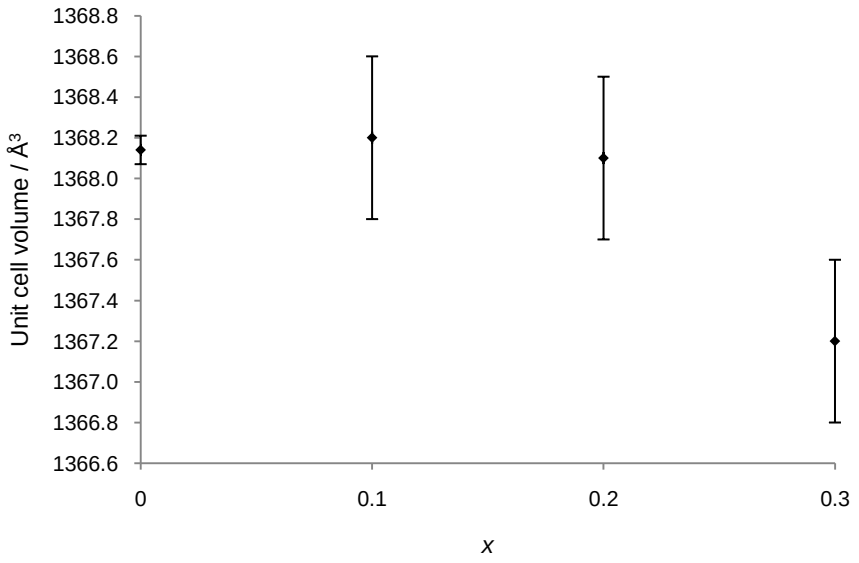

Figure 7-19: Plot of unit cell volume against composition (x) for the $Co_{2-x}Ni_xGeMo_3N$ series

Figure 7-17 demonstrates a general decrease in unit cell volume as the nickel content increases. The relationship is not linear, and so Vegard's law is not obeyed. However, the absence of significant impurities in the diffraction patterns of the products suggests synthesis of the solid solution was successful over the range attempted ($0.1 \leq x \leq 0.3$). In addition, the unit cell volume of the series reported by Sviridov *et al*. did not follow a linear variation with composition either.[178]

Further compositions in this series could be synthesised to determine the limit of solubility of Ni_2GeMo_3N in Co_2GeMo_3N, although Sviridov *et al*. have already shown that the solid solution exists over the full range of composition.[178] Magnetic susceptibility measurements

were also carried out by this research group; no evidence of long-range magnetic order was observed.

7.4 Synthesis of Filled *β*-Manganese Nitrides *via* Reduction-Nitridation

The filled β-manganese nitride, Ni_2Mo_3N, has been previously synthesised using the reduction-nitridation method.[85] In this work the synthesis of Ni_2Mo_3N was reproduced in order to test the synthetic apparatus, and a reaction carried out in order to determine whether a small interstitial (in this case nitrogen) is necessary to stabilise the filled β-manganese structure.

7.4.1 Ni_2Mo_3N

Stoichiometric amounts of nickel(II) oxide and molybdenum(VI) oxide were heated at 700 °C (48 hours), 750 °C (24 hours), 875 °C (24 hours) and 975 °C (24 hours). An x-ray powder diffraction pattern was recorded after the final reaction over the range $5 \leq 2\theta/° \leq 120$, with a counting time of 9.3 s per step.

Analysis of the x-ray diffraction pattern revealed that Ni_2Mo_3N had formed in high purity. Rietveld refinement was carried out using the structure of Ni_2Mo_3N published by Prior and Battle as the initial model.[85] A background subtraction was performed on the data in order to remove the contribution from the excess grease present on the sample mount. Data obtained from the refinement are given in Table 7-8. The Rietveld fit is shown in Figure 7-20.

Ni_2Mo_3N	Refined values			Literature values[85]		
Space group	$P4_132$					
Structure type	Filled β-Mn					
a / Å	6.6351(1)			6.63582(3)		
V / Å^3	292.11(2)			292.200(2)		
Atomic positions	***x***	***y***	***z***	***x***	***y***	***z***
Ni (8*c*)	0.0679(2)	0.0679(2)	0.0679(2)	0.0670(1)	0.0670(1)	0.0670(1)
Mo (12*d*)	⅛	0.2017(1)	0.4517(1)	⅛	0.20153(6)	0.45153(6)
N (4*a*)	⅜	⅜	⅜	⅜	⅜	⅜
Isotropic displacement parameters / Å^2	**Ni**	**Mo**	**N**	**Ni**	**Mo**	**N**
	0.0260(9)	0.0207(4)	0.032(6)	0.0108(9)	0.0086(7)	0.012(3)

R(F^2)	0.0853
χ^2	7.894

Table 7-8: Rietveld refinement data for Ni_2Mo_3N

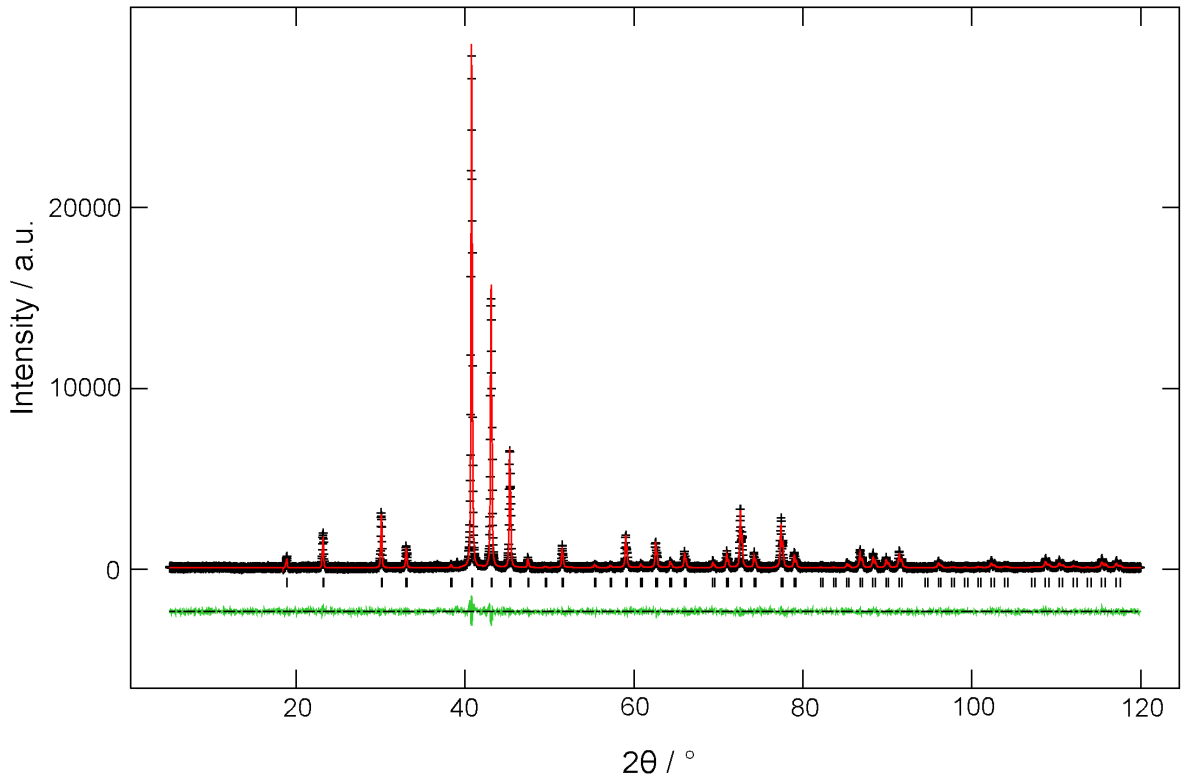

Figure 7-20: Observed (black), calculated (red) and difference (green) x-ray powder diffraction profiles for Ni_2Mo_3N. Tick marks indicate positions of allowed reflections

Although the value of χ^2 is quite high, the visual fit to the data is outstanding (in addition, R(F^2) = 0.0853), demonstrating that Ni_2Mo_3N formed in high purity.

Elemental (CHN) analysis was performed in order to determine the nitrogen content. The expected percentage of nitrogen in Ni_2Mo_3N is 3.34%; the actual percentage determined by elemental analysis was 3.15%. The stoichiometry of the phase according to the results of elemental analysis is therefore $Ni_2Mo_3N_{0.94}$.

7.4.2 Ni_2Mo_3

The synthesis of Ni_2Mo_3 was attempted to establish whether nitrogen is necessary to stabilise the filled β-manganese structure adopted by Ni_2Mo_3N. It was thought that as the

filled β-manganese compound, Ni_2Mo_3N, was synthesised using 10% hydrogen in nitrogen, the synthesis of the unfilled phase, Ni_2Mo_3, might be achieved using 10% hydrogen in argon. It was proposed that this theoretical composition would crystallise with the β-manganese structure, with the 8*c* sites occupied in the filled structure remaining empty.

Stoichiometric amounts of nickel(II) oxide and molybdenum(VI) oxide were heated at 700 °C (48 hours), 750 °C (24 hours), 875 °C (24 hours) and 975 °C (24 hours). An x-ray powder diffraction pattern was recorded after the final reaction over the range $5 \leq 2\theta/° \leq 70$, with a counting time of 1.0 s per step.

Analysis of the x-ray diffraction patterns indicated that a mixture of elemental molybdenum and a Ni-Mo alloy had formed. No phase adopting the β-manganese structure was present. This reaction demonstrated that the presence of 10% hydrogen in nitrogen is crucial to the formation of compounds in this system with a β-manganese metal eutaxy.

The importance of the presence of nitrogen in this reaction, and in the reaction carried out to form the unfilled η-carbide series M_2GeMo_3 (section 7.3.2), suggests that the interstitial atom in the M_2GeMo_3N series and in Ni_2Mo_3N is nitrogen rather than another interstitial atom such as oxygen. Results from CHN analysis reported earlier support this conclusion.

7.5 Precursor Routes to Binary Transition Metal Nitrides

This section of the chapter describes work carried out on the attempted synthesis of binary transition metal nitrides *via* the use of urea, either complexed to a transition metal centre or reacted at moderate temperature with binary metal oxides.

Urea ($(NH_2)_2C=O$) is capable of forming strong hydrogen bonds because of its donor (amine) and acceptor (carbonyl) functional groups. Urea can also bind to metal cations as a neutral ligand. A distinct preference for binding through the carbonyl oxygen atom rather than the amidic nitrogen atom is apparent, and this is likely to be due to the unavailability of the lone pair of electrons on the nitrogen. Urea complexes of this type frequently contain the ion $M(urea)_6^{n+}$, and sometimes the ion $M(urea)_4(H_2O)_2^{n+}$. Examples include $[Mn(urea)_6][ClO_4]_3$,[183] $[Mn(urea)_6][ClO_3]_2$ (*sic*),[184] $[Ni(urea)_4(H_2O)_2][NO_3]_2$ and $[Co(urea)_4(H_2O)_2][NO_3]_2$.[185]

Urea has been shown by Gomathi to be a nitriding source when mixed in excess with transition metal oxides (discussed in section 7.1.1).[171] It is likely that the thermal treatment of urea generates ammonia, which is thought to be the active nitriding species. In addition, certain binary metal nitrides including AlN, CrN and ζ-Fe_2N have been synthesised *via* heating metal-urea complexes under ammonia or nitrogen at temperatures of between 300-1000 °C.[186] In this work, this synthetic route was adapted in an attempt to form binary nitrides *via* heating metal-urea complexes under 10% hydrogen in nitrogen; the idea was to introduce a source of ammonia at the metal centre. Production of ammonia from urea may occur by protonation of the $-NH_2$ moieties on the urea molecules. Crystalline metal urea complexes prepared include $[Cr(urea)_4(H_2O)_2][NO_3]_3$, $[Fe(urea)_6][NO_3]_3$, $Cu(urea)_2(H_2O)_3(NO_3).(urea).(NO_3)$, $[Zn(urea)_4(H_2O)_2][NO_3]_2$, $[Co(urea)_4(H_2O)_2][NO_3]_2$ and $[Ni(urea)_4(H_2O)_2][NO_3]_2$. Their crystal structures and products of reduction are reported in the following sections. In addition, the synthetic route to ternary nitrides reported by Gomathi[171] was adapted in an attempt to synthesise binary nitrides by heating binary metal oxides with urea.

7.5.1 Preparation and Thermal Treatment of Transition Metal Urea Nitrate Complexes

Single crystals were prepared using the method outlined in section 2.1.2. Data used for the structural refinement of $[Cr(urea)_4(H_2O)_2][NO_3]$ and $[Fe(urea)_6][NO_3]$ were collected at the EPSRC National Crystallography Service in Southampton on a Bruker-Nonius KappaCCD diffractometer operating with Mo Kα radiation. The crystals were cooled to 120 K using an Oxford cryosystems Cobra nitrogen gas stream. Data for all other structures were collected at 150 K on a Stoe IPDS II diffractometer operating with Mo K radiation, as stated in section 2.2.4.1.

7.5.1.1 $[Cr(urea)_4(H_2O)_2][NO_3]_3$

A 1:4 stoichiometric mixture of chromium(III) nitrate nonahydrate (1.556 g, 3.889 mmol) and urea (0.9345 g, 15.56 mmol) was dissolved in ethanol (100 ml). Room temperature evaporation yielded a powder. Following re-dissolution in warm water and subsequent room temperature evaporation, pale green crystals of $[Cr(urea)_4(H_2O)_2][NO_3]_3$ formed.

The metal urea nitrate $[Cr(urea)_4(H_2O)_2][NO_3]_3$ crystallises in the centrosymmetric space group $P2_1/c$ with the unit cell parameters a = 18.3338(4) Å, b = 16.5472(4) Å, c = 13.9252(3) Å, β = 106.326(1)° and V = 4054.2(2) Å^3 with Z = 8, in a primitive but close to C-centred unit cell. Selected data from the structural refinement are given in Table 7-9. Full data from the refinement are given in the Appendix.

Empirical formula	$C_4H_{20}CrN_{11}O_{15}$	**Space group**	$P2_1/c$
***a* / Å**	18.3338(4)	**Crystal system**	Monoclinic
***b* / Å**	16.5472(4)	**Z**	8
***c* / Å**	13.9252(3)	**R(int)**	0.050
***β* / °**	106.326(1)	**Final R indices [I>2sigma(I)]**	R1 = 0.0613, wR2 = 0.1149
***V* / Å^3**	4054.19(16)	**R indices (all data)**	R1 = 0.0904, wR2 = 0.1303

Table 7-9: Selected data from the structural refinement of $[Cr(urea)_4(H_2O)_2][NO_3]_3$

Hydrogen atoms of water were located from the Fourier difference map, and subject to the restraint that all of the O-H bond lengths should be equal within a standard deviation of 0.03 Å. Hydrogen atoms of urea were placed using a riding model with the N-H distance fixed at 0.88 Å.

The asymmetric unit contains two symmetry independent $Cr(urea)_4(H_2O)_2^{3+}$ ions, both located on general positions, in addition to six unbound nitrate anions. A representation of the asymmetric unit is shown in Figure 7-21.

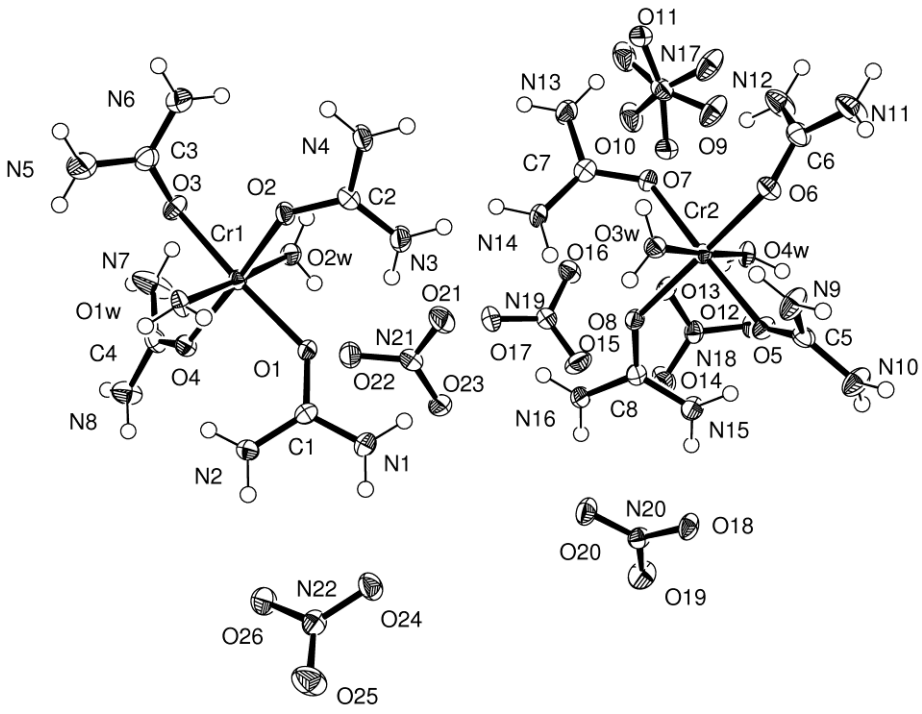

Figure 7-21: Asymmetric unit of $[Cr(urea)_4(H_2O)_2][NO_3]_3$ highlighting the two symmetry independent $Cr(urea)_4(H_2O)_2^{3+}$ ions and the six unbound nitrate anions

Each symmetry independent $Cr(urea)_4(H_2O)_2^{3+}$ ion is pseudo-octahedral; each Cr^{3+} ion is coordinated by two trans water molecules and four urea molecules bound through the oxygen atom in a close to square planar arrangement. The differences in bond lengths between Cr^{3+} ions and bound water are small: the two Cr1-OH_2 distances are 1.972(2) and 1.974(2) Å, while the two Cr2-OH_2 distances are 1.977(2) and 1.982(2) Å. In addition, the mean value of the Cr-O bond length between Cr^{3+} ions and urea is 1.957(2) Å; no systematic variation in these distances is present. Intramolecular hydrogen bonding between the bound urea molecules is limited. This is in contrast to other structures containing similar ions, such as $[Zn(urea)_4(H_2O)_2][NO_3]_2$ (discussed later), where there are short N-H···O contacts between bound ureas (N···O distances are 2.813(2) and 2.845(3) Å). There are three intramolecular N-H···O contacts between urea molecules bound to Cr1, with N···O distances of 2.843(4), 2.888(4) and 2.937(4) Å. The fourth molecule of urea is significantly twisted away from the plane, and therefore does not form hydrogen bonds between other bound urea molecules. There are also three intramolecular N-H···O contacts

between urea molecules bound to Cr2, with N···O distances of 2.820(4), 2.8978(4) and 3.037(4) Å. The fourth urea molecule is aligned away from the plane and so does not form hydrogen bonds between other bound urea molecules. However, it does form a short contact to bound water (N9···O3w), where the N···O distance is 2.983(4) Å. There is significant intermolecular hydrogen bonding between unbound nitrate anions and bound urea and water, which results in the formation of a 3D array; the three oxygen atoms of every nitrate act as hydrogen bond acceptors to urea and water. In addition, all but one N-H functions on the urea molecules act as hydrogen bond donors. One nitrate anion (central atom labelled N17) displays small-scale rotational disorder. The two nitrate orientations (major = 94.0(3)%) are offset by 52.9(10)°.

There are systematic weaknesses in the data for $h+k = 2n+1$, which imply that the unit cell is C-centred. However, the data are not absent, they are just weak, and attempts to solve the structure in a C-centred unit cell were unsatisfactory. The unit cell was therefore determined to be primitive, but close to C-centred. This is clear when considering the positions of Cr1 and Cr2 within the unit cell: Cr1 is located on (0.48837, 0.72417, 0.1823) and Cr2 is located on (0.0167, 0.7223, 0.312). $Cr2^{i}$ is generated by applying a symmetry operation of the space group ($-x$, $y-½$, $-z+½$) so that its coordinates are (−0.0167, 0.2223, 0.188). Applying a C-centring translation ($x+½$, $y+½$, z) generates a position (0.4833, 0.7223, 0.188) that is very close to that of Cr1. The Cr^{3+} ions therefore adopt an array which is close to being C-centred. However, small deviations away from C-centring occur by the ligands bound to each Cr^{3+} ion and by the charge-balancing nitrate, giving rise to the correct primitive symmetry.

The two symmetry independent $Cr(urea)_4(H_2O)_2^{3+}$ ions were overlaid by applying a cell-centring translation to Cr2 and all atoms bound to it. This is represented in Figure 7-22 and therefore demonstrates the absence of C-centring. The labelled atoms are the atoms attached to Cr1 which show the most deviation from the atoms attached to Cr2. This deviation could be quantified by examining the atomic coordinates of the atoms present in each molecule.

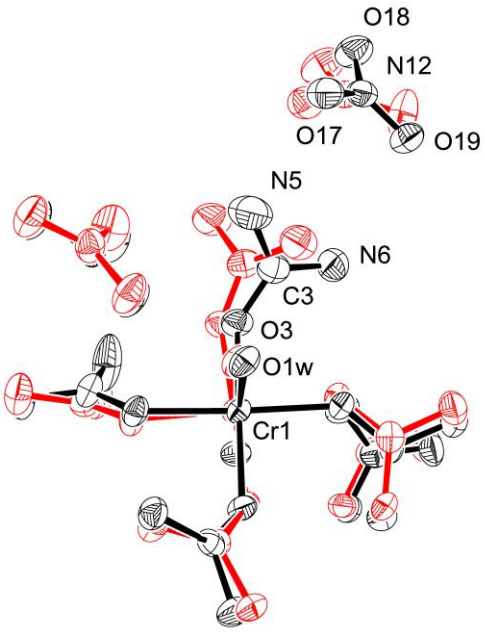

Figure 7-22: Diagram highlighting the different nitrate orientations about Cr1 and Cr2 (with hydrogen atoms omitted), and therefore the absence of C-centring

Thermal treatment of ground crystals of $[Cr(urea)_4(H_2O)_2][NO_3]_3$ under 10% hydrogen in nitrogen at 300 °C for 3 hours yielded Cr_2O_3. This is not surprising given the stability of this oxide.

7.5.1.2 $[Fe(urea)_6][NO_3]_3$

A 1:4 stoichiometric mixture of iron(III) nonahydrate (1.770 g, 4.385 mmol) and urea (1.053g, 17.54 mmol) was dissolved in 50% aqueous ethanol (100 ml). Room temperature evaporation of the solvent yielded orange crystals of $[Fe(urea)_6][NO_3]_3$.

The metal urea nitrate $[Fe(urea)_6][NO_3]_3$ crystallises in the non-centrosymmetric space group *C*2, with unit cell parameters a = 51.576(2) Å, b = 18.7325(8) Å, c = 12.1403(5) Å, β = 93.627(2)° and V = 11705.8(8) Å^3 with Z = 20. The true unit cell of $[Fe(urea)_6][NO_3]_3$ is a large C-centred cell which is closely related to a smaller cell of one fifth the volume, previously reported for an analogous structure ($[Co(urea)_6][NO_3]_3$).[187] Selected data from the structural refinement are given in Table 7-10. Full data from the refinement are given in the Appendix.

Empirical formula	$C_6H_{24}FeN_{15}O_{15}$	**Space group**	*C*2
***a* / Å**	51.576(2)	**Crystal system**	Monoclinic
***b* / Å**	18.7325(8)	**Z**	20
***c* / Å**	12.1403(5)	**R(int)**	0.096
***β* / °**	93.627(2)	**Final R indices [I>2sigma(I)]**	R1 = 0.0956, wR2 = 0.1691
***V* / Å^3**	11705.8(8)	**R indices (all data)**	R1 = 0.1777, wR2 = 0.2144

Table 7-10: Selected data from the structural refinement of $[Fe(urea)_6][NO_3]_3$

Hydrogen atoms were placed using a riding model with the N-H distance fixed at 0.88 Å.

There are six symmetry independent Fe^{3+} ions in the asymmetric unit, and each is surrounded by six urea molecules in approximately octahedral geometry. In addition, there are unbound charge-balancing nitrate anions. A representation of the coordination around one of the Fe^{3+} ions is shown in Figure 7-23.

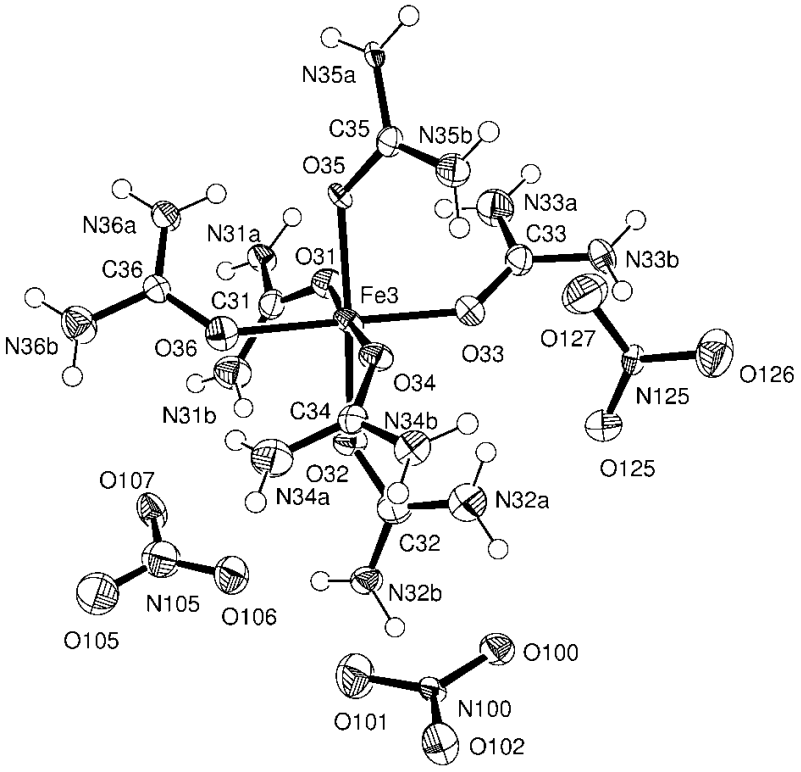

Figure 7-23: Portion of the asymmetric unit in $[Fe(urea)_6][NO_3]_3$, representing the coordination around an Fe^{3+} ion

Four of the six Fe^{3+} ions in the asymmetric unit are located on general positions (4*c* Wyckoff) and are surrounded by six urea molecules bound through the oxygen atom. The remaining two Fe^{3+} ions are located on the two-fold axis (2*a* and 2*b* Wyckoff) and are coordinated by three urea molecules. The two-fold axis generates the remaining urea molecules to complete the coordination about each Fe^{3+} ion. This arrangement gives rise to a Z' value equal to 5. In addition to the five $Fe(urea)_6^{3+}$ ions there are a total of 15 independent nitrate anions; 14 of these are located on general positions; two are located on the two-fold axis. The asymmetric unit of $[Fe(urea)_6][NO_3]_3$ is shown in Figure 7-24.

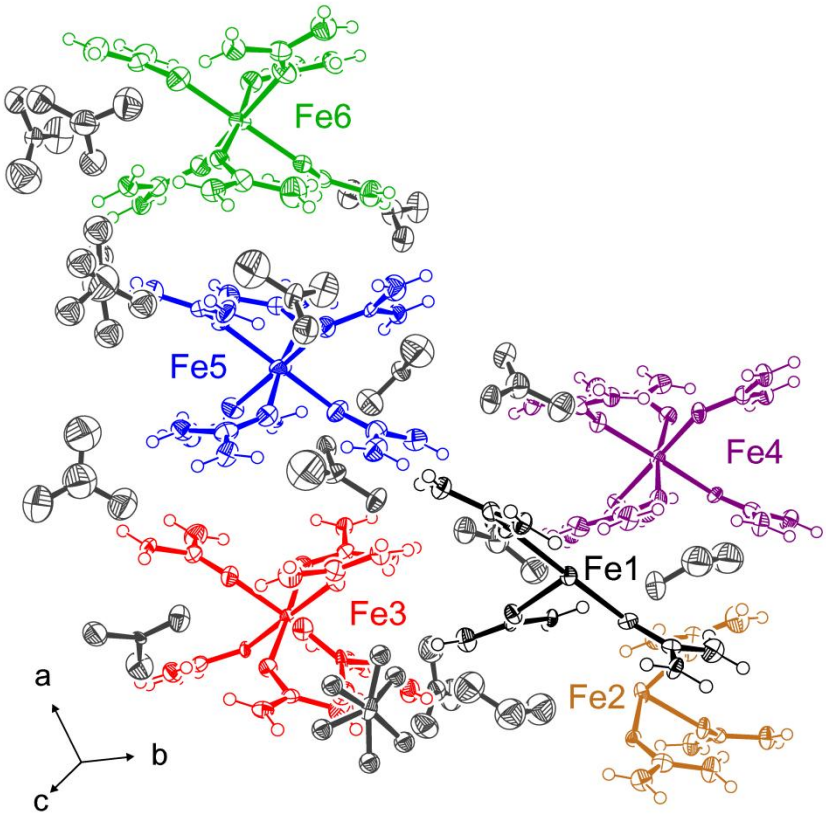

Figure 7-24: Asymmetric unit of $[Fe(urea)_6][NO_3]_3$. For clarity, each symmetry independent $Fe(urea)_6^{3+}$ ion is in a different colour; the nitrate anions are in grey

The 36 independent Fe-O bonds in the structure have a mean of 1.996(9) Å, with the standard deviation of the actual values equal to 0.019 Å, signifying a narrow distribution in these bond lengths.

There are some short intramolecular N-H···O hydrogen bonds between urea molecules on the same ion. In addition, each urea molecule is involved in the formation of N-H···O bonds to free nitrate.

The structure of $[Co(urea)_6][NO_3]_3$ reported by Durski and Gibinski is related to the structure of $[Fe(urea)_6][NO_3]_3$ reported here.[187] Initial attempts to index the diffraction images of $[Fe(urea)_6][NO_3]_3$ resulted in the small cell reported by Durski and Gibinski, but close inspection of the images revealed the presence of weaker reflections not consistent with the smaller cell. By including the weaker reflections in the indexing, the larger unit cell resulted. The small cell is pseudo C-centred and can be converted to the large cell by a five-fold expansion. This gives rise to a cell that is truly C-centred.

Thermal treatment of ground crystals of $[Fe(urea)_6][NO_3]_3$ under 10% hydrogen in nitrogen at 300 °C for 3 hours yielded a mixture of iron oxides.

7.5.1.3 $Cu(urea)_2(H_2O)_3(NO_3).(urea).(NO_3)$

A 1:4 stoichiometric mixture of copper(II) nitrate trihydrate (1.042 g, 4.313 mmol) and urea (1.035 g, 17.25 mmol) was dissolved in 70% aqueous ethanol (100 ml) with gentle warming. This yielded blue crystals of $Cu(urea)_2(H_2O)_3(NO_3).(urea).NO_3$ upon evaporation at room temperature.

The metal urea nitrate $Cu(urea)_2(H_2O)_3(NO_3).(urea).(NO_3)$ crystallises in the space group $P2_1/m$ with the unit cell parameters a = 9.489(3) Å, b = 13.059(3) Å, c = 7.103(2) Å, β = 100.28(3)° and V = 866.1(4) Å^3 with Z = 2. Selected data from the structural refinement are given in Table 7-11. Full data from the refinement are given in the Appendix.

Empirical formula	$C_4H_{21.27}CuN_{10}O_{12.64}$	**Space group**	$P2_1/m$
***a* / Å**	9.489(3)	**Crystal system**	Monoclinic
***b* / Å**	13.059(3)	**Z**	2
***c* / Å**	7.103(2)	**R(int)**	0.0774
***β* / °**	100.28(3)	**Final R indices [I>2sigma(I)]**	R1 = 0.0460, wR2 = 0.1098
***V* / Å^3**	866.1(4)	**R indices (all data)**	R1 = 0.0729, wR2 = 0.1203

Table 7-11: Selected data from the structural refinement of $Cu(urea)_2(H_2O)_3(NO_3).(urea).(NO_3)$

All hydrogen atoms were located from the Fourier difference map. All N-H bond lengths were restrained to be equal with a standard deviation of 0.03 Å. O-H bond lengths in bound water molecules were restrained to be 0.82(3) Å.

There is significant disorder in the species bound to the Cu^{2+} ion, leading to a major and minor orientation; the major form has the composition $Cu(urea)_2(H_2O)_3(NO_3).(urea).(NO_3)$. The Cu^{2+} ion in the major form is 6-coordinate, and is bound in a planar arrangement by two urea molecules and two water molecules in a *trans* fashion (Cu-O distances are 1.931(4) Å and 1.938(2) Å, respectively). A distorted octahedron is formed by two additional longer Cu-O distances to loosely bound nitrate and water (Cu-O distances are 2.577(6) Å and 2.441(6) Å, respectively). The loose binding of water and nitrate can be attributed to the elongation of the complex *via* Jahn-Teller distortion, a result of the presence of an unpaired electron in the e_g orbitals of the d^9 Cu^{2+} ion. The loosely bound nitrate exists in a second (and minor) orientation, with an occupancy of 0.363(6), and is related to the major nitrate by a displacement of 0.491(15) Å and a rotation of approximately 60°. In this position, the minor nitrate does not bind to the copper, and there is a close approach of an oxygen atom on the minor nitrate (O20B) with the oxygen atom (O3w) of the loosely bound water on the adjacent copper ion. This, coupled with an anomalously large displacement parameter for O3w when in the minor orientation suggests partial occupancy. O3w is therefore only present when the nitrate is in the major orientation. When the nitrate is in the minor orientation the formula is $Cu(urea)_2(H_2O)_2.(urea).(NO_3)_2$. A diagram of the coordination about the copper ion including both the major and minor nitrate orientations is shown in Figure 7-25.

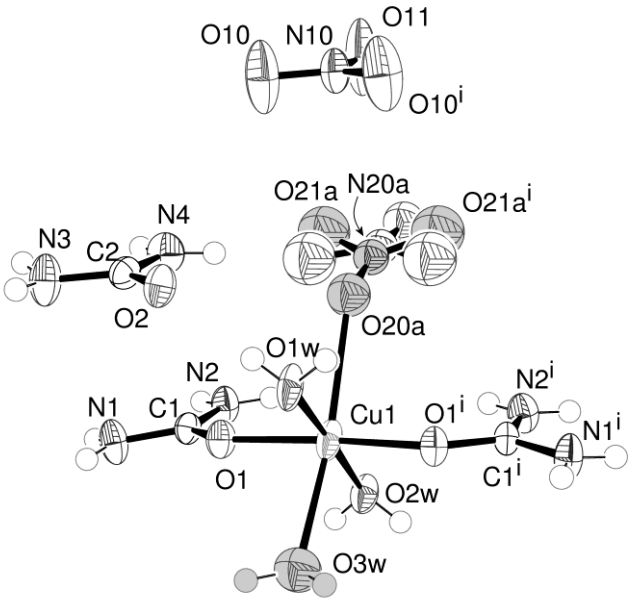

Figure 7-25: Coordination about the copper ion in $Cu(urea)_2(H_2O)_3(NO_3).(urea).(NO_3)$. The major nitrate and accompanying bound water are shaded in grey. The minor nitrate is unshaded. Atoms labelled *i* are a result of the symmetry operation $x, -y + ½, z$

Intramolecular hydrogen bonding is present between the many bound urea, bound nitrate and water molecules in the structure. Intermolecular hydrogen bonding between species bound to the copper and unbound nitrate and urea enables the formation of a 3D array. In particular, there is significant hydrogen bonding between the disordered nitrate anions and unbound urea molecules. This is highlighted in Figure 7-26.

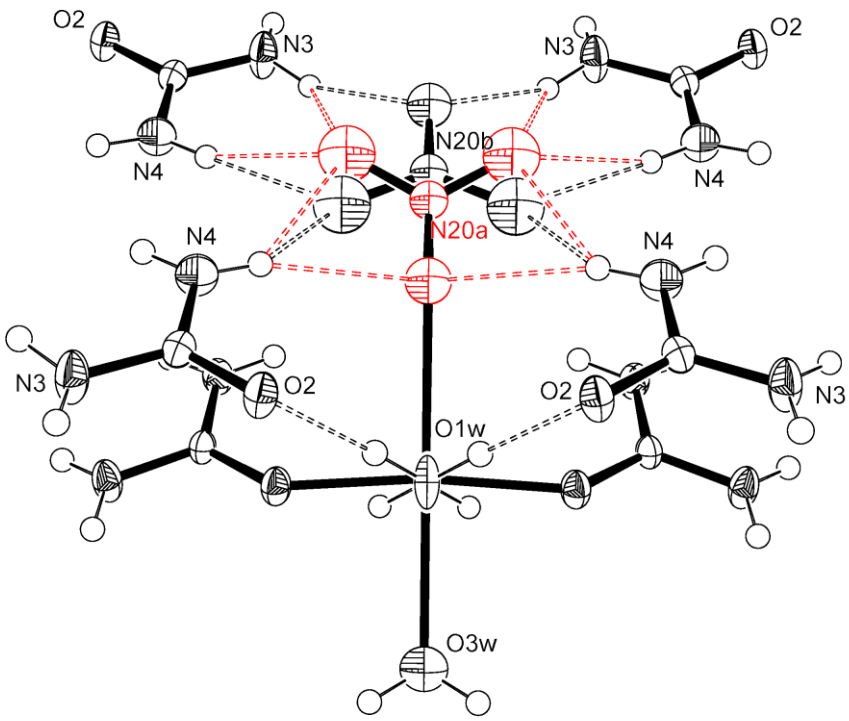

Figure 7-26: Representation of the hydrogen bonding between the disordered nitrate anions and the unbound urea molecules. The major nitrate (central atom N20a) is highlighted in red

Figure 7-26 demonstrates the hydrogen bonding between the major nitrate and the unbound urea (O21A···N4), but more so the hydrogen bonding between the minor nitrate and the unbound urea (O20B···N3 and O21B···N4). In addition, the binding of the major nitrate to the Cu^{2+} centre is augmented by hydrogen bonding to the hydrogen atoms attached to O3w.

Thermal treatment of ground crystals of $Cu(urea)_2(H_2O)_3(NO_3).(urea).(NO_3)$ under 10% hydrogen in nitrogen at 300 °C for 3 hours yielded elemental copper.

7.5.1.4 $[Zn(urea)_4(H_2O)_2][NO_3]_2$

A 1:4 stoichiometric mixture of zinc(II) nitrate hexahydrate (0.2566 g, 0.8626 mmol) and urea (0.2070 g, 3.45 mmol) was dissolved in 70% aqueous ethanol (100 ml) with gentle warming. This yielded colourless crystals of $[Zn(urea)_4(H_2O)_2][NO_3]_2$ upon evaporation at room temperature.

The metal urea nitrate $[Zn(urea)_4(H_2O)_2][NO_3]_2$ is isostructural to nickel and cobalt analogues described in later sections, and crystallises in the space group $P2_1/n$ with the unit

cell parameters a = 6.424(1) Å, b = 17.690(4) Å, c = 7.588(1) Å, β = 91.14(1)° and V = 862.1(3) Å^3 with Z = 2. Selected data from the structural refinement are given in Table 7-12. Full data from the refinement are given in the Appendix.

Empirical formula	$C_4H_{20}N_{10}O_{12}Zn$	**Space group**	$P2_1/n$
***a* / Å**	6.4239(11)	**Crystal system**	Monoclinic
***b* / Å**	17.690(4)	**Z**	2
***c* / Å**	7.5877(13)	**R(int)**	0.0763
***β* / °**	91.138(14)	**Final R indices [I>2sigma(I)]**	R1 = 0.0353, wR2 = 0.0791
***V* / Å^3**	862.1(3)	**R indices (all data)**	R1 = 0.0549, wR2 = 0.0844

Table 7-12: Selected data from the structural refinement of $[Zn(urea)_4(H_2O)_2][NO_3]_2$

All hydrogen atoms were located from the Fourier difference map. Chemically equivalent N-H and O-H bonds were restrained to be equal with a standard deviation of 0.03 Å.

The Zn^{2+} ion is 6-coordinate, with four urea molecules in an approximately planar arrangement, and water molecules bound in a *trans* fashion. Unbound charge balancing nitrate is also present. There is significant intramolecular hydrogen bonding, in particular between urea molecules bound to the same Zn^{2+} centre. This is depicted in Figure 7-27.

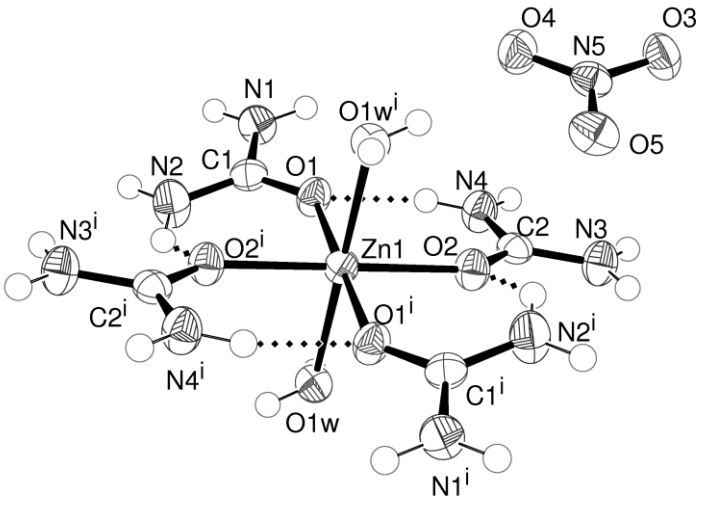

Figure 7-27: Coordination about the Zn^{2+} ion in $[Zn(urea)_4(H_2O)_2][NO_3]_2$. Hydrogen bonding between urea molecules is depicted by dotted lines. Atoms labelled *i* are a result of the symmetry operation $-x, -y, -z$

Zn-O bond lengths between Zn^{2+} and bound urea are 2.0892(14) and 2.0754(15) Å, and 2.1446(16) Å between Zn^{2+} and bound water. These bond lengths are similar to those reported for analogous cobalt and nickel compounds (discussed later), although slightly longer, which is expected given the larger ionic radius of Zn^{2+}.[188]

Intermolecular hydrogen bonding between urea, water and nitrate assembles the $[Zn(urea)_4(H_2O)_2]^{2+}$ ions into stacks which are one extended cation wide and are extended parallel to [001]. A representation of this is shown in Figure 7-28.

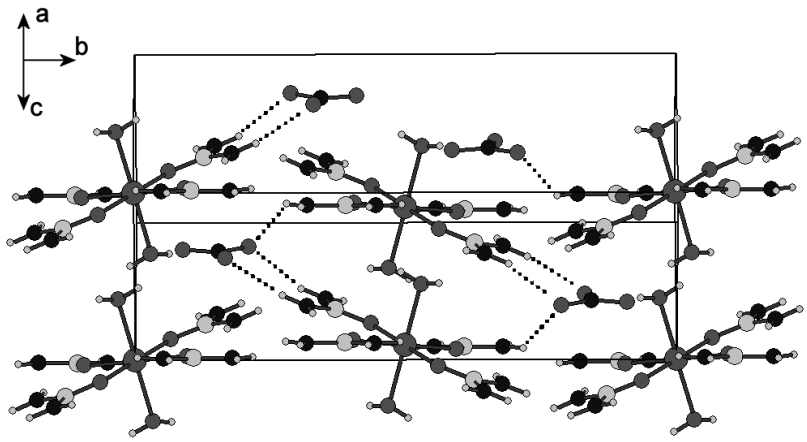

Figure 7-28: Representation of the intermolecular hydrogen bonding in $[Zn(urea)_4(H_2O)_2][NO_3]_2$ resulting in the formation of stacks aligned parallel to [001]

Thermal treatment of ground crystals of $[Zn(urea)_4(H_2O)_2][NO_3]_2$ under 10% hydrogen in nitrogen at 300 °C for 3 hours yielded ZnO. This is not surprising given the stability of this oxide.

7.5.1.5 $[Co(urea)_4(H_2O)_2][NO_3]_2$

A 1:4 stoichiometric mixture of cobalt(II) nitrate hexahydrate (1.268 g, 4.356 mmol) and urea (1.046 g, 17.42 mmol) was dissolved in 70% aqueous ethanol (100 ml). This yielded pink crystals of $[Co(urea)_4(H_2O)_2][NO_3]_2$ upon evaporation at room temperature.

At the time of structure solution (September 2007), a report of the crystal structure of $[Co(urea)_4(H_2O)_2][NO_3]_2$ appeared elsewhere (Krawczuk and Stadnicka, October 2007).[185] The complex crystallises in the space group $P2_1/n$, and is isostructural with the zinc analogue discussed in the previous section. The lattice parameters of

$[Co(urea)_4(H_2O)_2][NO_3]_2$ were compared to those reported by Krawczuk and Stadnicka[185] and were not significantly different.

Thermal treatment of ground crystals of $[Co(urea)_4(H_2O)_2][NO_3]_2$ under 10% hydrogen in nitrogen at 300 °C for 3 hours yielded a foam, which could not be characterised by x-ray powder diffraction.

7.5.1.6 $[Ni(urea)_4(H_2O)_2][NO_3]_2$

A 1:4 stoichiometric mixture of nickel(II) nitrate hexahydrate (1.267 g, 4.358 mmol) and urea (1.047 g, 17.43 mmol) was dissolved in ethanol (100 ml). After room temperature evaporation of the solvent, the powder was re-dissolved in warm water. This yielded pale green crystals of $[Ni(urea)_4(H_2O)_2][NO_3]_2$ upon evaporation at room temperature.

At the time of structure solution (September 2007), a report of the crystal structure of $[Ni(urea)_4(H_2O)_2][NO_3]_2$ appeared elsewhere (Krawczuk and Stadnicka, October 2007).[185] The complex crystallises in the space group $P2_1/n$, and is isostructural with the zinc analogue discussed earlier. Lattice parameters of $[Ni(urea)_4(H_2O)_2][NO_3]_2$ were determined to be a = 6.407(4) Å, b = 17.650(7) Å, c = 7.543(5) Å, β = 91.43(5)° and V = 852.7(8) Å^3 with Z = 2, which are similar to those reported by Krawczuk and Stadnicka.[185]

All hydrogen atoms were located from the Fourier difference map. All N-H and O-H bond lengths were restrained to be equal with a standard deviation of 0.03 Å.

Data from the structural refinement of $[Ni(urea)_4(H_2O)_2][NO_3]_2$ are given in the Appendix.

Thermal treatment of ground crystals of $[Ni(urea)_4(H_2O)_2][NO_3]_2$ under 10% hydrogen in nitrogen at 300 °C for 3 hours yielded elemental nickel.

7.5.2 Reaction of Transition Metal Nitrates with Urea

The method developed by Gomathi[171] for the formation of ternary interstitial molybdenum nitrides *via* the reaction of transition metal molybdate precursors with urea was adapted in an attempt to synthesise binary transition metal nitrides.

Stoichiometric amounts of hydrated transition metal nitrates with urea were ground in a 1:12 molar ratio and heated under a flow of 10% hydrogen in nitrogen at 800 °C for

3 hours. The products were ground and characterised by x-ray powder diffraction. This method did not result in the formation of binary transition metal nitrides, as shown in Table 7-13.

Metal nitrate	Product
$Cr(NO_3)_3.9H_2O$	Amorphous
$Mn(NO_3)_2.4H_2O$	MnO
$Fe(NO_3)_3.9H_2O$	Iron
$Co(NO_3)_2.6H_2O$	Cobalt
$Ni(NO_3)_2.6H_2O$	Nickel
$Cu(NO_3)_2.3H_2O$	Copper

Table 7-13: Products of the reaction of selected transition metal nitrates with urea under 10% hydrogen in nitrogen

7.6 Summary

The η-carbide phases Fe_2GeMo_3N, Co_2GeMo_3N and Ni_2GeMo_3N were synthesised in high purity. Fe_2GeMo_3N and Ni_2GeMo_3N were determined to be Pauli paramagnets. Co_2GeMo_3N exhibited quite different magnetic behaviour, and was determined by Sviridov *et al*. to undergo a transition to a spin-glass state at 8 K.[178] Attempts to synthesise the corresponding phases without the presence of nitrogen confirmed that nitrogen is necessary to stabilise the η-carbide structure. Attempts to form solid solutions of η-carbide nitrides were successful: $Co_{2-x}Fe_xGeMo_3N$ and $Co_{2-x}Ni_xGeMo_3N$ were synthesised in high purity between $0.1 \leq x \leq 0.3$. These solid solutions have been reported over the full range of composition.[178]

Synthesis of the filled β-manganese nitride Ni_2Mo_3N was reproduced from the literature. Attempts to synthesise Ni_2Mo_3 demonstrated that an interstitial atom, in this case nitrogen, is necessary to stabilise the filled β-manganese structure.

Metal urea nitrate complexes of the compositions $[Cr(urea)_4(H_2O)_2][NO_3]_3$, $[Fe(urea)_6][NO_3]_3$, $Cu(urea)_2(H_2O)_3(NO_3).(urea).(NO_3)$, $[Zn(urea)_4(H_2O)_2][NO_3]_2$, $[Co(urea)_4(H_2O)_2][NO_3]_2$ and $[Ni(urea)_4(H_2O)_2][NO_3]_2$ were prepared. Thermal treatment of the complexes under 10% hydrogen in nitrogen did not result in the formation of binary

transition metal nitrides. It is likely that this was a result of binding of urea to the metal centre through the oxygen atom, rather than a nitrogen atom. In addition, the thermal treatment of transition metal nitrates with urea under 10% hydrogen in nitrogen did not yield binary transition metal nitrides.

8.0 Conclusions

The work described in this thesis demonstrates that a new route to binary and ternary transition metal antimonides has been developed. Binary antimonides synthesised in high purity include the nickel arsenide phases NiSb and CoSb, the skutterudite phase $CoSb_3$, and also Cu_2Sb and SnSb. A degree of control over stoichiometry was noted when preparing binary antimonides. In addition, some other binary intermetallic compounds have been synthesised using this route, including impure iron germanides and nickel bismuthides. Substitutions in the high purity binary antimonides prepared were carried out in an attempt to prepare new compounds that may have useful technological properties, such as thermoelectric behaviour. The results of these are summarised below.

In the nickel arsenide system, the solid solution $Co_{1-x}Ni_xSb$ was prepared over the full composition range. As more nickel was introduced into the structure the unit cell expanded in an anisotropic fashion: on the whole the unit cell length *a* increased and the unit cell length *c* decreased. This interesting behaviour was compounded by a very interesting variation in Sb-Sb bond length observed across the series: the Sb-Sb bond length decreased to a minimum at $x = 0.5$. This trend could be explained by proposing filled, unfilled and half-filled Sb-derived bands in certain compositions in the series. Calculation of the density of states of these materials should be carried out in order to confirm this. No other ternary antimonides were prepared over the full range of composition. However, a reasonable amount of copper (up to $x = 0.4$) was introduced into NiSb. Ternary tellurides prepared in the nickel arsenide system could not be prepared over the full range of composition. However, the solid solution of NiTe in CoTe displayed miscibility over all values of *x* except $x = 0.75$. The Te-Te bond lengths in this series varied in a significantly different fashion from the Sb-Sb bond lengths in the analogous antimonide series ($Co_{1-x}Ni_xSb$), increasing as the amount of nickel in the structure was increased. This was one of the most striking results presented in this chapter. The reason for the different variations in metalloid-metalloid bond lengths is likely to be uncovered by carrying out density of states calculations. In both $CoSb_{1-x}Te_x$ and $NiSb_{1-x}Te_x$, nickel arsenide phases formed over a range of composition. It is likely that by maximising the mixing at each grinding step these compositions could be formed as single phases.

One of the greatest successes of this work was the preparation of the solid solution of $RhSb_3$ in $CoSb_3$ over the full range of miscibility. Previous reports have either been limited in the extent of substitution or in the purity of products. The thermoelectric behaviour of this series should be examined; it is likely that the introduction of rhodium into the structure will have resulted in a decrease in the thermal conductivity of the materials, and therefore an increase in the thermoelectric behaviour. In contrast, the solid solution of $IrSb_3$ in $CoSb_3$ was inaccessible in pure form using this synthetic route. It is likely that this was a result of the larger size of iridium atoms with respect to rhodium atoms. A small amount of tin was also able to be introduced onto the antimony site in $CoSb_3$, although it was not possible to identify the exact amount.

Many attempts at introducing various atoms into Cu_2Sb were carried out. However, only a small amount of nickel could be incorporated into the structure. The determination of the exact amount of nickel in the structure was complicated by the presence of impurities.

The work described in this thesis has demonstrated that the reduction of binary metal oxides under 10% hydrogen in argon can be applied to the synthesis of various binary and ternary metal antimonides. It is therefore likely that the route can be extended to the synthesis of other intermetallic compounds incorporating alternative metalloid elements, such as metal stannides, tellurides and arsenides. This could be a starting point for further work.

Work carried out on the synthesis of η-carbide and filled β-manganese nitrides was quite fruitful. The germanium-substituted η-carbide nitrides Fe_2GeMo_3N, Co_2GeMo_3N and Ni_2GeMo_3N were prepared and their magnetic behaviour studied. The synthesis, structures and magnetic behaviour observed are in agreement with other work on these compounds published whilst this work was underway.[178] Fe_2GeMo_3N and Ni_2GeMo_3N were determined to be Pauli paramagnets. The magnetic behaviour of Co_2GeMo_3N was quite different: the Curie law was obeyed until a small deviation from Curie behaviour occurred at very low temperatures. This was examined further by Sviridov *et al.*,[178] and was determined to be a result of a transition to a spin-glass state. Solid solutions of Fe_2GeMo_3N and Ni_2GeMo_3N in Co_2GeMo_3N were prepared over the range $0.1 \leq x \leq 0.3$. Experiments were carried out to determine whether nitrogen-free analogues of the η-carbide (filled

Ti_2Ni) series M_3Mo_3N (M = Fe, Co, Ni) and the filled β-manganese compound Ni_2Mo_3N could be synthesised. These reactions demonstrated that the presence of 10% hydrogen in *nitrogen* is essential for the formation of η-carbide and filled β-manganese phases containing these metals.

Transition metal urea complexes were prepared in an attempt to use them as precursors to binary nitrides. Single crystals of $[Cr(urea)_4(H_2O)_2][NO_3]_3$, $[Fe(urea)_6][NO_3]_3$, $Cu(urea)_2(H_2O)_3(NO_3).(urea).(NO_3)$, $[Zn(urea)_4(H_2O)_2][NO_3]_2$, $[Co(urea)_4(H_2O)_2][NO_3]_2$ and $[Ni(urea)_4(H_2O)_2][NO_3]_2$ were prepared and their crystal structures examined. The structures of $[Cr(urea)_4(H_2O)_2][NO_3]_3$ and $[Fe(urea)_6][NO_3]_3$ were particularly interesting: $[Cr(urea)_4(H_2O)_2][NO_3]_3$ crystallised in a primitive, but close to C-centred unit cell, and $[Fe(urea)_6][NO_3]_3$ crystallised in a C-centred cell which was closely related to a smaller pseudo C-centred cell previously reported for the same structure. Thermal treatment of the ground crystals of all complexes under 10% hydrogen in nitrogen did not yield binary nitrides.

9.0 Appendix

$Co_{0.82}Rh_{0.18}Sb_3$				
Atomic positions and occupancies	***x***	***y***	***z***	**Occupancy**
Co (8*c*)	¼	¼	¼	0.82
Rh (8*c*)	¼	¼	¼	0.18
Sb (24*g*)	0	0.3355(3)	0.1571(3)	1
Isotropic displacement parameters / Å^2	**Co**	**Rh**		**Sb**
	0.003(3)	0.003(3)		0.003(1)
R(F^2)		0.0708		
χ^2		1.326		

Table 9-1: Selected crystal data from the refinement of $Co_{0.82}Rh_{0.18}Sb_3$

$Co_{0.75}Rh_{0.25}Sb_3$				
Atomic positions and occupancies	***x***	***y***	***z***	**Occupancy**
Co (8*c*)	¼	¼	¼	0.75
Rh (8*c*)	¼	¼	¼	0.25
Sb (24*g*)	0	0.3353(3)	0.1564(4)	1
Isotropic displacement parameters / Å^2	**Co**	**Rh**		**Sb**
	0.038(4)	0.038(4)		0.031(2)
R(F^2)		0.0892		
χ^2		1.453		

Table 9-2: Selected crystal data from the refinement of $Co_{0.75}Rh_{0.25}Sb_3$

$Co_{0.625}Rh_{0.375}Sb_3$				
Atomic positions and occupancies	***x***	***y***	***z***	**Occupancy**
Co (8*c*)	¼	¼	¼	0.625
Rh (8*c*)	¼	¼	¼	0.375
Sb (24*g*)	0	0.3366(3)	0.1563(3)	1
Isotropic displacement parameters / Å^2	**Co**	**Rh**		**Sb**
	0.009(3)	0.009(3)		0.006(1)
R(F^2)		0.0534		
χ^2		1.340		

Table 9-3: Selected crystal data from the refinement of $Co_{0.625}Rh_{0.375}Sb_3$

$Co_{0.375}Rh_{0.625}Sb_3$				
Atomic positions and occupancies	***x***	***y***	***z***	**Occupancy**
Co (8*c*)	¼	¼	¼	0.375
Rh (8*c*)	¼	¼	¼	0.625
Sb (24*g*)	0	0.3369(3)	0.1550(3)	1
Isotropic displacement parameters / Å^2	**Co**	**Rh**		**Sb**
	0.028(3)	0.028(3)		0.026(2)
R(F^2)		0.0800		
χ^2		1.577		

Table 9-4: Selected crystal data from the refinement of $Co_{0.375}Rh_{0.625}Sb_3$

$Co_{0.25}Rh_{0.75}Sb_3$				
Atomic positions and occupancies	***x***	***y***	***z***	**Occupancy**
Co (8*c*)	¼	¼	¼	0.25
Rh (8*c*)	¼	¼	¼	0.75
Sb (24*g*)	0	0.3380(3)	0.1546(3)	1
Isotropic displacement parameters / Å^2	**Co**	**Rh**		**Sb**
	0.015(2)	0.015(2)		0.017(1)
R(F^2)		0.0759		
χ^2		1.460		

Table 9-5: Selected crystal data from the refinement of $Co_{0.25}Rh_{0.75}Sb_3$

$Co_{0.9}Ni_{0.1}Sb$				
Atomic positions and occupancies	***x***	***y***	***z***	**Occupancy**
Co (2*a*)	0	0	0	0.9
Ni (2*a*)	0	0	0	0.1
Sb (2*c*)	⅓	⅔	¼	1
Isotropic displacement parameters / Å^2	**Co**	**Ni**		**Sb**
	0.022(3)	0.022(3)		0.023(2)
R(F^2)		0.1073		
χ^2		1.149		

Table 9-6: Selected crystal data from the refinement of $Co_{0.9}Ni_{0.1}Sb$

$Co_{0.8}Ni_{0.2}Sb$				
Atomic positions and occupancies	***x***	***y***	***z***	**Occupancy**
Co	0	0	0	0.8
Ni	0	0	0	0.2
Sb	⅓	⅔	¼	1
Isotropic displacement parameters / Å^2	**Co**	**Ni**		**Sb**
	0.026(3)	0.026(3)		0.027(2)
R(F^2)		0.0979		
χ^2		1.166		

Table 9-7: Selected crystal data from the refinement of $Co_{0.8}Ni_{0.2}Sb$

$Co_{0.7}Ni_{0.3}Sb$				
Atomic positions and occupancies	***x***	***y***	***z***	**Occupancy**
Co	0	0	0	0.7
Ni	0	0	0	0.3
Sb	⅓	⅔	¼	1
Isotropic displacement parameters / Å^2	**Co**	**Ni**		**Sb**
	0.032(3)	0.032(3)		0.027(2)
R(F^2)		0.1221		
χ^2		1.124		

Table 9-8: Selected crystal data from the refinement of $Co_{0.7}Ni_{0.3}Sb$

$Co_{0.6}Ni_{0.4}Sb$				
Atomic positions and occupancies	***x***	***y***	***z***	**Occupancy**
Co	0	0	0	0.6
Ni	0	0	0	0.4
Sb	⅓	⅔	¼	1
Isotropic displacement parameters / Å^2	**Co**	**Ni**		**Sb**
	0.009(2)	0.009(2)		0.011(1)
R(F^2)		0.0520		
χ^2		1.180		

Table 9-9: Selected crystal data from the refinement of $Co_{0.6}Ni_{0.4}Sb$

$Co_{0.4}Ni_{0.6}Sb$				
Atomic positions and occupancies	***x***	***y***	***z***	**Occupancy**
Co	0	0	0	0.4
Ni	0	0	0	0.6
Sb	⅓	⅔	¼	1
Isotropic displacement parameters / Å^2	**Co**	**Ni**		**Sb**
	0.016(2)	0.016(2)		0.017(1)
R(F^2)		0.0528		
χ^2		1.244		

Table 9-10: Selected crystal data from the refinement of $Co_{0.4}Ni_{0.6}Sb$

$Co_{0.3}Ni_{0.7}Sb$				
Atomic positions and occupancies	***x***	***y***	***z***	**Occupancy**
Co	0	0	0	0.3
Ni	0	0	0	0.7
Sb	⅓	⅔	¼	1
Isotropic displacement parameters / Å^2	**Co**	**Ni**		**Sb**
	0.026(2)	0.026(2)		0.024(1)
R(F^2)		0.0515		
χ^2		1.252		

Table 9-11: Selected crystal data from the refinement of $Co_{0.3}Ni_{0.7}Sb$

$Co_{0.2}Ni_{0.8}Sb$				
Atomic positions and occupancies	***x***	***y***	***z***	**Occupancy**
Co	0	0	0	0.2
Ni	0	0	0	0.8
Sb	⅓	⅔	¼	1
Isotropic displacement parameters / Å^2	**Co**	**Ni**		**Sb**
	0.025(2)	0.025(2)		0.022(1)
R(F^2)		0.0518		
χ^2		1.222		

Table 9-12: Selected crystal data from the refinement of $Co_{0.2}Ni_{0.8}Sb$

$Co_{0.1}Ni_{0.9}Sb$				
Atomic positions and occupancies	***x***	***y***	***z***	**Occupancy**
Co	0	0	0	0.1
Ni	0	0	0	0.9
Sb	⅓	⅔	¼	1
Isotropic displacement parameters / $Å^2$	**Co**	**Ni**		**Sb**
	0.041(3)	0.041(3)		0.034(2)
$R(F^2)$		0.0864		
χ^2		1.087		

Table 9-13: Selected crystal data from the refinement of $Co_{0.1}Ni_{0.9}Sb$

Composition	$[Cr(urea)_4(H_2O)_2][NO_3]_3$
Empirical formula	$C_4H_{20}CrN_{11}O_{15}$
Formula weight / g mol^{-1}	514.31
Temperature / K	120(2)
Wavelength / Å	0.71073
Crystal system	Monoclinic
Space group	$P2_1/c$
a / Å	18.3338(4)
b / Å	16.5472(4)
c / Å	13.9252(3)
β / °	106.326(1)
V / $Å^3$	4054.19(16)
Z	8
Density(calculated) / mg m^{-3}	1.685
Absorption coefficient / mm^{-1}	0.66
$F(000)$	2120
Theta range for data collection / °	2.94-27.78
Index ranges	$-22 \leq h \leq 23, -21 \leq k \leq 21, -18 \leq l \leq 18$
Reflections collected	42166
Independent reflections	9284 [R(int) = 0.050]
Completeness to theta = 27.78°	99.6%
Absorption correction	Multi-scan
Refinement method	Full-matrix least-squares on F^2
Data / restraints / parameters	9284 / 58 / 595
Goodness-of-fit on F^2	1.048
Final R indices [I>2sigma(I)]	R1 = 0.0613, wR2 = 0.1149
R indices (all data)	R1 = 0.0904, wR2 = 0.1303
Largest diff. peak and hole / e $Å^{-3}$	0.88 and −0.47

Table 9-14: Refinement data for $[Cr(urea)_4(H_2O)_2][NO_3]_3$

Atom	*x* (x 10^4)	*y* (x 10^4)	*z* (x 10^4)	U / Å^2 (x 10^3)
N(12)	-496(2)	8920(2)	4021(2)	33(1)
C(6)	-897(2)	8588(2)	3182(3)	23(1)
Cr(1)	4788(1)	7242(1)	1823(1)	14(1)
O(4)	5597(1)	6430(1)	2275(2)	19(1)
O(3)	5532(1)	8113(2)	2089(2)	22(1)
O(2)	4006(1)	8044(1)	1274(2)	18(1)
O(1W)	4857(1)	7114(2)	442(2)	20(1)
O(1)	4018(1)	6389(1)	1675(2)	17(1)
O(2W)	4724(1)	7407(2)	3200(2)	20(1)
O(23)	3619(2)	5330(2)	4510(2)	33(1)
O(22)	4442(1)	6055(2)	4038(2)	27(1)
O(21)	3282(2)	6481(2)	3771(2)	33(1)
N(21)	3772(2)	5960(2)	4099(2)	24(1)
C(3)	5599(2)	8740(2)	1588(3)	24(1)
N(2)	4486(2)	5304(2)	1036(2)	22(1)
N(6)	5216(2)	9403(2)	1633(3)	31(1)
N(4)	3024(2)	8894(2)	994(2)	24(1)
N(1)	3275(2)	5306(2)	1193(2)	25(1)
C(2)	3333(2)	8186(2)	1318(2)	18(1)
N(5)	6061(2)	8721(2)	1010(3)	44(1)
N(3)	2943(2)	7660(2)	1698(2)	27(1)
C(4)	6226(2)	6434(2)	2970(3)	22(1)
C(1)	3933(2)	5680(2)	1306(2)	17(1)
N(8)	6657(2)	5779(2)	3114(2)	29(1)
N(7)	6457(2)	7068(2)	3554(3)	47(1)
Cr(2)	167(1)	7223(1)	3124(1)	14(1)
O(6)	-667(1)	7992(1)	2774(2)	21(1)
O(7)	894(1)	8086(1)	3704(2)	18(1)
O(8)	1000(1)	6443(1)	3322(2)	17(1)
O(5)	-576(1)	6357(1)	2652(2)	19(1)
O(13)	1373(1)	6569(2)	5814(2)	22(1)
O(4W)	74(1)	7078(2)	4494(2)	19(1)
O(3W)	274(1)	7438(1)	1770(2)	18(1)

N(17)	1418(2)	9070(2)	6188(2)	24(1)
O(9)	768(2)	8780(2)	5911(2)	35(1)
O(10)	1960(2)	8709(2)	6761(2)	35(1)
O(11)	1534(2)	9763(2)	5860(2)	28(1)
O(11B)	1446(18)	8306(8)	6340(30)	28(1)
O(10B)	1962(13)	9495(16)	6620(30)	35(1)
O(9B)	762(10)	9363(18)	5830(30)	35(1)
N(9)	-1305(2)	6783(2)	1123(2)	29(1)
O(12)	642(1)	5977(2)	6590(2)	25(1)
N(18)	1211(2)	5954(2)	6259(2)	20(1)
O(14)	1617(2)	5345(2)	6360(2)	30(1)
N(16)	1829(2)	5447(2)	3922(2)	21(1)
N(11)	-1583(2)	8884(2)	2725(3)	36(1)
O(18)	951(1)	3665(2)	4777(2)	27(1)
N(20)	1638(2)	3473(2)	5156(2)	21(1)
O(20)	2149(1)	3868(2)	4918(2)	29(1)
N(15)	573(2)	5278(2)	3839(2)	25(1)
O(19)	1803(2)	2897(2)	5740(2)	33(1)
N(10)	-1699(2)	5764(2)	1965(2)	29(1)
N(13)	1884(2)	8933(2)	4144(2)	27(1)
C(5)	-1184(2)	6315(2)	1924(2)	20(1)
N(14)	2008(2)	7741(2)	3380(2)	25(1)
C(8)	1122(2)	5733(2)	3686(2)	17(1)
C(7)	1585(2)	8239(2)	3742(2)	19(1)
O(17)	4294(1)	6002(2)	8390(2)	26(1)
O(16)	3557(1)	6529(2)	9197(2)	26(1)
N(19)	3713(2)	5949(2)	8695(2)	20(1)
O(15)	3298(2)	5349(2)	8525(2)	34(1)
O(26)	4072(1)	3651(2)	167(2)	31(1)
O(24)	2869(1)	3824(2)	5(2)	28(1)
O(25)	3237(2)	2912(2)	-877(2)	40(1)
N(22)	3392(2)	3461(2)	-240(2)	22(1)

Table 9-15: Atomic positions and temperature factors of atoms in $[Cr(urea)_4(H_2O)_2][NO_3]_3$

Bond lengths / Å		Bond angles / °	
N(12)-C(6)	1.313(5)	C(6)-N(12)-H(12A)	120.0
N(12)-H(12A)	0.8800	C(6)-N(12)-H(12B)	120.0
N(12)-H(12B)	0.8800	H(12A)-N(12)-H(12B)	120.0
C(6)-O(6)	1.268(4)	O(6)-C(6)-N(12)	123.3(3)
C(6)-N(11)	1.333(4)	O(6)-C(6)-N(11)	117.4(3)
Cr(1)-O(3)	1.947(2)	N(12)-C(6)-N(11)	119.2(3)
Cr(1)-O(2)	1.948(2)	O(3)-Cr(1)-O(2)	88.23(10)
Cr(1)-O(1)	1.966(2)	O(3)-Cr(1)-O(1)	174.58(10)
Cr(1)-O(4)	1.968(2)	O(2)-Cr(1)-O(1)	91.14(10)
Cr(1)-O(2W)	1.972(2)	O(3)-Cr(1)-O(4)	91.12(10)
Cr(1)-O(1W)	1.974(2)	O(2)-Cr(1)-O(4)	175.42(10)
O(4)-C(4)	1.280(4)	O(1)-Cr(1)-O(4)	89.92(10)
O(3)-C(3)	1.276(4)	O(3)-Cr(1)-O(2W)	86.71(10)
O(2)-C(2)	1.274(4)	O(2)-Cr(1)-O(2W)	92.78(10)
O(1W)-H(1WB)	0.80(2)	O(1)-Cr(1)-O(2W)	87.95(10)
O(1W)-H(1WA)	0.80(2)	O(4)-Cr(1)-O(2W)	91.71(10)
O(1)-C(1)	1.273(4)	O(3)-Cr(1)-O(1W)	91.81(10)
O(2W)-H(2WB)	0.80(2)	O(2)-Cr(1)-O(1W)	86.09(10)
O(2W)-H(2WA)	0.80(2)	O(1)-Cr(1)-O(1W)	93.51(10)
O(23)-N(21)	1.258(4)	O(4)-Cr(1)-O(1W)	89.40(10)
O(22)-N(21)	1.265(4)	O(2W)-Cr(1)-O(1W)	178.17(11)
O(21)-N(21)	1.235(4)	C(4)-O(4)-Cr(1)	132.5(2)
C(3)-N(6)	1.314(5)	C(3)-O(3)-Cr(1)	132.0(2)
C(3)-N(5)	1.324(5)	C(2)-O(2)-Cr(1)	136.3(2)
N(2)-C(1)	1.332(4)	Cr(1)-O(1W)-H(1WB)	120(3)
N(2)-H(2B)	0.8800	Cr(1)-O(1W)-H(1WA)	113(3)
N(2)-H(2A)	0.8800	H(1WB)-O(1W)-H(1WA)	112(4)
N(6)-H(6B)	0.8800	C(1)-O(1)-Cr(1)	135.0(2)
N(6)-H(6A)	0.8800	Cr(1)-O(2W)-H(2WB)	114(3)
N(4)-C(2)	1.324(4)	Cr(1)-O(2W)-H(2WA)	117(3)
N(4)-H(4A)	0.8800	H(2WB)-O(2W)-H(2WA)	115(4)
N(4)-H(4C)	0.8800	O(21)-N(21)-O(23)	121.0(3)
N(1)-C(1)	1.325(4)	O(21)-N(21)-O(22)	120.4(3)
N(1)-H(1A)	0.8800	O(23)-N(21)-O(22)	118.6(3)

N(1)-H(1B)	0.8800	O(3)-C(3)-N(6)	121.2(3)
C(2)-N(3)	1.327(4)	O(3)-C(3)-N(5)	119.3(3)
N(5)-H(5A)	0.8800	N(6)-C(3)-N(5)	119.5(4)
N(5)-H(5B)	0.8800	C(1)-N(2)-H(2B)	120.0
N(3)-H(3A)	0.8800	C(1)-N(2)-H(2A)	120.0
N(3)-H(3B)	0.8800	H(2B)-N(2)-H(2A)	120.0
C(4)-N(8)	1.321(4)	C(3)-N(6)-H(6B)	120.0
C(4)-N(7)	1.322(5)	C(3)-N(6)-H(6A)	120.0
N(8)-H(8A)	0.8800	H(6B)-N(6)-H(6A)	120.0
N(8)-H(8B)	0.8800	C(2)-N(4)-H(4A)	120.0
N(7)-H(7B)	0.8800	C(2)-N(4)-H(4C)	120.0
N(7)-H(7A)	0.8800	H(4A)-N(4)-H(4C)	120.0
Cr(2)-O(6)	1.943(2)	C(1)-N(1)-H(1A)	120.0
Cr(2)-O(8)	1.958(2)	C(1)-N(1)-H(1B)	120.0
Cr(2)-O(5)	1.959(2)	H(1A)-N(1)-H(1B)	120.0
Cr(2)-O(7)	1.966(2)	O(2)-C(2)-N(4)	118.2(3)
Cr(2)-O(4W)	1.977(2)	O(2)-C(2)-N(3)	122.4(3)
Cr(2)-O(3W)	1.982(2)	N(4)-C(2)-N(3)	119.4(3)
O(7)-C(7)	1.278(4)	C(3)-N(5)-H(5A)	120.0
O(8)-C(8)	1.274(4)	C(3)-N(5)-H(5B)	120.0
O(5)-C(5)	1.281(4)	H(5A)-N(5)-H(5B)	120.0
O(13)-N(18)	1.269(4)	C(2)-N(3)-H(3A)	120.0
O(4W)-H(4WA)	0.80(2)	C(2)-N(3)-H(3B)	120.0
O(4W)-H(4WB)	0.79(2)	H(3A)-N(3)-H(3B)	120.0
O(3W)-H(3WB)	0.80(2)	O(4)-C(4)-N(8)	118.9(3)
O(3W)-H(3WA)	0.80(2)	O(4)-C(4)-N(7)	122.2(3)
N(17)-O(10B)	1.231(13)	N(8)-C(4)-N(7)	118.9(3)
N(17)-O(10)	1.240(4)	O(1)-C(1)-N(1)	118.9(3)
N(17)-O(9)	1.240(4)	O(1)-C(1)-N(2)	121.9(3)
N(17)-O(9B)	1.262(13)	N(1)-C(1)-N(2)	119.2(3)
N(17)-O(11)	1.275(4)	C(4)-N(8)-H(8A)	120.0
N(17)-O(11B)	1.281(13)	C(4)-N(8)-H(8B)	120.0
N(9)-C(5)	1.324(4)	H(8A)-N(8)-H(8B)	120.0
N(9)-H(9B)	0.8800	C(4)-N(7)-H(7B)	120.0
N(9)-H(9A)	0.8800	C(4)-N(7)-H(7A)	120.0
O(12)-N(18)	1.255(4)	H(7B)-N(7)-H(7A)	120.0

N(18)-O(14)	1.238(4)	O(6)-Cr(2)-O(8)	173.78(10)
N(16)-C(8)	1.333(4)	O(6)-Cr(2)-O(5)	88.34(10)
N(16)-H(16B)	0.8800	O(8)-Cr(2)-O(5)	90.35(10)
N(16)-H(16A)	0.8800	O(6)-Cr(2)-O(7)	91.24(10)
N(11)-H(11A)	0.8800	O(8)-Cr(2)-O(7)	90.56(9)
N(11)-H(11B)	0.8800	O(5)-Cr(2)-O(7)	175.31(10)
O(18)-N(20)	1.261(3)	O(6)-Cr(2)-O(4W)	92.64(10)
N(20)-O(19)	1.233(4)	O(8)-Cr(2)-O(4W)	93.44(10)
N(20)-O(20)	1.261(4)	O(5)-Cr(2)-O(4W)	89.68(10)
N(15)-C(8)	1.321(4)	O(7)-Cr(2)-O(4W)	85.67(10)
N(15)-H(15B)	0.8800	O(6)-Cr(2)-O(3W)	85.71(10)
N(15)-H(15A)	0.8800	O(8)-Cr(2)-O(3W)	88.29(10)
N(10)-C(5)	1.325(4)	O(5)-Cr(2)-O(3W)	93.26(10)
N(10)-H(10A)	0.8800	O(7)-Cr(2)-O(3W)	91.36(10)
N(10)-H(10B)	0.8800	O(4W)-Cr(2)-O(3W)	176.58(11)
N(13)-C(7)	1.327(4)	C(6)-O(6)-Cr(2)	137.3(2)
N(13)-H(13B)	0.8800	C(7)-O(7)-Cr(2)	135.2(2)
N(13)-H(13A)	0.8800	C(8)-O(8)-Cr(2)	134.9(2)
N(14)-C(7)	1.325(4)	C(5)-O(5)-Cr(2)	132.4(2)
N(14)-H(14A)	0.8800	Cr(2)-O(4W)-H(4WA)	122(3)
N(14)-H(14B)	0.8800	Cr(2)-O(4W)-H(4WB)	114(3)
O(17)-N(19)	1.255(4)	H(4WA)-O(4W)-H(4WB)	109(4)
O(16)-N(19)	1.267(4)	Cr(2)-O(3W)-H(3WB)	109(3)
N(19)-O(15)	1.233(4)	Cr(2)-O(3W)-H(3WA)	113(3)
O(26)-N(22)	1.257(4)	H(3WB)-O(3W)-H(3WA)	123(5)
O(24)-N(22)	1.257(4)	O(10B)-N(17)-O(10)	64.3(14)
O(25)-N(22)	1.245(4)	O(10B)-N(17)-O(9)	161.6(19)
		O(10)-N(17)-O(9)	122.7(3)
		O(10B)-N(17)-O(9B)	121.8(14)
		O(10)-N(17)-O(9B)	160(2)
		O(9)-N(17)-O(9B)	45.6(14)
		O(10B)-N(17)-O(11)	57.8(16)
		O(10)-N(17)-O(11)	118.6(3)
		O(9)-N(17)-O(11)	118.7(3)
		O(9B)-N(17)-O(11)	75.6(16)
		O(10B)-N(17)-O(11B)	119.5(13)

O(10)-N(17)-O(11B)	55.3(15)
O(9)-N(17)-O(11B)	70.2(14)
O(9B)-N(17)-O(11B)	115.7(13)
O(11)-N(17)-O(11B)	160.8(18)
C(5)-N(9)-H(9B)	120.0
C(5)-N(9)-H(9A)	120.0
H(9B)-N(9)-H(9A)	120.0
O(14)-N(18)-O(12)	121.2(3)
O(14)-N(18)-O(13)	119.5(3)
O(12)-N(18)-O(13)	119.2(3)
C(8)-N(16)-H(16B)	120.0
C(8)-N(16)-H(16A)	120.0
H(16B)-N(16)-H(16A)	120.0
C(6)-N(11)-H(11A)	120.0
C(6)-N(11)-H(11B)	120.0
H(11A)-N(11)-H(11B)	120.0
O(19)-N(20)-O(18)	120.1(3)
O(19)-N(20)-O(20)	120.7(3)
O(18)-N(20)-O(20)	119.1(3)
C(8)-N(15)-H(15B)	120.0
C(8)-N(15)-H(15A)	120.0
H(15B)-N(15)-H(15A)	120.0
C(5)-N(10)-H(10A)	120.0
C(5)-N(10)-H(10B)	120.0
H(10A)-N(10)-H(10B)	120.0
C(7)-N(13)-H(13B)	120.0
C(7)-N(13)-H(13A)	120.0
H(13B)-N(13)-H(13A)	120.0
O(5)-C(5)-N(9)	122.4(3)
O(5)-C(5)-N(10)	118.4(3)
N(9)-C(5)-N(10)	119.1(3)
C(7)-N(14)-H(14A)	120.0
C(7)-N(14)-H(14B)	120.0
H(14A)-N(14)-H(14B)	120.0
O(8)-C(8)-N(15)	122.2(3)
O(8)-C(8)-N(16)	118.4(3)

N(15)-C(8)-N(16)	119.4(3)
O(7)-C(7)-N(14)	122.8(3)
O(7)-C(7)-N(13)	118.4(3)
N(14)-C(7)-N(13)	118.8(3)
O(15)-N(19)-O(17)	121.9(3)
O(15)-N(19)-O(16)	119.5(3)
O(17)-N(19)-O(16)	118.6(3)
O(25)-N(22)-O(26)	120.2(3)
O(25)-N(22)-O(24)	120.2(3)
O(26)-N(22)-O(24)	119.6(3)

Table 9-16: Bond lengths and angles in $[Cr(urea)_4(H_2O)_2][NO_3]_3$

Composition	$[Fe(urea)_6][NO_3]_3$
Empirical formula	$C_6H_{24}FeN_{15}O_{15}$
Formula weight / g mol^{-1}	602.25
Temperature / K	120(2)
Wavelength / Å	0.71073
Crystal system	Monoclinic
Space group	*C*2
a / Å	51.576(2)
b / Å	18.7325(8)
c / Å	12.1403(5)
β / °	93.627(2)
V / $Å^3$	11705.8(8)
Z	20
Density(calculated) / mg m^{-3}	1.709
Absorption coefficient / mm^{-1}	0.744
F(000)	6220
Theta range for data collection / °	2.98-25.51
Index ranges	$-62 \leq h \leq 62, -22 \leq k \leq 22, -14 \leq l \leq 14$
Reflections collected	92522
Independent reflections	21657 [R(int) = 0.096]
Completeness to theta = 25.51°	99.8%
Absorption correction	Multi-scan
Refinement method	Full-matrix least-squares on F^2
Data / restraints / parameters	21657 / 1221 / 1656
Goodness-of-fit on F^2	1.094
Final R indices [I>2sigma(I)]	R1 = 0.0956, wR2 = 0.1691
R indices (all data)	R1 = 0.1777, wR2 = 0.2144
Largest diff. peak and hole / e $Å^{-3}$	1.258 and −0.605
Mean bond lengths / Å	Fe-O 1.996(19)
	C-O 1.276(17)
	C-N 1.326(18)
	N-O 1.247(13)

Table 9-17: Refinement data for $[Fe(urea)_6][NO_3]_3$

Atom	x (x 10^4)	y (x 10^4)	z (x 10^4)	U / Å^2 (x 10^3)
C(1)	289(4)	2896(10)	-637(16)	21(4)
C(2)	134(3)	4656(9)	2382(14)	13(3)
C(3)	-484(4)	5145(11)	-233(16)	22(4)
C(21)	-292(4)	10187(10)	5273(16)	20(4)
C(22)	-47(4)	8413(11)	2591(17)	25(4)
C(23)	-483(4)	7902(11)	4496(16)	27(4)
C(31)	1268(4)	5532(10)	6363(16)	24(4)
C(32)	878(4)	3689(11)	4550(17)	30(4)
C(33)	1482(4)	3253(10)	7218(16)	25(4)
C(34)	519(4)	3230(9)	6697(14)	19(4)
C(35)	1150(4)	3770(10)	9329(16)	21(4)
C(36)	727(3)	5526(9)	7550(14)	18(3)
C(41)	929(4)	9976(10)	-360(16)	25(4)
C(42)	1291(4)	8218(11)	1718(17)	27(4)
C(43)	679(4)	8196(10)	2303(15)	24(4)
C(44)	1025(4)	10020(10)	4436(16)	21(4)
C(45)	514(4)	10508(11)	1580(16)	25(4)
C(46)	1461(4)	10501(11)	2446(16)	22(4)
C(51)	1913(3)	4814(9)	1518(14)	22(3)
C(52)	2296(3)	2992(9)	3341(14)	26(4)
C(53)	1722(4)	3003(10)	4399(16)	32(4)
C(54)	2140(3)	4722(9)	6293(14)	22(3)
C(55)	1539(4)	5308(10)	3642(17)	34(4)
C(56)	2491(4)	5282(10)	4245(16)	31(4)
C(61)	2945(4)	3408(10)	-1465(16)	31(4)
C(62)	3303(3)	5223(10)	537(14)	27(4)
C(63)	2737(3)	5234(9)	1310(15)	24(3)
C(64)	3103(4)	3521(10)	3344(16)	29(4)
C(65)	2543(4)	2942(12)	580(18)	36(5)
C(66)	3507(4)	2955(10)	1393(15)	27(3)
Fe(1)	0	4202(2)	0	19(1)
Fe(2)	0	8811(2)	5000	22(1)
Fe(3)	1006(1)	4154(1)	6937(2)	18(1)

Fe(4)	981(1)	9567(1)	2058(2)	19(1)
Fe(5)	2016(1)	4342(2)	3899(2)	32(1)
Fe(6)	3023(1)	3889(1)	923(2)	25(1)
N(1A)	480(3)	2459(8)	-387(13)	25(4)
N(1B)	89(3)	2683(9)	-1379(13)	23(4)
N(2A)	109(3)	5352(7)	2193(12)	14(3)
N(2B)	220(3)	4466(9)	3368(13)	30(4)
N(3A)	-548(4)	5823(11)	-322(16)	39(4)
N(3B)	-647(3)	4627(9)	-590(12)	22(3)
N(21A)	-194(3)	10354(9)	6238(14)	29(4)
N(21B)	-430(3)	10686(9)	4690(15)	30(4)
N(22A)	-123(4)	8643(11)	1610(16)	44(5)
N(22B)	-10(3)	7726(9)	2768(14)	25(4)
N(23A)	-626(3)	8422(9)	4046(14)	31(4)
N(23B)	-559(4)	7236(9)	4466(14)	29(4)
N(31A)	1465(3)	5999(8)	6612(12)	23(3)
N(31B)	1090(4)	5698(10)	5594(14)	35(4)
N(32A)	914(4)	3001(10)	4776(16)	39(4)
N(32B)	790(3)	3916(8)	3542(12)	26(3)
N(33A)	1651(4)	3749(10)	7584(15)	38(4)
N(33B)	1561(3)	2558(9)	7301(14)	25(4)
N(34A)	351(4)	3735(10)	6329(14)	38(4)
N(34B)	455(3)	2554(8)	6623(13)	25(3)
N(35A)	1245(3)	3995(7)	10332(12)	18(3)
N(35B)	1097(3)	3077(9)	9159(14)	28(4)
N(36A)	909(3)	5721(8)	8248(12)	24(3)
N(36B)	529(3)	5971(9)	7267(14)	34(4)
N(41A)	952(3)	10663(9)	-227(15)	32(4)
N(41B)	866(3)	9680(8)	-1366(12)	28(3)
N(42A)	1160(3)	8069(8)	754(12)	23(3)
N(42B)	1421(3)	7734(9)	2289(14)	30(4)
N(43A)	562(3)	7729(9)	1702(14)	33(4)
N(43B)	796(3)	8041(9)	3291(14)	30(4)
N(44A)	1009(4)	10704(10)	4262(16)	35(5)
N(44B)	1106(3)	9779(10)	5440(13)	30(4)

N(45A)	424(4)	11186(9)	1516(14)	29(4)
N(45B)	353(3)	10016(9)	1112(14)	32(4)
N(46A)	1551(4)	11180(10)	2480(14)	33(4)
N(46B)	1605(4)	9994(11)	2924(15)	41(5)
N(51A)	1844(3)	4631(10)	505(14)	43(4)
N(51B)	1926(3)	5498(8)	1742(12)	29(3)
N(52A)	2467(3)	2523(9)	3691(14)	42(4)
N(52B)	2115(3)	2808(8)	2539(13)	33(4)
N(53A)	1535(3)	2562(8)	4101(13)	31(3)
N(53B)	1898(3)	2834(8)	5235(12)	30(3)
N(54A)	2099(3)	5421(8)	6141(12)	22(3)
N(54B)	2238(3)	4471(10)	7270(14)	42(4)
N(55A)	1473(4)	5991(10)	3635(15)	43(4)
N(55B)	1371(3)	4806(9)	3324(14)	40(4)
N(56A)	2567(4)	5950(10)	4324(16)	46(5)
N(56B)	2643(4)	4777(10)	4693(14)	43(4)
N(61A)	2995(3)	2715(8)	-1238(14)	31(4)
N(61B)	2876(4)	3632(11)	-2479(15)	42(5)
N(62A)	3451(3)	5766(10)	1044(14)	47(4)
N(62B)	3169(3)	5412(9)	-365(13)	35(4)
N(63A)	2881(3)	5442(10)	2178(14)	44(4)
N(63B)	2561(3)	5718(10)	923(14)	42(4)
N(64A)	3203(3)	3794(9)	4315(13)	35(4)
N(64B)	3068(3)	2833(8)	3207(13)	31(4)
N(65A)	2474(3)	2281(9)	579(14)	34(4)
N(65B)	2383(4)	3451(11)	163(16)	52(5)
N(66A)	3577(4)	2279(10)	1423(16)	45(4)
N(66B)	3652(4)	3484(9)	1813(15)	42(4)
N(100)	250(3)	2269(6)	3742(12)	18(3)
N(105)	750(3)	6091(8)	3208(17)	44(5)
N(110)	1248(3)	6143(8)	702(16)	41(4)
N(115)	2033(3)	7070(7)	4229(11)	32(4)
N(120)	3722(3)	2696(7)	4699(12)	25(3)
N(125)	1012(2)	1413(6)	7106(8)	14(3)
N(130)	698(3)	7611(7)	8637(12)	29(4)

N(135)	993(2)	2562(7)	1879(11)	29(3)
N(140)	0	6961(13)	0	64(9)
N(145)	2763(3)	7320(7)	2412(13)	35(4)
N(150)	3035(3)	1145(9)	1249(13)	52(5)
N(160)	1737(3)	2332(7)	215(13)	30(3)
N(165)	0	5846(14)	5000	66(7)
N(170)	1703(4)	819(11)	5650(18)	76(6)
N(180)	-296(3)	733(6)	1730(11)	21(3)
N(190)	2277(3)	740(9)	2438(18)	88(8)
O(1)	274(3)	3478(7)	-132(11)	22(3)
O(2)	78(2)	4184(7)	1651(10)	22(3)
O(3)	-256(3)	4994(7)	186(11)	20(3)
O(21)	-282(3)	9569(7)	4877(11)	25(3)
O(22)	-12(3)	8863(8)	3368(11)	32(3)
O(23)	-256(2)	8031(7)	4974(10)	20(3)
O(31)	1285(3)	4907(7)	6805(11)	26(3)
O(32)	931(3)	4170(7)	5287(10)	24(3)
O(33)	1263(3)	3407(7)	6818(11)	26(3)
O(34)	751(3)	3394(7)	7089(10)	23(3)
O(35)	1090(2)	4229(6)	8568(9)	16(3)
O(36)	725(3)	4899(7)	7069(12)	28(3)
O(41)	971(2)	9517(6)	432(10)	24(3)
O(42)	1262(3)	8847(7)	2194(11)	26(3)
O(43)	694(3)	8852(7)	1924(11)	26(3)
O(44)	987(2)	9567(6)	3663(10)	21(3)
O(45)	718(2)	10380(6)	2069(10)	18(3)
O(46)	1241(3)	10363(7)	1991(11)	26(3)
O(51)	1952(3)	4338(7)	2258(10)	32(3)
O(52)	2295(2)	3602(6)	3806(10)	25(3)
O(53)	1732(3)	3607(6)	3964(11)	28(3)
O(54)	2079(3)	4275(7)	5545(10)	31(3)
O(55)	1759(3)	5128(7)	4076(11)	34(3)
O(56)	2274(2)	5148(6)	3761(10)	28(3)
O(61)	2986(3)	3911(7)	-731(11)	36(3)
O(62)	3308(3)	4616(7)	937(11)	33(3)

O(63)	2741(2)	4620(6)	893(9)	21(3)
O(64)	3080(2)	3969(7)	2556(10)	31(3)
O(65)	2772(2)	3101(6)	998(10)	24(3)
O(66)	3282(3)	3115(7)	877(12)	36(3)
O(100)	473(2)	2032(7)	3909(11)	27(3)
O(101)	214(3)	2935(7)	3767(13)	43(3)
O(102)	57(3)	1868(7)	3589(12)	32(3)
O(105)	522(3)	6345(10)	3060(14)	51(4)
O(106)	801(3)	5432(7)	3069(12)	39(3)
O(107)	926(2)	6533(7)	3470(12)	33(3)
O(110)	1057(3)	6551(9)	454(14)	53(4)
O(111)	1469(3)	6400(9)	850(13)	43(4)
O(112)	1188(3)	5502(7)	801(12)	42(3)
O(115)	1982(3)	6711(8)	5031(13)	57(4)
O(116)	2164(3)	7649(8)	4336(14)	61(4)
O(117)	1980(4)	6820(12)	3267(15)	84(6)
O(120)	3784(4)	3322(8)	4867(16)	81(5)
O(121)	3836(3)	2325(7)	4079(11)	48(3)
O(122)	3534(3)	2377(11)	5078(17)	92(6)
O(125)	959(3)	1663(7)	6217(9)	36(3)
O(126)	1082(3)	785(7)	7237(10)	43(3)
O(127)	984(3)	1750(8)	7971(11)	45(4)
O(130)	534(3)	7174(8)	8917(13)	54(4)
O(131)	861(3)	7457(9)	7987(13)	53(4)
O(132)	716(3)	8217(8)	9067(14)	61(4)
O(135)	987(4)	1931(10)	1675(17)	94(6)
O(136)	1193(2)	2919(6)	2155(10)	31(3)
O(137)	790(2)	2894(7)	1684(11)	30(3)
O(140)	25(3)	6650(7)	896(10)	38(3)
O(141)	0	7632(12)	0	72(7)
O(145)	2943(3)	6882(8)	2684(13)	56(4)
O(146)	2544(3)	7075(7)	2283(12)	41(3)
O(147)	2805(3)	7970(7)	2425(13)	55(4)
O(150)	2958(3)	1509(7)	2039(11)	49(3)
O(151)	3198(3)	666(8)	1358(13)	48(4)

O(152)	2963(3)	1429(9)	359(13)	66(4)
O(160)	1919(4)	1910(10)	300(17)	84(6)
O(161)	1513(3)	2101(8)	118(12)	44(4)
O(162)	1784(4)	2998(8)	260(15)	69(5)
O(165)	219(3)	5556(10)	5255(15)	65(5)
O(166)	0	6492(13)	5000	69(6)
O(170)	1863(4)	845(11)	4991(15)	84(6)
O(171)	1669(3)	231(9)	6133(14)	69(5)
O(172)	1541(3)	1307(9)	5598(14)	66(4)
O(180)	-300(3)	146(6)	2199(10)	23(2)
O(181)	-147(2)	842(6)	981(9)	23(2)
O(182)	-458(2)	1195(6)	1961(11)	23(2)
O(184)	-481(7)	720(20)	2340(30)	23(2)
O(183)	-194(8)	149(13)	1470(40)	23(2)
O(185)	-191(8)	1299(13)	1490(40)	23(2)
O(192)	2158(3)	1320(8)	2504(15)	51(3)
O(191)	2458(3)	683(9)	1746(14)	51(3)
O(190)	2173(3)	175(8)	2771(15)	51(3)
O(193)	2093(6)	850(20)	3060(30)	51(3)
O(195)	2480(5)	1120(20)	2650(40)	51(3)
O(194)	2283(8)	177(19)	1890(40)	51(3)

Table 9-18: Atomic positions and temperature factors of atoms in $[Fe(urea)_6][NO_3]_3$

Composition	$Cu(urea)_2(H_2O)_3(NO_3).(urea)(NO_3)$
Empirical formula	$C_4H_{21.27}CuN_{10}O_{12.64}$
Formula weight / g mol^{-1}	475.33
Temperature / K	150(2)
Wavelength / Å	0.71073
Crystal system	Monoclinic
Space group	$P2_1/m$
a / Å	9.489(3)
b / Å	13.059(3)
c / Å	7.103(2)
β / °	100.28(3)
V / $Å^3$	866.1(4)
Z	2
Density(calculated) / mg m^{-3}	1.823
Absorption coefficient / mm^{-1}	1.351
F(000)	490.7
Theta range for data collection / °	2.68-27.00
Index ranges	$-12 \leq h \leq 12, -16 \leq k \leq 16, -9 \leq l \leq 8$
Reflections collected	9707
Independent reflections	1968 [R(int) = 0.0774]
Completeness to theta = 27.00°	99.9%
Absorption correction	Semi-empirical from equivalents
Refinement method	Full-matrix least-squares on F^2
Data / restraints / parameters	1968 / 33 / 171
Goodness-of-fit on F^2	0.973
Final R indices [I>2sigma(I)]	R1 = 0.0460, wR2 = 0.1098
R indices (all data)	R1 = 0.0729, wR2 = 0.1203
Largest diff. peak and hole / e $Å^{-3}$	1.075 and −0.998

Table 9-19: Refinement data for $Cu(urea)_2(H_2O)_3(NO_3).(urea)(NO_3)$

Atom	x (x 10^4)	y (x 10^4)	z (x 10^4)	U / Å^2 (x 10^3)
Cu(1)	8478(1)	2500	3870(1)	23(1)
O(1W)	9175(4)	2500	6594(5)	26(1)
O(2W)	7881(4)	2500	1126(5)	24(1)
O(1)	8641(2)	1022(2)	4024(3)	21(1)
N(1)	8482(3)	-667(2)	3560(4)	25(1)
N(2)	6644(3)	356(2)	2156(4)	23(1)
C(1)	7927(3)	259(2)	3252(5)	17(1)
O(2)	8666(2)	988(2)	8922(4)	24(1)
N(3)	8414(4)	-723(2)	8735(5)	30(1)
C(2)	7926(3)	216(2)	8300(5)	19(1)
N(4)	6648(3)	315(3)	7187(5)	27(1)
N(10)	4001(5)	2500	9282(7)	26(1)
O(10)	4561(3)	1672(2)	9822(6)	53(1)
O(11)	2804(5)	2500	8255(8)	53(1)
O(20B)	3032(12)	2500	3345(17)	37(1)
N(20B)	4294(15)	2500	4220(20)	26(1)
O(21B)	4900(14)	1636(8)	4647(16)	58(1)
N(20A)	4790(8)	2500	4561(11)	26(1)
O(20A)	6090(7)	2500	5124(10)	37(1)
O(21A)	4124(8)	1674(5)	4466(9)	58(1)
O(3W)	10986(7)	2500	3506(10)	40(2)

Table 9-20: Atomic positions and temperature factors of atoms in $Cu(urea)_2(H_2O)_3(NO_3).(urea)(NO_3)$

Bond lengths / Å		Bond angles / °	
Cu(1)-O(1W)	1.930(4)	O(1W)-Cu(1)-O(2W)	177.05(18)
Cu(1)-O(2W)	1.930(4)	O(1W)-Cu(1)-O(1)	86.22(7)
Cu(1)-O(1)	1.938(2)	O(2W)-Cu(1)-O(1)	93.60(7)
Cu(1)-O(1)#1	1.938(2)	O(1W)-Cu(1)-O(1)#1	86.22(7)
O(1W)-H(1)	0.79(3)	O(2W)-Cu(1)-O(1)#1	93.60(7)
O(2W)-H(2)	0.80(3)	O(1)-Cu(1)-O(1)#1	169.79(13)
O(1)-C(1)	1.273(4)	Cu(1)-O(1W)-H(1)	112(4)

N(1)-C(1)	1.322(4)	Cu(1)-O(2W)-H(2)	119(4)
N(1)-H(1A)	0.83(2)	C(1)-O(1)-Cu(1)	136.4(2)
N(1)-H(1B)	0.83(2)	C(1)-N(1)-H(1A)	122(3)
N(2)-C(1)	1.329(4)	C(1)-N(1)-H(1B)	119(3)
N(2)-H(2A)	0.82(2)	H(1A)-N(1)-H(1B)	119(5)
N(2)-H(2B)	0.82(2)	C(1)-N(2)-H(2A)	122(3)
O(2)-C(2)	1.263(4)	C(1)-N(2)-H(2B)	117(3)
N(3)-C(2)	1.328(4)	H(2A)-N(2)-H(2B)	121(5)
N(3)-H(3A)	0.83(2)	O(1)-C(1)-N(1)	118.7(3)
N(3)-H(3B)	0.83(2)	O(1)-C(1)-N(2)	122.6(3)
C(2)-N(4)	1.330(4)	N(1)-C(1)-N(2)	118.7(3)
N(4)-H(4A)	0.82(2)	C(2)-N(3)-H(3A)	119(3)
N(4)-H(4B)	0.82(2)	C(2)-N(3)-H(3B)	123(3)
N(10)-O(11)	1.235(6)	H(3A)-N(3)-H(3B)	117(5)
N(10)-O(10)	1.236(3)	O(2)-C(2)-N(3)	120.4(3)
N(10)-O(10)#1	1.236(3)	O(2)-C(2)-N(4)	121.4(3)
O(20B)-N(20B)	1.246(18)	N(3)-C(2)-N(4)	118.1(3)
N(20B)-O(21B)	1.279(13)	C(2)-N(4)-H(4A)	117(3)
N(20B)-O(21B)#1	1.279(13)	C(2)-N(4)-H(4B)	117(3)
N(20A)-O(20A)	1.227(10)	H(4A)-N(4)-H(4B)	126(5)
N(20A)-O(21A)	1.246(7)	O(11)-N(10)-O(10)	118.8(2)
N(20A)-O(21A)#1	1.246(7)	O(11)-N(10)-O(10)#1	118.8(2)
O(3W)-H(3C)	0.88(3)	O(10)-N(10)-O(10)#1	122.2(4)
		O(20B)-N(20B)-O(21B)	118.0(9)
		O(20B)-N(20B)-O(21B)#1	118.0(8)
		O(21B)-N(20B)-O(21B)#1	123.9(17)
		O(20A)-N(20A)-O(21A)	119.3(5)
		O(20A)-N(20A)-O(21A)#1	119.3(5)
		O(21A)-N(20A)-O(21A)#1	119.9(10)

Table 9-21: Bond lengths and angles in $Cu(urea)_2(H_2O)_3(NO_3).(urea)(NO_3)$

Composition	$[Zn(urea)_4(H_2O)_2][NO_3]_2$
Empirical formula	$C_4H_{20}N_{10}O_{12}Zn$
Formula weight / g mol^{-1}	465.65
Temperature / K	150(2)
Wavelength / Å	0.71073
Crystal system	Monoclinic
Space group	$P2_1/n$
a / Å	6.4239(11)
b / Å	17.690(4)
c / Å	7.5877(13)
β / °	91.138(14)
V / $Å^3$	862.1(3)
Z	2
Density(calculated) / mg m^{-3}	1.794
Absorption coefficient / mm^{-1}	1.509
F(000)	480
Theta range for data collection / °	2.30-29.58
Index ranges	$-8 \leq h \leq 8, -23 \leq k \leq 24, -10 \leq l \leq 10$
Reflections collected	6891
Independent reflections	2363 [R(int) = 0.0763]
Completeness to theta = 29.58°	98.0%
Absorption correction	None
Refinement method	Full-matrix least-squares on F^2
Data / restraints / parameters	2363 / 34 / 156
Goodness-of-fit on F^2	0.930
Final R indices [I>2sigma(I)]	R1 = 0.0353, wR2 = 0.0791
R indices (all data)	R1 = 0.0549, wR2 = 0.0844
Largest diff. peak and hole / e $Å^{-3}$	0.848 and −1.314

Table 9-22: Refinement data for $[Zn(urea)_4(H_2O)_2][NO_3]_2$

Atom	*x* (x 10^4)	*y* (x 10^4)	*z* (x 10^4)	U / Å^2 (x 10^3)
C(1)	-2694(3)	1088(1)	-2348(3)	20(1)
O(1)	-1222(2)	953(1)	-1274(2)	23(1)
N(1)	-3188(3)	1806(1)	-2751(3)	25(1)
N(2)	-3741(4)	540(1)	-3174(3)	31(1)
C(2)	3294(3)	1291(1)	594(3)	19(1)
O(2)	2546(2)	641(1)	818(2)	22(1)
N(3)	5090(3)	1481(1)	1424(3)	25(1)
N(4)	2349(3)	1807(1)	-412(3)	25(1)
O(3)	7628(3)	2893(1)	368(2)	29(1)
O(4)	4983(3)	3325(1)	-1130(2)	29(1)
O(5)	7142(3)	4106(1)	135(2)	28(1)
N(5)	6576(3)	3443(1)	-200(2)	22(1)
Zn(1)	0	0	0	18(1)
O(1W)	1486(3)	-317(1)	-2396(2)	22(1)

Table 9-23: Atomic positions and temperature factors of atoms in $[Zn(urea)_4(H_2O)_2][NO_3]_2$

Bond lengths / Å		Bond angles / °	
C(1)-O(1)	1.259(3)	O(1)-C(1)-N(2)	122.26(19)
C(1)-N(2)	1.329(3)	O(1)-C(1)-N(1)	119.8(2)
C(1)-N(1)	1.344(3)	N(2)-C(1)-N(1)	117.9(2)
O(1)-Zn(1)	2.0891(14)	C(1)-O(1)-Zn(1)	136.27(13)
N(1)-H(1A)	0.846(17)	C(1)-N(1)-H(1A)	119(2)
N(1)-H(1B)	0.827(16)	C(1)-N(1)-H(1B)	120(2)
N(2)-H(2A)	0.856(16)	H(1A)-N(1)-H(1B)	117(3)
N(2)-H(2B)	0.849(17)	C(1)-N(2)-H(2A)	120(2)
C(2)-O(2)	1.258(2)	C(1)-N(2)-H(2B)	117(2)
C(2)-N(4)	1.330(3)	H(2A)-N(2)-H(2B)	119(3)
C(2)-N(3)	1.346(3)	O(2)-C(2)-N(4)	122.3(2)
O(2)-Zn(1)	2.0754(15)	O(2)-C(2)-N(3)	119.4(2)
N(3)-H(3A)	0.852(16)	N(4)-C(2)-N(3)	118.29(19)
N(3)-H(3B)	0.860(16)	C(2)-O(2)-Zn(1)	139.43(15)
N(4)-H(4A)	0.853(17)	C(2)-N(3)-H(3A)	116(2)

N(4)-H(4B)	0.855(16)	C(2)-N(3)-H(3B)	120(2)
O(3)-N(5)	1.256(2)	H(3A)-N(3)-H(3B)	112(3)
O(4)-N(5)	1.249(3)	C(2)-N(4)-H(4A)	117(2)
O(5)-N(5)	1.253(2)	C(2)-N(4)-H(4B)	123(2)
Zn(1)-O(2)#1	2.0754(15)	H(4A)-N(4)-H(4B)	120(3)
Zn(1)-O(1)#1	2.0891(14)	O(4)-N(5)-O(5)	120.14(18)
Zn(1)-O(1W)	2.1446(16)	O(4)-N(5)-O(3)	119.53(17)
Zn(1)-O(1W)#1	2.1446(16)	O(5)-N(5)-O(3)	120.3(2)
O(1W)-H(1)	0.79(3)	O(2)#1-Zn(1)-O(2)	180.00(11)
O(1W)-H(2)	0.83(3)	O(2)#1-Zn(1)-O(1)	90.92(6)
		O(2)-Zn(1)-O(1)	89.08(6)
		O(2)#1-Zn(1)-O(1)#1	89.08(6)
		O(2)-Zn(1)-O(1)#1	90.92(6)
		O(1)-Zn(1)-O(1)#1	180.00(12)
		O(2)#1-Zn(1)-O(1W)	87.99(6)
		O(2)-Zn(1)-O(1W)	92.01(6)
		O(1)-Zn(1)-O(1W)	89.32(6)
		O(1)#1-Zn(1)-O(1W)	90.68(6)
		O(2)#1-Zn(1)-O(1W)#1	92.01(6)
		O(2)-Zn(1)-O(1W)#1	87.99(6)
		O(1)-Zn(1)-O(1W)#1	90.68(6)
		O(1)#1-Zn(1)-O(1W)#1	89.32(6)
		O(1W)-Zn(1)-O(1W)#1	180.00(12)
		Zn(1)-O(1W)-H(1)	118(2)
		Zn(1)-O(1W)-H(2)	110(2)
		H(1)-O(1W)-H(2)	106(3)

Table 9-24: Bond lengths and angles in $[Zn(urea)_4(H_2O)_2][NO_3]_2$

Composition	$[Ni(urea)_4(H_2O)_2][NO_3]_2$
Empirical formula	$C_4H_{20}N_{10}NiO_{12}$
Formula weight / g mol^{-1}	458.96
Temperature / K	150(2)
Wavelength / Å	0.71073
Crystal system	Monoclinic
Space group	$P2_1/n$
a / Å	6.407(4)
b / Å	17.650(7)
c / Å	7.543(5)
β / °	91.43(5)
V / $Å^3$	852.7(8)
Z	2
Density(calculated) / mg m^{-3}	1.788
Absorption coefficient / mm^{-1}	1.223
F(000)	476
Theta range for data collection / °	2.94-32.00
Index ranges	$-9 \leq h \leq 9, -26 \leq k \leq 24, -11 \leq l \leq 9$
Reflections collected	8754
Independent reflections	2876 [R(int) = 0.0532]
Completeness to theta = 32.00°	96.9%
Absorption correction	None
Refinement method	Full-matrix least-squares on F^2
Data / restraints / parameters	2876 / 28 / 164
Goodness-of-fit on F^2	1.018
Final R indices [I>2sigma(I)]	R1 = 0.0404, wR2 = 0.1007
R indices (all data)	R1 = 0.0574, wR2 = 0.1103
Largest diff. peak and hole / e $Å^{-3}$	0.631 and −1.127

Table 9-25: Refinement data for $[Ni(urea)_4(H_2O)_2][NO_3]_2$

10.0 References

[1] W. Hume-Rothery, Atomic Theory For Students Of Metallurgy, *The Institute of Metals*, London, 1946.

[2] W. Hume-Rothery, G. W. Mabbott and K. M. Channel-Evans, *Philos. Trans. R. Soc. London, Ser. A*, 1934, **233**, 1-97.

[3] D. H. Gregory, M. G. Barker, P. P. Edwards, M. Slaski and D. J. Siddons, *J. Solid State Chem*., 1998, **137**, 62-70.

[4] E. Magnone, M. Miyayama and E. Traversa, *Cryst. Res. Technol*., 2010, **45**, 355-364.

[5] J. D. Corbett, *Inorg. Chem*., 2010, **49**, 13-28.

[6] A. R. West, Solid State Chemistry And Its Applications, *Wiley*, New York, 1990.

[7] M. Wang, Y. Zhang and M. Muhammed, *Nanostruct. Mater*., 1999, **12**, 237-240.

[8] A. L. Hector and I. P. Parkin, *Z. Naturforsch., B: Chem. Sci*., 1994, **49**, 477-482.

[9] C. J. Carmalt, D. E. Morrison and I. P. Parkin, *Polyhedron*, 2000, **19**, 829-833.

[10] R. E. Cable and R. E. Schaak, *Chem. Mater*., 2005, **17**, 6835-6841.

[11] C. E. M. Campos, J. C. de Lima, T. A. Grandi, M. Schmitt and P. S. Pizani, *J. Phys.: Condens. Matter*, 2006, **18**, 8613-8622.

[12] P. Amornpitoksuk and S. Suwanboon, *J. Alloys Compd*., 2009, **473**, 373-375.

[13] J. W. Sharp, E. C. Jones, R. K. Williams, P. M. Martin and B. C. Sales, *J. Appl. Phys*., 1995, **78**, 1013-1018.

[14] Z. Bukowski, D. Badurski, J. Stępień-Damm and R. Troć, *Solid State Commun.*, 2002, **123**, 283-286.

[15] T. Caillat, A. Borshchevsky and J. P. Fleurial, *J. Appl. Phys*., 1996, **80**, 4442-4449.

[16] J. Xie, G. S. Cao, X. B. Zhao, M. J. Zhao, Y. D. Zhong, L. Z. Deng, Y. H. Guan and Z. T. Wu, *J. Mater. Sci*., 2004, **39**, 1105-1107.

[17] J. Xie, X. B. Zhao, H. M. Yu, H. Qi, G. S. Cao and J. P. Tu, *J. Alloys Compd*., 2007, **441**, 231-235.

[18] L. M. L. Fransson, J. T. Vaughey, R. Benedek, K. Edstrom, J. O. Thomas and M. M. Thackeray, *Electrochem. Commun*., 2001, **3**, 317-323.

[19] H. Nowotny and J. Pesl, *Monatsh. Chem*., 1951, **82**, 336-343.

[20] B. Grison and P. A. Beck, *Acta Crystallogr*., 1962, **15**, 807-808.

[21] V. M. Goldschmidt, *Physica*, 1927, **7**, 74-79.

[22] H. Nagasaki, I. Wakabayashi and S. Minomura, *J. Phys. Chem. Solids*, 1969, **30**, 329-337.

[23] A. Kjekshus and K. P. Walseth, *Acta Chem. Scand*., 1969, **23**, 2621-2630.

[24] T. Rosenqvist, *Acta Metall*., 1953, **1**, 761-763.

[25] R. N. Kuz'min, *Kristallografiya*, 1958, **3**, 366-367.

[26] K. Endresen, S. Furuseth, K. Selte, A. Kjekshus, T. Rakke and A. F. Andresen, *Acta Chem. Scand. Ser. A*, 1977, **31**, 249-252.

[27] R. Berger, *Acta Chem. Scand. Ser. A*, 1977, **31**, 514-516.

[28] B. Frick, J. Schoenes, F. Hulliger and O. Vogt, *Solid State Commun*., 1984, **49**, 1133-1137.

[29] A. S. Mikhaylushkin, J. Nylén and U. Häussermann, *Chem. Eur. J*., 2005, **11**, 4912-4920.

[30] Y. Mozharivsky, A. O. Pecharsky, S. Bud'ko and G. J. Miller, *Chem. Mater*., 2004, **16**, 1580-1589.

[31] K. J. Range, J. Pfauntsch and U. Klement, *Acta Crystallogr., Sect. C: Cryst. Struct. Commun*., 1988, **44**, 2196-2197.

[32] M. G. Haase, H. Block and W. Jeitschko, *Z. Anorg. Allg. Chem*., 2001, **627**, 1941-1948.

[33] E. Garcia and J. D. Corbett, *J. Solid State Chem*., 1988, **73**, 452-467.

[34] A. F. Wells, Structural Inorganic Chemistry, *Oxford University Press*, New York, 1984.

[35] D. J. Vaughan and J. R. Craig, Mineral Chemistry Of Metal Sulfides, *Cambridge University Press*, New York, 1978.

[36] S. Furuseth, K. Selte and A. Kjekshus, *Acta Chem. Scand*., 1967, **21**, 527-536.

[37] A. Kjekshus, T. Rakke and A. F. Andresen, *Acta Chem. Scand. Ser. A*, 1974, **28**, 996-1000.

[38] H. D. Lutz, M. Jung and G. Waeschenbach, *Z. Anorg. Allg. Chem*., 1987, **554**, 87-91.

[39] M. Rieder, J. C. Crelling, O. Sustai, M. Drabek, Z. Weiss and M. Klementova, *Int. J. Coal Geol*., 2007, **71**, 115-121.

[40] A. A. Temperley and H. W. Lefevre, *J. Phys. Chem. Solids*, 1966, **27**, 85-92.

[41] A. Kjekshus, T. Rakke and A. F. Andresen, *Acta Chem. Scand. Ser. A*, 1977, **31**, 235-259.

[42] T. Harada, T. Kanomata, Y. Takahashi, O. Nashima, H. Yoshida and T. Kaneko, *J. Alloys Compd*., 2004, **383**, 200-204.

[43] E. Makovicky, Crystal Structures of Sulfides and Other Chalcogenides, in: D. J. Vaughan (Ed.), Sulfide Mineralogy and Geochemistry, Reviews in Mineralogy and Geochemistry 61, *Mineralogical Society of America*, Chantilly, Virginia, 2006, pp. 7-125

[44] M. J. Bürger, *Z. Kristallogr*., 1936, **95**, 83-113.

[45] A. Kjekshus, *Acta Chem. Scand*., 1971, **25**, 411-422.

[46] P. I. Kripiakevich, Structure Types of Intermetallic Compounds, *Nauka*, Moscow, 1977.

[47] K. Schubert, Kristallstrukturen zweikomponentiger Phasen, *Springer*, Berlin,1964.

[48] H. Nowotny and K. Schubert, *Z. Metallkd*., 1946, **37**, 17-23.

[49] A. Kjekshus and T. Rakke, *Acta Chem. Scand. Ser. A*, 1974, **28**, 99-103.

[50] N. N. Greenwood and A. Earnshaw, Chemistry Of The Elements, *Butterworth-Heinemann*, Oxford, 1997.

[51] J. Nuss, U. Wedig and M. Jansen, *Z. Kristallogr*., 2006, **221**, 554-562.

[52] W. N. Stassen, M. Sato and L. D. Calvert, *Acta Crystallogr., Sect. B: Struct. Sci*., 1970, **26**, 1534-1540.

[53] T. Z. Vitkina, N. D. Zhigadlo and V. M. Ryzhkovskii, *Cryst. Res. Technol*., 1988, **23**, 945-948.

[54] S. Derakhshan, A. Assoud, K. M. Kleinke, E. Dashjav, X. Qui, S. J. L. Billinge and H. Kleinke, *J. Am. Chem. Soc*., 2004, **126**, 8295-8302.

[55] J. -E. Jørgensen and S. E. Rasmussen, *Acta Crystallogr., Sect. B: Struct. Sci*., 1982, **38**, 346-347.

[56] P. M. Clark, S. Lee and D. C. Fredrickson, *J. Solid State Chem*., 2005, **178**, 1269-1283.

[57] B. A. Hatt, J. K. R. Page and V. G. Rivlin, *J. Low Temp. Phys*., 1973, **10**, 285-298.

[58] H. Boller and E. Parthé, *Acta Crystallogr*., 1963, **16**, 830-833.

[59] S. Furuseth, K. Selte and A. Kjekshus, *Acta Chem. Scand*., 1965, **19**, 95-106.

[60] G. Melnyk and W. Tremel, *J. Alloys Compd*., 2003, **349**, 164-171.

[61] L. M. Hoistad, *Inorg. Chem*., 1995, **34**, 2711-2717.

[62] E. Günzel and K. Schubert, *Z. Metallkd.*, 1958, **49**, 124-133.

[63] W. Burkhardt and K. Schubert, *Z. Metallkd.*, 1959, **50**, 442-452.

[64] U. Häussermann, M. Elding-Pontén, C. Svensson and S. Lidin, *Chem. Eur. J.*, 1998, **4**, 1007-1015.

[65] P. M. de Wolff, *Acta Crystallogr., Sect. A: Found. Crystallogr*., 1985, **41**, 278-280.

[66] A. R. West, Basic Solid State Chemistry, *Wiley*, Chichester, 1999.

[67] K. D. M. Harris and M. Tremayne, *Chem. Mater*., 1996, **8**, 2554-2570.

[68] P. F. Peterson, E. S. Božin, T. Proffen and S. J. L. Billinge, *J. Appl. Cryst*., 2003, **36**, 53-64.

[69] R. J. D. Tilley, Crystals and Crystal Structures, *Wiley*, Chichester, 2006.

[70] W. Clegg, Crystal Structure Determination, *Oxford University Press*, New York, 1998.

[71] J. P. Glusker, M. Lewis and M. Rossi, Crystal Structure Analysis for Chemists and Biologists, *VCH Publishers*, Cambridge, 1994.

[72] H. M. Rietveld, *J. Appl. Crystallogr*., 1969, **2**, 65-71.

[73] A. C. Larson and R. B. Von Dreele, "General Structure Analysis System (GSAS)", *Los Alamos National Research Laboratory Report LAUR 86-748*, 1994.

[74] R. A. Young, The Rietveld Method, *Oxford University Press*, New York, 1993.

[75] L. B. McCusker, R. B. Von Dreele, D. E. Cox, D. Louër and P. Scardi, *J. Appl. Cryst*., 1999, **32**, 36-50.

[76] G. M. Sheldrick, SHELXL-97 – A program for crystal structure refinement, University of Göttingen, Germany, 1997, Release 97-2.

[77] S. K. R. Patil, N. S. Mangale, S. V. Khare and S. Marsillac, *Thin Solid Films*, 2008, **517**, 824-827.

[78] R. M. Fix, R. G. Gordon and D. M. Hoffman, *Chem. Mater.*, 1990, **2**, 235-241.

[79] K. Watari, *J. Ceram. Soc. Japan*, 2001, **109**, S7-S16.

[80] R. J. Cava, H. W. Zandbergen, B. Batlogg, H. Eisaki, H. Takagi, J. J. Krajewski, W. F. Peck Jr., E. M. Gyorgy and S. Uchida, *Nature*, 2002, **372**, 245-247.

[81] J. M. D. Coey and H. Sun, *J. Magn. Magn. Mater*., 1990, **87**, L251-L254.

[82] S. T. Oyama, The Chemistry Of Transition Metal Carbides And Nitrides, *Blackie Academic And Professional*, London, 1996.

[83] F. J. DiSalvo and S. J. Clarke, *Curr. Opin. Solid State Mater. Sci*., 1996, **1**, 241-249.

[84] J.-G. Choi, J. Ha, J.-W. Hong, *Appl. Catal., A*, 1998, **168**, 47-56.

[85] T. J. Prior and P. D. Battle, *J. Solid State Chem*., 2003, **172**, 138-147.

[86] T. J. Prior, S. E. Oldham, V. J. Couper and P. D. Battle, *Chem. Mater*., 2005, **17**, 1867-1873.

[87] S. E. Oldham, P. D. Battle, S. J. Blundell, M. L. Brooks, F. L. Pratt and T. J. Prior, *J. Mater. Chem*., 2005, **15**, 3402-3408.

[88] T. J. Prior and P. D. Battle, *J. Mater. Chem*., 2004, **14**, 3001-3007.

[89] P. J. Baker, P. D. Battle, S. J. Blundell, F. Grandjean, T. Lancaster, G. J. Long, S. E. Oldham and T. J. Prior, *Phys. Rev. B: Condens. Matter*, 2008, **77**, 134405.

[90] B. Pei, B. Björkman, B. Sundman and B. Jansson, *Calphad*, 1995, **19**, 1-15.

[91] J. Maier and E. Wachtel, *Z. Metallkd*., 1972, **63**, 411-418.

[92] I. V. Chumak, V. V. Pavlyuk, G. S. Dmytriv and J. Stepień-Damm, *J. Alloys Compd*., 2000, **307**, 223-225.

[93] Y. Zhang, C. Li, Z. Du and T. Geng, *Calphad*, 2008, **32**, 56-63.

[94] K. P. Gupta, *J. Phase Equilib*., 2000, **21**, 472-478.

[95] Y. Kawaharada, K. Kurosaki, M. Uno and S. Yamanaka, *J. Alloys Compd*., 2001, **315**, 193-197.

[96] X. L. Song, J. Y. Yang, J. Y. Peng, Y. H. Chen, W. Zhu and T. J. Zhang, *J. Alloys Compd*., 2005, **399**, 276-279.

[97] B. K. Qin, X. L. Li, S. S. Li, T. C. Su, H. A. Ma and X. P. Jia, *J. Inorg. Mater*., 2010, **25**, 23-26.

[98] L. Wang, K. F. Cai, Y. Y. Wang, H. Li and H. F. Wang, *Appl. Phys. A*, 2009, **97**, 841-845.

[99] H. Li, X. F. Tang, X. L. Su, Q. J. Zhang and C. Uher, *J. Phys. D: Appl. Phys*., 2009, **42**, 145409.

[100] R. C. Mallik, J. Y. Jung, V. D. Das, S. C. Ur and I. H. Kim, *Solid State Commun*., 2007, **141**, 233-237.

[101] W. Y. Zhao, C. L. Dong, P. Wei, W. Guan, L. S. Liu, P. C. Zhai, X. F. Tang and Q. J. Zhang, *J. Appl. Phys*., 2007, **102**, 113708.

[102] S. C. Ur and I. H. Kim, *J. Korean Phys. Soc*., 2009, **55**, 942-946.

[103] T. Itoh, E. Hattori and K. Kitagawa, *J. Propul. Power*, 2008, **24**, 359-364.

[104] S. C. Ur and I. H. Kim, *J. Korean Phys. Soc*., 2008, **53**, 2415-2418.

[105] M. J. Kim, S. C. Ur and I. H. Kim, *J. Kor. Inst. Met. Mater*., 2007, **45**, 191-194.

[106] H. Kleinke, *Chem. Mater*., 2010, **22**, 604-611.

[107] P. Terzieff and H. Ipser, *Monatsh. Chem.*, 1992, **124**, 35-42.

[108] Y. Xue, K. Liu, J. Li and N. Chen, *Mat. Res. Bull*., 2005, **40**, 1172-1176.

[109] R. Leubolt, H. Ipser, P. Terzieff and K. L. Komarek, *Z. Anorg. Allg. Chem*., 1986, **533**, 205-214.

[110] P. Feschotte and D. Lorin, *J. Less-Common Met*., 1989, **155**, 255-269.

[111] Y. Z. Huang, W. X. Yuan and Z. Y. Qiao, *Chinese J. Rar. Mat*., 2004, **28**, 707-710.

[112] M. C. Le Clanche, S. Députier, J. C. Jégaden, R. Guérin, Y. Ballini and A. Guivarc'h, *J. Alloys Compd*., 1994, **206**, 21-29.

[113] A. Kjekshus, P. G. Peterzéns, T. Rakke and A. F. Andresen, *Acta Chem. Scand. Ser. A*, 1979, **33**, 469-480.

[114] K. Cenzual, L. M. Gelato, M. Penzo and E. Parthé, *Acta Crystallogr., Sect. B: Struct. Sci*., 1991, **47**, 433-439.

[115] J. Nuss and M. Jansen, *Z. Anorg. Allg. Chem*., 2002, **628**, 1152-1157.

[116] P. Jensen, A. Kjekshus and T. Skansen, *Acta Chem. Scand*., 1966, **20**, 403-416.

[117] A. Osawa, *Nature*, 1927, **124**, 14.

[118] V. M. Goldschmidt, *Skrifter utgitt av det Norske Videnskaps-Akademi i Oslo 1*, 1927, 1-156.

[119] W. Morris Jones and E. G. Bowen, *Nature*, 1930, **126**, 846-847.

[120] G. Hägg and A. G. Hybinette, *Philos. Mag. Ser*., 1935, **20**, 913-929.

[121] C. A. MacKay, *J. Appl. Crystallogr*., 1969, **2**, 295-297.

[122] V. Vassiliev, M. Lalaurain and J. Hertz, *J. Alloys Compd*., 1997, **247**, 223-233.

[123] E. P. Nikolaeva, V. A. Grigorenko, S. D. Gagarkina and P. Y. Tsypkina, *Zap. Vseross. Mineral. Ova*., 1970, **99**, 68-70.

[124] D. Rose, *Neues Jahrb. Mineral. Monatsh*., 1981, **3**, 117-126.

[125] L. Norén, R. L. Withers, S. Schmid, F. J. Brink and V. Ting, *J. Solid State Chem*., 2006, **179**, 404-412.

[126] J. P. Turbil, Y. Billiet and A. Michel, *C. R. Hebd. Seances Acad. Sci*., 1969, **269**, 309-311.

[127] K. Yasukochi, K. Kanematsu and T. Ohoyama, *J. Phys. Soc. Jpn*., 1961, **16**, 429-433.

[128] G. Hägg and G. Funke, *Z. Phys. Chem. B*, 1929, **6**, 272-283.

[129] P. Feschotte and J.-M. Rosset, *J. Less-Common Met*., 1988, **143**, 31-37.

[130] M. Ruck, *Z. Anorg. Allg. Chem*., 1999, **625**, 2050-2054.

[131] M. Ruck and T. Söehnel, Z. Naturforsch., B: Chem. Sci., 2006, 61, 785-791.

[132] T. J. Prior, *Private Communication*.

[133] A. I. Vogel, A Textbook of Quantitative Inorganic Analysis, Including Elementary Instrumental Analysis, Fourth Edition, *Longman*, London, 1978.

[134] J. E. Huheey, E. A. Keiter and R. L. Keiter, Inorganic Chemistry: Principles of Structure and Reactivity, Fourth Edition, *Harper Collins*, New York, 1993.

[135] A. J. Bard, R. Parsons and J. Jordan, Standard Potentials in Aqueous Solution, *Marcel Dekker*, New York, 1985.

[136] C. S. G. Phillips and R. J. P. Williams, Inorganic Chemistry Volume 1, *Oxford University Press*, New York, 1965.

[137] J. Gopalakrishnan, S. Pandey and K. Kasthuri, *Chem. Mater*., 1997, **9**, 2113-2116.

[138] J. Naud and D. Parijs, *Mater. Res. Bull*., 1972, **7**, 301-308.

[139] Y. Kabalov, E. V. Sokolova, E. M. Spiridonov and F. M. Spiridonov, *Dokl. Akad. Nauk*., 1994, **335**, 709-711.

[140] H. Fjellvåg, K. Selte and F. E. Stave, *Acta Chem. Scand*., 1984, **38**, 687-691.

[141] J. M. Da, C. Brochado Oliveira and I. R. Harris, *J. Mater. Sci*., 1983, **18**, 3649-3660.

[142] M. Ellner, *Z. Metallkd*., 1976, **67**, 246-249.

[143] P. de Meester de Betzembroeck and J. Naud, *Bull. Soc. Chim. Belg*., 1971, **80**, 107-116.

[144] G. I. Kulesko and A. L. Seryagin, *Fiz. Met. Metalloved*., 1968, **26**, 140-143.

[145] Y. Chen, J. Shen and N. X. Chen, *Solid State Commun*., 2009, **149**, 121-125.

[146] R. Guérin and A. Guivarc'h, *J. Appl. Phys*., **66**, 2122-2128.

[147] D. M. R. Lo Cascio and H. Bakker, *Phys. Status Solidi A*, 1993, **135**, 611-619.

[148] L. Vegard, *Z. Angew. Phys*., 1921, **5**, 17-26.

[149] C. S. Barrett, P. Cucka and K. Haefner, *Acta Cryst*., 1963, **16**, 451-453

[150] Y. Kabalov and E. Sokolova, *Mater. Sci. Forum*, 1998, **278-281**, 785-790.

[151] I.-K. Suh, H. Ohta and Y. Waseda, *J. Mater. Sci*., 1988, **23**, 757-760.

[152] K. O. Klepp and K. L. Komarek, *Monatsh. Chem*., 1972, **103**, 934-946.

[153] G. I. Makovetskii and G. M. Shakhlevich, *Neorg. Mater*., 1982, **18**, 186-189.

[154] V. N. Kamat Dalal and H. V. Keer, *J. Less-Common Met*., 1975, **40**, 145-151.

[155] L. D. Gulay and I. D. Olekseyuk, *J. Alloys Compd*., 2004, **376**, 131-138.

[156] K. T. Wojciechowski, *J. Alloys Compd*., 2007, **439**, 18-24.

[157] A. Harnwunggmoung, K. Kurosaki, A. Charoenphakdee, A. Yusufum H. Muta and S. Yamanaka, *Mater. Trans*., 2010, **51**, 882-886.

[158] A. Borshchevsky, J. –P. Fleurial, E. Allevato and T. Caillat, *Proceedings ICT '94 - Thirteenth International Conference on Thermoelectrics*, 1995, **316**, 3-6.

[159] E. G. Moshopoulou, R. M. Ibberson, J. L. Sarrao, J. D. Thompson and Z. Fisk, *Acta Crystallogr., Sect. B: Struct. Sci*., 2006, **62**, 173-189.

[160] H. E. Swanson and G. M. Ugrinic, *J. Res. Nat. Bur. Stand*., 1955, **539**, 1-75.

[161] X. Shi, W. Zhang, L. D. Chen and C. Uher, *Int. J. Mat. Res*., 2008, **99**, 638-643.

[162] J. –P. Fleurial, T. Caillat and A. Borshchevsky, *Proceedings ICT '97 – Sixteenth International Conference on Thermoelectrics*, 1997, 1-11.

[163] A. Kjekshus and T. Rakke, *Acta Chem. Scand*., 1970, **24**, 3317-3325.

[164] M. H. Müller and H. W. Knott, *Trans. Metall. Soc. AIME*, 1963, **227**, 674.

[165] J. Leciejewicz, *J. Less-Common Met*., 1964, **7**, 318-320.

[166] D. S. Bem, C. P. Gibson and H.-C. zur Loye, *Chem. Mater*., 1993, **5**, 397-399.

[167] S. K. Jackson, R. C. Layland and H.-C. zur Loye, *J. Alloys Compd*., 1999, **291**, 94-101.

[168] K. S. Weil and P. N. Kumta, *Mater. Sci. Eng., B*, 1996, **38**, 109-117.

[169] K. S. Weil and P. N. Kumta, *J. Alloys Compd*., 1998, **265**, 96-103.

[170] K. S. Weil and P. N. Kumta, *Acta Crystallogr., Sect. C: Cryst. Struct. Commun*., 1997, **53**, 1745-1748.

[171] A. Gomathi, *Mater. Res. Bull*., 2006, **42**, 870-874.

[172] P. S. Herle, M. S. Hegde, K. Sooryanarayana, T. N. Guru Row and G. N. Subbanna, *Inorg. Chem*., 1998, **37**, 4128-4130.

[173] R. N. Panda, G. Balaji, P. K. Pandey and N. S. Gajbhiye, *Hyperfine Interact*., 2008, **184**, 245-250.

[174] H. M. Zhang, Z. Zhao, C. M. Xu, A. J. Duan, W. Y. Lin, H. J. Tian and I. E. Wachs, *Mater. Res. Bull*., 2006, **41**, 2334-2340.

[175] P. S. Herle, M. S. Hegde, K. Sooryanarayana, T. N. Guru Row and G. N. Subbanna, *J. Mater. Chem*., 1998, **8**, 1435-1440.

[176] A. El-Himri, D. Marrero-López and P. Núñez, *J. Solid State Chem*., 2004, **177**, 3219-3223.

[177] A. El-Himri, F. Sapiña, R. Ibañez and A. Beltrán, *J. Mater. Chem*., 2001, **11**, 2311-2314.

[178] L. A. Sviridov, P. D. Battle, F. Grandjean, G. J. Long and T. J. Prior, *Inorg. Chem*., 2010, **49**, 1133-1143.

[179] H. G. von Schnering and R. Nesper, *Acta Chem. Scand*., 1991, **45**, 870-872.

[180] A. S. Cooper, *Acta Crystallogr*., 1962, **15**, 578-582.

[181] R. Mackay, G. J. Miller and H. F. Franzen, *J. Alloys Compd*., 1994, **204**, 109-118.

[182] S. M. Hunter, D. McKay, R. I. Smith, J. S. J. Hargreaves and D. H. Gregory, *Chem. Mater*., 2010, **22**, 2898-2907.

[183] H. Aghabozorg, G. J. Palenik, R. C. Stoufer and J. Summers, *Inorg. Chem*., 1982, **21**, 3903-3907.

[184] T. Todorov, R. Petrova, K. Kossev, J. Macícek and O. Angelova, *Acta Crystallogr., Sect. C: Cryst. Struct. Commun.*, 1998, **54**, 927-929.

[185] A. Krawczuk and K. Stadnicka, *Acta Crystallogr., Sect. C: Cryst. Struct. Commun*., 2007, **63**, 448-450.

[186] Y. Qui and L. Gao, *J. Am. Ceram. Soc*., 2004, **87**, 352-357.

[187] Z. Durski and T. Gibinski, *Rocz. Chem*.,1972, **46**, 1945-1951.

[188] R. D. Shannon, *Acta Crystallogr., Sect. A: Found. Crystallogr*., 1976, **32**, 751-767.